INFORMATION TO USERS

This manuscript has been reproduced from the microfilm master. UMI films the text directly from the original or copy submitted. Thus, some thesis and dissertation copies are in typewriter face, while others may be from any type of computer printer.

The quality of this reproduction is dependent upon the quality of the copy submitted. Broken or indistinct print, colored or poor quality illustrations and photographs, print bleedthrough, substandard margins, and improper alignment can adversely affect reproduction.

In the unlikely event that the author did not send UMI a complete manuscript and there are missing pages, these will be noted. Also, if unauthorized copyright material had to be removed, a note will indicate the deletion.

Oversize materials (e.g., maps, drawings, charts) are reproduced by sectioning the original, beginning at the upper left-hand corner and continuing from left to right in equal sections with small overlaps. Each original is also photographed in one exposure and is included in reduced form at the back of the book.

Photographs included in the original manuscript have been reproduced xerographically in this copy. Higher quality 6" x 9" black and white photographic prints are available for any photographs or illustrations appearing in this copy for an additional charge. Contact UMI directly to order.

UMI®

Bell & Howell Information and Learning
300 North Zeeb Road, Ann Arbor, MI 48106-1346 USA
800-521-0600

Reproduced with permission of the copyright owner. Further reproduction prohibited without permission.

Reproduced with permission of the copyright owner. Further reproduction prohibited without permission.

A

SPECTRAL ELLIPSOMETRY AND REFLECTION DIFFERENCE ANISOTROPY STUDIES OF SEMICONDUCTORS: OPTICAL PROPERTY MEASUREMENT AND MODELING

By

Todd Holden

A dissertation submitted to the Graduate Faculty in Physics in partial fulfillment of the requirements for the degree of Doctor of Philosophy, The City University of New York

1999

Reproduced with permission of the copyright owner. Further reproduction prohibited without permission.

UMI Number: 9946176

Copyright 1999 by
Holden, Todd Marshall

All rights reserved.

UMI Microform 9946176
Copyright 1999, by UMI Company. All rights reserved.

This microform edition is protected against unauthorized
copying under Title 17, United States Code.

UMI
300 North Zeeb Road
Ann Arbor, MI 48103

Reproduced with permission of the copyright owner. Further reproduction prohibited without permission.

© 1999

TODD HOLDEN

All Rights Reserved

Reproduced with permission of the copyright owner. Further reproduction prohibited without permission.

This Manuscript has been read and accepted for the Graduate Faculty in Physics in satisfaction of the dissertation requirement for the degree of Doctor of Philosophy.

July 28, 1999
Date

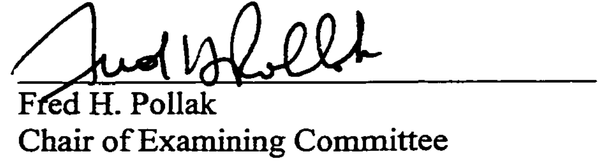

Fred H. Pollak
Chair of Examining Committee

July 28, 1999
Date

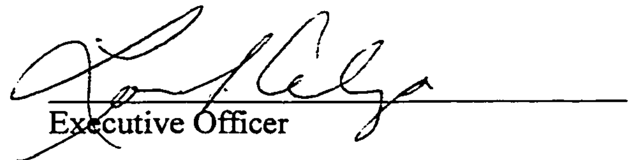

Executive Officer

John Freeouf
Ken Miyano
Maria Tamargo
Micha Tomkiewicz

Supervisory Committee

THE CITY UNIVERSITY OF NEW YORK

Reproduced with permission of the copyright owner. Further reproduction prohibited without permission.

Abstract

SPECTRAL ELLIPSOMETRY AND REFLECTION DIFFERENCE ANISOTROPY STUDIES OF SEMICONDUCTORS: OPTICAL PROPERTY MEASUREMENT AND MODELING

by

Todd Holden

Adviser: Professor Fred H. Pollak

To model spectral ellipsometry (SE) data, we introduced a new model of the dielectric function for diamond and zincblende-type semiconductors. Our model is the first to include discrete and band-to-band Coulomb enhanced (BBCE) effects, i.e., continuum exciton at the fundamental bandgap, the spin orbit split gap, and the higher lying E_1, $E_1+\Delta_1$ doublet. Our analysis has yielded experimental evaluation of the 2D exciton binding energies at the E_1, $E_1+\Delta_1$ CP's, R_1. We show that the features near the E_1, $E_1+\Delta_1$ CP's are actually due to the bound exciton, which can be several hundred meV below the these CP's. The extracted R_1 values using our model are in good agreement with effective-mass **k•p** theory.

Reproduced with permission of the copyright owner. Further reproduction prohibited without permission.

We have measured and modeled the optical constants of $Zn_{0.53}Cd_{0.47}Se$/InP in the range 0.8-5.5 eV. Because of the high quality of our samples, we have been able to extract a number of imports materials parameters, including excitonic binding energies at E_0, $E_0+\Delta_0$ and E_1, $E_1+\Delta_1$. We find the native oxide thickness to be ≈ 20 Å.

Using SE in the range 0.3-5.45 eV we have evaluated the dielectric function of a series of *n*- and *p*-doped $In_{0.66}Ga_{0.34}As$ samples. The Burstein-Moss (BM) shift was taken into account using a Fermi level filling factor in addition to the excitonic and BBCE terms at the fundamental absorption edge. The *n*-type samples had pronounced nonparabolicity at the highest doping level.

We used reflection difference anisotropy (RDA) spectroscopy to evaluate the sign and magnitude of the near surface electric field [$\mathscr{E}(z)$] in NID, *n*-type, and *p*-type LTG:GaAs (001). We also have performed a self-consistent Poisson's calculation to determine $\mathscr{E}(z)$ since this material has a non-conventional space charge region. Even for the most heavily *p*-doped samples the band-bending is still *n*-type, although near flatband. Our experiment and calculation agree well with midgap surface Fermi level pinning and "effective depletion widths" ≤22Å.

We used RDA to study optical anisotropies induced by the difference of misfit (60°) dislocation density along the [110] direction compared to the $[1\bar{1}0]$ direction in InGaAs/AlGaAs/GaAs HEMT structures.

Reproduced with permission of the copyright owner. Further reproduction prohibited without permission.

We performed an RDA study of ordered $Ga_{0.5}In_{0.5}P$/GaAs and $In_{0.48}(Ga_{1-x}Al_x)_{0.52}P$/GaAs grown by MOCVD.

Reproduced with permission of the copyright owner. Further reproduction prohibited without permission.

Acknowledgments

I gratefully thank Fred H. Pollak who took great time and effort to educate me in solid state physics and kept me productive throughout the course of this thesis. He is the person most responsible for making me into a true physicist (besides myself), and I believe I will never be able to repay him for this. Many thanks go to John Freeouf who taught me much about ellipsometry and was always able to find the faults in or open new horizons on any topic we discussed. I also thank my committee members Ken Miyano, Maria Tamargo, and Micha Tomkiewicz for interesting discussions and education.

Special thanks go to my brother Jon Holden and Sean Kelly who sustained me throughout the time of the writing of this thesis. They were also instrumental in the final preparation of this document. Thanks to my parents Marvin and Leslie Holden and my other brother Eric Holden for bringing me up, supporting me, and putting up with me over the years.

I thank the secretaries in the Brooklyn College Physics Department, Laura Incampo, Mary Shea, and Suzanne Whiter, for taking care of me. Also thanks to the department chair, Peter Lesser, and all faculty for a well organized and personal department. In addition thanks to many special and important friends for keeping me sane, among them, Lionel Aigouy, Rosalie Diego, Liz and Jim Ritter, Bing Xiao Yang, Chester White, Mario Roque, Martin Munoz, Kun Wei, Scott Friedberg, Marie Stack, Paul Huang, Facundo Ruiz, Ludmilla Malikova, Irwin Meyer, Pascal Chevrot, Alex Moulin, Seymore Bernstein, David Daitch, Laurie Ferguson, Miguel Coelho, and Fabio Gardenal.

Reproduced with permission of the copyright owner. Further reproduction prohibited without permission.

Contents

Abstract iv

Acknowledgments vii

List of Figures xiii

List of Tables xx

List of Commonly Used Symbols xxi

List of Abbreviations xxvii

Introduction 1

Chapter 1. Ellipsometry 6

1.1 Historical Overview 6

1.2 Overview of the Measurement Technique 9

1.3 Experimental Technique (Phase Modulated Ellipsometry) 15

1.3.1 Basic Theory of PME 18

1.3.2 Alignment of the Apparatus 23

1.3.2.1 Sample alignment 24

1.3.2.2 Angle of Incidence Calibration 26

1.3.2.3 Alignment of Polarizer, Modulator, and Analyzer Angles 27

1.3.2.4 Modulation Amplitude Calibration 27

1.3.2.5 Monochromator Calibration 29

1.3.3 Etching Procedures 29

1.3.3.1 Fume Hood Etching 31

1.3.3.2 Etching on the Sample Stand 33

Reproduced with permission of the copyright owner. Further reproduction prohibited without permission.

1.4 Experimental Details Mid-IR 36
1.4.1 Workings of FTIR spectrometer 39
1.4.2 Deviations Due to Refraction at the Polarizers 42
1.4.3 Calibration of the Instrument 43
1.4.3.1 Alignment of the Light Beam 44
1.4.3.2 Alignment of the Analyzer and Polarizer 44
1.4.3.3 Calibration – Correction for Imperfect Polarizers 46
1.4.3.4 Calibration – Mirror and Retarder Corrections 48
1.4.4 Measurement Details (FTIR) 52
1.4.4.1 Various Settings – Advanced Scan Menu 56
1.4.4.2 Etching Procedures (FTIR) 60
1.4.4.3 Purge Gas Generator 61
1.5 Application to physical (structural) models 63
1.5.1 Two-phase model 63
1.5.2 Three-Phase Model and Effects of Real Surfaces 70
1.5.3 *m*-phase model 74
1.5.4 Effective Medium Theory 84
1.6 Theory – Dielectric Function 94
1.6.1 Relations Between Optical Properties 95
1.6.2 Band Structure/Critical Points 100
1.6.3 Effective Mass Approximation-Envelope Function 108
1.6.4 Relation of Dielectric Function To Quantum Transitions 117

Reproduced with permission of the copyright owner. Further reproduction prohibited without permission.

1.6.5 Relation of Dielectric Function To Quantum Transitions Considering Excitonic Effects 126

1.6.6 Indirect Transitions 130

1.6.7 The Krammers Kronig Relation and Dielectric Function Symmetries 138

1.7 Modeling – lineshape 143

1.7.1 E_0 and $E_0+\Delta_0$ Features 147

1.7.2 E_1 and $E_1+\Delta_1$ Features 158

1.7.3 Discussion of E_1 Exciton Binding Energies 166

1.7.4 E_0' and E_2 Features 171

1.7.5 Indirect Transitions Features 172

1.7.6 Total Dielectric Function/Other Considerations 174

1.8 Experimental Results 178

1.8.1 $Zn_{0.53}Cd_{0.47}Se$ Lattice Matched to InP 178

1.8.1.1 Introduction 179

1.8.1.2 Experimental Details 181

1.8.1.3 Results and Analysis 184

1.8.1.4 Oxide Effects 196

1.8.1.5 Discussion 201

1.8.2 *n*- and *p*-Type $In_{0.66}Ga_{0.34}As$ on InP 204

1.8.2.1 Introduction 205

1.8.2.2 Experimental Details 206

1.8.2.3 Results and Analysis 208

1.8.2.3 Discussion of Results 217

Reproduced with permission of the copyright owner. Further reproduction prohibited without permission.

Chapter 2. Reflection Difference Anisotropy 227

2.1 Historical Overview 227

2.2 Overview of the Measurement Technique 229

2.3 Experimental Details (Phase Modulated RDA) 232

2.3.1 Elimination of Background 234

2.3.2 Alignment of the Apparatus 235

2.3.2.1 Sample Leveling 236

2.3.2.2 Sample Alignment 236

2.3.3 Signal to Noise Ratio Problems in the IR 237

2.3.4 Etching Procedures 238

2.3.5 Extension to FTIR-based RDA 238

2.4 Theory of Selected RDA signals 242

2.4.1 Linear Electro-Optic Effect Near E_1 and $E_1+\Delta_1$ Transitions 242

2.4.2 Strain Field Associated with Misfit Dislocations 251

2.4.3 Ordering 257

2.5 Experimental Results 262

2.5.1 Undoped *n*- and *p*-doped Low Temperature Grown GaAs 262

2.5.1.1 Introduction 263

2.5.1.2 Experimental Details 264

2.5.1.2 Experimental Results and Discussion 266

2.5.2 High Electron Mobility Transistors Structures 277

2.5.2.1 Introduction 278

2.5.2.2 Experimental Details 279

Reproduced with permission of the copyright owner. Further reproduction prohibited without permission.

2.5.2.2 Experimental Results and Discussion 282

2.5.3 Ordered GaInP and InGaAsP 285

2.5.3.1 Introduction 285

2.5.3.2 Experimental Details 287

2.5.3.3 Experimental Results and Discussion 288

Chapter 3. Summary and Conclusions 292

Appendix A. Extraction of Ellipsometric Parameters from Raw Data 296

A.1 A Brief Overview of Polarization States of Light 296

A.2 Mueller Matrix Formalism 299

A.3 Jones Matrix Formalism 305

A.4 Higher Order Corrections For Rotating Analyzer Systems 307

A.5 Extraction of Ellipsometric Parameters for Imperfect Polarizers 308

Appendix B. Effects of Light Focusing 312

References 316

Reproduced with permission of the copyright owner. Further reproduction prohibited without permission.

List of Figures

Figure 1. Light reflecting from a sample surface at angle ϕ. The incident light is linearly polarized with electric field components $\mathscr{E}_{ip}$ and $\mathscr{E}_{is}$ in the directions parallel and perpendicular to the plane of propagation, respectively. The reflected light is elliptically polarized with electric field components $\mathscr{E}_{rp}$ and $\mathscr{E}_{rs}$ in the directions parallel and perpendicular to the plane of propagation, respectively, which are in general out of phase with each other. This illustrates the basic principle of ellipsometry, that both the magnitude and phase of light reflected from a surface depend on the polarization of light, converting linearly polarized light into elliptically polarized light based on the dielectric function of the reflector 7

Figure 2. $|\tilde{r}_p|$, $|\tilde{r}_s|$, δ_p, and δ_s, the magnitude and phase of the reflection coefficient as a function of angle of incidence for the *p*- and *s*-eigenpolarizations, for $\varepsilon_1 = 8$ and $\varepsilon_2 = 1.8$. Maximum sensitivity is achieved at the pseudo-Brewster's angle (about 71° in this case) 11

Figure 3. Ψ and Δ as a function of angle of incidence for $\varepsilon_1 = 8$ and $\varepsilon_2 = 1.8$ (values for $Zn_{0.53}Cd_{0.47}Se$ at 2.5 eV). 13

Figure 4. Experimental setup for PME. (a) shows normal configuration for energies above 1.5 eV. (b) shows a second configuration with the monochromator before the sample in order to avoid signal from sample photoluminescence. (b) has an extra fiber optic cable in the light path 16

Figure 5. Autocollimator for adjusting sample tilt. (a) Schematic of the collimator. An image of crosshairs is created from a light path which includes a reflection from the sample and focused to the viewport by a lens at the bottom of the collimator. This image was compared to the reference of the fixed crosshairs viewed directly. (b) The image seen upon looking through the viewport. The sample stand level was adjusted until the reflected crosshairs did not move when the sample stand was rotated 25

Figure 6. Experimental setup for fume hood etching. After etching, the sample is placed into a dry methanol bath for transfer to the sample stand. Measurement was made under flowing N_2. A fan was used to keep the dry N_2 away from the PEM 32

Figure 7. Experimental setup for etching on the sample stand. (a) Detail of covered sample stand shown upright for clarity. (b) Covered sample stand mounted on ellipsometer. (c) Top view of researcher etching

Reproduced with permission of the copyright owner. Further reproduction prohibited without permission.

sample. Exit hole is covered during etching to keep splash off ellipsometer........34

Figure 8a. Experimental setup for MIR measurement (ellipsometer inside FTIR spectrometer)........37

Figure 8b. Detail of ellipsometer used for MIR measurement........38

Figure 9. Schematic of a Michelson interferometer. The exiting interfering light beam has an intensity based on the position of the moving mirror, x........40

Figure 10. Height/tilt alignment. Beam A is used to adjust the tilt, then beam B is used to adjust the height. Three motorized screws are used to adjust the height and tilt........54

Figure 11. "Advanced Scan" dialog box with typical settings........57

Figure 12. Purge gas generator setup........62

Figure 13. Two phase model. Light is incident from medium a on a semi-infinite substrate (medium b). $\hat{\mathbf{n}}$ is we define the unit normal vector to the surface. The electric field magnitude components parallel to the plane of incidence, the electric field magnitude components perpendicular to the plane of incidence, and wave vectors of the incident, transmitted, and reflected light are ($\mathscr{E}_{ip}$, $\mathscr{E}_{is}$, $\mathbf{k}_i^L$), ($\mathscr{E}_{tp}$, $\mathscr{E}_{ts}$, $\mathbf{k}_t^L$), and ($\mathscr{E}_{rp}$, $\mathscr{E}_{rs}$, $\mathbf{k}_r^L$) respectively. The s and p-components of the electric fields make up the incident, transmitted and reflected electric field vectors, $\mathbf{E}_i$, $\mathbf{E}_t$, and $\mathbf{E}_r$, respectively........65

Figure 14. Three phase model. Multiple reflections occur at the two interfaces causing interference........71

Figure 15. Calculated pseudodielectric function for a GaAs substrate with native oxide overlayers of various thicknesses as shown........75

Figure 16. A stack of m layers with planar parallel interfaces, the top and bottom (ambient and substrate) layers being semi-infinite. Dielectric functions and angles of incidence for each layer are labeled by the layer index........77

Figure 17. Two phase system using the notation of this section. This is exactly the geometry of section 1.5.1, if we make the identifications $\mathscr{E}_i \rightarrow \mathscr{E}_a^+$, $\mathscr{E}_t \rightarrow \mathscr{E}_b^+$, and $\mathscr{E}_r \rightarrow \mathscr{E}_a^-$........80

Figure 18. Schematic diagram of the simple cubic lattice used in the derivation of the Clausius-Mossotti relation. $\mathbf{E}_{int}$ is a uniform applied field........86

Reproduced with permission of the copyright owner. Further reproduction prohibited without permission.

Figure 19. Band structure of GaAs (Ref. 56) showing the E_0, $E_0+\Delta_0$, E_1, $E_1+\Delta_1$, E_2, E_0', and E_{ind} interband CPs 103

Figure 20. The two likely indirect gap absorption processes. In the path labeled 1, an electron is excited via a virtual (non-energy conserving) transition by absorption of a photon (1). This transition still conserves momentum due to the translation symmetry of the crystal. A second virtual transition takes the electron from this state to the final state at a different **k** vector, $\mathbf{q} = \mathbf{k}_c - \mathbf{k}_v$ through the absorption or emission of a phonon(1'). A second possible phonon assisted indirect optical transition is labeled 2 132

Figure 21. Dielectric Function of $In_{0.66}Ga_{0.34}As$ showing major features at E_0, $E_0+\Delta_0$, E_1-R_1, $E_1+\Delta_1-R_1$, E_2, and E_0' along with the fit developed in this section. For this material, the E_2 and E_0' CPs are at nearly the same energy and were not resolved, so a they were treated as a single structure 144

Figure 22. Contribution to the dielectric function of $\tilde{\varepsilon}_{E_1^{CP}}(E)$ and $\tilde{\varepsilon}_{E_1^{CP}+\Delta_1}(E)$ based on Eqs. (243) and (248) and the fit parameters for $Zn_{0.53}Cd_{0.47}Se$ from Table xxx. The solid, dotted, and dashed lines represent the total, bound exciton, and BBCE contributions to the dielectric function. The arrows at the bottom of the figure denote the values of E_1, E_1-R_1, $E_1+\Delta_1$, and $E_1+\Delta_1-R_1$ 167

Figure 23. The ellipsometric data (a) $\cos(\Delta)$ and (b) $\tan(\psi)$ of $Zn_{0.53}Cd_{0.47}Se$/InP (oxide removed) measured at an angle of incidence of 70° in the range 0.8-5.5 eV 182

Figure 24. Electronic energy-band structure of zincblende ZnSe calculated by nonlocal empirical pseudopotential method after Ref. 56 185

Figure 25. Electronic energy-band structure of zincblende CdSe calculated by nonlocal empirical pseudopotential method, showing the main interband critical points after Ref. 83 186

Figure 26. The solid lines are the experimental values of ε_1 and ε_2 (oxide removed) in the range 0.8-5.5 eV. The dashed lines are the fits to Eq. (263) 188

Figure 27. The solid lines are the experimental values of n and κ (oxide removed) in the range 0.8-5.5 eV. The dashed lines are the fits 189

Figure 28. The solid line is the experimental value of ε_2 (oxide removed) in the region of E_0. The dashed line is the fit Eq. 263 190

Reproduced with permission of the copyright owner. Further reproduction prohibited without permission.

Figure 29. The solid lines are the experimental values of $d\varepsilon_1/dE$ and $d\varepsilon_2/dE$. The dashed lines are the fits to Eq. (245) 194

Figure 30. The solid lines are the experimental values of $d^2\varepsilon_1/dE^2$ and $d^2\varepsilon_2/dE^2$. The dashed lines are the fits to Eq. (246) 195

Figure 31. Individual contributions of the various transitions to ε_1 197

Figure 32. Individual contributions of the various transitions to ε_2 198

Figure 33. The solid lines are $<\varepsilon_1>$ and $<\varepsilon_2>$ for the as-received sample (native oxide). The dashed lines are ε_1 and ε_2 after removal of the oxide 199

Figure 34. The solid lines are $<\varepsilon_1>$ and $<\varepsilon_2>$ for the as-received sample (native oxide). The dashed lines are ε_1 and ε_2 after removal of the oxide 200

Figure 35. Experimental values of ε_1 for *p*-type samples A-E. ε_1 for samples B, C, D, and E are displaced in increments of two units for clarity 209

Figure 36. Experimental values of ε_2 for *p*-type samples A-E. ε_2 for samples B, C, D, and E are displaced in increments of two units for clarity. The dashed line is a fit to sample A based on Eq. (264) 210

Figure 37. Experimental values of ε_1 for *n*-type samples F-K. ε_1 for samples G, H, I, J, and K are displaced in increments of two units for clarity 211

Figure 38. Experimental values of ε_2 for *n*-type samples F-K. ε_2 for samples G, H, I, J, and K are displaced in increments of two units for clarity 212

Figure 39. Experimental values (solid lines) of ε_2 in the region of the fundamental absorption edge for *p*-type samples A and E. Dashed lines are the fits 213

Figure 40. Experimental values (solid lines) of ε_2 in the region of the fundamental absorption edge for *n*-type samples F and K. Dashed lines are the fits 214

Figure 41. Electronic energy-band structure of zincblende InAs calculated by nonlocal empirical pseudopotential method after Ref. 56 216

Figure 42. The solid lines are the numerical values of the second derivative of ε_1 and ε_2 for sample F (from Figs. 37 and 38). The dashed lines are fits to Eq. (265) yielding the values of E_1-R_1 and of $E_1+\Delta_1-R_1$ indicated by the arrows 218

Figure 43. Solid squares and triangles are E_{abs} for *n*- and *p*-type samples, respectively, as a function of (dopant concentration)$^{2/3}$. The solid lines are fits to a linear function 220

Reproduced with permission of the copyright owner. Further reproduction prohibited without permission.

Figure 44. $|\Delta(E_1\text{-}R_1)|$ and $|\Delta(E_1+\Delta_1\text{-}R_1.)|$ as a function of doping concentration for the *n*- and *p*-type samples. Representative error bars are shown 226

Figure 45. RDA meaurement. Light reflecting off a surface at near-normal incidence. The difference between reflectance for light polarized along the two principal axes measures the optical anisotopy of the sample 228

Figure 46. RDA setup. (a) is configuation used above 1.5 eV. (b) shows the configuation used in below 1.5 eV, which has three fiber optic cables in the light path instead of two 233

Figure 47. RDA data taken for a polarizer using the FTIR based ellipsometer 240

Figure 48. RDA data taken for a polarizer using the phase modulation based (ISA) ellipsometer 241

Figure 49. Zincblende structure. Bonds in the $[\bar{1}11]$ and $[1\bar{1}1]$ directions (shown as white) all have As on the bottom and Ga on top, while bonds in the [111] and $[\bar{1}\bar{1}1]$ directions (shown as black) have Ga on the bottom and As on top. (a) shows the conventional zincblende cell. (b) shows the same conventional cell looking down in the [001] direction 244

Figure 50. Diagram of the <111> states under the influence of an electric field along the [001] direction 248

Figure 51. Schematic representation of the formation of misfit dislocations. (a) unstrained lattice, (b) thickness of the film less than the critical thickness, h_c, and (c) thickness of the film greater than h_c – misfit dislocations are generated 252

Figure 52. Illustration of zone folding due to complete CuPt-type ordering. (a) shows a schematic band for the zincblende structure along the Λ direction. (b) shows the situation for an ordered material. The BZ now ends at $\mathbf{k} = \pi/2a[111]$ instead of $\pi/a[111]$, and the part of the band originally between $\mathbf{k} = \pi/2a[111]$ and $\pi/a[111]$ now shows up as a new band in the smaller BZ, which we call the zone-folded band 259

Figure 53. Schematic depiction of states for random and ordered alloys. Two major effects of the zone folding are the splitting of the E_0 transition due to the splitting of the valence band ($\Gamma_{8v} \rightarrow \Gamma_{4v},\Gamma_{5v} + \Gamma_{6v}$) and the reduction of E_0 due to the lowering of the lowest lying (Γ_{6c}) conduction band 260

Figure 54. RDA spectra of sample Nos. R1 (dotted line), 2 (solid line), R2 (dashed line), and R3 (dot-dashed line). The positions of the "E_1" and "$E_1+\Delta_1$" features are denoted by arrows at the bottom of the figure 267

Reproduced with permission of the copyright owner. Further reproduction prohibited without permission.

Figure 55. RDA spectra of sample Nos. 1 (solid line), 2 (dotted line), 3 (dashed line), 4 (dot-dashed line), and 5 (dot-dot-dashed line). The positions of the "E_1" and "$E_1+\Delta_1$" features are denoted by arrows at the bottom of the figure 268

Figure 56. $d(\Delta R/R)/dE$ spectra of sample Nos. 2 (solid line), R1 (dotted line), and R2 (dashed line). The positions of the "E_1" and "$E_1+\Delta_1$" features are denoted by arrows at the bottom of the figure 270

Figure 57. $d(\Delta R/R)/dE$ spectra of sample Nos. 1 (solid line), 2 (dotted line), 3 (dashed line), 4 (dot-dashed line), and 5 (dot-dot-dashed line). The positions of the E_1 and $E_1+\Delta_1$ features are denoted by arrows at the bottom of the figure 272

Figure 58. Self-consistent Poisson's, continuity calculation of the field distribution $\mathcal{E}(z)$ for sample Nos. 1 (solid line), 2 (dotted line), 3 (dashed line), 4 (dot-dashed line), 5 assuming complete doping (dot-dot-dashed line), and 5 assuming an incomplete doping of p=4x10^{19} cm^{-3} (long dashed line) 274

Figure 59. Schematic band diagram for HEMT structures 280

Figure 60. RDA signal for samples #1-#4. The arrows at the bottom of the figure indicate the E_0 transitions for GaAs and $Ga_{0.75}Al_{0.25}As$ 283

Figure 61. ΔRDA for samples #2-#4. ΔRDA is defined as the difference between the RDA signal for the sample and the RDA signal for sample #1. The arrows at the bottom of the figure indicate the E_0 transitions for GaAs and $Ga_{0.75}Al_{0.25}As$ 284

Figure 62. Real and imaginary parts of the RDA signal for ordered (solid lines) and random (dashed lines) $In_{0.48}(Ga_{1-x}Al_x)_{0.52}P$/GaAs. For clarity, the real and imaginary parts of the random sample have been displaced by –0.02 and –0.03, respectively. The positions of E_0 and E_1 are indicated by arrows 289

Figure 63. Real and imaginary parts of the RDA signal for ordered InGaP. The positions of E_0 is indicated by the arrow at the bottom of the figure....291

Figure A1. Path of electric field vector over time for elliptically polarized light. $\mathcal{E}_p$ and $\mathcal{E}_s$ are the electric field components parallel and perpendicular to the plane of incidence, respectively They are related to Ψ^L by $\tan\Psi^L = \frac{|\mathcal{E}_p|}{|\mathcal{E}_s|}$. The eccentricity of the ellipse is determined by the relative phase of the s- and p-polarized light, $\Delta^L = \delta_p^L - \delta_s^L$ 298

Reproduced with permission of the copyright owner. Further reproduction prohibited without permission.

Figure B1. Simulation of ellipsometric parameters using a three phase model with and without focusing effects considered (solid and dashed lines, respectively). The structure consists of 1 μm $1.06x10^{19}$ *n*-doped $In_{0.66}Ga_{0.34}As$ (sample J in section 1.8.2) on an InP substrate. (a) Ψ and Δ for the range 0.3-5.5 eV. (b) Ψ and Δ near and below the bandgap of the $In_{0.66}Ga_{0.34}As$ layer - 0.3-1.5 eV 314

Figure B2. Dielectric function of the $1.06x10^{19}$ *n*-doped InGaAs layer as extracted using a three phase model with InP substrate for the ellipsometric parameters given in Fig. B1. (solid and dashed lines, respectively). The structure consists of 1 μm (sample J in section 1.8.2) on an InP substrate. (a) ε_1 and ε_2 for the range 0.3-5.5 eV. (b) Ψ and Δ near and below the bandgap of InGaAs: 0.3-1.5 eV 315

Reproduced with permission of the copyright owner. Further reproduction prohibited without permission.

List of Tables

Table I. Etchants for Various Materials 25

Table II. Extracted R_1 values for several materials using our model and theoretical values given by Eq. (251) 165

Table III. Material parameters used in the calculation of the optical constants of $Zn_{0.53}Cd_{0.47}Se/InP$. Values for ZnSe from Ref. 79 also are listed....................186

Table IV. Doping levels and fitting parameters for the fundamental absorption edge. Γ_0 was 60 meV for all samples....................202

Table V. Materials parameters for the fit of ε_2 for sample A 217

Table VI. Energies and broadening parameters for the E_1-R_1 and $E_1+\Delta_1$-R_1 transitions obtained from a fit to Eq. (265)....................219

Table VII. Doping levels, $\mathscr{E}_{eff}$ (experiment and simulation), $\mathscr{E}(0)$, γ, $1/\alpha_{eff}$, and V_{BI} for the five LTG:GaAs samples....................259

Table VIII. Misfit dislocation densities along the [110] and [$1\bar{1}0$] directions for different InGaAs channel thicknesses and different substrates 275

Reproduced with permission of the copyright owner. Further reproduction prohibited without permission.

List of Commonly Used Symbols

Symbol	Meaning
$\tilde{\varepsilon}$	complex dielectric function = $\varepsilon_1 + i\,\varepsilon_2$
$\tilde{\varepsilon}_i$	complex dielectric for the ith layer
$\langle\tilde{\varepsilon}\rangle$	complex pseudo-dielectric function
$\tilde{r}_p$	complex Fresnel reflection coefficients for p-polarized light
$\tilde{r}_s$	complex Fresnel reflection coefficients for s-polarized light
$\tilde{r}_{[011]}$	complex Fresnel reflection coefficient along the $[110]$ direction
$\tilde{r}_{[0\bar{1}1]}$	complex Fresnel reflection coefficient along the $[1\bar{1}0]$ direction
$\tilde{\rho}$	$\tilde{\rho} = \frac{\tilde{r}_p}{\tilde{r}_s} = \tan\Psi e^{i\Delta}$
$\tilde{n}$	complex index of refraction: $\tilde{n} = n + i\kappa$
$\tilde{\mu}$	complex magnetic permeability
$\hat{\mathbf{n}}$	unit vector normal to the surface
$\tilde{\chi}(\omega)$	electric susceptibility
$\psi_{l,\mathbf{k}}(\mathbf{r})$	Bloch function for band index l and wavevector $\mathbf{k}$
$\hbar$	Planck's constant
$\mathbf{M}_{eR,ep}(\mathbf{k},\mathbf{k}')$	indirect interband transition matrix
$\frac{\Delta R}{R}$	real component of the RDA signal
ϕ	angle of incidence

Reproduced with permission of the copyright owner. Further reproduction prohibited without permission.

Symbol	Meaning
Ψ	conventional ellipsometric angle, $\tan \Psi = \lvert\tilde{r}_p\rvert / \lvert\tilde{r}_s\rvert$
Δ	conventional ellipsometric angle, $\Delta=\delta_p-\delta_s$
ω	angular frequency of light
κ	imaginary index of refraction
ξ	polarizability
α	absorption coefficient
Γ	the center of the Brillouin zone
Δ	direction from Γ to X
Λ	direction from Γ to L
Ω	volume of the crystal
$\mathcal{E}$	electric field magnitude
$\Delta\theta$	imaginary component of the RDA signal
$\Phi(r, t)$	scalar potential
$\delta(t)$	time dependent phase shift (introduced by PEM)
μ^*	reduced electron-hole effective mass
$\mathcal{E}^+(z)$, $\mathcal{E}^-(z)$	complex electric field amplitudes of the forward- and backward-travelling plane waves
ε_0	static dielectric constant
ε_1	real component of dielectric function
ε_2	imaginary component of dielectric function
δ_{ij}	Kronecker delta function
τ_{max}	maximum polarizer transmission
τ_{min}	minimum polarizer transmission

Reproduced with permission of the copyright owner. Further reproduction prohibited without permission.

Symbol	Meaning
A	analyzer position
a	lattice constant
$A(\mathbf{r}, t)$	vector potential
a_{ex}	effective Bohr radius
A_M	modulation voltage amplitude
b	Burger's vector
c	speed of light
c_{ij}	conventional components of the elastic stiffness tensor (Young's modulus)
D	electric displacement
$D(E)dE$	JDOS
d_{14}	piezoelectric constant
d_i	layer thickness
E	photon energy
e	electron charge
$\mathbf{e}$	strain tensor
$\hat{\mathbf{e}}$	light polarization vector
$\mathbf{E}$, $\mathbf{B}$, $\mathbf{k}$	electric field, magnetic induction and wave propagation vectors
E_0', $E_0'+\Delta_0'$	energies of the second lowest lying and spin orbit split CP at the Γ point of the BZ
E_0, $E_0+\Delta_0$	energies of the lowest lying and spin orbit split CP at the Γ point of the BZ
E_1, $E_1+\Delta_1$	energies 2D spin orbit split doublet CP along the <111> (Λ) directions
E_2	energy of CP near X point and along the Σ direction

Reproduced with permission of the copyright owner. Further reproduction prohibited without permission.

Symbol	Meaning
E_c	energy of the conduction band
E_g	bandgap energy of interest
E_{ind}	energy of lowest lying indirect CP
E_v	energy of the valence band
e_{xy}	shear strain
$F(\mathbf{r})$	envelope function
f_i	volume fraction of the ith phase
$\mathbf{G}$	reciprocal lattice vector
$\mathbf{H}$	magnetic field
H_{1e}	one-electron Hamiltonian
h_c	critical thickness
H_{ep}	electron-phonon Hamiltonian
H_{eR}	electromagnetic radiation field Hamiltonian
I	light intensity
I_0	initial light intensity
I_C	Fourier cosine component of light intensity
I_{DC}	direct current light intensity
I_S	Fourier sine component of light intensity
$J_n(A_M)$	n^{th} Bessel function of A_M
$\mathbf{k}$	electron wavevector, crystal momentum/$\hbar$
$\mathbf{k}'$	electron wavevector, crystal momentum/$\hbar$
$\mathbf{k}_0$	electron wave vector at a particular BZ CP
$\mathbf{k}_1$, $\mathbf{k}_2$	real and imaginary parts of the wave propagation vectors

Reproduced with permission of the copyright owner. Further reproduction prohibited without permission.

Symbol	Meaning
$\mathbf{k}_e$	electron wave vector
$\mathbf{k}_{ex}$	exciton wave vector
$\mathbf{k}_h$	hole wave vector
$\mathbf{k}^L$	light wave vector
L	Brillouin zone edge at $\mathbf{k} = \pi/a$ [111]
$\mathbf{l}$	dislocation core direction vector
M	modulator position
m^*	electron effective mass
m_0	free electron mass
n	real index of refraction
N_D	donor concentration
P	polarizer position
$\mathbf{p}$	momentum operator ($= -i\hbar\nabla$)
$\mathbf{p}_i$	point dipole polarization
R	ground state exciton binding energy (the Rydberg) for the E_0
$\mathbf{r}$	position vector
R_1	2D ground state exciton binding energy (Rydberg) for the E_1 CP
R_i	lattice vector
t	time
u	time averaged energy density of a wave traveling into the material
$u_{l,\mathbf{k}}(\mathbf{r})$	cell periodic part of Bloch function
$V(\mathbf{r})$	potential
X	Brillouin zone edge at $\mathbf{k} = 2\pi/a$ [100]

Reproduced with permission of the copyright owner. Further reproduction prohibited without permission.

Symbol	Meaning
z	z component of position vector (depth from sample surface)

Reproduced with permission of the copyright owner. Further reproduction prohibited without permission.

List of Abbreviations

Abbreviation	Meaning
SE	spectroscopic or spectral ellipsometry
RDA	reflectance difference anisotropy
CP	critical point
BE	bound exciton
BBCE	band to band Coulomb enhancement
CE	continuum exciton
2D	two dimensional
3D	three dimensional
NIR	near infra-red
UV	ultraviolet
FTIR	Fourier transform infra-red
MIR	mid infrared
BM	Burstien-Moss
NSEF	near-surface electric fields
SCR	space charge region
LTG	low temperature grown
HEMT	high electron mobility transistor
QW	quantum well
RAE	rotating analyzer ellipsometry
RPE	rotating polarizer ellipsometry

Reproduced with permission of the copyright owner. Further reproduction prohibited without permission.

Abbreviation	Meaning
PME	photo modulated ellipsometry
PEM	photoelastic modulator
EMA	effective medium approximation
BS	band structure
KK	Kramers-Kronig
JDOS	joint density of states
DHO	damped harmonic oscillator
MBE	molecular-beam-expitaxy
MOCVD	Metal-Organic Chemical Vapor Deposition
TPV	Thermophotovoltaic
LEO	linear electro-optic
NID	not-intentionally doped
FKO	Franz-Keldysh oscillation
TEM	transmission electron microscopy
VGF	vertical gradient freeze
LEC	liquid encapsulated Czochralski
LTDD	low threading dislocation density
HTDD	high threading dislocation density
DC	direct current

Reproduced with permission of the copyright owner. Further reproduction prohibited without permission.

Introduction

Optical techniques are powerful methods for studying both isotropic and anisotropic properties of semiconductors. In this thesis, we have investigated the electronic properties of a number of new semiconductor materials and semiconductor interfaces with two of the most useful optical techniques: spectroscopic ellipsometry (SE), which probes primarily bulk optical properties as well as sample structure, and reflectance difference anisotropy (RDA) spectroscopy, which is sensitive to optical anisotropies that can be due to surfaces, near-surface electric fields, buried hetero interfaces, dislocations, and ordering.

SE is a powerful method for determining the intrinsic optical functions (either the real and imaginary index of refraction, n and κ, or the real and imaginary dielectric function, ε_1 and ε_2) of the material. The structure of these optical functions is primarily due to direct and indirect interband transitions, exciton interactions, phonons (polar materials), and free carrier effects. In the energy range of our measurements, the first two are the most important, with most of the observed structure coming near interband critical points (CP's) (extrema of the interband energy levels of the band structure). In an interband transition, an electron from a valence band is excited into a conduction band (also scattering a phonon in the case of indirect transitions), leaving behind a positively charged hole in the valence band. The electron-hole pair so formed interact via the Coulomb potential with two main effects on the optical function: (1) peaks occur below

Reproduced with permission of the copyright owner. Further reproduction prohibited without permission.

interband CP's due to discrete bound two-particle states formed by the Coulomb attraction called bound excitons (BE's) and (2) an enhancement of interband transition probability for transition energies at or above the CP's called band to band Coulomb enhancement (BBCE) or sometimes continuum exciton (CE). Both of these effects vary depending on the nature of the CP. The importance of the excitonic effects grows with increasing exciton binding energy, *R*.

In this thesis, we present the first correct modeling of the dielectric function for diamond and zincblende-type semiconductors[1] including discrete as well as band-to-band Coulomb enhanced (BBCE) effects, i.e., continuum exciton at the several interband critical points (CPs), including the fundamental bandgap, the spin orbit split gap, and the higher lying E_1, $E_1+\Delta_1$ doublet (transitions along the <111> directions of the Brioullin zone), which are two dimensional (2D) in nature since the effective mass for these CP's in the <111>-type direction is much greater than that in the other two directions. Because of the inclusion of these effects, we are able to obtain an excellent fit to the experimental data for $Zn_{0.53}Cd_{0.47}Se$/InP and 0.6 eV bandgap $In_{0.66}Ga_{0.34}As$ yielding several physically important parameters such as energy gaps, oscillator strength, broadening and exciton binding energies. In particular, our analysis has yielded the only experimental evaluation of the exciton binding energies at the E_1, $E_1+\Delta_1$ CP's, R_1, except for one study based on low temperature (10 K) reflectivity which measured R_1 for CdTe and ZnTe.[2] Our analysis shows that the features in the vicinity of the E_1, $E_1+\Delta_1$ CP's are actually due to the bound exciton, which can be several hundred meV below the these CP's. Although the excitonic nature of the E_1, $E_1+\Delta_1$ CP's is well established,[2-7] all but a few papers label

Reproduced with permission of the copyright owner. Further reproduction prohibited without permission.

the main BE features as the E_1, $E_1+\Delta_1$ CP energies rather than as the exciton energy. The extracted R_1 values for $Zn_{0.53}Cd_{0.47}Se$ and $In_{0.66}Ga_{0.34}As$ and those of GaSb,[8] $Ga_{1-x}In_xAs_ySb_{1-y}$ ($x\approx0.15$, $y\approx0.15$),[9] CdTe,[10] and CdS[10] determined by others using our model are in good agreement with effective-mass **k•p** theory. Our results, particularly for exciton continuum effects at E_1, have considerable implications for recent first-principles band structure calculations which include exciton effects.[11,12]

For this work we have set up two ellipsometers, including facilities for etching samples and taking measurements under N_2 purge in order to eliminate effects due to the native oxides on the semiconductor surfaces. One of the ellipsometers operates in the near infra-red (NIR), visible, and ultraviolet (UV) (0.8-5.3 eV), while a Fourier transform infra-red (FTIR) ellipsometer operates in the mid infrared (MIR) and NIR (0.1-1.1 eV). The overlap of the two systems in the NIR gives use the unique ability to measure continuously over the range 0.1-5.3 eV. This allowed us to make the first near-bandgap ellipsometric measurements on 0.6 eV bandgap $In_{0.66}Ga_{0.34}As$ and study the pronounced Burstien-Moss (BM) shift of the bandgap to higher energies due to band filling in highly doped materials. Both the material and its BM shift have uses in thermo-photovoltaic applications.

SE is also quite sensitive to sample structure, and has been used to study extremely thin layers within a structure. We have used this sensitivity to determine native oxide thickness on the semiconductors we studied.

Reproduced with permission of the copyright owner. Further reproduction prohibited without permission.

While SE measures isotropic properties of materials, RDA is used to detect in-plane optical anisotropies by measuring the difference in near normal reflectivity between light polarized along the [110] and [$1\bar{1}0$] principal axes in the plane of the (001) surface of zincblende- and diamond-type semiconductors. Since materials with full cubic symmetry have no RDA signal (that is the [110] and [$1\bar{1}0$] directions are equivalent in the bulk of a perfect cubic crystal), RDA signals come only from regions that do not have full cubic symmetry, such as surfaces, [13-17] near-surface electric fields (NSEF) (zincblende),[18-25] ordering, [26-29] strain fields (including those arising from dislocations),[30,31] and buried heterojunctions.[32-34]

We have used RDA to investigate the nature of the space charge region (SCR) in a series of undoped and *n*- and *p*-doped low temperature grown (LTG) GaAs. The SCR plays an important role in semiconductor devices. RDA measures a linear electro-optic induced anisotropy and can measure even high near surface electric fields (NSEFs) well. The NSEFs in these materials is dominated by a high concentration ($\approx 10^{20}$ cm^{-3}) of deep donors ($\approx$ 0.45 eV from the conduction band) associated with arsenic antisite defects. This creates an electric field distribution for which the analytic expressions found in the literature for uniform field and conventional (linear) SCR[23] do not apply. We developed a new analysis for these samples based on a self-consistent Poisson's, continuity simulation of the electric field. Our results show that the surface Fermi level is pinned near midgap as in normal GaAs and that the space charge region is very narrow ($\approx$ 20 Å). These results are important for understanding device applications such as using LTG:GaAs as an ohmic contact to GaAs.

Reproduced with permission of the copyright owner. Further reproduction prohibited without permission.

We have also studied misfit dislocation related RDA signal in $Ga_{0.75}Al_{0.25}As/Ga_{0.79}In_{0.21}As/GaAs$ high electron mobility transistor (HEMT) structures. In these structures misfit (60°) dislocations form in the $Ga_{0.79}In_{0.21}As$ quantum well (QW) region due to strain relaxation and propagate somewhat into the GaAs and $Ga_{0.75}Al_{0.25}As$ regions when the QW is thicker than some critical thickness. The theory of how such dislocations near the surface create a RDA signal has been recently worked out.[30] We present the first RDA study of such misfit dislocations caused by strain relaxation. By comparing the RDA signal of partially strain relieved HEMT structures to a psuedomorphic one, we see RDA signals near the fundamental bandgaps of both GaAs and $Ga_{0.75}Al_{0.25}As$ which increase with increasing misfit dislocation density. The performance of HEMT devices is greatly degraded by the presence of misfit dislocations.

Finally, we measured the RDA signal due to ordering along the [111] direction in $Ga_{0.5}In_{0.5}P/GaAs$ and $In_{0.48}(Ga_{1-x}Al_x)_{0.52}P/GaAs$. In both materials, we observed signal at the fundamental bandgap of the ordered material due to an order induced valence band splitting. For the $In_{0.48}(Ga_{1-x}Al_x)_{0.52}P$ material, we observed strong signal at E_1 in addition to the signal at the fundamental bandgap, neither of which were present in disordered material. For the $Ga_{0.5}In_{0.5}P$ material we also observed a transition probably related to order induced changes of the Brioullin zone.

Reproduced with permission of the copyright owner. Further reproduction prohibited without permission.

Chapter 1. Ellipsometry

1.1 Historical Overview

SE is an optical technique that measures the change in polarization state of light upon non-normal reflection. Paul Drude was the first to study optical properties using ellipsometry, publishing the equations of ellipsometry in 1887[35] and the first experimental results in 1888.[36] Using Maxwell's equations, he showed that the polarization dependence of non-normal incidence reflectance could be used to determine both real and imaginary component of the dielectric function. Figure 1 shows light reflecting from a sample surface at an angle of incidence, ϕ. The incident light is linearly polarized with electric field components $\mathscr{E}_{ip}$ and $\mathscr{E}_{is}$ in the directions parallel and perpendicular to the plane of propagation, respectively. The reflected light is elliptically polarized with electric field components $\mathscr{E}_{rp}$ and $\mathscr{E}_{rs}$ in the directions parallel and perpendicular to the plane of propagation, respectively, which are in general out of phase with each other. This illustrates the basic principle of ellipsometry, that both the magnitude and phase of light reflected from a surface depend on the polarization of light, converting linearly polarized light into elliptically polarized light based on the dielectric function of the reflector.

Reproduced with permission of the copyright owner. Further reproduction prohibited without permission.

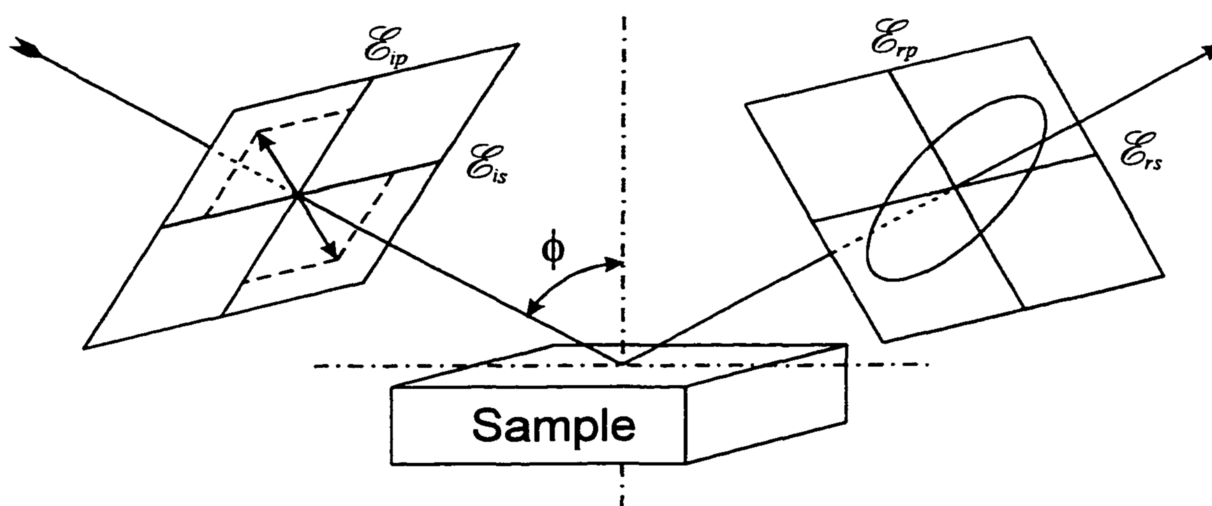

Figure 1. Light reflecting from a sample surface at angle ϕ. The incident light is linearly polarized with electric field components $\mathscr{E}_{ip}$ and $\mathscr{E}_{is}$ in the directions parallel and perpendicular to the plane of propagation, respectively. The reflected light is elliptically polarized with electric field components $\mathscr{E}_{rp}$ and $\mathscr{E}_{rs}$ in the directions parallel and perpendicular to the plane of propagation, respectively, which are in general out of phase with each other. This illustrates the basic principle of ellipsometry, that both the magnitude and phase of light reflected from a surface depend on the polarization of light, converting linearly polarized light into elliptically polarized light based on the dielectric function of the reflector

Reproduced with permission of the copyright owner. Further reproduction prohibited without permission.

Drude studied several metals[37] and Sb_2S_3, an orthorhombic (optically biaxial) crystal, obtaining results in reasonable agreement with present day accepted values.[38-40] He also realized the importance of even a thin surface oxide and studied oxide growth on freshly cleaved surfaces. Drude went on to develop the exact generalized theory of ellipsometry of absorbing materials covered by inhomogenous films, but the limited computational facilities of the time necessitated approximations to simplify the interpretation. For 75 years following Drude's pioneering work, only a handful of ellipsometric studies were done, and little improvement was made in experimental technique.

In the late 1960s, ellipsometry experienced a renaissance thanks to the availability of computers for numeric processing. This allowed automation of data acquisition, leading to the invention of spectral ellipsometry (SE), the acquisition of ellipsometric data for an entire spectrum (hundreds of wavelengths). For example by 1975, Aspnes and Studna had developed a system that could measure 200 wavelengths in 1 hour.[41] The two most important types of automated ellipsometers are those using a rotation polarizer [rotating analyzer ellipsometry (RAE) or rotating polarizer ellipsometry (RPE)] and those using a photoelastic modulator to change the phase of one polarization of the incident light [phase modulated ellipsometry (PME)].[42] In either case data can be taken quickly and without any feedback adjustments, using a computer to extract the required parameters from the raw data. In 1980, Aspnes reported that the imaginary part of the pseudo dielectric function (that is the dielectric function inferred in the presence of but neglecting surface roughness and oxide) is strongly affected by surface quality and is maximized at the E_2 peak (due to electronic interband transitions along [110] (Σ) or near

Reproduced with permission of the copyright owner. Further reproduction prohibited without permission.

the X point of the Brioullin Zone) for an oxide free smooth surface.[43] This observation allowed perfection of polishing and etching techniques to greatly improve experimental determination of dielectric functions. The sensitivity of the E_2 peak to the condition of the surface is not surprising since the light penetration depth is very small in this region.

A more complete history of ellipsometry can be found in the work by K. Vedam.[44]

1.2 Overview of the Measurement Technique

To illustrate its principle of ellipsometry, consider linearly polarized light reflected under non-normal incidence onto a sample (as shown in Fig. 1). If the light is neither s nor p polarized (i.e. perpendicular or parallel to the plane of incidence), the Fresnel Equations tell us that the s and p components will experience a different (1) phase shift and (2) attenuation upon reflection. Thus the reflected light will be elliptically polarized. The polarization ellipse can be determined, for example, by monitoring the sinusoidal intensity variation of the light after passing a rotating polarizer (a.k.a. analyzer). With the azimuth angle of the ellipse and its ellipticity two independent quantities are determined, which in turn allow one to solve the Fresnel Equations for both the real and imaginary parts of the dielectric function. In SE, one extracts the following two experimental parameters:

1. The ratio of the magnitude of reflectivities for the two eigenpolarizations.

Reproduced with permission of the copyright owner. Further reproduction prohibited without permission.

2. The relative phase shift upon reflection for the two eigenpolarizations.

These two parameters are expressed as the complex ratio

$$\begin{aligned} \tilde{\rho} &= \frac{\tilde{r}_p}{\tilde{r}_s} = \tan\Psi e^{i\Delta} \\ \tilde{r}_p &= |\tilde{r}_p| e^{i\delta_p} \\ \tilde{r}_s &= |\tilde{r}_s| e^{i\delta_s} \\ \Delta &= \delta_p - \delta_s \end{aligned} \tag{1}$$

Where $\tilde{r}_p$ ($= \frac{\mathscr{E}_{rp}}{\mathscr{E}_{ip}}$ in Fig. 1) is the complex reflection coefficient for light polarized parallel to the plane of incidence, $\tilde{r}_s$ ($= \frac{\mathscr{E}_{rs}}{\mathscr{E}_{is}}$) is the complex reflection coefficient for light polarized perpendicular to the plane of incidence, and Ψ and Δ are the traditional ellipsometric angles. $\tan\Psi = |\tilde{r}_p|/|\tilde{r}_s|$ is the amplitude of this ratio and $\Delta=\delta_p-\delta_s$ is the phase difference between the p and s polarized light, δ_p and δ_s being the phase of the parallel and perpendicular reflected light respectively. $|\tilde{r}_p|$, $|\tilde{r}_s|$, δ_p, and δ_s are shown in Fig. 2 for reflection from a semi-infinite material with real dielectric of $\varepsilon_1 = 8$ and imaginary dielectric of $\varepsilon_2 = 1.8$ (values for $Zn_{0.53}Cd_{0.47}Se$ at 2.5 eV). From the diagram, one can see why ellipsometry is usually carried out at high angles of incidence, since at the pseudo-Brewster's angle (about 71° in Fig. 2), one gets the maximum difference between the two magnitudes and the most change in the phase difference.

Reproduced with permission of the copyright owner. Further reproduction prohibited without permission.

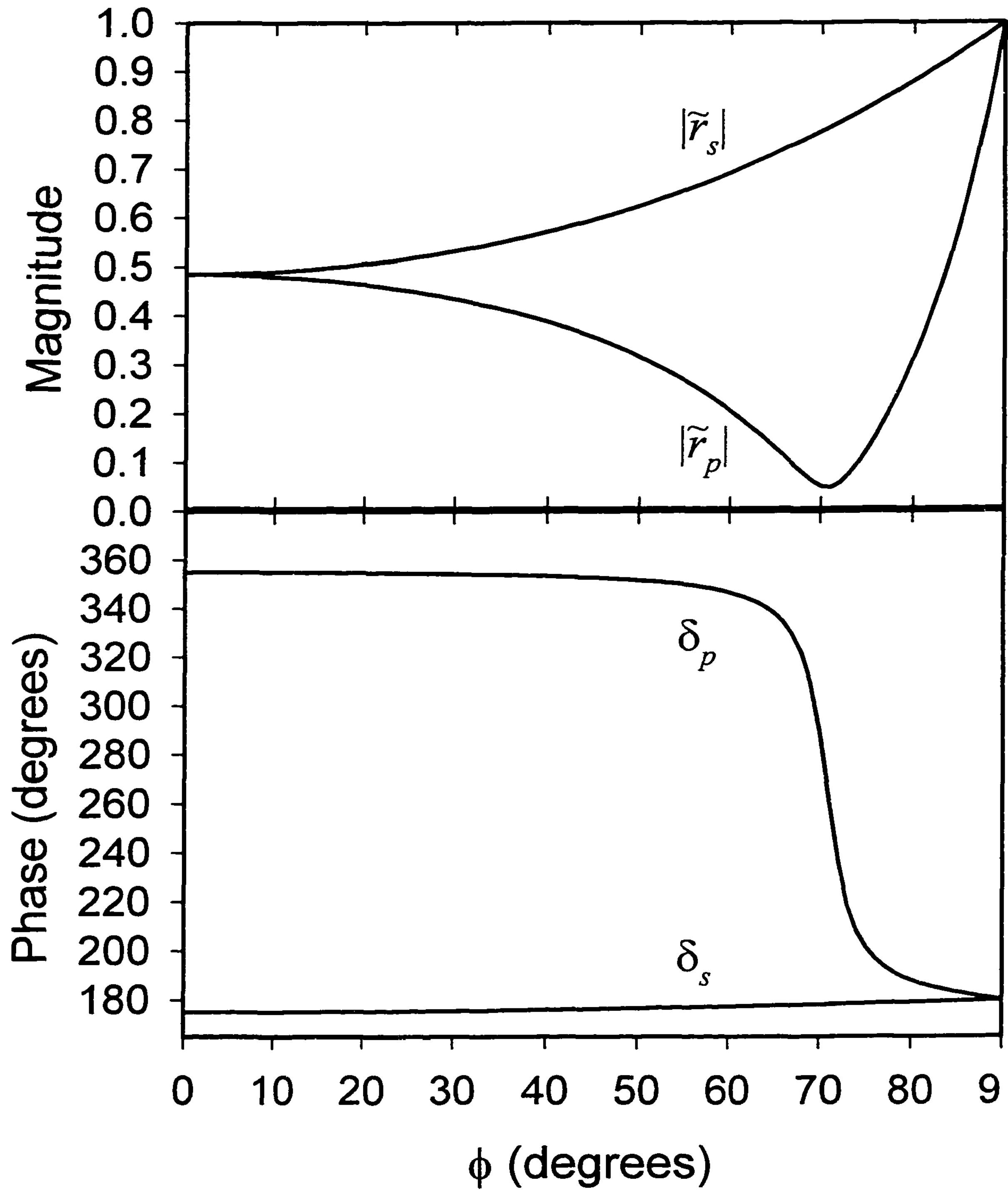

Figure 2. $|\tilde{r}_p|$, $|\tilde{r}_s|$, δ_p, and δ_s, the magnitude and phase of the reflection coefficient as a function of angle of incidence for the *p*- and *s*-eigenpolarizations, for $\varepsilon_1 = 8$ and $\varepsilon_2 = 1.8$. Maximum sensitivity is achieved at the pseudo-Brewster's angle (about 71° in this case).

Reproduced with permission of the copyright owner. Further reproduction prohibited without permission.

Ψ and Δ as a function of angle of incidence for $\varepsilon_1 = 8$ and $\varepsilon_2 = 1.8$ (values for $Zn_{0.53}Cd_{0.47}Se$ at 2.5 eV) are shown in Fig. 3.

Although Ψ and Δ were chosen because they are the output of the original null ellipsometer, they do have important physical meaning. Ψ is sensitive to the angle of incidence compared to the pseudo-Brewster's angle (the angle of minimum intensity for *p* polarized light), being minimum at this angle. Ψ is 45° for ϕ=0° and ϕ=90°. Δ is somewhat related to the absorptivity of the sample. For a transparent sample, Δ is either 180° (below Brewster's angle) or 0° (above Brewster's angle). For an absorbing sample, Δ will be between these values and will approach 90° as absorptivity increases. In either case Δ=90° at the (pseudo-)Brewster's angle, Δ=180° for ϕ=0°, and Δ=0° for ϕ=90°. The data shown in Fig. 3, the rapid decline in Δ near the pseudo-Brewster's angle indicates that the material is not very absorptive ($\varepsilon_2 = 1.8$), while the fairly large pseudo-Brewster's angle (at about 71°) indicates a large real dielectric ($\varepsilon_1 = 8$).

SE is a powerful technique, since it overcomes two major problems that plague normal incidence reflectance measurements: the phase problem (in ellipsometry the phase is measured and does not have to be calculated by Kramers-Kronig transform technique which involve extrapolations) and the reference problem (ellipsometry measures relative, not absolute, intensities).

Reproduced with permission of the copyright owner. Further reproduction prohibited without permission.

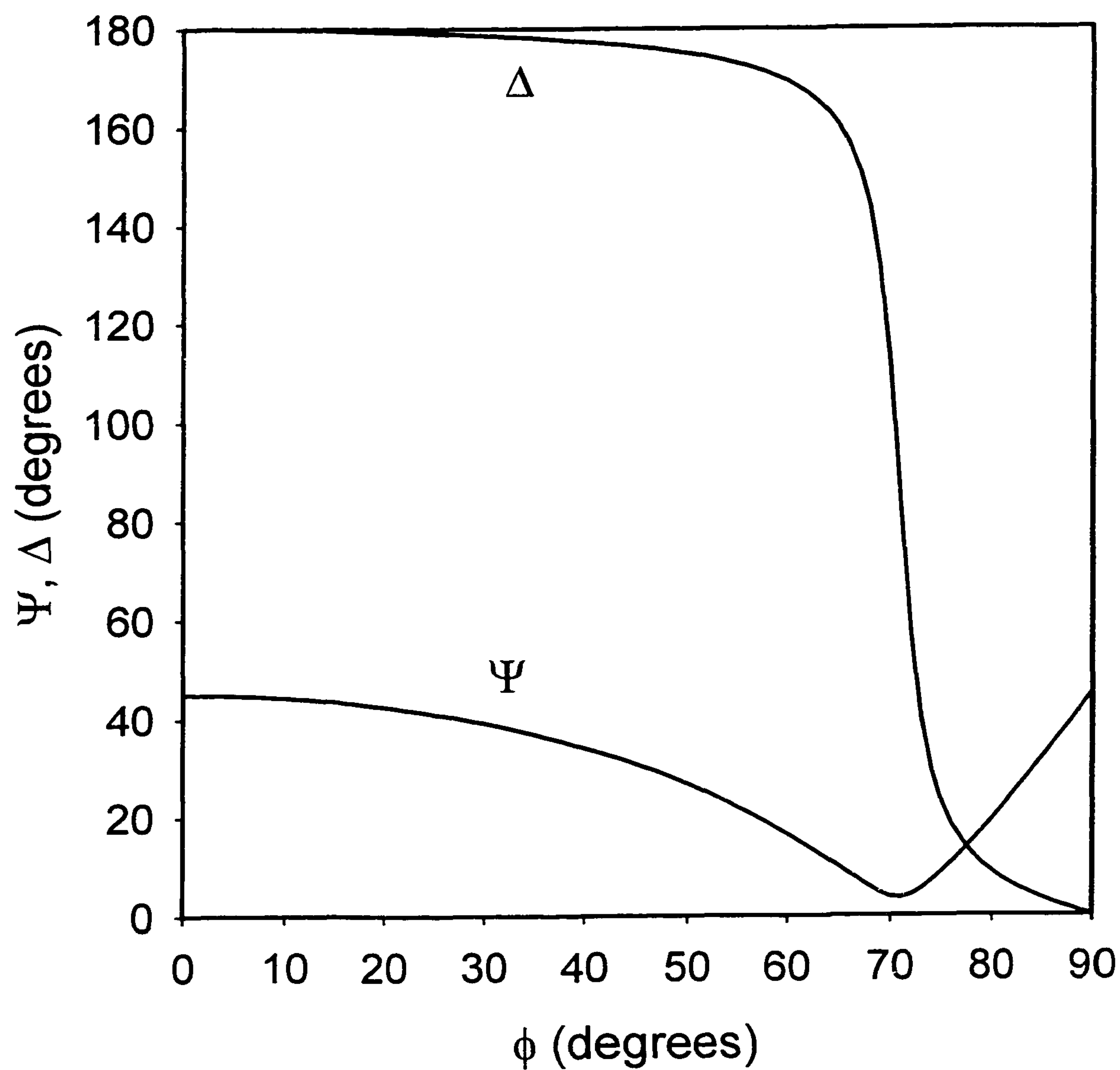

Figure 3. Ψ and Δ as a function of angle of incidence for $\varepsilon_1 = 8$ and $\varepsilon_2 = 1.8$ (values for $Zn_{0.53}Cd_{0.47}Se$ at 2.5 eV).

Reproduced with permission of the copyright owner. Further reproduction prohibited without permission.

Once $\tilde{\rho}$ is known, the dielectric constants can be determined based on Maxwell's equations and the correct model for the sample structure. Several models are discussed later in section 1.5, the simplest being the two phase model for a single interface between two semi-infinite media, *a* and *b*, in which case

$$\tilde{\varepsilon}_b = \varepsilon_{1,b} + i\varepsilon_{2,b} = \tilde{\varepsilon}_a\left[\sin^2\phi + \sin^2\phi\tan^2\phi\left(\frac{1-\tilde{\rho}}{1+\tilde{\rho}}\right)^2\right] \tag{2}$$

Where ϕ is the incidence angle of the light (in medium *a*), $\varepsilon_{1,b}$ and $\varepsilon_{2,b}$ are the real and imaginary parts of the dielectric function of the sample, respectively, and $\tilde{\varepsilon}_a$ is the complex dielectric function of the ambient (≈ 1 for air).

Often one must consider a multilayer structure in order to measure the dielectric function of a material for various reasons. Most materials have native oxide layers. Even an oxide layer of only 20Å can cause errors of 10% or more in the extracted dielectric function if ignored. Surface roughness will cause similar errors (as explained in section 1.5.2). In addition, many new materials can only be grown as thin films thus requiring one to take the bottom interface and the substrate material into account. In these cases, computer iteration as well as some knowledge of the sample structure is required in order to extract the dielectric function. The advantage of measuring this type of sample is that other parameters beside the dielectric function, such as layer thicknesses and oxide properties, can be determined. This is especially true when additional information is

Reproduced with permission of the copyright owner. Further reproduction prohibited without permission.

obtained through multiple angle of incidence measurements and etching studies. Details on calculating the ellipsometric angles for a layered stack can be found in section 1.5.

1.3 Experimental Technique (Phase Modulated Ellipsometry)

The setup for phase modulated ellipsometry (PME) (used in the UV, Visible, and NIR for this thesis) is shown in Fig. 4. Light from a 125-W xenon arc lamp was passed through an optical fiber to a Glan-type polarizer made of two calcite precision prisms then to a rectangular-shaped fused silica photoelastic modulator, which introduces a time dependent phase difference between the *s*- and *p*-polarized light exiting the modulator. The light is then reflected from the sample surface, after which the light passes through a second fixed polarizer (called the analyzer) then a second optical fiber, and then to a monochromator. For data above 1.5 eV, a double monochromator was used with a photomultiplier detector mounted on the monochromator exit slit, as shown in Fig. 4(a). For data from 0.75 to 1.5 eV, a different monochromator was placed immediately after the xenon arc lamp and the monochromatic light exiting the analyzer was passed through an optical fiber to an $In_xGa_{1-x}As$ detector, as shown in Fig. 4(b). The signal output from the detector was then sent to a spectralink controller then to a computer to collect the data and calculate Ψ and Δ.

Reproduced with permission of the copyright owner. Further reproduction prohibited without permission.

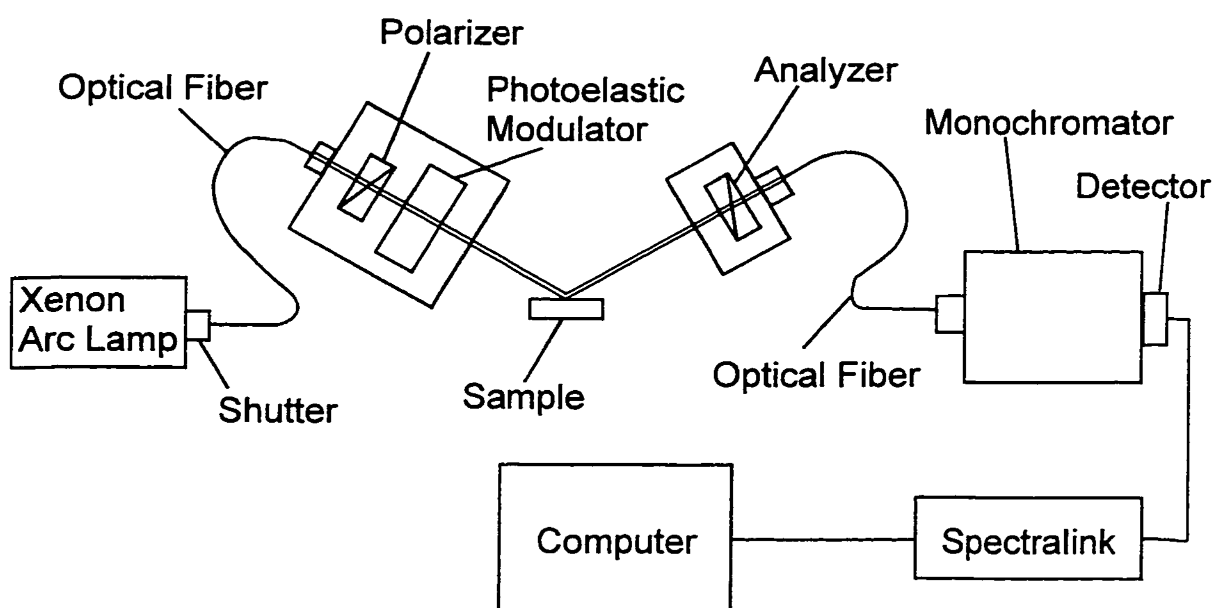

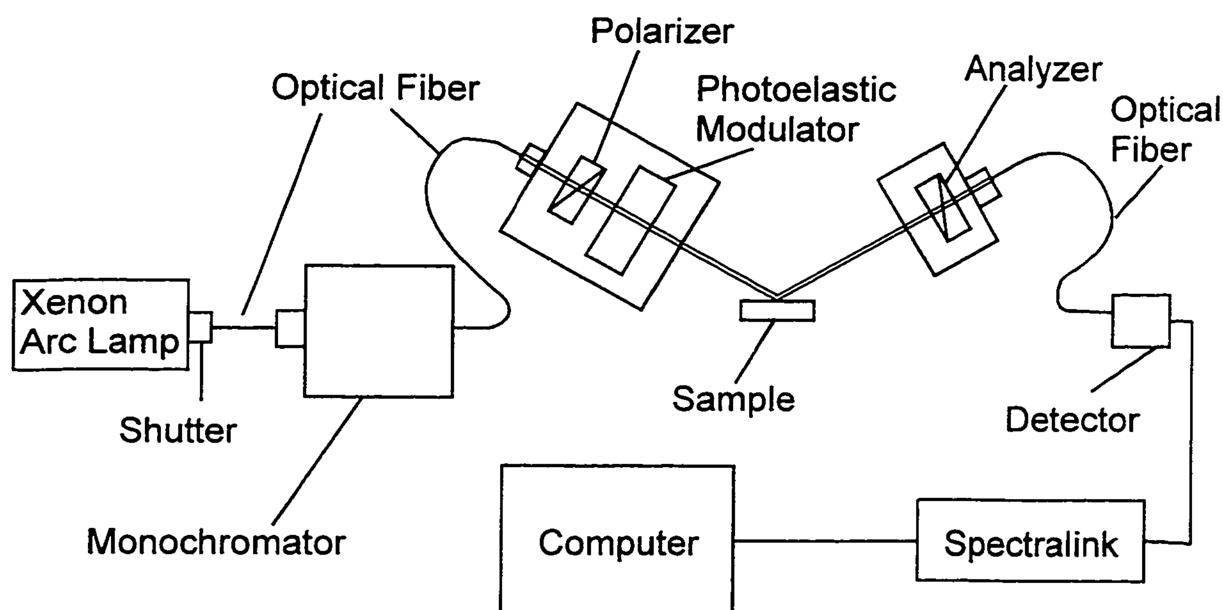

Figure 4. Experimental setup for PME. (a) shows normal configuration for energies above 1.5 eV. (b) shows a second configuration with the monochromator before the sample in order to avoid signal from sample photoluminescence. (b) has an extra fiber optic cable in the light path.

Reproduced with permission of the copyright owner. Further reproduction prohibited without permission.

Spectroscopic data acquisition was controlled through a (Spectralink) electronic controller box interfaced to a computer. This controller box was left on at all times as it also maintained the constant temperature of the modulator, which is necessary for stable modulation and thus accurate measurement. This setup allowed the automation of all aspects of measurement including movement of various positioning motors, movement of the monochromator, regulation of the modulation voltage at each wavelength of light, polarizer and modulator positioning during calibration, insertion of a mirror to change detectors, and insertion of mirrors in various spectral ranges to reduce parasitic signals and noise. Although the controller box generally functioned well, after several years it began to suffer random errors due to a degenerating power supply. This lead us to first move the autocolumnation lamp to a separate power supply, and finally to replace the power supply module.

Besides the change in detector mentioned above, there were several minor changes made during the measurement to accommodate the different measured spectral ranges. As there are no available optical fibers that are transparent over the entire measured energy spectrum, one set of optical fibers was used in the infrared and another in visible and ultraviolet regimes. In addition, a filter was put into the light path just before the monochromator for the wavelength range below 530 nm in order to cut unwanted high frequency light which would be transmitted as the second order reflection from the monochromator gratings. In addition two band-pass filters were used to eliminate unwanted light for measurements in specific wavelength ranges: one was used for wavelengths greater that 1130 nm and the other for wavelengths less than 350 nm. All of

Reproduced with permission of the copyright owner. Further reproduction prohibited without permission.

these changes were handeled automatically by the computer controlling the measurement, with the exception of the changing of the optical fibers. Automatic changes used during data acquisition were set in the Miscellaneous/Equipment menu, but these could be overridden for single wavelength measurement using the Views menu.

1.3.1 Basic Theory of PME

The photoelastic modulator is the key to this type of ellipsometer. It is usually oriented with its axis rotated 45° from that of the polarizer. Thus, half the light is oriented along the modulator's fast axis, and half along the slow axis. The modulator introduces a time dependent phase shift $\delta(t)$ between its two eigenmodes. This creates a time dependent intensity at the detector from which the ellipsometric parameters (Ψ and Δ) of the sample can be determined. This is worked out in Appendix A using both the Jone's Matrix formalism and Mueller matrix formalism, with the result given in Eqs. (A14) and (A15). Most measurements were made in the particularly convenient configuration of polarizer angle=P=45°, modulator angle=M=0°, analyzer angle=A=45° (all angles referenced to the normal to the light path included in the plane of incidence). In this case the final light intensity at the detector, given by Eqs. (A14) and (A15), takes the form:

$$I = I_{DC} + I_S \sin \delta(t) + I_C \cos \delta(t) \quad (3a)$$

Where

Reproduced with permission of the copyright owner. Further reproduction prohibited without permission.

$$I_S/I_{DC} = \sin 2\Psi \sin \Delta \qquad \text{(3b)}$$
$$I_C/I_{DC} = \sin 2\Psi \cos \Delta$$

From which the ellipsometric parameters (Δ and Ψ) can be extracted. However, in a few cases where $\Psi \gtrsim 45°$ (such as some layered structures and very reflective metals), this configuration does not allow an accurate determination of Ψ. In these cases, an alternative configuration is used with P=90°, M=45°, and A=45°, in which case one instead obtains

$$I_S/I_{DC} = \sin 2\Psi \sin \Delta \qquad \text{(3c)}$$

$$I_C/I_{DC} = \cos 2\Psi$$

so that Ψ can be determined accurately. In these cases it is often useful to measure in both configurations since accurate values of Δ near Δ=0°,180° can only be obtained with the first configuration.

An ideal photoelastic modulator (PEM) produces a phase difference of

$$\delta(t) = A_M \sin(\omega t) \qquad \text{(4)}$$

where ω is the frequency of modulation (about 55kHz) and A_M is the modulation amplitude which is proportional to V*E, V being the amplitude of the voltage applied to

Reproduced with permission of the copyright owner. Further reproduction prohibited without permission.

the PEM, E the photon energy of the light. Using this form, the phase shift terms in Eq. (3a) can be evaluated as

$$\sin\delta(t) = 2J_1(A_M)\sin\omega t + 2J_3(A_M)\sin 3\omega t + \ldots \qquad (5)$$
$$\cos\delta(t) = J_0(A_M) + 2J_2(A_M)\cos 2\omega t + 2J_4(A_M)\cos 4\omega t + \ldots$$

where $J_n(A_M)$ is the nth order Bessel function of A_M. Combining Eqs. (1) and (3c), the measured light can be related to I_0, I_S, and I_C:

$$\begin{pmatrix} S_0 \\ S_\omega \\ S_{2\omega} \end{pmatrix} = \begin{pmatrix} 1 & 0 & J_0(A_M) \\ 0 & 2T_1J_1(A_M) & 0 \\ 0 & 0 & 2T_2J_2(A_M) \end{pmatrix} \begin{pmatrix} I_0 \\ I_S \\ I_C \end{pmatrix} \qquad (6)$$

where S_0 is the DC light intensity, S_ω and $S_{2\omega}$ are the measured light intensities at the first and second harmonics of modulation frequency respectively, and T_1 and T_2 are attenuation coefficients of the detection system (near unity).[45] In the calibration procedure, the modulation amplitude is chosen so that $J_0(A_M) = 0$.

The matrix of Eq. (6) could be expanded to cover terms of higher order harmonics to possibly obtain additional real time calibration information; however, this seemed neither necessary nor simple with the current system.

In the presence of higher order harmonics in the phase modulation, we follow the presentation of Drévillon.[46] In this case, we must replace Eq. (4) with

Reproduced with permission of the copyright owner. Further reproduction prohibited without permission.

$$\delta(t) = \sum_n A_{M,n} \sin(n\omega t) \tag{7}$$

Then we replace Eq. (6) by

$$\begin{pmatrix} S_0 \\ S'_\omega \\ S'_{2\omega} \end{pmatrix} = \begin{pmatrix} 1 & cc_{s,0} & J_0(A_M) + cc_{c,0} \\ 0 & 1 + cc_{s,\omega} & cc_{c,\omega} \\ 0 & cc_{s,2\omega} & 1 + cc_{c,2\omega} \end{pmatrix} \begin{pmatrix} I_0 \\ I_S \\ I_C \end{pmatrix} \tag{8a}$$

where

$$\begin{aligned} S'_\omega &= \frac{S_\omega}{2T_1 J_1(A_M)} \\ S'_{2\omega} &= \frac{S'_{2\omega}}{2T_2 J_2(A_M)} \end{aligned} \tag{8b}$$

and the coefficients $cc_{i,j}$ can be considered as second order corrections. The modulation was chosen for:

$$J_0(A_M) + cc_{c,0} = 0 \tag{9}$$

using the procedure given in section 1.3.2.4.

Reproduced with permission of the copyright owner. Further reproduction prohibited without permission.

This leaves only the determination of the various constants. For this, we define 7 running configurations defined by the orientation of the optical elements (A, M, and P). For our setup, P-M=45° always. The configurations are:

$$\begin{array}{ll} a{:}A = 0°, M = 45° & e{:}A = -45°, M = 0° \\ b{:}A = 45°, M = 45° & f{:}A = -45°, M = 90° \\ c{:}A = -45°, M = 45° & g{:}A = 45°, M = 90° \\ d{:}A = 45°, M = 0° & \end{array} \tag{10}$$

We further define the ratios

$$\begin{aligned} R_{\omega}^{i} &= \frac{S_{\omega}}{2J_1(A_M)S_0} \\ R_{2\omega}^{i} &= \frac{S_{2\omega}}{2J_2(A_M)S_0} \end{aligned} \tag{11}$$

where the superscript i refers to one of the seven configurations given in Eq. (10).

Then all of the remaining parameters in Eq. (8a) can be determined from

Reproduced with permission of the copyright owner. Further reproduction prohibited without permission.

$$
\begin{aligned}
cc_{s,\omega} &= R_{\omega}^{a} \\
T_2 &= R_{2\omega}^{a} \\
\cos 2\Psi &= \frac{R_{2\omega}^{b} + R_{2\omega}^{c}}{T_2} \\
\cos\Delta &= \frac{R_{2\omega}^{d} + R_{2\omega}^{f}}{2T_2 \sin 2\Psi} \\
cc_{s,2\omega} &= \frac{R_{2\omega}^{d} + R_{2\omega}^{g}}{2\sin 2\Psi \sin\Delta} \\
cc_{s,2\omega} &= \frac{R_{2\omega}^{d} + R_{2\omega}^{e}}{2T_2 \sin^2 2\Psi \sin\Delta \cos\Delta} \\
T_1 &= \frac{R_{\omega}^{b} + R_{\omega}^{c}}{2\sin 2\Psi \sin\Delta}
\end{aligned}
\qquad (12)
$$

These parameters must be calculated and stored for each wavelength measured during the automated procedure described in section 1.3.2.4.

1.3.2 Alignment of the Apparatus

Accurate ellipsometry requires precise alignment of all components including the angle of incidence; the polarizer, analyzer, and modulator angles; and the sample. The following three sections detail the alignment of these components of the ellipsometer.

Reproduced with permission of the copyright owner. Further reproduction prohibited without permission.

1.3.2.1 Sample alignment

Sample tilt alignment is achieved using an autocolumnator [Fig. 5(a)]. An image of crosshairs is created from a light path which includes a reflection from the sample and focused to the viewport by a lens at the bottom of the columnator. This image was compared to the reference of the fixed crosshairs viewed directly. The image seen upon looking through the viewport is shown in Fig. 5(b). The reflected crosshairs appear lighter and rotated by about 30° relative to the fixed crosshairs. When the sample is flat the origins of the two sets of crosshairs should coincide; however, this could be changed even by small inadvertent bumps to the columnator. Thus to insure that the sample was not tilted it was necessary to rotate the sample stand and watch for movement of the reflected crosshairs. The sample was aligned without tilt when the reflected crosshairs did not move when the sample was rotated. In addition to aligning the tilt of the sample, the intensity and movement of the reflected crosshairs gave a qualitative assessment of the sample surface quality.

Before measurement, the sample height also needed adjusted. This was done by rotating the height adjustment at the base of the sample stand. The height was assumed correct when the DC intensity (S_0 on the active view screen) was maximized.

Different parts of the sample were sometimes measured without realignment by using the scanning motors at the base of the sample stand (accessed through the move motors command (alt-m) on the active view screen. This feature was particularly useful for

Reproduced with permission of the copyright owner. Further reproduction prohibited without permission.

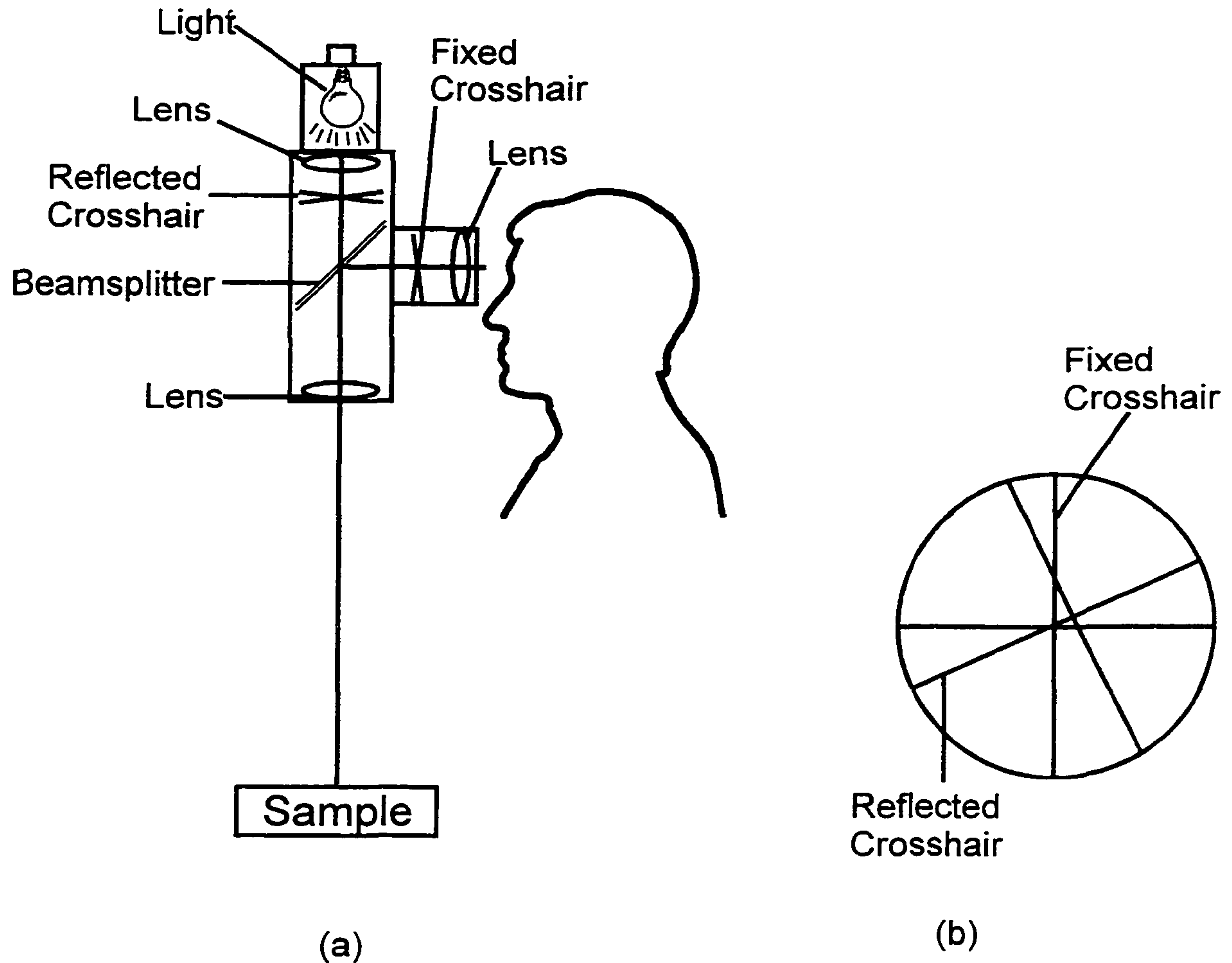

Figure 5. Autocollimator for adjusting sample tilt. (a) Schematic of the collimator. An image of crosshairs is created from a light path which includes a reflection from the sample and focused to the viewport by a lens at the bottom of the collimator. This image was compared to the reference of the fixed crosshairs viewed directly. (b) The image seen upon looking through the viewport. The sample stand level was adjusted until the reflected crosshairs did not move when the sample stand was rotated.

Reproduced with permission of the copyright owner. Further reproduction prohibited without permission.

small samples as it allowed for positioning of the light spot on the center of the sample without moving the sample relative to the sample stand (and thus changing the tilt).

1.3.2.2 Angle of Incidence Calibration

Initial angle of incidence calibration was performed according to the method specified in the ISA ellipsometer manual. The sample stand was lowered and the analyzer and polarizer heads were adjusted 180° apart measured by maximizing DC intensity (S_0 on the active view screen) for the direct light path. Care was taken so that the cutoff switches on the analyzer and polarizer heads were not activated and thus did not need to be removed. After this, the polarizer and analyzer heads were moved to 70° and an aluminum sample was mounted and aligned as described in the previous section. Then the analyzer head was moved to obtain maximum intensity. The polarizer and analyzer angles of incidence were then set to their average through the calibration/goniometer menu. This appeared to determine the angle of incidence to within about 0.5°.

The final determination of the angle of incidence was obtained by measuring a high quality silicon sample with only a native oxide on a smooth surface after all other calibrations and alignments had been done. This data was then analyzed using a model of reference silicon[47] with a thin layer (initial guess of 30Å) of native oxide (SiO_2)[48] to extract the angle of incidence and oxide thickness from a least squares fit.[49] This determined the angle of incidence to within about 0.1°.

Reproduced with permission of the copyright owner. Further reproduction prohibited without permission.

1.3.2.3 Alignment of Polarizer, Modulator, and Analyzer Angles

The accuracy of Ψ and Δ cannot be expected to be any better than the accuracy of the polarizer, modulator, and analyzer angles. With this in mind it was important to insure the accuracy of these. The polarizer was attached to the modulator at an angle of 45° from the factory, so it was only necessary to determine the modulator and analyzer angles. Initial alignment of these was done by looking at the direct readouts on the analyzer and modulator (this was necessary only in very rare cases). It can be seen from the general form of the equations for PME [Eqs. (A14) and (A15) appendix A] that the modulator angle (M) and the analyzer angle (A) affect the measured intensities. Specifically, I_S is 0 for $A = 0°$ and that I_C is 0 when $M = A = 0°$. Thus M and A can be calibrated to 0° simply by the first and second harmonic intensities of the modulation frequencies (S_ω and $S_{2\omega}$ respectively on the view menu) to 0.

1.3.2.4 Modulation Amplitude Calibration

The modulation amplitude is another crucial parameter for accurate determination of ellipsometric data. The actual modulation required varies slightly over time. In addition, changes in temperature and humidity can affect the modulation. In the past it was necessary to perform the modulator calibration (after alignment of the modulator and analyzer angles) about once every 2 weeks for best results. However, the shifts in modulation amplitudes were usually restricted to energies above 4 eV. The modulation calibration was checked daily by measuring a known silicon sample with a native oxide

Reproduced with permission of the copyright owner. Further reproduction prohibited without permission.

to insure that the system gave consistent results. Modulation calibration also needed to be done whenever the electronic controller box was turned off and whenever the power failed because the temperature of the modulator was not maintained constant in these cases.

The automated calibration procedure proceeded as follows. An aluminum sample was mounted and aligned. The modulator and analyzer were calibrated and moved to 0° as described in section 1.3.2.3. The modulation voltage was determined at serveral wavelengths, such that I_C does not affect the DC intensity, S_0 [that is, $J_0(A_M) = 0$ in the first approximation as shown by Eq. (4)]. First the analyzer position was set to 0° to insure that $I_S = 0$ [see Eq. (A15)] so that it could not affect the calibration (even considering higher order corrections). Next, S_0 [$=I_0+\{J_0(A)+cc_{c,0}\}I_C(M)$ from Eq. (8a)] was measured for several different modulation amplitudes for $M = +45°$ and $M = -45°$. The desired amplitude was that for which S_0 was the same for the two modulator positions. This can be seen from Eqs. (A14) and (A15) appendix A for A=0° [$I_C(M=+45°) = -I_C(M=-45°)$, also $\Psi \approx 45°$ for aluminum making I_C large].

$$I_C = \sin 2M\,(\cos 2\Psi - 1) \approx -\sin 2M \tag{13}$$

Thus there is a change is sign of I_C for the two modulator positions and $S_0(M=+45°) = S_0(M=-45°)$ only for the desired modulator amplitude. The modulation final amplitudes were stored in three files (J0IR.DAT, J0VIS.DAT, and J0UV.DAT) for interpolation and use during the data runs.

Reproduced with permission of the copyright owner. Further reproduction prohibited without permission.

1.3.2.5 Monochromator Calibration

The actual monochromator position can be set like the goniometer positions using the view menu of the elli software. It was often necessary to reset the position of the DH10 monochromator for the first run of the day. This was always done so that 3eV in the view menu corresponded to 413.3 nm on the monochromator readout. Also, the monochromator would usually be off by about 1 nm whenever the units of light were switched from energy to wavelength in the Miscellaneous/Equipment menu.

The calibration of the monochromators was tested using a mercury vapor line source. The line source was used as input light for the monochromator/detector assembly. A maximum in intensity was obtained for each of the lines in the mercury spectrum and compared to the accepted values. The monochromators were found to be accurate to within 1 meV in this manner.

1.3.3 Etching Procedures

Several etchants were used for this study for various lengths of time, summarized in Table I. A number of other etchants as well as polishing procedures for bulk cut samples can be found in Aspnes' papers.[47]

Reproduced with permission of the copyright owner. Further reproduction prohibited without permission.

Table I. Etchants for Various Materials

Material	Etchant	Result
$Zn_{0.53}Cd_{0.47}Se$	10% HF in DIW	Clean smooth surface after about 1 minute
$Zn_{0.53}Cd_{0.47}Se$	0.05% Br/Methanol	Rough surface after about 5 seconds
$In_{0.66}Ga_{0.34}As$	1:1 HCl (concentrated solution):Methanol	Smooth surface after 5 one second sprays
GaSb	3:1 HCl (concentrated solution):Methanol	Smooth surface after 10 one second sprays
GaAs	KOH/Ethanol (dissolved tablets into ethanol to make saturated solution)	Smooth surface after 15 one second sprays

Depending on the safety handling requirements of the etchant, the etching was done either under a fume hood or directly on the sample stand. The procedures for each are listed in the next two sections.

In either case, the effectiveness of the etch was evaluated by examining the imaginary part of the dielectric function near the E_2 peak. The E_2 peak is sensitive to surface oxide and surface roughness because the light penetration depth is small in this region. A more detailed explanation of why the E_2 peak is maximized for a clean smooth surface is given in section 1.5.2. The samples were etched until the samples showed no further improvement, and the times given above are times required to reach this state. Etching on the sample stage greatly simplified this maximization procedure as repeated etching did not require dismounting and remounting the sample.

Reproduced with permission of the copyright owner. Further reproduction prohibited without permission.

1.3.3.1 Fume Hood Etching

Due to the extreme corrosiveness of Br and the extreme danger of HF acid, the two etches involving these were done under a fume hood. A diagram of the fume hood etching procedure is given in figure 6. A small bath of the etchant was prepared under the fume hood. During the etching, the sample was kept in motion in an attempt to keep the etch uniform. To minimize oxidation due to the oxygen and water in the air, the sample was placed in a dry methanol bath immediately after etching. The sample was then transferred into a glove bag filled with dry N_2 gas. About 1 minute after the transfer (to purge the air that came into the bag along with the sample), the sample was removed from the methanol bath and blown dry by nitrogen (the nitrogen flow rate was greatly increased for the blow dry). Finally, the sample was transferred to the sample stand, aligned, and measured still under dry flowing nitrogen.

An experimental difficulty arose in maintaining the sample under dry nitrogen during the measurement: exposure of the modulation head of the ellipsometer to this nitrogen resulted in a large ($\approx$ 20%) change in the measured dielectric function. Care was therefore taken to prevent such exposure by means of small entrance holes for the incident beam, spacing between the glove bag and the modulation head, and a small fan to divert nitrogen leaving the bag. Such care was not required with the rotating analyzer ellipsometer system used in the far infrared, and the reasons for this effect on the modulation system remain unclear.

Reproduced with permission of the copyright owner. Further reproduction prohibited without permission.

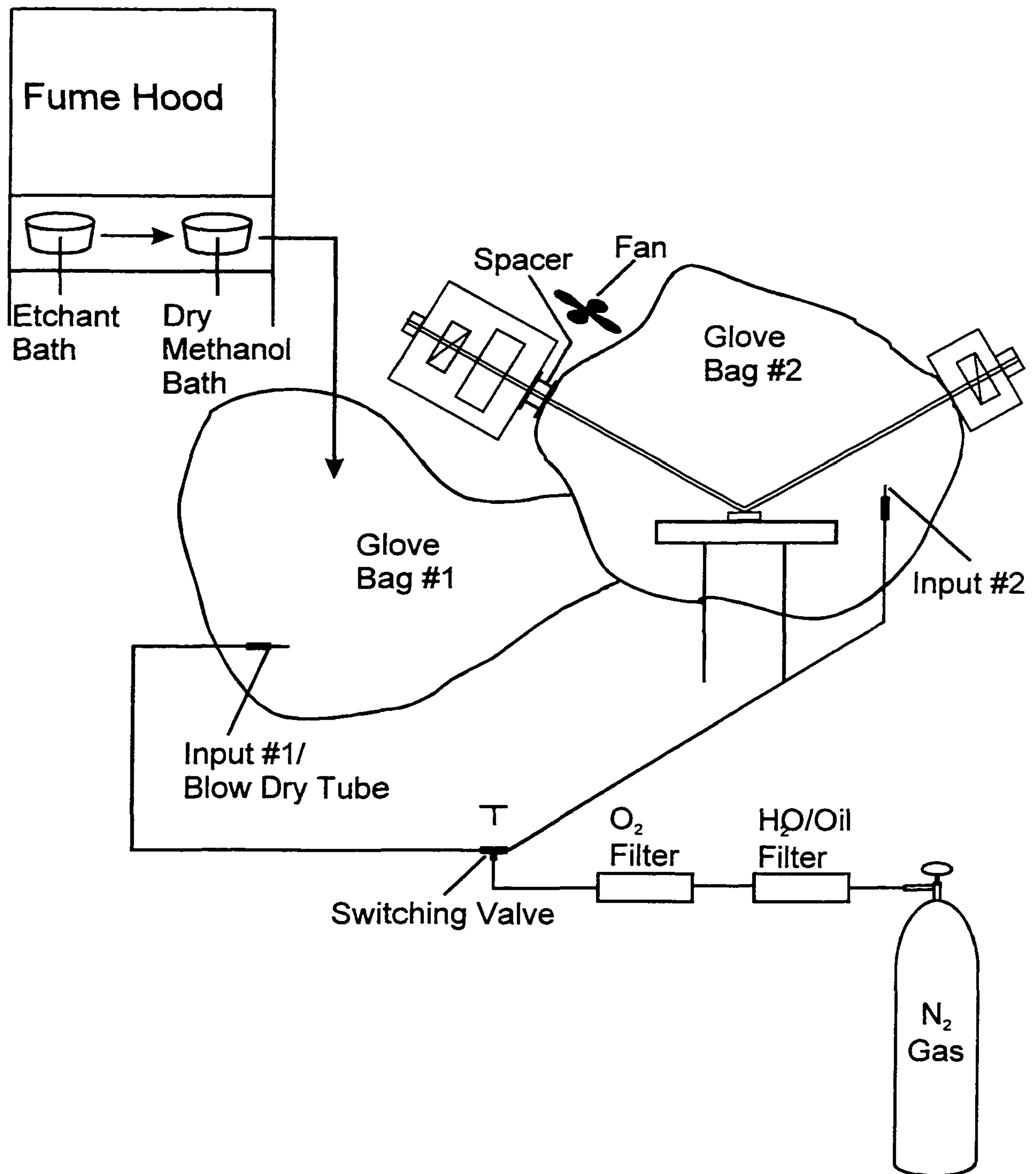

Figure 6. Experimental setup for fume hood etching. After etching, the sample is placed into a dry methanol bath for transfer to the sample stand. Measurement was made under flowing N_2. A fan was used to keep the dry N_2 away from the PEM.

Reproduced with permission of the copyright owner. Further reproduction prohibited without permission.

1.3.3.2 Etching on the Sample Stand

To simplify etching (at least for relatively safe etchants), the system was configured so that the sample could be mounted vertically. A new sample stage made out of Teflon was designed to prevent etching of the stage. This stage had a small hole at the center for vacuum suction mounting and a drain hole at the edge (positioned at the bottom). The sample stage was covered by a high density polyethylene (HDPE) container. Small cracks were sealed using tape. 2 cm x 0.5 cm slits were cut in the sides of the cover for the entrance and exit light beams. In addition, a hole was cut in the top of the cover to allow use of the autocollimator, but this hole was most useful as a viewport during etching. Low density polyethylene (LDPE) tubing was attached to a drain cut in the stage to remove the excess etchant and rinse fluid. A diagram of this new configuration for etching is shown in Fig. 7. The detail of the sample enclosure in Fig. 7(a) is shown horizontal for clarity although the sample was always mounted vertically.

When etching on the sample stand, special care was taken to insure that none of the etchant splashes onto the instrumentation since this could have destroyed the instrument. Also important was the use of proper safety equipment (goggles and gloves) to prevent damage to the researcher.

The actual etching proceeded as follows. HDPE Wash bottles containing the etchant and rinse were prepared. After mounting and aligning the sample, the monochromator was moved to the energy of the E_2 peak and the pseudo-dielectric function was noted from the

Reproduced with permission of the copyright owner. Further reproduction prohibited without permission.

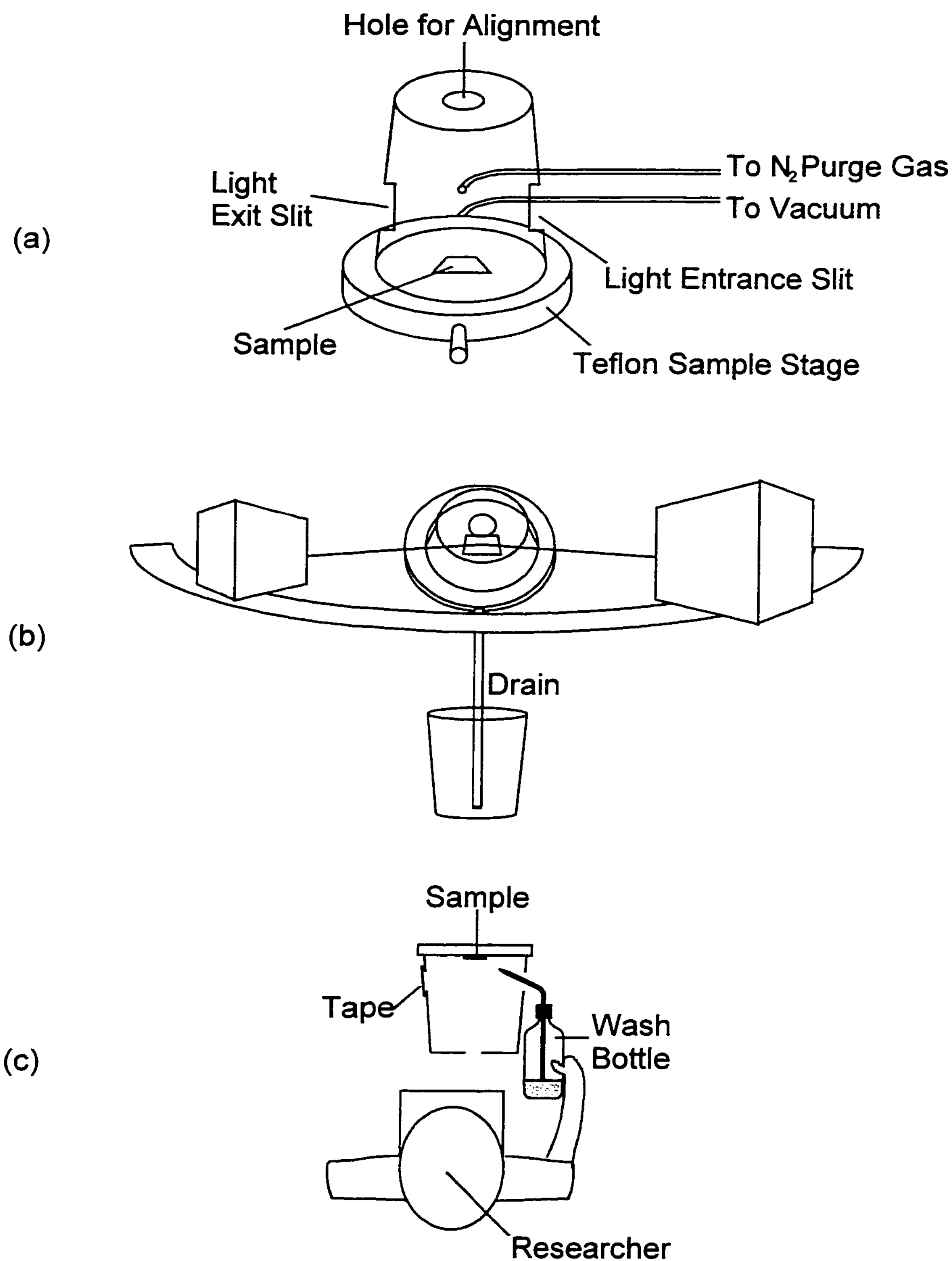

Figure 7. Experimental setup for etching on the sample stand. (a) Detail of covered sample stand shown upright for clarity. (b) Covered sample stand mounted on ellipsometer. (c) Top view of researcher etching sample. Exit hole is covered during etching to keep splash off ellipsometer.

Reproduced with permission of the copyright owner. Further reproduction prohibited without permission.

view menu. Then the light exit slit was covered with tape to prevent etchant from splashing into the analyzer head. The tip of the wash bottle containing etchant was positioned through the light entrance slit close to the sample. A series of 1 second sprays of etchant were directed at the sample the number of sprays being the etch time. Immediately following this, the sample was rinsed in a like manner usually with 5 to 10 sprays of methanol or DIW. Immediately following the rinse, a second nitrogen line was placed through the light entrance slit to blow the sample dry (high flow rate). The entire procedure was watched by the experimenter through the hole for autocolumnation alignment. Finally, the (wet) tape was carefully removed from the light exit slit, and the dielectric function at the E_2 peak energy was again measured. When a good value at E_2 was obtained, a scan across the entire spectral range was made.

It was noted that moisture inside the nitrogen cover could have a marked (up to 10%) effect on the measured dielectric function. This was most likely due to a thin layer of liquid condensing onto the surface of the sample. Following this discovery, extra steps were taken to insure dryness inside nitrogen chamber during etching. A chemwipe on a stick (a giant q-tip) was inserted through the hole for alignment and held behind the sample to absorb most of the liquid splashed during the etching and rinsing of the sample. A second giant q-tip was used to dry out the inside of the cover after etching.

Reproduced with permission of the copyright owner. Further reproduction prohibited without permission.

1.4 Experimental Details Mid-IR

Ellipsometric data for the range 0.3-1.0 eV were taken using a Sentech model 950 variable angle ellipsometer inserted into a Biorad model 175C Fourier transform infrared (FTIR) spectrometer.

The experimental equipment is shown in figures 8(a) and 8(b). Light from the source was passed through an aperture and reflected through Michelson interferometer, consisting of a beam splitter, a fixed mirror, and a movable mirror. Due to the difference between the optical path length to the fixed mirror and that to the movable mirror, the two light beams interfered upon recombining. The position of the movable mirror was very precisely calculated base on the interference of He-Ne laser light, which was placed in the center of the IR beam by means of a hole in the first focusing mirror. Next, the light was reflected to the Sentech ellipsometer inside the Biorad sample compartment, which is shown in detail in Fig. 8(b). In the ellipsometer, the light was passed through the polarizer, optionally off a phase retarder, reflected onto the sample, then reflected to the analyzer, and finally to the detector. All of the reflections were off gold mirrors, except those from the sample and the beam splitter. The only components which moved during the measurement were the movable mirror in the Michelson interferometer, the retarder (into the light path for the second half of the measurement), and the analyzer. The effect of the focusing of the light beam on the measured data is covered in appendix B.

Reproduced with permission of the copyright owner. Further reproduction prohibited without permission.

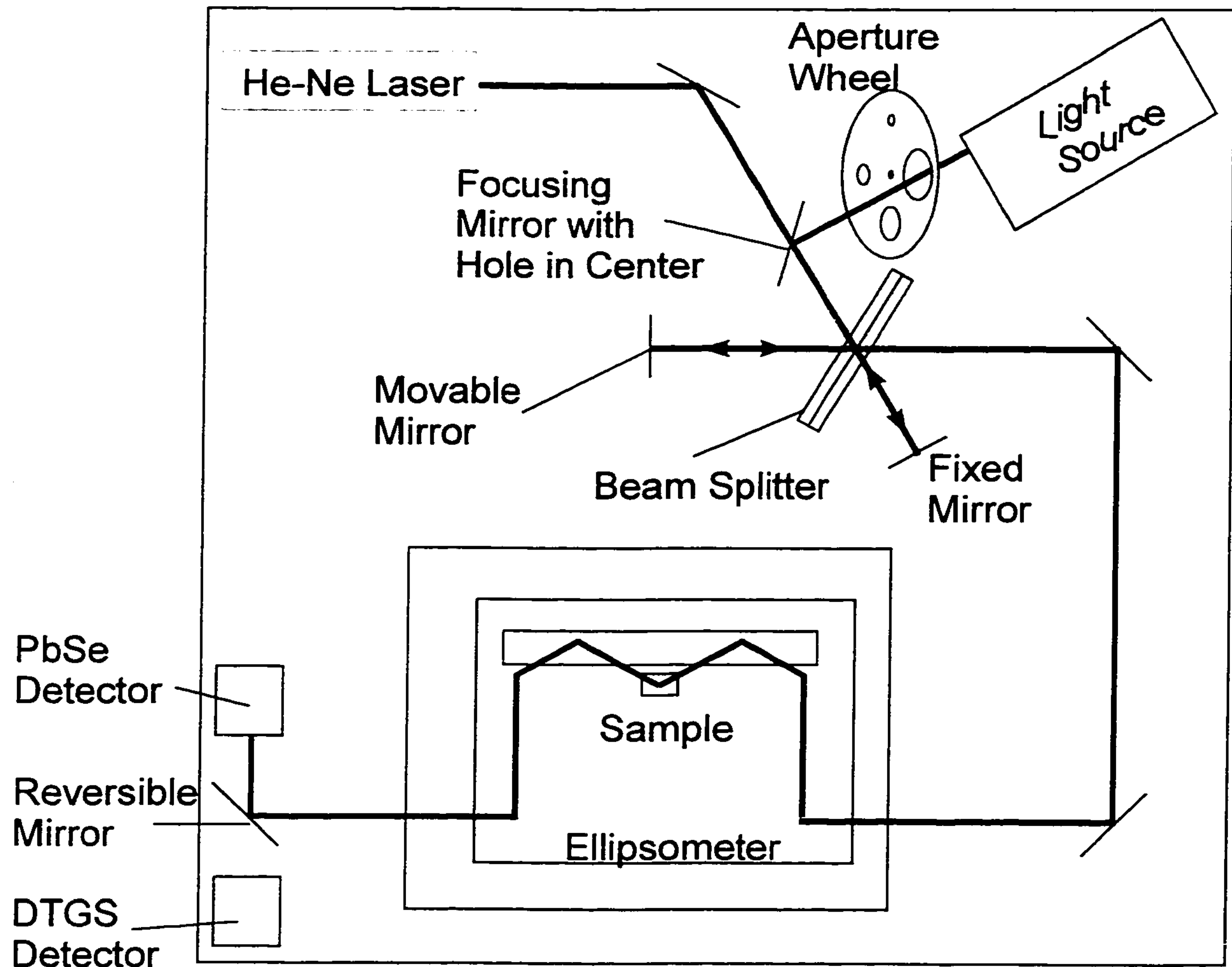

Figure 8(a). Experimental setup for MIR measurement (ellipsometer inside FTIR spectrometer).

Reproduced with permission of the copyright owner. Further reproduction prohibited without permission.

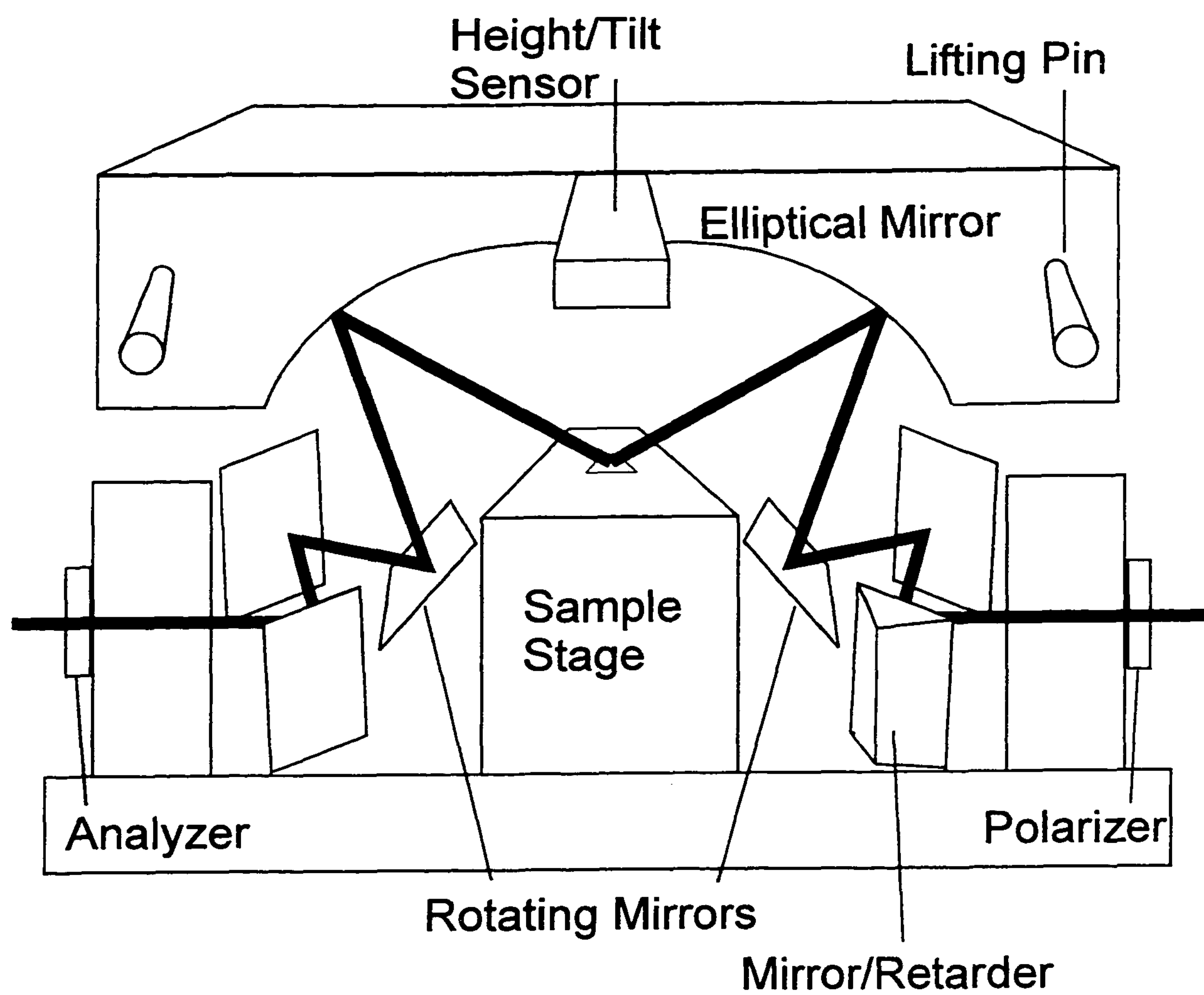

Figure 8(b). Detail of ellipsometer used for MIR measurement.

Reproduced with permission of the copyright owner. Further reproduction prohibited without permission.

For topics outside of the scope of this thesis, a good coverage of FTIR based ellipsometry can be found in the book by Röseler.[50]

1.4.1 Workings of FTIR spectrometer

FTIR spectrometry is based on the Michelson interferometer (Fig. 9). The incident light is split into two paths by a beam splitter. If the moving mirror is at the same distance from the beam splitter as the fixed mirror, the path lengths are the same and the two light beams recombining constructively. Otherwise, the light will interfere based on its wavelength and the position of the moving mirror. The two light beams can be considered to be of the same intensity since the (initially unpolarized) light undergoes one beam splitter reflection, one mirror reflection, and one beam splitter transmission. In this case, the light intensity exiting the interferometer for monochromatic light will be

$$I(x, \omega) = 2\, I(\omega) \cos^2(\omega x/c) \tag{14}$$

where $I(\omega)$ is the intensity of each of the two light beams for the given wavelength of light, x is the displacement of the moving mirror from that of the fixed mirror (= half the path length difference), and ω is the angular frequency of the light, and c is the speed of light.

Reproduced with permission of the copyright owner. Further reproduction prohibited without permission.

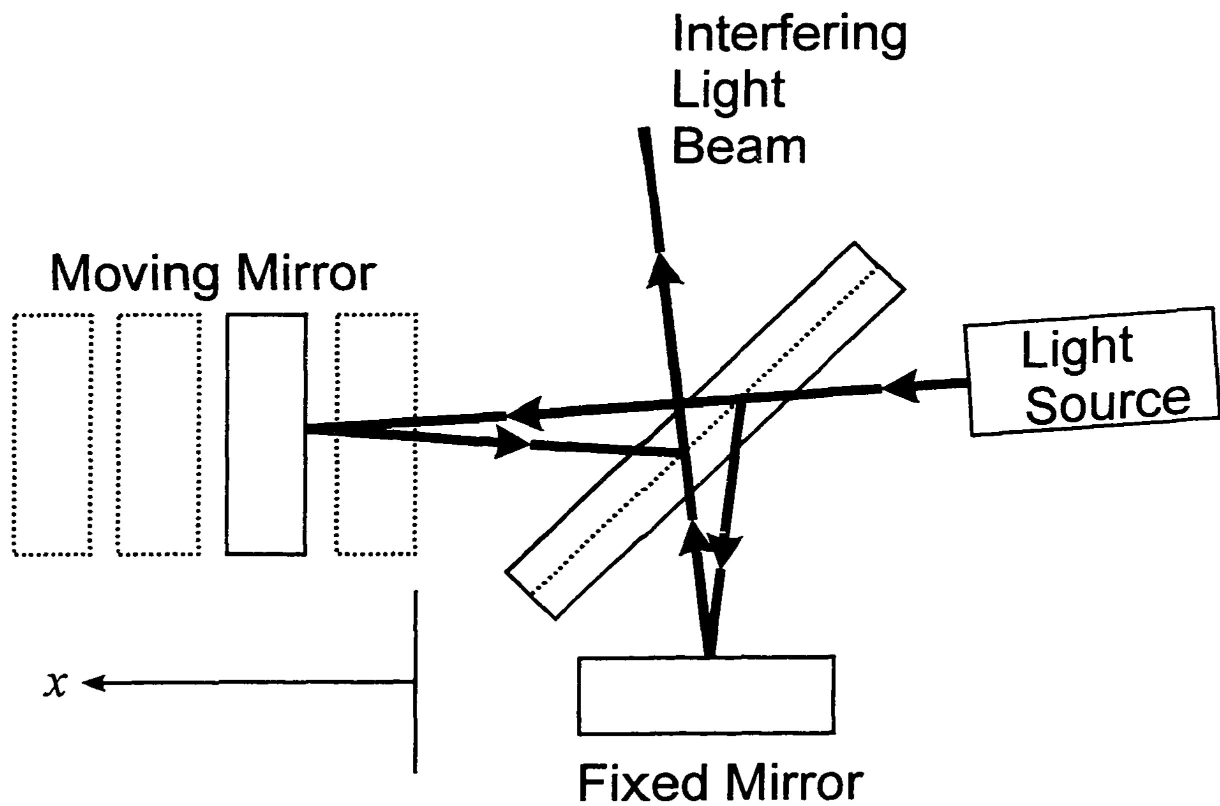

Figure 9. Schematic of a Michelson interferometer. The exiting interfering light beam has an intensity based on the position of the moving mirror, x.

Reproduced with permission of the copyright owner. Further reproduction prohibited without permission.

If the source has a continuous spectrum, the superposition principal gives a total intensity:

$$I(x) = \int_{-\infty}^{\infty} 2I(\omega)\cos^2(\frac{\omega x}{c})d\omega = \int_{-\infty}^{\infty} I(\omega)d\omega + \int_{-\infty}^{\infty} I(\omega)\cos(\frac{2\omega x}{c})d\omega \tag{15}$$

If we now redefine $I(x)$ by subtracting off the first integral on the right side of Eq. (15) (which is independent of position and thus easy to remove electronically), we see that we now have the Fourier transformation of the intensity spectrum. Thus we have our basic equation for Fourier transform spectroscopy:

$$\begin{aligned} I(x) &= \int_{-\infty}^{\infty} I(\omega)\cos(\frac{2\omega x}{c})d\omega \\ I(\omega) &= \frac{2}{\pi c}\int_{-\infty}^{\infty} I(x)\cos(\frac{2\omega x}{c})dx \end{aligned} \tag{16}$$

In practice, the infinite limits in the integral can not be achieved. This brings about a limit to the resolution of the instrument, as can be seen by considering that a signal of finite width will destructively interfere to yield nearly zero signal beyond some value of x.

Reproduced with permission of the copyright owner. Further reproduction prohibited without permission.

1.4.2 Deviations Due to Refraction at the Polarizers

During the course of this work, it was difficult to obtain good information with this system. Late in the work, a major problem was discovered caused by deviation of the light beam due to refraction at the polarizers.

We found that the analyzer was refracting the light beam by at least about 0.1°. This caused the light to trace a small circular path on the detector as the analyzer rotated during the measurement. We verified the beam deviation by shining a red laser through the analyzer and watching the beam trace out a circle on the wall (5m away) as the analyzer rotated. The angle of the beam deviation upon passing through the polarizer was found to be:

Polarizer	Beam Deviation
MIR polarizer:	15'
MIR analyzer:	6'
NIR polarizer:	6'
NIR analyzer:	15'

We further verified the problem by visually watching the focused light on the detector as the analyzer moved and by measuring the transmitted intensity for analyzer angles 180° from each other. Although the deviations were small, we observed the light shifting slightly off the detector (which was only about 2 mm in diameter). In addition for the

Reproduced with permission of the copyright owner. Further reproduction prohibited without permission.

best polarizer (the MIR analyzer), the intensity spectrum for 0° had a peak intensity of 1.32 while that for 180° had a peak intensity of 1.40, a 6% difference. The NIR analyzer had peak values of 1.31 and 1.59 for these angles, respectively. This showed that the problem was significant and that the problem was due to the beam deviation of the polarizer.

Currently, we are searching for polarizers with smaller deviations to improve future measurements. With testing, it should not be hard to find one with a small enough deviation (we only need 1 because the polarizer does not move during the measurement). Indeed, Graesby-Specac has said they can manufacture a polarizer with less than 15 arc seconds deviation. In addition, a detector with a larger detecting element would probably also improve the situation (although probably at the cost of extra noise).

1.4.3 Calibration of the Instrument

Calibration of the instrument is a fairly long process which must be done every time the optical components (the retarder and polarizers) are changed. It was found that this process could be minimized without a noticeable affect on measurement accuracy by using the mid infrared optics for both the mid and near infrared measurements. Perhaps with further improvements to the instrument, the near infrared optics will become more important.

Reproduced with permission of the copyright owner. Further reproduction prohibited without permission.

The calibration steps are described below. They include alignment of the analyzer and polarizer, corrections for imperfect polarizers, alignment of the light beam, and mirror and retarder corrections.

1.4.3.1 Alignment of the Light Beam

Although the path of the light beam through the instrument has been done by Biorad and Sentech technicians and should not need to be changed, it is crucial to the working of the ellipsometer and fairly simple to check. This is generally done in low light using a small piece of white paper to intercept the light and the eye. If the light cannot be seen, as is the case for the MIR light source, one can use the three laser spots (the center laser spot should be near the center of the light). Beam alignment is crucial since the size of the detector element is only about 2 mm. The detectors are mounted very precisely and can be aligned separately at the Biorad factory. When looking in the detector area, one should be careful not to leave the fluorescent lights on as this can damage the PbSe detector.

1.4.3.2 Alignment of the Analyzer and Polarizer

Analyzer and polarizer alignments are made using of a fixed polarizer reference. The automated routines for determining the offsets relative to a mechanical switch are

Reproduced with permission of the copyright owner. Further reproduction prohibited without permission.

accessed through the Calibration button on the main measurement window. To start the procedure, the sample stand, retarder/entrance mirror, and exit mirror are removed from the ellipsometer. Thus the light only encounters the two polarizers when passing (straight) through the ellipsometer. Then the polarizer is removed from the ellipsometer and mounted on a fixed stand at nearly horizontal polarization. This is placed in the path of the beam at the center of the compartment and centered on the light beam using either the light beam itself or, in the MIR, the center laser spot, which should be near the center of the light beam. Spectra are then measure for several analyzer positions (usually 8 although 16 can be used to extract the fourth harmonic, which is related to detector non-linearity), and Fourier analysis of these spectra determines the angle of the fixed polarizer relative to the analyzer. The spectra for this alignment measurement should be taken for a photon energy range where the polarizers have good polarization. The fixed polarizer is then turned around (rotated 180°) and the procedure is repeated. The two angles determined for the fixed polarizer relative to the analyzer should average to 0°. If they do not, the offset from the calibration switch (given in the c:\grams\irspec.ini file) is updated so that they will.

An alternative procedure to the one given above can be used for comparison. The angle of the analyzer relative to the fixed polarizer can also be found by taking several scans with the analyzer in the range from -5° to +5° in 1° intervals. A quadratic or $\cos^2 \theta$ fit can then be used to find the angle of maximum transmission. This should be the angle of the fixed polarizer. A program was written to do this automatically, and the result was close to that given by the standard offset procedure.

Reproduced with permission of the copyright owner. Further reproduction prohibited without permission.

After the offset (the position of the fixed hardware switch) of the analyzer is determined, the polarizer is dismounted from the stand and mounted into its normal measurement position on the moveable polarizer stand. The polarizer is then set to 45° and spectra again are measured for eight analyzer positions. This time, the Fourier analysis of these spectra determines the angle of the analyzer relative to the polarizer. From this, an offset (from a fixed hardware switch) is determined for the polarizer. Like the analyzer, the polarizer's offset can alternatively be determined by moving the analyzer to 0° and taking spectra for several polarizer angles near 0°.

1.4.3.3 Calibration – Correction for Imperfect Polarizers

No real polarizer completely polarizes light. This is particularly true in the NIR region for our polarizers. Fortunately, this can be easily handled in the Mueller matrix formalism. (It can also be handled in the Jones matrix formalism, but one must then consider separate matrices for the major and minor polarization axes.)

To measure just the characteristics of the two polarizers, all other components of the ellipsometer except the FTIR light source (i.e. the retarder, sample stand and several mirrors) were removed from the instrument, as for the polarizer alignment procedure above. Thus the instrument consisted only of the two polarizers, mounted in their normal positions. In our correction, we assumed that the two polarization characteristics of the

Reproduced with permission of the copyright owner. Further reproduction prohibited without permission.

polarizer and analyzer were identical. Then we considered that the polarizers are well characterized by their maximum and minimum transmission, τ_{max} and τ_{min} respectively. We further define the parameters

$$\cos\theta = \frac{\tau_{max} - \tau_{min}}{\tau_{max} + \tau_{min}}, \quad \text{and} \quad \sin\theta = \frac{2\sqrt{\tau_{max}\tau_{min}}}{\tau_{max} + \tau_{min}} \tag{17}$$

Since only the two polarizers are currently in the light path, the detected signal will be that given by Eqs. (A28) and (A29) with $\Psi = 45°$ and $\Delta = 0°$ (that is the light leaving the sample is the same as the light coming into the sample since there is no sample). So we obtain the detected signal for this case as

$$I = I'_{DC} + I'_S \sin 2A + I'_C \cos 2A \tag{18a}$$

where

$$\begin{aligned} I'_{DC} &= s_0 \\ I'_S &= s_0 \cos^2\theta \\ I'_C &= s_1 \sin\theta\cos\theta \end{aligned} \tag{18b}$$

As mentioned in the appendix, with our system, the incident light is very nearly unpolarized, so I'_C should be (and is) approximately zero for our system. In fact the

Reproduced with permission of the copyright owner. Further reproduction prohibited without permission.

current Sentech software forces this parameter to zero. This allows the extraction of $\cos^2\theta$. The values of Ψ and Δ can then be extracted according to Eq. (A29).

1.4.3.4 Calibration – Mirror and Retarder Corrections

After the polarizer corrections were made, the mirrors, retarder, and sample stand were replaced into the instrument. Although the instrument was then configured for measurement, corrections had to be made for the eight bounces off of gold mirrors between the two polarizers, and the retarder characteristics had to be determined for each wavelength to be measured. This was done using the automated Sentech procedures accessed by "New Mirror Corr" and "New Retarder Corr" buttons after pressing the "Menu/Start" button on the main measurement menu.

A gold mirror was mounted on the sample stand and measured as normal (without the retarder). The value of $\tilde{\rho}$ was determined normally by Eq. (A29); however, the $\tilde{\rho}$ determined in this manner has special meaning since it includes not only a contribution from the reflection from the gold surface, but also a contribution from the reflection from the eight mirrors. The data was analyzed using the equation

$$\begin{gathered}\tilde{\rho} = \tilde{\rho}_{gold}\tilde{\rho}_{mirrors} \\ or \\ \tan\Psi e^{i\Delta} = \tan\Psi_{gold}\tan\Psi_{mirrors} e^{i(\Delta_{gold}+\Delta_{mirrors})}\end{gathered} \tag{19}$$

Reproduced with permission of the copyright owner. Further reproduction prohibited without permission.

where $\tilde{\rho}_{gold} = \tan\Psi_{gold} e^{i\Delta_{gold}}$ and $\tilde{\rho}_{mirrrors} = \tan\Psi_{mirrors} e^{i\Delta_{mirrors}}$ are the ratios of complex reflectivies for *s*- and *p*-polarized for gold and the system of mirrors respectively. Note that $\tilde{\rho}_{mirrrors}$ is actually the product of reflections from all eight mirrors. When measuring a series of reflective surfaces, we simply multiply by the various values of tanΨ and add the vaious values of Δ to get the composite values of tanΨ and Δ. Using Eq. (19), the values of $\Psi_{mirrors}$ and $\Delta_{mirrors}$ were extracted and stored to a file to correct the measured values of Ψ and Δ according to the equation

$$\tilde{\rho}_{sample} = \frac{\tilde{\rho}_{measured}}{\tilde{\rho}_{mirrors}}$$
$$or \qquad (20)$$
$$\tan\Psi_{sample} e^{i\Delta_{sample}} = \frac{\tan\Psi_{measured}}{\tan\Psi_{mirrors}} e^{i(\Delta_{measured} - \Delta_{mirrors})}$$

The correction factors for the mirrors are usually small. The four mirrors on either side of the sample tend to amount to a value of $\tilde{\rho}_{mirror} \approx 1$ since two of the mirrors are oriented so that the plane of incidence is vertical while the other two are oriented so that the plane of incidence is horizontal. In addition since the mirrors are gold, tan$\Psi \approx 1$ for reflections of any angle of incidence off the mirrors.

After the mirror correction has been done, the retarder was moved into the path of the light beam and a new measurement of the gold sample was taken. Now the measured value of $\tilde{\rho}$ is

Reproduced with permission of the copyright owner. Further reproduction prohibited without permission.

$$\tilde{\rho} = \tilde{\rho}_{gold}\tilde{\rho}_{ret,mirrors}$$
$$or \qquad (21)$$
$$\tan\Psi e^{i\Delta} = \tan\Psi_{gold}\tan\Psi_{ret,mirrors}e^{i(\Delta_{gold}+\Delta_{ret,mirrors})}$$

where $\tilde{\rho}_{gold}$ is the same as in Eq. (19) and $\tilde{\rho}_{mirrors} = \tan\Psi_{mirrors}e^{i\Delta_{mirrors}}$ is the ratios of complex reflectivies for s and p polarized for system of mirrors and the retarder respectively. Like $\tilde{\rho}_{mirrors}$, $\tilde{\rho}_{ret,mirrors}$ is the product of several components, in this case the reflections from all eight mirrors and the passage of light through the retarding prism. Using Eq. (21), the values of $\Psi_{ret,mirrors}$ and $\Delta_{ret,mirrors}$ were extracted and stored to a file to correct the measured values of Ψ and Δ taken with the retarder in the light path according to the equation

$$\tilde{\rho}_{sample} = \frac{\tilde{\rho}_{measured}}{\tilde{\rho}_{ret,mirrors}}$$
$$or \qquad (22)$$
$$\tan\Psi_{sample}e^{i\Delta_{sample}} = \frac{\tan\Psi_{measured}}{\tan\Psi_{ret,mirrors}}e^{i(\Delta_{measured}-\Delta_{ret,mirrors})}$$

The correction factors for the mirrors is again small, but now, the retarder introduces approximately 90° change in Δ (that is $\Delta_{ret,mirrors} \approx \Delta_{mirrors} + 90° \approx 90°$). Of course this is the 90° change in delta which is necessary to get accurate measurements for samples with $\Delta \approx 0°$ or $\Delta \approx 180°$.

Reproduced with permission of the copyright owner. Further reproduction prohibited without permission.

It should be noted that these correction procedures could be done with other reference samples besides the gold mirror, although the calibration procedure is only automated for a gold reference sample. In particular, this may result in better results for samples which are transparent or have a small absorption coefficient, that is with samples which are not similar to gold. For example, using a transparent reference such as silicon with a native oxide might yield better results than gold. The calibration procedure would then procede as follows.

First, the structure of the reference sample must be very well determined. This might be accomplished by using high quality silicon with a native oxide, and measuring the sample in the visible (where we have a much more accurate ellipsometer) to determine the exact oxide thickness. Reference data from Palik[38-40] could then be used to obtain the properties of the reference sample in the infrared. One would then make a measurement using the retarder. This then would result in two files for the raw data as mentioned in the Measurement Procedures section below (_elbfsm.spc for the measurement without the retarder and _elbfsmr.spc for the measurement with the retarder). Next, one would set up correction files with Ψ=45° and Δ=0° to extract the total Ψ and Δ using the Sentech software and the raw data files [or one could just calculate Ψ and Δ directly using Eq. (A29)]. These could then be used to obtain the correction factors for the mirrors and retarder from equations like Eqs. (20) and (22) only with $\tilde{\rho}_{gold}, \Psi_{gold}, and\, \Delta_{gold}$ replace by $\tilde{\rho}_{Si}, \Psi_{Si}, and\, \Delta_{Si}$ respectively. These last three being the ellipsometric parameters for the silicon with native oxide reference sample mentioned above. As mentioned above, this procedure could be done with any reference sample for

Reproduced with permission of the copyright owner. Further reproduction prohibited without permission.

which properties can be accurately and reliably determined in the infrared. It may even be used to improve accuracy by taking into account any surface roughness on the gold reference sample. This method was tried with a silicon sample, but the lower reflectance seemed to impair the measurement, making it less accurate than for gold (even though silicon is a better known reference). This lower accuracy when calibrating with the silicon sample is probably also related to the polarizer deviation problem discussed in section 1.4.2.

1.4.4 Measurement Details (FTIR)

Once correction files have been created, the measurement proceeded as follows.

The system was prepared for NIR measurement. That is the CaF_2 beam splitter, ZnSe NIR polarizers, and the NIR retarder were put in place in the instrument. Measurement for other energy ranges was also possible as specified in the following table. The NIR optical components were good for measurements in the range 2900-11000 cm^{-1}, although it was noisy on the upper end of that range. The system also had optical components for MIR and FIR measurements, extending the range of the instrument to as far as 100 cm^{-1} (100 μm). The entire FTIR was kept under constant purge to eliminate absorption due to water and carbon dioxide.

Reproduced with permission of the copyright owner. Further reproduction prohibited without permission.

To start the measurement, the sample was placed on the sample stand and aligned using height/tilt (H/T) sensor and three stepper driven height screws (labeled Screw1, Screw 2, and Screw 3) as shown in Fig. 10. Screw 1 and Screw 2 run together without Screw 3 to adjust the tilt from front to back, while Screw 2 and Screw 3 were used to adjust the tilt from side to side. All three screws were driven together to adjust the height without affecting the tilt. Two LED light beams (Beam A and Beam B) were reflected from the sample and collected by two array of sensors as shown in Fig. 10. Beam A was directed directly down at the sample and the sample tilt was adjusted until the reflected beam showed that the sample was at normal incidence. After this, Beam B (at non-normal incidence) was used to adjust the sample height until the proper height for measurement was obtained. The LED light beams were pre-aligned by Sentech so that the ellipsometer light would focus properly on the sample and the detector, and so that the angle of incidence would be measured correctly.

The automated measurement was then started by pressing the Menu/Start button then the Measure Ψ,Δ button. Once this was done, the polarizer was moved to 45° and spectra were taken for eight analyzer angles (0°, 45°, 90°, 135°, 180°, 225°, 270°, and 315°) and saved in the file _elmfsb.spc. Of course only 3 angles are needed to extract the parameters, but the additional angles tends to average out non-uniformities in the system. Immediately following this, the retarder was moved into the light path and the analyzer was again scanned through the eight angles, the retarder data being stored in the file _elmfsbr.spc.

Reproduced with permission of the copyright owner. Further reproduction prohibited without permission.

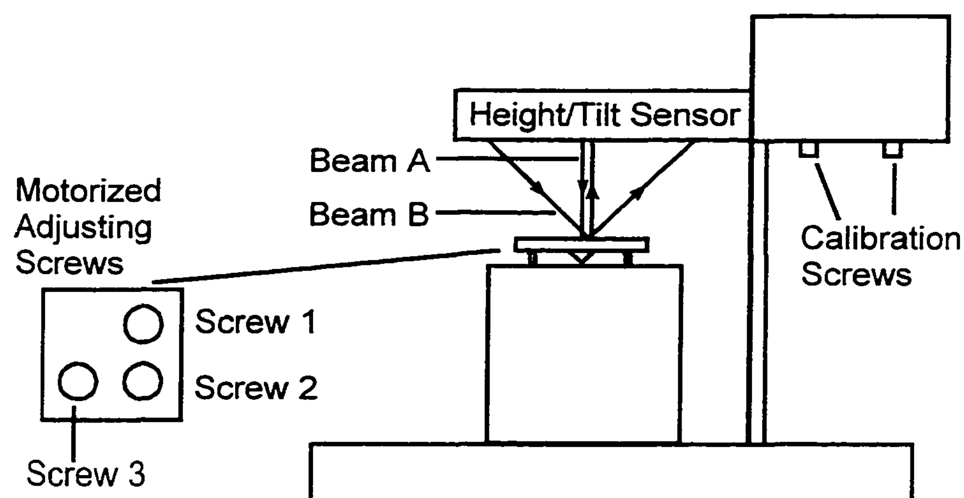

Figure 10. Height/tilt alignment. Beam A is used to adjust the tilt, then beam B is used to adjust the height. Three motorized screws are used to adjust the height and tilt.

Reproduced with permission of the copyright owner. Further reproduction prohibited without permission.

Next, values of Ψ and Δ were extracted separately for each of these configurations (with and without the retarder) according to Eqs. (A28) and (A29) in Appendix A. Then Ψ and Δ for the sample were extracted for each of these using the procedure specified section 1.4.3.4.

Next it was necessary to determine improved values of Ψ and Δ based upon the two measurements with and without the retarder. Here, we use Ψ_{wo}, Δ_{wo} and Ψ_w, Δ_w to denote the ellipsometric parameters as measured without and with the retarder in the light path respectively. It was assumed that a surface roughness or something else might change the phase of s-polarized light relative to p-polarized light upon reflectance without changing the relative magnitude. In this case, the values of Δ determined above might be inaccurate. Considering Eq. (A29) and the fact that the retarder introduced a phase shift of about 90°, it is seen that the actual parameters extracted are proportional to sin Δ and cos Δ for measurement with and without the retarder, respectively. Keeping this in mind, we introduce a phase polarization defined as

$$P_{ph} = \sqrt{\cos^2 \Delta_{wo} + \sin^2 \Delta_w} \qquad (23)$$

Then a corrected value of Δ was obtained according to

$$\Delta = \arccos(\frac{\cos \Delta_{wo}}{P_{ph}}) = \arcsin(\frac{\sin \Delta_w}{P_{ph}}) \qquad (24)$$

Reproduced with permission of the copyright owner. Further reproduction prohibited without permission.

This correction was expected to be small for our samples as the surfaces were smooth and clean. For some runs, the value of P_{ph} could be as low as 0.4. In these cases it was believed the extremely low values of P_{ph} were due to other problems in the system (see for example section 1.4.2) rather than phase depolarization at the surface of the sample, so these data were not used final data extraction for this thesis.

1.4.4.1 Various Settings – Advanced Scan Menu

Several parameters for the measurement are set through the Advanced Scan Menu (accessed through the "Collect/Advanced Scan Menu" menu option on the Sentech main measurement screen), which is shown in Fig. 11. In this section, we discuss several parameters set here for the measurement, including file name, comment, number of scans, resolution, sampling, detector, light source, aperture, gain amplitude, the wavelength range, the scan button, and the align button. The other parameters were not changed for the course of this work.

The file name and file comment shown here are those either for a single scan without any changes to the ellipsometer settings or for an ellipsometric determination.

The number of scans is the number of times the moveable FTIR mirror repeats its movement to average out noise. Usually 200 or more was required for smooth spectra.

Reproduced with permission of the copyright owner. Further reproduction prohibited without permission.

Figure 11. “Advanced Scan” dialog box with typical settings.

Reproduced with permission of the copyright owner. Further reproduction prohibited without permission.

The resolution setting is set in terms of cm^{-1} ($8\ cm^{-1} \approx 1$ meV). Higher resolution scans require more time. For this work, settings of 16 cm^{-1} or 32 cm^{-1} were used.

The two buttons next to sampling (UDR-2 and UDR-1) specify the undersampling ratio, which controls the rate at which the FTIR interferogram is sampled. UDR-2 is used for FIR and MIR scans (up to 7900 cm^{-1}) while UDR-1 is used for NIR scans (if part of the spectrum is above 7900 cm^{-1}). For this work, UDR-1 was used for most of the scans.

The detector set here is chosen by a 45° focusing mirror which moves to direct the light at one of two detectors (front and back). The front detector is a cooled DTGS detector. This detector was used for all the data taken by this system presented in this thesis. The back detector is PbSe based with a useful range of about 0.3-1.2 eV. Due to non-linearity problems with this detector, the extracted values of Ψ and Δ were inaccurate. Thus this detector was only used for preliminary studies, fast data acquisition was favored at the expense of accuracy. The detector was more accurate for lower light intensities (that is when using a neutral density filter to decrease the light intensity). In the case of either detector, the detector gain could be set through the gain amplitude dialog box. For the DTGS detector, this was usually set to 16.

The light source dialog box is used to select between two light sources, one for MIR and FIR and another for NIR. The NIR light source was used for all data presented here since the other light source had very little light intensity above 0.75 eV. When the ellipsometer was configured for dedicated NIR mode, the light source is set to "on".

Reproduced with permission of the copyright owner. Further reproduction prohibited without permission.

The aperture dialog box is used to control an aperture wheel in front of the light source. The hole size is specified in terms of the maximum energy resolution possible for that particular aperture (a poorly columnated beam limits FTIR resolution because different path lengths are obtained for slightly different angles of the beam). For this research, the smallest (0.25 cm^{-1}) aperture setting was used.

The wavelength range is specified through the Start WN and End WN boxes. These are the range in cm^{-1} (8066 cm^{-1} = 1 eV) for the measurement. For an FTIR system, the scan time does not depend of the wavelength range as all positions of the moveable mirror must be measured in order to determine the intensity for any single wavelength or all wavelengths. For this study, 2500-10000 cm^{-1} was used as the wavelength range for all measurements.

Two of the buttons at the bottom of this screen are useful: the scan button and the align button. The scan button can be used to do a simple intensity scan without moving any of the ellipsometer components. This is useful, for example, to check alignment and intensity before the final ellipsometeric scan. The align button is used to do an automated alignment of the beam splitter. The alignment of the beam splitter is critical for the correct functioning of the FTIR. The automated alignment procedure should be done whenever the FTIR is turned off or bumped. In addition, the automatic beam splitter alignment procedure was run daily during the course of this research.

Reproduced with permission of the copyright owner. Further reproduction prohibited without permission.

1.4.4.2 Etching Procedures (FTIR)

As mentioned in the UV/VIS/NIR etching procedure section, the affects of a thin surface layer (such as a native oxide or surface roughness) are most noticeable near the E_2 peak for zincblende type semiconductors. Unfortunately, this means that it is not simple to evaluate the effectiveness of an etch in the infrared regime (as the E_2 peak is usually in the visible or ultraviolet regime). For this reason, etches for this study were always carried out on the UV/VIS/NIR system and then transferred to the FTIR ellipsometer for measurement. The procedure was as follows.

A glove bag was placed over the top of the FTIR ellipsometer, enclosing the FTIR sample compartment and a workspace on top of the FTIR instrument. The glove bag and the entire FTIR were purged with nitrogen gas for about 30 minutes prior to measurement on the FTIR ellipsometer. The sample was etched as described in the UV/VIS/NIR etching procedure section, and measured in the range 1.5-5.3 eV. Following the etch and UV/VIS/NIR measurement, the sample was maintained under flowing nitrogen while the entire sample stage and cover were removed from the UV/VIS/NIR ellipsometer. Then the various holes in the sample stage cover were sealed and the vacuum line and nitrogen line were disconnected. The covered sample stage (and sample) were then quickly transferred to the FTIR ellipsometer glove bag. After a few minutes to reestablish the nitrogen purge, the sample was removed from the UV/VIS/NIR ellipsometer sample stage and mounted and measured on the FTIR ellipsometer. After the measurement, the sample was transferred back to the UV/VIS/NIR ellipsometer still under nitrogen and

Reproduced with permission of the copyright owner. Further reproduction prohibited without permission.

again measured in the UV/VIS/NIR range. If the second UV/VIS/NIR measurement indicated more than 3 Å oxide growth, the data was discarded and the entire procedure redone.

1.4.4.3 Purge Gas Generator

Many of the components of the FTIR system, including the beam splitters and retarders, are extremely hydrophilic and need to be kept in a water free environment. In addition, water and carbon dioxide have absorption bands in the infrared and thus must be eliminated in order to achieve accurate spectra. This was achieved using a Whatman 75-52 purge gas generator to supply continuous 24 hours a dry carbon dioxide free air to the system. (during etching experiments, bottled "pre-purified" nitrogen gas was used instead to prevent oxidation.)

The purge gas generator is shown in Fig. 12. Air was compressed using a Quincy compressor. The input pressure had to be maintained at about 90 psi in order for the purge gas generator to work properly. The compressed air flowed from the compressor through regulator valve and a Balston A912A-DX filter to the Whatman 75-52 FTIR purge gas generator system. Finally, the exit gas from the generator was passed through a 72-420 flow controller for delivery to the FTIR system at about 15 liters per minute. The purge gas generator required no maintenance except for a change of filter in the Balston A912A-DX about once a year and a less frequent change of the filter on the exit

Reproduced with permission of the copyright owner. Further reproduction prohibited without permission.

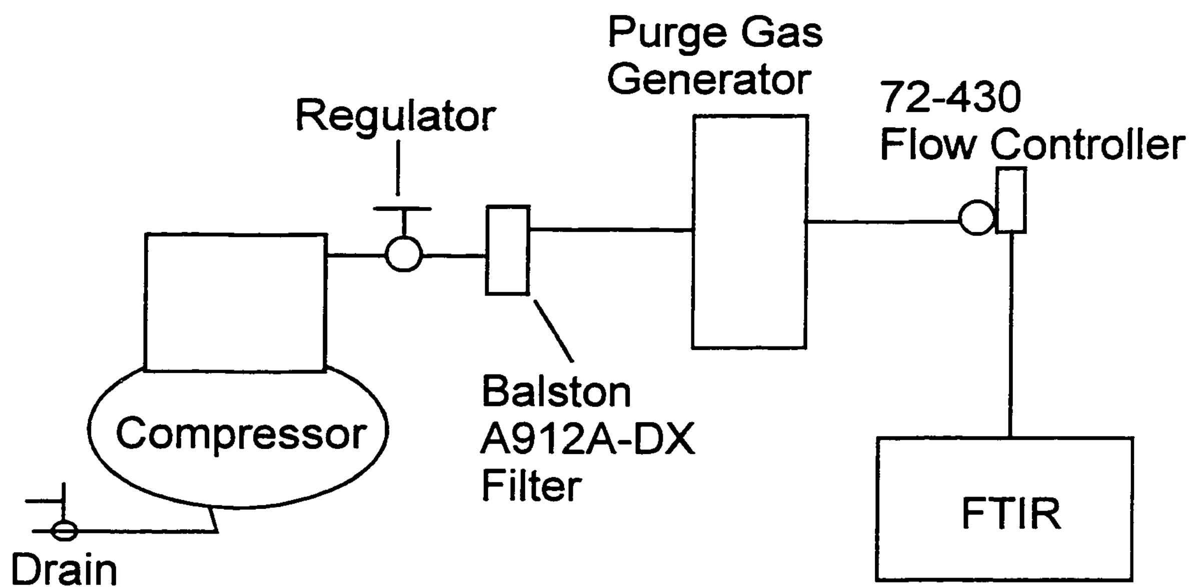

Figure 12. Purge gas generator setup.

Reproduced with permission of the copyright owner. Further reproduction prohibited without permission.

of the purge gas generator when it changed from yellow to green. In addition, the compressor oil was changed every few months. Also the compressor was drained of water monthly by releasing all air in the compressor and opening the valve on the bottom.

1.5 Application to physical (structural) models

In this section, we develop the theory for light reflecting from layered structures. We start with the simplest two-phase model (ambient and substrate). the we move on to the three-phase model where we also consider the effects of thin overlayers such as and oxide film or surface roughness. Then we develop the theory for handling any number of layers in the sample using matrix methods. Finally, we consider physical mixtures within a single layer using the effective medium approximation (EMA).

1.5.1 Two-phase model

The two-phase model is the simplest reflecting system to analyze. In addition, the results of the two-phase model can be extended to determine expressions for the more complicated three- and n-phase models. We follow the development given in Jackson for most of this section.[51]

Reproduced with permission of the copyright owner. Further reproduction prohibited without permission.

The two-phase model consists of two semi-infinite materials meeting at a planar boundary. Light is incident on the boundary from medium a and is partially reflected back to medium a and partially transmitted into medium b as shown in Fig. 13. Also shown in Fig. 13, we define the unit normal vector to the surface, $\hat{\mathbf{n}}$, and the electric field magnitude components parallel to the plane of incidence, the electric field magnitude components perpendicular to the plane of incidence, and wave vectors of the incident, transmitted, and reflected light as ($\mathscr{E}_{ip}$, $\mathscr{E}_{is}$, $\mathbf{k}_i^L$), ($\mathscr{E}_{tp}$, $\mathscr{E}_{ts}$, $\mathbf{k}_t^L$), and ($\mathscr{E}_{rp}$, $\mathscr{E}_{rs}$, $\mathbf{k}_r^L$), respectively. The s and p-components of the electric fields make up the incident, transmitted and reflected electric field vectors, $\mathbf{E}_i$, $\mathbf{E}_t$, and $\mathbf{E}_r$, respectively. The magnetic induction fields $\mathbf{B}_i$, $\mathbf{B}_t$, and $\mathbf{B}_r$ are perpendicular to $\mathbf{E}_i$, $\mathbf{E}_t$, and $\mathbf{E}_r$, respectively. Also, mediums a an b have complex indices of refraction ($\tilde{n} = n + i\kappa$) defined as

$$\begin{aligned} \tilde{n}_a &= \sqrt{\tilde{\mu}_a \tilde{\varepsilon}_a} \\ \tilde{n}_b &= \sqrt{\tilde{\mu}_b \tilde{\varepsilon}_b} \end{aligned} \qquad (25)$$

where $\tilde{\mu}_a, \tilde{\varepsilon}_a$ and $\tilde{\mu}_b, \tilde{\varepsilon}_b$ are the complex magnetic permeabilities and complex dielectric functions of mediums a and b, respectively.

We assume we have plane waves and use Maxwell's equations to obtain $\mathbf{B}$ from $\mathbf{E}$, we obtain for the three waves

Reproduced with permission of the copyright owner. Further reproduction prohibited without permission.

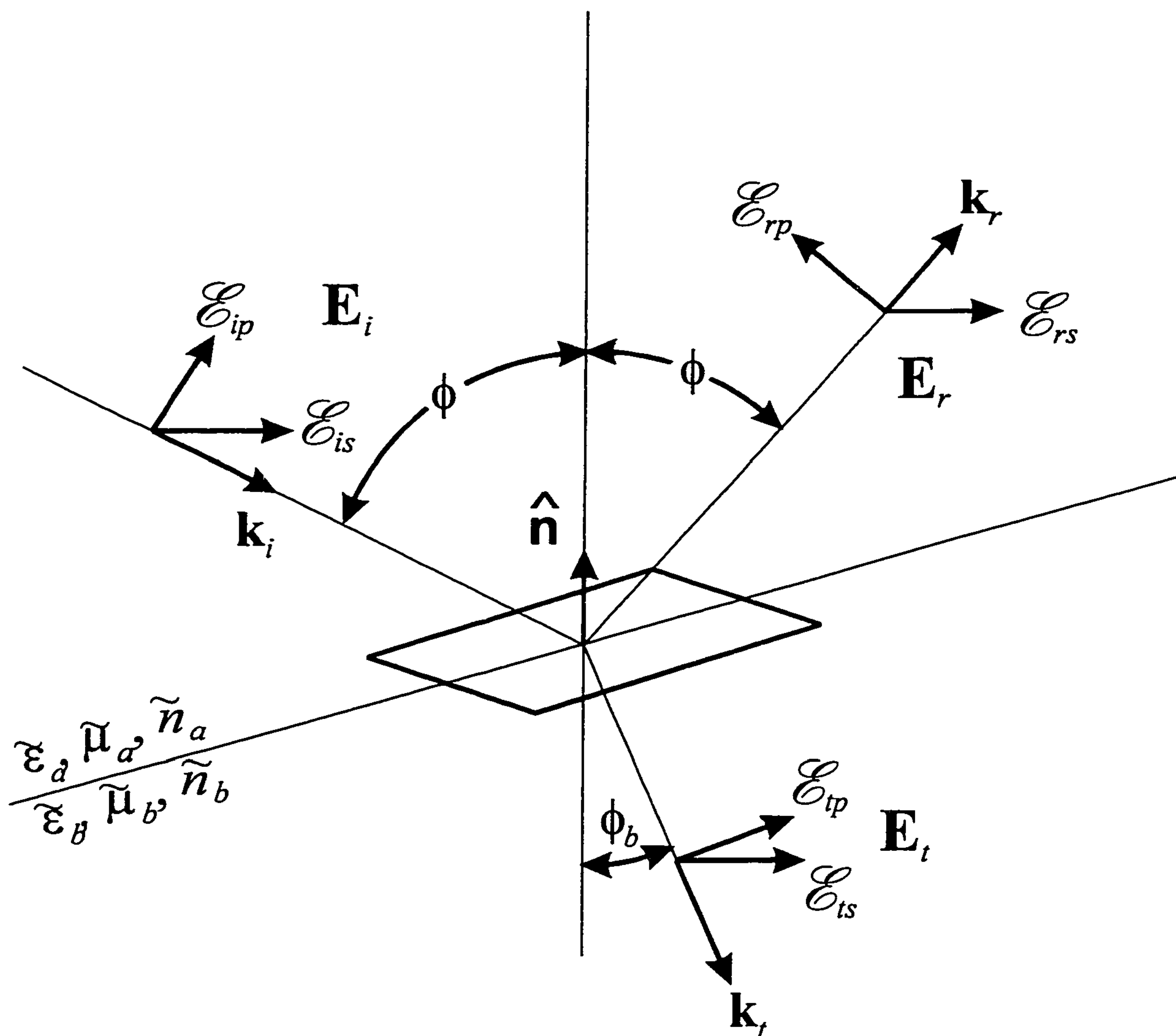

Figure 13. Two phase model. Light is incident from medium a on a semi-infinite substrate (medium b). $\hat{\mathbf{n}}$ is we define the unit normal vector to the surface. The electric field magnitude components parallel to the plane of incidence, the electric field magnitude components perpendicular to the plane of incidence, and wave vectors of the incident, transmitted, and reflected light are ($\mathscr{E}_{ip}$, $\mathscr{E}_{is}$, $\mathbf{k}_i^L$), ($\mathscr{E}_{tp}$, $\mathscr{E}_{ts}$, $\mathbf{k}_t^L$), and ($\mathscr{E}_{rp}$, $\mathscr{E}_{rs}$, $\mathbf{k}_r^L$) respectively. The s and p-components of the electric fields make up the incident, transmitted and reflected electric field vectors, $\mathbf{E}_i$, $\mathbf{E}_t$, and $\mathbf{E}_r$, respectively.

Reproduced with permission of the copyright owner. Further reproduction prohibited without permission.

$$\text{Incident}\quad \begin{cases} \mathbf{E}_i = \mathscr{E}_i \hat{\mathbf{e}}_i e^{i\mathbf{k}_i^L \bullet \mathbf{r} - i\omega t} \\ \mathbf{B}_i = \sqrt{\tilde{\mu}_a \tilde{\varepsilon}_a} \dfrac{\mathbf{k}_i^L \times \mathbf{E}_i}{k^L} \end{cases}$$

$$\begin{matrix}\text{Transmitted} \\ \text{(Refracted)}\end{matrix}\quad \begin{cases} \mathbf{E}_t = \mathscr{E}_t \hat{\mathbf{e}}_t e^{i\mathbf{k}_t^L \bullet \mathbf{r} - i\omega t} \\ \mathbf{B}_t = \sqrt{\tilde{\mu}_b \tilde{\varepsilon}_b} \dfrac{\mathbf{k}_t^L \times \mathbf{E}_t}{k_t^L} \end{cases} \qquad (26)$$

$$\text{Reflected}\quad \begin{cases} \mathbf{E}_r = \mathscr{E}_r \hat{\mathbf{e}}_r e^{i\mathbf{k}_r^L \bullet \mathbf{r} - i\omega t} \\ \mathbf{B}_r = \sqrt{\tilde{\mu}_a \tilde{\varepsilon}_a} \dfrac{\mathbf{k}_r^L \times \mathbf{E}_r}{k^L} \end{cases}$$

where $\mathscr{E}_i, \hat{\mathbf{e}}_i, \mathbf{k}_i^L$, $\mathscr{E}_t, \hat{\mathbf{e}}_t, \mathbf{k}_t^L$, and $\mathscr{E}_r, \hat{\mathbf{e}}_r, \mathbf{k}_r^L$ are the complex electric field magnitudes (that is they contains phase information), electric field polarization vectors, and light wave propagation vectors for the incident, transmitted, and reflected light, respectively. ω is the angular frequency of the light. The *s*- and *p*-components of the field magnitudes shown in Fig. 13 are then defined as

$$\begin{aligned} \mathscr{E}_{ip} &= \mathscr{E}_i \hat{\mathbf{e}}_i \bullet \hat{\mathbf{p}} \\ \mathscr{E}_{is} &= \mathscr{E}_i \hat{\mathbf{e}}_i \bullet \hat{\mathbf{s}} \\ \mathscr{E}_{tp} &= \mathscr{E}_t \hat{\mathbf{e}}_t \bullet \hat{\mathbf{p}} \\ \mathscr{E}_{ts} &= \mathscr{E}_t \hat{\mathbf{e}}_t \bullet \hat{\mathbf{s}} \\ \mathscr{E}_{rp} &= \mathscr{E}_r \hat{\mathbf{e}}_r \bullet \hat{\mathbf{p}} \\ \mathscr{E}_{rs} &= \mathscr{E}_r \hat{\mathbf{e}}_r \bullet \hat{\mathbf{s}} \end{aligned} \qquad (27)$$

where $\hat{\mathbf{p}}$ and $\hat{\mathbf{s}}$ are the unit vectors parallel and perpendicular to the plane of incidence, respectively.

Reproduced with permission of the copyright owner. Further reproduction prohibited without permission.

The light wave propagation vector magnitudes are given by

$$k^L = \left|\mathbf{k}_i^L\right| = \left|\mathbf{k}_r^L\right| = \frac{\omega}{c}\sqrt{\tilde{\mu}_a\tilde{\varepsilon}_a}$$
$$k_t^L = \left|\mathbf{k}_t^L\right| = \frac{\omega}{c}\sqrt{\tilde{\mu}_b\tilde{\varepsilon}_b} \tag{28}$$

Next, we consider the cases for light polarized perpendicular to the plane of incidence (*s*-polarization) and light polarized parallel to the plane of incidence (*p*-polarization). Maxwell's equations applied at the boundary tell us that the normal components of **D** and **B** and the tangential components of **E** and **H** are continuous. Applying these boundary at the interface between the two media, we obtain

$$[\tilde{\varepsilon}_a(\mathscr{E}_i\hat{\mathbf{e}}_i + \mathscr{E}_r\hat{\mathbf{e}}_r) - \tilde{\varepsilon}_b\mathscr{E}_t\hat{\mathbf{e}}_t]\bullet\hat{\mathbf{n}} = 0$$
$$[\mathbf{k}_i^L \times \mathscr{E}_i\hat{\mathbf{e}}_i + \mathbf{k}_r^L \times \mathscr{E}_r\hat{\mathbf{e}}_r - \mathbf{k}_t^L \times \mathscr{E}_t\hat{\mathbf{e}}_t]\bullet\hat{\mathbf{n}} = 0$$
$$(\mathscr{E}_i\hat{\mathbf{e}}_i + \mathscr{E}_r\hat{\mathbf{e}}_r - \mathscr{E}_t\hat{\mathbf{e}}_t)\times\hat{\mathbf{n}} = 0 \tag{29}$$
$$[\frac{1}{\tilde{\mu}_a}(\mathbf{k}_i^L \times \mathscr{E}_i\hat{\mathbf{e}}_i + \mathbf{k}_r^L \times \mathscr{E}_r\hat{\mathbf{e}}_r) - \frac{1}{\tilde{\mu}_b}\mathbf{k}_t^L \times \mathscr{E}_t\hat{\mathbf{e}}_t]\times\hat{\mathbf{n}} = 0$$

For light (**E** field) polarized perpendicular to the plane of incidence, the third and forth lines of Eq. (29) are

$$\mathscr{E}_{is} + \mathscr{E}_{rs} - \mathscr{E}_{ts} = 0$$
$$[\sqrt{\frac{\tilde{\varepsilon}_a}{\tilde{\mu}_a}}(\mathscr{E}_{is} - \mathscr{E}_{rs})\cos\phi - \sqrt{\frac{\tilde{\varepsilon}_b}{\tilde{\mu}_b}}\mathscr{E}_{ts}\cos\phi_b = 0 \tag{30}$$

Reproduced with permission of the copyright owner. Further reproduction prohibited without permission.

where ϕ is the angle of incidence, ϕ_b is the angle of refraction, and $\mathscr{E}_{is}$, $\mathscr{E}_{ts}$, and $\mathscr{E}_{rs}$ are the magnitudes of the incident, transmitted, and reflected *s*-polarized light, respectively. From these we obtain the Fresnel reflection and transmission coefficients for *s*-polarized light, $\tilde{r}_s$ and $\tilde{t}_s$, respectively.

$$\tilde{r}_s = \frac{\mathscr{E}_{rs}}{\mathscr{E}_{is}} = \frac{\tilde{n}_a \cos\phi - \frac{\tilde{\mu}_a}{\tilde{\mu}_b}\sqrt{\tilde{n}_b^2 - \tilde{n}_a^2 \sin^2\phi}}{\tilde{n}_a \cos\phi + \frac{\tilde{\mu}_a}{\tilde{\mu}_b}\sqrt{\tilde{n}_b^2 - \tilde{n}_a^2 \sin^2\phi}} = |\tilde{r}_s| e^{i\delta_s}$$
$$\tilde{t}_s = \frac{\mathscr{E}_{ts}}{\mathscr{E}_{is}} = \frac{2\,\tilde{n}_a \cos\phi}{\tilde{n}_a \cos\phi + \frac{\tilde{\mu}_a}{\tilde{\mu}_b}\sqrt{\tilde{n}_b^2 - \tilde{n}_a^2 \sin^2\phi}} \tag{31}$$

For light (**E** field) polarized parallel to the plane of incidence, the third and forth lines of Eq. (29) are

$$\cos\phi(\mathscr{E}_{ip} - \mathscr{E}_{rp}) - \cos\phi_b \mathscr{E}_{tp} = 0$$
$$[\sqrt{\frac{\tilde{\varepsilon}_a}{\tilde{\mu}_a}}(\mathscr{E}_{ip} + \mathscr{E}_{rp}) - \sqrt{\frac{\tilde{\varepsilon}_b}{\tilde{\mu}_b}}\mathscr{E}_{tp} = 0 \tag{32}$$

where and $\mathscr{E}_{ip}$, $\mathscr{E}_{tp}$, and $\mathscr{E}_{rp}$ are the magnitudes of the incident, transmitted, and reflected *p*-polarized light, respectively. From these we obtain the Fresnel reflection and transmission coefficients for *p*-polarized light, $\tilde{r}_p$ and $\tilde{t}_p$, respectively.

Reproduced with permission of the copyright owner. Further reproduction prohibited without permission.

$$\tilde{r}_p = \frac{\mathscr{E}_{rp}}{\mathscr{E}_{ip}} = \frac{\frac{\tilde{\mu}_a}{\tilde{\mu}_b}\tilde{n}_b^2\cos\phi - \tilde{n}_a\sqrt{\tilde{n}_b^2 - \tilde{n}_a^2\sin^2\phi}}{\frac{\tilde{\mu}_a}{\tilde{\mu}_b}\tilde{n}_b^2\cos\phi + \tilde{n}_a\sqrt{\tilde{n}_b^2 - \tilde{n}_a^2\sin^2\phi}} = |\tilde{r}_p|e^{i\delta_p}$$

$$\tilde{t}_p = \frac{\mathscr{E}_{tp}}{\mathscr{E}_{ip}} = \frac{2\,\tilde{n}_a\tilde{n}_b\cos\phi}{\frac{\tilde{\mu}_a}{\tilde{\mu}_b}\tilde{n}_b^2\cos\phi + \tilde{n}_a\sqrt{\tilde{n}_b^2 - \tilde{n}_a^2\sin^2\phi}} \tag{33}$$

As required by the geometry, $\tilde{r}_p = -\tilde{r}_s$ and $\tilde{t}_p = \tilde{t}_s$ for normal incidence (ϕ = 0), so ellipsometry at normal incidence is not useful for isotropic materials.

For most materials, $\tilde{\mu} \approx 1$, so we take $\tilde{\mu}_a = \tilde{\mu}_b = 1$. Then we can simplify and determine the ellipsometric parameters, Ψ and Δ as

$$\tilde{\rho} = \frac{\tilde{r}_p}{\tilde{r}_s} = \tan\Psi e^{i\Delta} = \frac{\sin^2\phi - \cos\phi\sqrt{\frac{\tilde{\varepsilon}_b}{\tilde{\varepsilon}_a} - \sin^2\phi}}{\sin^2\phi + \cos\phi\sqrt{\frac{\tilde{\varepsilon}_b}{\tilde{\varepsilon}_a} - \sin^2\phi}} \tag{34}$$

which can be rearranged to obtain

$$\tilde{\varepsilon}_b = \varepsilon_{1,b} + i\varepsilon_{2,b} = \tilde{\varepsilon}_a\left[\sin^2\phi + \sin^2\phi\tan^2\phi\left(\frac{1-\tilde{\rho}}{1+\tilde{\rho}}\right)^2\right] \tag{35}$$

Reproduced with permission of the copyright owner. Further reproduction prohibited without permission.

1.5.2 Three-Phase Model and Effects of Real Surfaces

The three-phase model consists of a semi-infinite ambient, a semi-infinite substrate, and a layer between these two as shown in Fig. 14. Light is incident from the ambient (layer a) at an angle ϕ, is refracted into a film (layer b) of thickness d_b at an angle ϕ_b, and is refracted into the substrate (layer c) at an angle ϕ_c. In addition, there are multiple reflections at the top and bottom of layer b, which cause interference with the primary reflected wave. We consider only the case where layer b is thin compared to the diameter of the light beam, so that these interfering beams can be considered coincident with the primary reflected wave.

This problem can be solved by performing a sum of all the interfering rays caused by the reflections at the two interfaces; however, the method presented in the next section ("m-Phase Model") is much simpler. Therefore, we present the result here and leave the derivation for the next section. The three phase model Fresnel reflection coefficients for p- and s-polarized light, respectively, are

$$\tilde{r}_{p,3} = \frac{\tilde{Z}\tilde{r}_{p,bc} + \tilde{r}_{p,ab}}{\tilde{Z}\tilde{r}_{p,ab}\tilde{r}_{p,bc} + 1}$$
$$\tilde{r}_{s,3} = \frac{\tilde{Z}\tilde{r}_{s,bc} + \tilde{r}_{s,ab}}{\tilde{Z}\tilde{r}_{s,ab}\tilde{r}_{s,bc} + 1} \qquad (36a)$$

Reproduced with permission of the copyright owner. Further reproduction prohibited without permission.

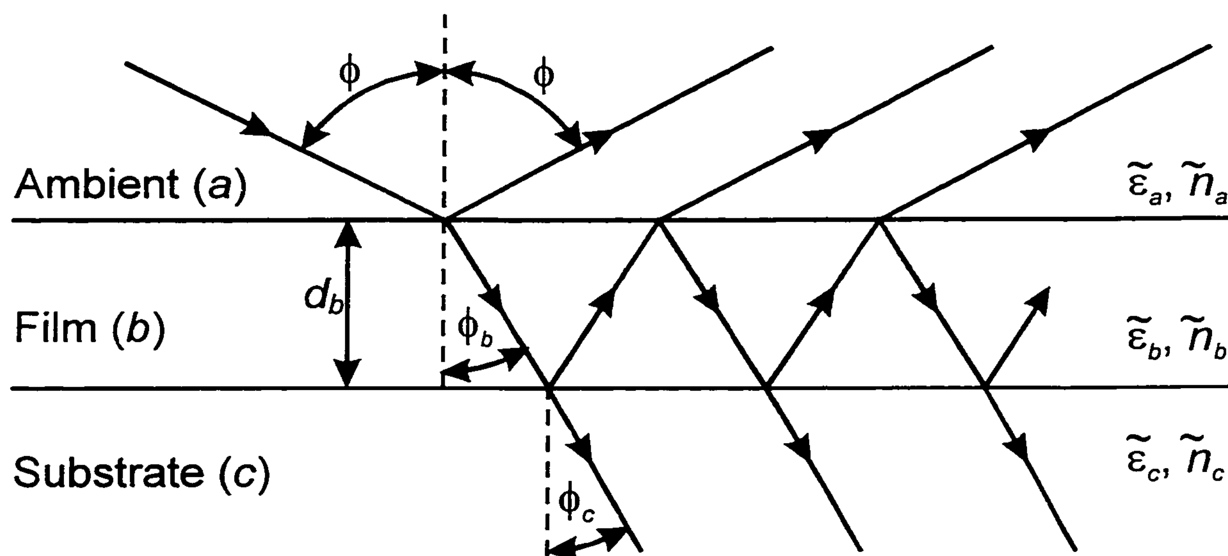

Figure 14. Three phase model. Multiple reflections occur at the two interfaces causing interference.

Reproduced with permission of the copyright owner. Further reproduction prohibited without permission.

where $\tilde{r}_{p,ab}$, $\tilde{r}_{p,bc}$, $\tilde{r}_{s,ab}$, and $\tilde{r}_{s,bc}$ are the two phase Fresnel reflection coefficients for *p*-polarized light between materials *a* and *b*, *p*-polarized light between materials *b* and *c*, *s*-polarized light between materials *a* and *b*, and *s*-polarized light between materials *b* and *c*, respectively, as defined by Eqs. (31) and (33). Also

$$\tilde{Z} = e^{\frac{2i\omega d_b}{c}\sqrt{\tilde{\varepsilon}_b - \tilde{\varepsilon}_a \sin^2\phi}} \tag{36b}$$

where d_b is the thickness of layer *b*.

The three phase model is very useful as it describes a system of an epilayer grown on a substrate, or a bulk material with a native oxide film. Unfortunately, this cannot be analytically inverted to give us a closed form solution for the dielectric function of layer *b* or layer *c* even if the value of d_b and the dielectric function of the other layer are known.

We can, however, find the effects of a thin surface oxide film or surface roughness pointed out by Aspnes.[52] By assuming d_b is small compared to the wavelength of the light and retaining only the first order terms in d_b of a power series expansion of Eq. (36a).

Reproduced with permission of the copyright owner. Further reproduction prohibited without permission.

$$\tilde{r}_{p,3} \approx 1 + \frac{2i\omega d_b}{c}\tilde{n}_a \cos\phi \left[\frac{\tilde{\varepsilon}_a(\tilde{\varepsilon}_c - \tilde{\varepsilon}_b)[\tilde{\varepsilon}_c\tilde{\varepsilon}_b - \tilde{\varepsilon}_a(\tilde{\varepsilon}_c + \tilde{\varepsilon}_b)\sin^2\phi]}{\tilde{\varepsilon}_b(\tilde{\varepsilon}_c - \tilde{\varepsilon}_a)[\tilde{\varepsilon}_c\tilde{\varepsilon}_b - \tilde{\varepsilon}_a(\tilde{\varepsilon}_c + \tilde{\varepsilon}_a)\sin^2\phi]} \right]$$
$$\tilde{r}_{s,3} \approx 1 + \frac{2i\omega d_b}{c}\tilde{n}_a \cos\phi \left[\frac{\tilde{\varepsilon}_c - \tilde{\varepsilon}_b}{\tilde{\varepsilon}_c - \tilde{\varepsilon}_a} \right] \tag{37}$$

and

$$\tilde{\rho}_3 \approx 1 + \frac{2i\omega d_b}{c}\tilde{n}_a \cos\phi \left[\frac{\tilde{\varepsilon}_c(\tilde{\varepsilon}_b - \tilde{\varepsilon}_a)(\tilde{\varepsilon}_c - \tilde{\varepsilon}_a)}{\tilde{\varepsilon}_b(\tilde{\varepsilon}_c - \tilde{\varepsilon}_a)(\tilde{\varepsilon}_c \cot^2\phi - \tilde{\varepsilon}_a)} \right] \tag{38}$$

Taking this value of ρ and substituting it into the equation for the two phase model [Eq. (35)], we find that the pseudo-dielectric function $\langle\varepsilon_c\rangle$ so derived is

$$\langle\tilde{\varepsilon}_c\rangle \approx \tilde{\varepsilon}_c + \frac{2i\omega d_b}{c} \frac{\tilde{\varepsilon}_c(\tilde{\varepsilon}_c - \tilde{\varepsilon}_b)(\tilde{\varepsilon}_b - \tilde{\varepsilon}_a)}{\tilde{\varepsilon}_b(\tilde{\varepsilon}_c - \tilde{\varepsilon}_a)} \sqrt{\frac{\tilde{\varepsilon}_c}{\tilde{\varepsilon}_a} - \sin^2\phi} \tag{39}$$

If $|\varepsilon_c| >> \varepsilon_a$, as is often the case with semiconductors, this reduces to

$$\langle\tilde{\varepsilon}_c\rangle \approx \tilde{\varepsilon}_c + \frac{2i\omega d_b \tilde{n}_c}{c\tilde{n}_a\tilde{\varepsilon}_b}(\tilde{\varepsilon}_c - \tilde{\varepsilon}_b)(\tilde{\varepsilon}_b - \tilde{\varepsilon}_a) \tag{40}$$

At this point, we can see why the pseudo-dielectric function is more sensitive at some energies than others. This is very important as it allows us to distinguish a clean abrupt surface from one that is not as well prepared. Oxide films tend to be transparent and

Reproduced with permission of the copyright owner. Further reproduction prohibited without permission.

fairly low dielectric function. If we also have an ε_c which has a small real part and a large imaginary part, the imaginary part of the measured pseudo-dielectric function will be greatly reduced from the value of the true dielectric function. This is the case near the E_2 feature for most diamond- and zincblende-type semiconductors, allowing immediate evaluation of the success of a particular etching procedure.

Figure 15 shows the simulated pseudo-dielectric function for GaAs with several different native oxide thicknesses. As expected, the imaginary part of the dilectric function near the E_2 feature is greatly reduced, while the real part of the dilectric function is little changed in this region. Also as predicted by Eqs. (39) and (40), the difference between the pseudo-dielectric function and the true dielectric function for GaAs is approximately proportional to the oxide layer thickness. Reference data for GaAs[47] and GaAs-oxide[53] were taken from Aspnes *et al.*

1.5.3 *m*-phase model

We consider a stack of layers with planar parallel interfaces, the top and bottom (ambient and substrate) layers being semi-infinite, as shown in Fig. 16. Dielectric functions and angles of incidence for each layer are labeled by the layer index. This can be handled by performing a sum of all the interfering rays caused by the reflections at every interface. However, since there will be infinite reflections for all but the top (ambient) and bottom (substrate) layers, this procedure becomes unwieldy especially for more than three

Reproduced with permission of the copyright owner. Further reproduction prohibited without permission.

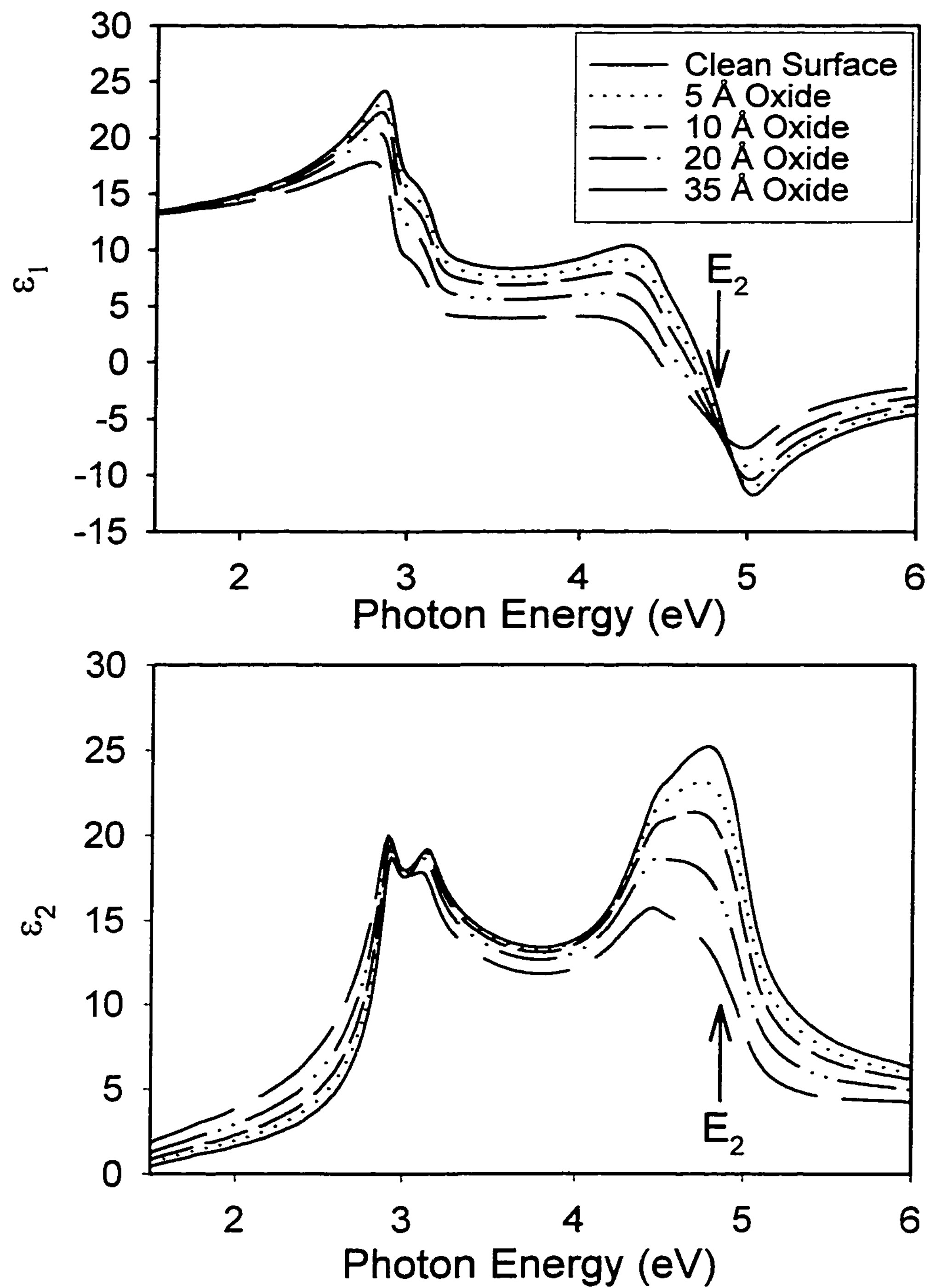

Figure 15. Calculated pseudodielectric function for a GaAs substrate with native oxide overlayers of various thicknesses as shown.

Reproduced with permission of the copyright owner. Further reproduction prohibited without permission.

phases. Instead we present a method based on 2x2 matrices, which is easily applied even to systems with many layers. The presentation in this section is similar to that given in Azzam and Bashara.[42]

The stack is illuminated by a single plane wave (that is the diameter of the light beam is much larger than the thickness of the layered stack) from the top. Therefore, the electric field in an arbitrary layer, i, will correspond to a superposition of plane waves propagating down (toward the substrate) at an angle ϕ_i with respect to the z-axis and plane waves propagating up (toward the ambient) at an angle $-\phi_i$ with respect to the z-axis.

We let $\mathscr{E}^+(z)$ and $\mathscr{E}^-(z)$ denote the complex amplitudes of the forward- and backward-travelling plane waves respectively and represent the electric field at an depth z into the layered stack as

$$\mathbf{E}(z) = \begin{bmatrix} \mathscr{E}^+(z) \\ \mathscr{E}^-(z) \end{bmatrix} \tag{41}$$

Since the system is linear, the electric field at an arbitrary point in the stack, z_1, must be related to the electric field at another arbitrary point in the stack, z_2, by a 2x2 matrix.

Reproduced with permission of the copyright owner. Further reproduction prohibited without permission.

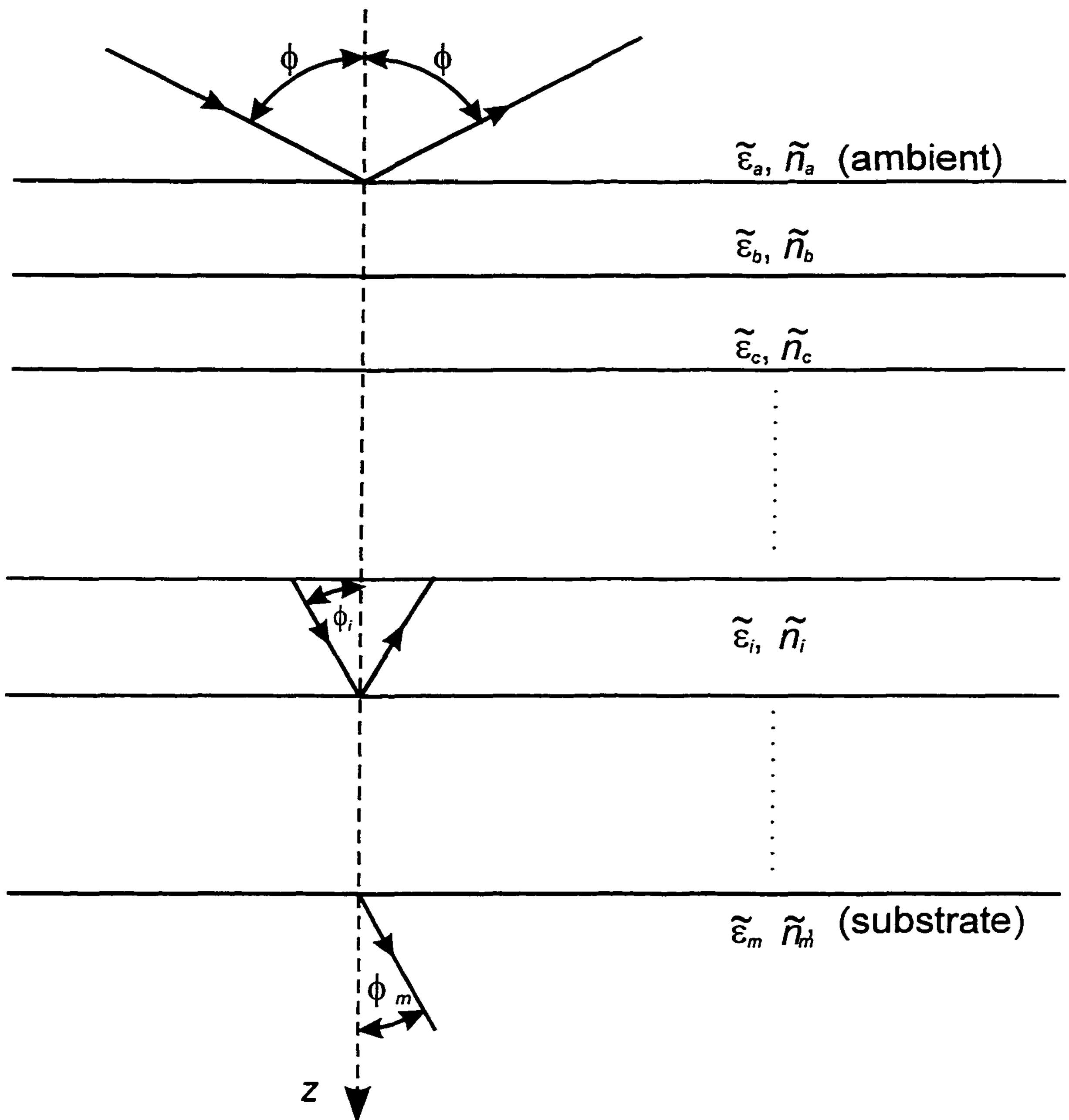

Figure 16. A stack of m layers with planar parallel interfaces, the top and bottom (ambient and substrate) layers being semi-infinite. Dielectric functions and angles of incidence for each layer are labeled by the layer index.

Reproduced with permission of the copyright owner. Further reproduction prohibited without permission.

$$\begin{bmatrix} \mathscr{E}^+(z_1) \\ \mathscr{E}^-(z_1) \end{bmatrix} = \begin{bmatrix} S_{11} & S_{12} \\ S_{21} & S_{22} \end{bmatrix} \begin{bmatrix} \mathscr{E}^+(z_2) \\ \mathscr{E}^-(z_2) \end{bmatrix}$$

or simply (42)

$$\mathbf{E}(z_1) = \mathbf{S}_{z_1,z_2}\mathbf{E}(z_2)$$

The task is to find the **S** matrix for the entire stack. We can break the stack down into a series of layers and interfaces between layers. First, we consider the interfaces. If we let z_1 be just above the top interface of the ith layer and z_2 be just below it, then Eq. (42) becomes

$$\begin{bmatrix} \mathscr{E}^+(z_1) \\ \mathscr{E}^-(z_1) \end{bmatrix} = \begin{bmatrix} I_{11} & I_{12} \\ I_{21} & I_{22} \end{bmatrix} \begin{bmatrix} \mathscr{E}^+(z_2) \\ \mathscr{E}^-(z_2) \end{bmatrix}$$

or (43)

$$\mathbf{E}(z_i - \delta) = \mathbf{I}_{i-1,i}\mathbf{E}(z_i + \delta)$$

where z_i is the position of the ith interface, δ is infinitesimal, and $\mathbf{I}_{i\text{-}1,i}$ is the matrix that characterizes the interface between the i-1 and i layers alone.

If we consider the time reversed version of Eq. (43), the downward propagating waves become upward propagating waves and vice versa while the interface remains unchanged. So, Eq. (43) becomes

Reproduced with permission of the copyright owner. Further reproduction prohibited without permission.

$$\begin{bmatrix} \mathcal{E}^-(z_1) \\ \mathcal{E}^+(z_1) \end{bmatrix} = \begin{bmatrix} I_{11} & I_{12} \\ I_{21} & I_{22} \end{bmatrix} \begin{bmatrix} \mathcal{E}^-(z_2) \\ \mathcal{E}^+(z_2) \end{bmatrix} \tag{44}$$

by comparing Eq. (43) with Eq. (44) we see that

$$I_{11} = I_{22} \text{ and } I_{12} = I_{21} \tag{45}$$

Therefore, we need only determine two components of the **I** matrix. To do this, we consider the special case of the two phase system, as shown in Fig. 17. This is exactly the geometry of section 1.5.1, if we make the identifications $\mathcal{E}_i \rightarrow \mathcal{E}_a^+$, $\mathcal{E}_t \rightarrow \mathcal{E}_b^+$, and $\mathcal{E}_r \rightarrow \mathcal{E}_a^-$. Then, using the results of that section, we find

$$\begin{aligned} \mathcal{E}_b^+ &= \tilde{t}_{ab} \mathcal{E}_a^+ \\ \mathcal{E}_a^- &= \tilde{r}_{ab} \mathcal{E}_a^+ \end{aligned} \tag{46}$$

where $\tilde{t}_{ab}$ and $\tilde{r}_{ab}$ are the two-phase Fresnel transmission and reflection coefficients defined by Eq. (31) and Eq. (42) for *s*- and *p*-polarized light respectively.

In the notation of this section, we have

Reproduced with permission of the copyright owner. Further reproduction prohibited without permission.

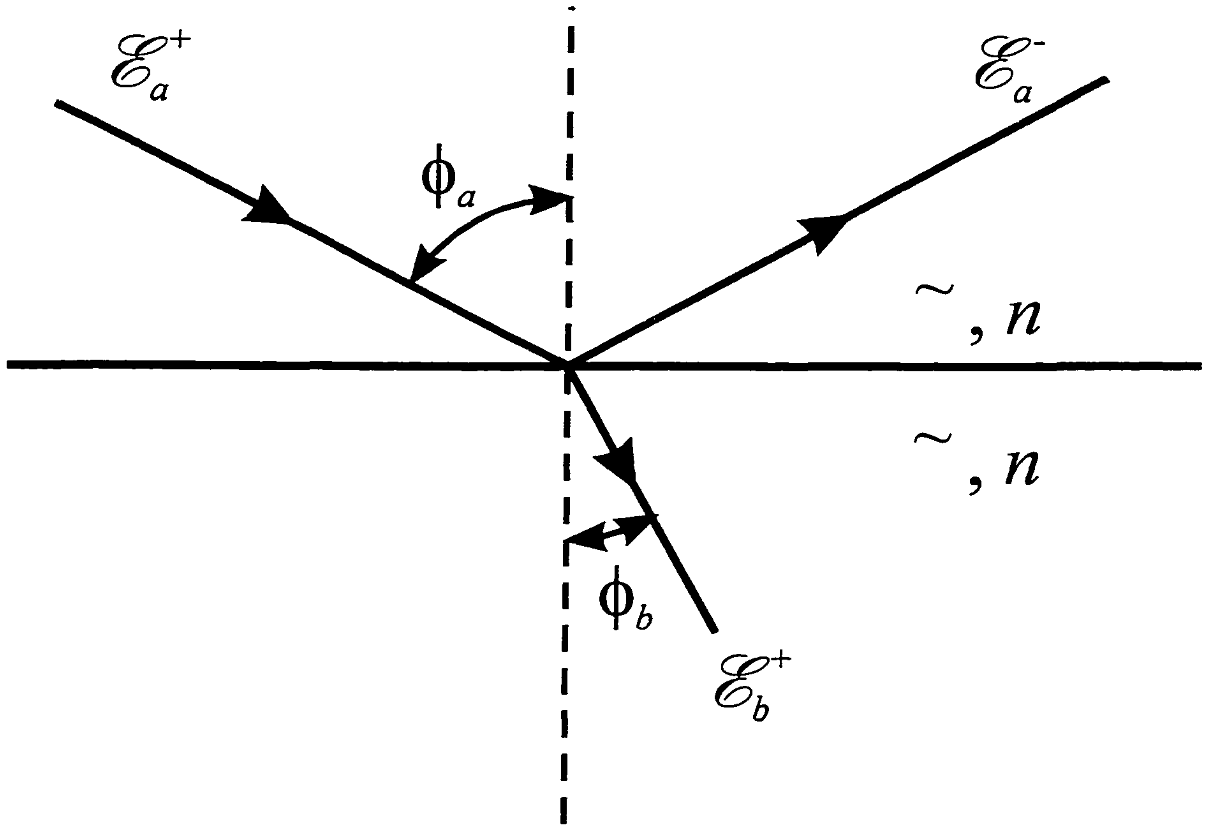

Figure 17. Two phase system using the notation of this section. This is exactly the geometry of section 1.5.1, if we make the identifications $\mathscr{E}_i \rightarrow \mathscr{E}_a^+$, $\mathscr{E}_t \rightarrow \mathscr{E}_b^+$, and $\mathscr{E}_r \rightarrow \mathscr{E}_a^-$.

Reproduced with permission of the copyright owner. Further reproduction prohibited without permission.

$$\begin{bmatrix} \mathscr{E}_a^+ \\ \mathscr{E}_a^- \end{bmatrix} = \begin{bmatrix} I_{11} & I_{12} \\ I_{21} & I_{22} \end{bmatrix} \begin{bmatrix} \mathscr{E}_b^+ \\ 0 \end{bmatrix}$$

or (47)

$$\mathscr{E}_a^+ = I_{11}\mathscr{E}_b^+$$
$$\mathscr{E}_a^- = I_{21}\mathscr{E}_b^+$$

Comparing Eq. (46) with Eq. (47), we find that $I_{11} = 1/\tilde{t}_{ab}$ and $I_{21} = \tilde{r}_{ab}/\tilde{t}_{ab}$ which combined with Eq. (45) gives

$$\mathbf{I}_{ab} = \begin{bmatrix} \dfrac{1}{\tilde{t}_{ab}} & \dfrac{\tilde{r}_{ab}}{\tilde{t}_{ab}} \\ \dfrac{\tilde{r}_{ab}}{\tilde{t}_{ab}} & \dfrac{1}{\tilde{t}_{ab}} \end{bmatrix} = \frac{1}{\tilde{t}_{ab}} \begin{bmatrix} 1 & \tilde{r}_{ab} \\ \tilde{r}_{ab} & 1 \end{bmatrix}. \qquad (48)$$

Now, we consider the matrix relating the electric field at the top of a layer to that at the bottom. This is in fact simple as this corresponds to propagation of a plane wave [Eq. (26)] through a homogeneous layer with index of refraction $\tilde{n}_i$ and thickness d_i ($=z_{i+1} - z_i$). Thus the relation is simply

$$\begin{bmatrix} \mathscr{E}^+(z_i+\delta) \\ \mathscr{E}^-(z_i+\delta) \end{bmatrix} = \begin{bmatrix} e^{i\beta} & 0 \\ 0 & e^{-i\beta} \end{bmatrix} \begin{bmatrix} \mathscr{E}^+(z_{i+1}-\delta) \\ \mathscr{E}^-(z_{i+1}-\delta) \end{bmatrix}$$

or (49a)

$$\mathbf{E}(z_i+\delta) = \mathbf{L}_i\mathbf{E}(z_{i+1}-\delta)$$

Reproduced with permission of the copyright owner. Further reproduction prohibited without permission.

where

$$\beta = \frac{\omega d_i \tilde{n}_i}{c}\cos\phi_i \tag{49b}$$

and we have defined the matrix for propagation within a single layer (from just inside the top interface to just inside the bottom interface), $\mathbf{L}_i$ as

$$\mathbf{L}_i = \begin{bmatrix} e^{i\beta} & 0 \\ 0 & e^{-i\beta} \end{bmatrix} \tag{50}$$

Finally, we can compose the matrix for an entire m layer stack (with a representing the ambient and m representing the substrate) as

$$\mathbf{S} = \mathbf{I}_{a,b}\mathbf{L}_b\mathbf{I}_{b,c}\mathbf{L}_c \ldots \mathbf{L}_l\mathbf{I}_{l,m} \tag{51}$$

Then, the reflection and transmission coefficients can be obtained for the stack by remembering that we are considering the situation with one forward moving incident and one backward moving reflected beam in the ambient ($\mathscr{E}_a^+$ and $\mathscr{E}_a^-$ respectively) and one forward moving transmitted beam in the substrate ($\mathscr{E}_m^+$).

Reproduced with permission of the copyright owner. Further reproduction prohibited without permission.

$$\begin{bmatrix} \mathscr{E}_a^+ \\ \mathscr{E}_a^- \end{bmatrix} = \begin{bmatrix} S_{11} & S_{12} \\ S_{21} & S_{22} \end{bmatrix} \begin{bmatrix} \mathscr{E}_m^+ \\ 0 \end{bmatrix} \tag{52}$$

so we have our reflection and transmission coefficients for an m-phase stack for either s- or p-polarized light:

$$\begin{aligned} \tilde{r}_m &= \frac{E_a^-}{E_a^+} = \frac{S_{21}}{S_{11}} \\ \tilde{t}_m &= \frac{E_s^+}{E_a^+} = \frac{1}{S_{11}} \end{aligned} \tag{53}$$

This technique is naturally very useful for computer simulations used to extract data from measurements on layered structures. As a simple example of the technique, we derive the expressions for a three-phase model [Eq. (36a)]. For either s- or p-polarized light, the 2x2 matrix for the three-phase model is

$$\begin{aligned} \mathbf{S} &= \frac{1}{\tilde{t}_{ab}\tilde{t}_{bc}} \begin{bmatrix} 1 & \tilde{r}_{ab} \\ \tilde{r}_{ab} & 1 \end{bmatrix} \begin{bmatrix} e^{i\beta_b} & 0 \\ 0 & e^{-i\beta_b} \end{bmatrix} \begin{bmatrix} 1 & \tilde{r}_{bc} \\ \tilde{r}_{bc} & 1 \end{bmatrix} \\ &= \frac{e^{i\beta}}{\tilde{t}_{ab}\tilde{t}_{bc}} \begin{bmatrix} (1+\tilde{r}_{ab}\tilde{r}_{bc}e^{-2i\beta_b}) & (\tilde{r}_{bc}+\tilde{r}_{ab}e^{-2i\beta_b}) \\ (\tilde{r}_{ab}+\tilde{r}_{bc}e^{-2i\beta_b}) & (\tilde{r}_{ab}\tilde{r}_{bc}+e^{-2i\beta_b}) \end{bmatrix} \end{aligned} \tag{54}$$

Combining this with Eq. (53), we have derived the result we initially stated in Eq. (36)

Reproduced with permission of the copyright owner. Further reproduction prohibited without permission.

$$\tilde{r}_3 = \frac{\tilde{Z}\tilde{r}_{bc} + \tilde{r}_{ab}}{\tilde{Z}\tilde{r}_{ab}\tilde{r}_{bc} + 1}$$
$$\tilde{t}_3 = \frac{\tilde{t}_{ab}\tilde{t}_{bc}}{\tilde{Z}\tilde{r}_{ab}\tilde{r}_{bc} + 1} \tag{55a}$$

where

$$\tilde{Z} = e^{\frac{4\pi i d_b}{\lambda}\sqrt{\tilde{\varepsilon}_b - \tilde{\varepsilon}_a \sin^2\phi}} \tag{55b}$$

and we have used Snell's law to put β_b in terms of the ambient angle of incidence. That is

$$\tilde{n}_b \cos\phi_b = \sqrt{\tilde{\varepsilon}_b \cos^2\phi_b} = \sqrt{\tilde{\varepsilon}_b - \tilde{\varepsilon}_b \sin^2\phi_b} = \sqrt{\tilde{\varepsilon}_b - \tilde{\varepsilon}_a \sin^2\phi} \tag{56}$$

1.5.4 Effective Medium Theory

We are often faced with the case that a layer in our model is not a single phase, but rather a physical mixture of two or more materials. This is the case for a sample with a rough surface (a mixture of air, material, and possibly oxide) or a non-abrupt interface (an extra interface layer which is a mixture of the two materials).

Reproduced with permission of the copyright owner. Further reproduction prohibited without permission.

The effective medium approximation (EMA) relates the polarizabilities (which in turn are related to the dielectric functions) of two or more materials in a physical mixture to an effective dielectric function. Thus it is an extension to the Clausius-Mossotti relation, which relates the dielectric function of a single material to the polarizabilities of its constituent atoms. Therefore, we begin this section with a derivation of the Clausius-Mossotti relation from the microscopic perspective and extend it to derive the EMA. The method used here is similar to that given by Aspnes.[54]

We start with points of polarizability ζ arrayed at the lattice sites ($\mathbf{r} = \mathbf{R}_i$) of an infinite simple cubic lattice as shown in Fig. 18. The cubic lattice is chosen because we are interested in isotropic materials. We apply a uniform electric field $\mathbf{E}_{int}$ which induces a point dipole at each lattice site with electric fields of the form

$$\mathbf{E}(\mathbf{p}_i,\mathbf{r}_i) = -\nabla\left(\frac{\mathbf{p}_i \bullet \hat{\mathbf{r}}_i}{r_i^2}\right) = \frac{3(\mathbf{p}_i \bullet \hat{\mathbf{r}}_i)\hat{\mathbf{r}}_i - \mathbf{p}_i}{r_i^3} \quad (57)$$

where $\mathbf{r}_i = \mathbf{r} - \mathbf{R}_i$ is the position relative to the lattice site and $\mathbf{p}_i$ is the point dipole polarization induced at each lattice site

$$\mathbf{p}_i = \zeta\mathbf{E}(\mathbf{R}_i) \quad (58)$$

So, we can write the total field as

Reproduced with permission of the copyright owner. Further reproduction prohibited without permission.

Figure 18. Schematic diagram of the simple cubic lattice used in the derivation of the Clausius-Mossotti relation. $\mathbf{E}_{int}$ is a uniform applied field.

Reproduced with permission of the copyright owner. Further reproduction prohibited without permission.

$$\mathbf{E}(\mathbf{r}) = \mathbf{E}_{\text{int}} + \sum_i \mathbf{E}(\mathbf{p}_i, \mathbf{r} - \mathbf{R}_i) \tag{59}$$

By lattice symmetry, the field (and thus the polarization) at each lattice point, $\mathbf{R}_i$, must be the same. We define this using Eq. (59) as

$$\mathbf{E}_{\text{loc}} \equiv \mathbf{E}(0) = \mathbf{E}_{\text{int}} + \sum_{i \neq 0} \mathbf{E}(\zeta \mathbf{E}_{\text{loc}}, -\mathbf{R}_i) = \mathbf{E}_{\text{int}} \tag{60}$$

where we have explicitly eliminated the singular term from the lattice site at the origin ($\mathbf{R}_0 = 0$). The summation in Eq. (60) vanishes shell by shell for the simple cubic lattice we are considering (it also vanishes for diamond and zincblende lattices). Thus we have the solution to the microscopic problem

$$\begin{aligned} \mathbf{E}(\mathbf{r}) &= \mathbf{E}_{\text{loc}} + \sum_i \mathbf{E}(\zeta \mathbf{E}_{\text{loc}}, \mathbf{r} - \mathbf{R}_i) \\ \mathbf{p}(\mathbf{r}) &= \sum_i \zeta \mathbf{E}_{\text{loc}} \delta(\mathbf{r} - \mathbf{R}_i) \\ \mathbf{E}_{\text{loc}} &= \mathbf{E}_{\text{int}} \end{aligned} \tag{61}$$

The delta function in Eq. (61) indicates that the dipoles are located only at lattice sites.

Now we relate these microscopic quantities to the macroscopic quantities we normally deal with: the dipole moment per unit volume, **P**, the electromagnetic field, **E**, and the electromagnetic displacement, **D**, which are related by the macroscopic equations:

Reproduced with permission of the copyright owner. Further reproduction prohibited without permission.

$$\mathbf{D} = \tilde{\varepsilon}\mathbf{E} = \mathbf{E} + 4\pi\mathbf{P} \tag{62}$$

Taking the volume of the system to be Ω, we find

$$\mathbf{P} = \frac{1}{\Omega}\int_{\Omega} \mathbf{p}(\mathbf{r})d^3r = \eta\zeta\mathbf{E}_{\text{loc}} \tag{63}$$

where η is the number of lattice points per unit volume ($\eta = a^{-3}$ if a is the lattice constant). Next, $\mathbf{E}$ is simply the volume average of $\mathbf{E}(\mathbf{r})$. We first find the volume integral of $\mathbf{E}(\mathbf{p}, \mathbf{r})$ over a unit cell to be

$$\int_{\text{cell vol}} \mathbf{E}(\mathbf{p},\mathbf{r})d^3r = -\int_{\text{cell vol}} \nabla\left(\frac{\mathbf{p}\bullet\hat{\mathbf{r}}}{r^2}\right)d^3r = -\int_{\text{cell surf}} \left(\frac{\mathbf{p}\bullet\hat{\mathbf{r}}}{r^2}\right)\hat{n}d^2r = -\frac{4\pi\mathbf{p}}{3} \tag{64}$$

Then, using Eq. (64) to take the volume average of the first line of Eq. (61), we obtain

$$\mathbf{E} = \mathbf{E}_{\text{loc}} - \frac{4\pi\eta\zeta\mathbf{E}_{\text{loc}}}{3} = \mathbf{E}_{\text{loc}} - \frac{4\pi\mathbf{P}}{3} \tag{65}$$

If we use Eq. (63) to eliminate $\mathbf{P}$ from Eqs. (62) and (65), we obtain

Reproduced with permission of the copyright owner. Further reproduction prohibited without permission.

$$\tilde{\varepsilon}\mathbf{E} = \mathbf{E} + 4\pi\eta\zeta\mathbf{E}_{\text{loc}}$$
$$\mathbf{E} = \mathbf{E}_{\text{loc}} - \frac{4\pi\eta\zeta\mathbf{E}_{\text{loc}}}{3} \tag{66}$$

Then we use the first line above to eliminate $\mathbf{E}_{\text{loc}}$ from the second line, and we obtain the Clausius-Mossitti equation.

$$\frac{\tilde{\varepsilon}-1}{\tilde{\varepsilon}+2} = \frac{4\pi\eta\zeta}{3} \tag{67}$$

With the above derivation, extension to the EMA is simple. To start with, we randomly assign different polarizabilities ζ_a, ζ_b, …, ζ_m to the lattice sites.

Because the assignment is random and we are still using a simple cubic lattice, the summation in Eq. (60) is still 0 so that $\mathbf{E}_{\text{loc}} = \mathbf{E}_{\text{int}}$ as before. The volume averages now yeild

$$\mathbf{P} = (\eta_a\zeta_a + \eta_b\zeta_b + \cdots + \eta_m\zeta_m)\mathbf{E}_{\text{loc}}$$
$$\mathbf{E} = \mathbf{E}_{\text{loc}} - \frac{4\pi\mathbf{P}}{3} \tag{68}$$

where η_a, η_b,…, η_m are the volume densities for each type of point dipole. Performing the algebraic elimination as we did for Eq. (67), we obtain

Reproduced with permission of the copyright owner. Further reproduction prohibited without permission.

$$\frac{\tilde{\varepsilon}-1}{\tilde{\varepsilon}+2}=\frac{4\pi}{3}(\eta_a\zeta_a+\eta_b\zeta_b+\cdots+\eta_m\zeta_m) \tag{69}$$

Eq. (69) can be expressed more conveniently by using the Clausius-Mossotti relation [Eq. (67)] to express it in terms of the dielectric functions $\tilde{\varepsilon}_a, \tilde{\varepsilon}_b, \ldots, \tilde{\varepsilon}_m$ of the pure phases a, $b, \ldots, m$

$$\frac{\tilde{\varepsilon}-1}{\tilde{\varepsilon}+2}=f_a\frac{\tilde{\varepsilon}_a-1}{\tilde{\varepsilon}_a+2}+f_b\frac{\tilde{\varepsilon}_b-1}{\tilde{\varepsilon}_b+2}+\cdots+f_m\frac{\tilde{\varepsilon}_m-1}{\tilde{\varepsilon}_m+2} \tag{70}$$

where f_i is the volume fraction of the ith phase

$$f_i=\frac{\eta_i}{\sum_{j=a}^{m}\eta_j}, \qquad \sum_{i=a}^{m} f_i=1 \tag{71}$$

Eq. (70) is the Lorentz-Lorenz effective-medium expression. The above derivation is general, but the final expression, Eq. (70), is not appropriate if the microscopic regions are large enough to possess their own dielectric identity. In this case, our assumption up to this point that the point dipoles are distributed randomly on the cubic lattice is no longer valid. However, assuming the regions are small compared to the light wavelength, we can still proceed from a microscopic viewpoint. We assume for simplicity that we have material composed predominately of material a of dielectric $\tilde{\varepsilon}_a$ with small spherical

Reproduced with permission of the copyright owner. Further reproduction prohibited without permission.

inclusions of dielectric function $\tilde{\varepsilon}_b, \tilde{\varepsilon}_c, \ldots, \tilde{\varepsilon}_m$. The solution for a sphere of dielectric function $\tilde{\varepsilon}_i$ of radius r_i embedded in a medium of dielectric $\tilde{\varepsilon}_a$ for an applied field $\mathbf{E}_0$ uniform at large distances is[55]

$$\mathbf{E}(\mathbf{r}) = \begin{cases} \dfrac{3\tilde{\varepsilon}_a}{\tilde{\varepsilon}_i + 2\tilde{\varepsilon}_a}\mathbf{E}_0 & \|\mathbf{r}\| < r_i \\ \mathbf{E}_0 + \mathbf{E}(\mathbf{p}_i, \mathbf{r}) & \|\mathbf{r}\| > r_i \end{cases} \tag{72}$$

where $\mathbf{E}(\mathbf{p}_a,\mathbf{r})$ is defined by Eq. (57) with

$$\mathbf{p}_i = \frac{\tilde{\varepsilon}_i - \tilde{\varepsilon}_a}{\tilde{\varepsilon}_i + 2\tilde{\varepsilon}_a} r_i^3 \mathbf{E}_0 \tag{73}$$

since all of the regions now have a well defined dielectric function, Eq. (62) can be applied within each region to obtain the polarization vector for medium i as

$$\mathbf{P}_i(\mathbf{r}) = \frac{\tilde{\varepsilon}_i - 1}{4\pi}\mathbf{E}(\mathbf{r}) \tag{74}$$

Using this, the volume average of Eq. (62) becomes

$$\frac{\tilde{\varepsilon}}{\Omega}\int_{\Omega}\mathbf{E}(\mathbf{r})d^3r = \frac{1}{\Omega}\sum_{i=1}^{m}\tilde{\varepsilon}_i\int_{\Omega_i}\mathbf{E}(\mathbf{r})d^3r \tag{75}$$

Reproduced with permission of the copyright owner. Further reproduction prohibited without permission.

In other words, once we have a solution for the electric field throughout the structure, the effective dielectric time the average electric field is simply the sum of average field in each region times the volume of the region weighted by the dielectric function for that region. With the form of the electric field given in Eq. (72), this becomes

$$\tilde{\varepsilon}\mathbf{E}_0\left[f_a+\sum_{i=b}^{m}\frac{3\tilde{\varepsilon}_a f_i}{\tilde{\varepsilon}_i+2\tilde{\varepsilon}_a}\right]=\mathbf{E}_0\left[\tilde{\varepsilon}_a f_a+\sum_{i=b}^{m}\frac{3f_i\tilde{\varepsilon}_i\tilde{\varepsilon}_a}{\tilde{\varepsilon}_i+2\tilde{\varepsilon}_a}\right] \tag{76}$$

where f_i is the volume fraction of the ith phase. Note that the term $\mathbf{E}(\mathbf{p}_i,\mathbf{r})$ in the second line of Eq. (72) does not contribute to Eq. (76) because the origin of the dipole is not in medium a, so the volume integral over medium a yields 0.

$$f_i=\begin{cases}\dfrac{4\pi r_i^3}{3\Omega} & i\neq a\\[2ex] 1-\displaystyle\sum_{j=b}^{m}f_j & i=a\end{cases} \tag{77}$$

Then Eq. (76) simplifies to

$$\tilde{\varepsilon}-\tilde{\varepsilon}_a=\sum_{i=b}^{m}\left[\tilde{\varepsilon}-\tilde{\varepsilon}_a+\frac{3\tilde{\varepsilon}_a(\tilde{\varepsilon}_i-\tilde{\varepsilon})}{\tilde{\varepsilon}_i+2\tilde{\varepsilon}_a}\right]f_i \tag{78}$$

which can be written

Reproduced with permission of the copyright owner. Further reproduction prohibited without permission.

$$\frac{\tilde{\varepsilon}-\tilde{\varepsilon}_a}{\tilde{\varepsilon}+2\tilde{\varepsilon}_a}=\sum_{i=b}^{m}\left[\frac{\tilde{\varepsilon}_i-\tilde{\varepsilon}_a}{\tilde{\varepsilon}_i+2\tilde{\varepsilon}_a}\right]f_i \tag{79}$$

Eq. (79) is the Maxwell-Garnett effective-medium expression. This expression is valid if the material is predominately material a; however, its validity becomes questionable as the volume fractions of the other materials increases. In particular, if we assume we have a 50%/50% mixture of two materials, Eq. (79) yields two different expressions for the effective dielectric of the mixture depending on which material is selected for the host material [material a in Eq. (79)]. Not only is this esthetically undesirable, but it also does not allow one to grade smoothly from material a to material b to model a rough interface. Bruggeman resolved this dilemma by purposing that we should consider all of the phases to be small inclusions in a material with a dielectric of the effective medium itself. Then Eq. (79) becomes

$$0=\sum_{i=a}^{m}\left[\frac{\tilde{\varepsilon}_i-\tilde{\varepsilon}}{\tilde{\varepsilon}_i+2\tilde{\varepsilon}}\right]f_i \tag{80}$$

which is now symmetric with respect to all materials. Eq. (80) is the Bruggeman effective-medium expression, which was used whenever an EMA was needed throughout this dissertation.

Reproduced with permission of the copyright owner. Further reproduction prohibited without permission.

Finally, we note that all three effective-medium expressions [Eqs. (70), (79), and (80)] can be expressed as

$$\frac{\tilde{\varepsilon}-\tilde{\varepsilon}_h}{\tilde{\varepsilon}+2\tilde{\varepsilon}_h}=\sum_{i=a}^{m}\left[\frac{\tilde{\varepsilon}_i-\tilde{\varepsilon}_h}{\tilde{\varepsilon}_i+2\tilde{\varepsilon}_h}\right]f_i \tag{81}$$

where $\tilde{\varepsilon}_h$, the host dielectric function, is 1, $\tilde{\varepsilon}_a$, and $\tilde{\varepsilon}$ for the Lorentz-Lorenz, Maxwell Garnett, and Bruggeman effective medium expressions respectively. The three expressions are different based on screening effects due to the inclusions being embedded in nothing (void), material a, or the effective medium.

It should also be noted that effective medium expression is affected by the geometry of the inclusions. The spherical geometry assumed here is certainly reasonable for an isotropic mixture. For a discussion on the effects of geometry, see Ref. 54.

1.6 Theory – Dielectric Function

In this chapter, we present a basic background for a theoretical model of the dielectric function. We start with a review of relations between various optical properties (some of which have already been mentioned in passing). Then we discuss the allowed energy

Reproduced with permission of the copyright owner. Further reproduction prohibited without permission.

states for an electron in a periodic crystal, that is the band structure. We then move on to a discussion of the effective mass approximation and how it can be used to interpret various perturbations to the ideal one electron states given by band structure calculations. Finally, in the last two sections, we relate band structure to the dielectric function.

1.6.1 Relations Between Optical Properties

The most often used optical functions are the complex dielectric function ($\tilde{\varepsilon}$), the complex index of refraction ($\tilde{n}$), the absorption coefficient (α), and the complex wave propagation vector (**k**). These are all related by the macroscopic Maxwell equations and their solution for plane waves propagating through a medium (light). The macroscopic Maxwell equations are

$$\begin{aligned} &\nabla \bullet \mathbf{D} = 4\pi\rho \qquad && \nabla \times \mathbf{H} = \frac{4\pi}{c}\mathbf{J} + \frac{1}{c}\frac{\partial \mathbf{D}}{\partial t} \\ &\nabla \bullet \mathbf{B} = 0 && \nabla \times \mathbf{B} + \frac{1}{c}\frac{\partial \mathbf{B}}{\partial t} = 0 \end{aligned} \tag{82}$$

where **D** is the electric displacement, **E** is the electric field, **H** is the magnetic field, **B** is the magnetic induction, **J** is the current density vector, ρ is the free charge density, and c is the speed of light in vacuum.

In addition, we have the ancillary definitions

Reproduced with permission of the copyright owner. Further reproduction prohibited without permission.

$$\mathbf{D} = \tilde{\varepsilon}(\omega)\mathbf{E} = \mathbf{E} + 4\pi\mathbf{P} = [1 + 4\pi\tilde{\chi}(\omega)]\mathbf{E}$$
$$\mathbf{B} = \tilde{\mu}(\omega)\mathbf{H} \tag{83}$$

where **P** is the averaged polarization (dipole average as discussed in section 1.5.4. We note that although $\varepsilon(x,t;x',t')$ and $\mu(x,t;x',t')$ are real, their Fourier transforms, $\tilde{\varepsilon}(\omega)$ and $\tilde{\mu}(\omega)$ are in general complex. In particular

$$\tilde{\varepsilon}(\omega) = \varepsilon_1(\omega) + i\varepsilon_2(\omega). \tag{84}$$

A non-zero value for $\varepsilon_2(\omega)$ indicates the **D** is out of phase with **E**.

We consider an infinite material with no free charge or current (ρ=0, **J**=0). Then Eq. (82) yields the wave equation for **E** with the well known plane wave solution[51]

$$\mathbf{E} = \mathbf{E}_0 e^{i\tilde{\mathbf{k}}\bullet\mathbf{r} - i\omega t} \tag{85}$$

where we have taken the convention that the real part of Eq. (85) is the electric field [also **D** will correspond to the real part of Eq. (83)] and **r** is the position vector, $\mathbf{E}_0$ is the electric field intensity at $\mathbf{r} = 0,\ t = 0$ and

$$\left\|\tilde{\mathbf{k}}(\omega)\right\| = \tilde{k}(\omega) = k_1 + ik_2 = \sqrt{\tilde{\varepsilon}(\omega)\tilde{\mu}(\omega)}\,\frac{\omega}{c} \tag{86}$$

Reproduced with permission of the copyright owner. Further reproduction prohibited without permission.

and the direction of **k** is the direction the wave is traveling. The velocity, v, of such a wave is

$$\tilde{v}(\omega) = \frac{c}{\sqrt{\tilde{\varepsilon}(\omega)\tilde{\mu}(\omega)}} \tag{87}$$

The complex velocity above is admittedly strange. The real part is the normal phase velocity of the propagating wave. The imaginary part corresponds to a exponential damping of the wave as it propagates through the medium. Eq. (87) allows us to define the complex index of refraction in the normal way

$$\tilde{n}(\omega) = n(\omega) + i\kappa(\omega) = \frac{c}{\tilde{v}(\omega)} = \sqrt{\tilde{\varepsilon}(\omega)\tilde{\mu}(\omega)} \tag{88}$$

Finally, we can find the absorption coefficient by considering the time averaged energy density, u, of a wave traveling into the material.[51]

$$u \propto \|\mathbf{E}\|^2 = \|\mathbf{E}_0\|^2 e^{-2k_2 d} \tag{89}$$

where d is the distance the wave has traveled in the medium. From Eq. (89), we can define the absorption coefficient, α, and skin depth, δ, as

Reproduced with permission of the copyright owner. Further reproduction prohibited without permission.

$$\alpha = \frac{1}{\delta} = 2k_2 \tag{90}$$

some authors[51] define the skin depth according to the electric field and thus find a length double that of Eq. (90) for the skin depth.

Finally we can relate the imaginary part of the dielectric function to the conductivity for low frequencies. We assume the medium obeys Ohm's law.

$$\mathbf{J} = \sigma\mathbf{E} \tag{91}$$

We also let ε_0 be the dielectric function neglecting any effects of the conductivity. Then the Maxwell-Ampère equation [the right side of first line of Eq. (82)] becomes

$$\nabla \times \mathbf{H} = \frac{4\pi}{c}\sigma\mathbf{E} + \frac{-i\omega\tilde{\varepsilon}_0(\omega)}{c}\mathbf{E} = -\frac{i\omega}{c}\left(\tilde{\varepsilon}_0(\omega) + i\frac{4\pi\sigma}{\omega}\right)\mathbf{E} \tag{92}$$

If we interpret the terms in parentheses on the right side of Eq. (92) as due to the dielectric properties of the medium instead of a result of Ohm's law, we find

$$\tilde{\varepsilon}(\omega) = \tilde{\varepsilon}_0(\omega) + i\frac{4\pi\sigma}{\omega} \tag{93}$$

Reproduced with permission of the copyright owner. Further reproduction prohibited without permission.

For low frequencies, we expect $\tilde{\varepsilon}_0(\omega)$ to be real since all of the dissipation of the of the electric field is due to the conductivity of the material. Thus

$$\varepsilon_2(\omega \approx 0) = \frac{4\pi\sigma}{\omega} \tag{94}$$

This shows that the imaginary part of the dielectric function of a conducting medium has a singularity at $\omega = 0$.

As in the previous section, we assume we have non-magnetic materials, that is $\mu = 1$. With this simplification, we can derive several relations among the optical functions using Eqs. (84), (86), (87), and (90) and the relation $c = \omega\lambda/2\pi$.

$$\begin{aligned}
\varepsilon_1 &= n^2 - \kappa^2 \\
\varepsilon_2 &= 2n\kappa \\
n &= \sqrt{\frac{\sqrt{\varepsilon_1^2 + \varepsilon_2^2} + \varepsilon_1}{2}} \\
\kappa &= \sqrt{\frac{\sqrt{\varepsilon_1^2 + \varepsilon_2^2} - \varepsilon_1}{2}} \\
\tilde{k} &= \frac{\tilde{n}\omega}{c} \\
\alpha &= \frac{1}{\delta} = 2k_2 = \frac{2\omega\kappa}{c} = \frac{4\pi\kappa}{\lambda} = \frac{2\pi\varepsilon_2}{n\lambda} = \frac{\omega\varepsilon_2}{nc}
\end{aligned} \tag{95}$$

Reproduced with permission of the copyright owner. Further reproduction prohibited without permission.

1.6.2 Band Structure/Critical Points

The band structure (BS) of a material is the allowed energy states as a function of wavevector, **k**. Over the last thirty or so years, there have been many approaches to solving this problem in crystals, for example semi-emperical pseudopotential,[7,56] **k•p**[7], and tight binding.[7] For the purposes of this section we only want to show the basic principles of the problem, so we use the adiabatic approximation that states that the atomic nuclei and core electrons can be considered to be at rest compared to the valence electrons. In addition, we make use of the mean-field approximation, which states that each valence electron experiences the same average potential $V(\mathbf{r})$. With these assumptions, the Schrödinger equation for each electron is identical and is given by

$$H_{1e}\psi_{l,\mathbf{k}}(\mathbf{r}) = \left(-\frac{\hbar^2\nabla^2}{2m_0} + V(\mathbf{r}) \right)\psi_{l,\mathbf{k}}(\mathbf{r}) = E_{l,\mathbf{k}}\psi_{l,\mathbf{k}}(\mathbf{r}) \tag{96}$$

where H_{1e} is the one-electron Hamiltonian, and $\psi_{l,\mathbf{k}}$ and $E_{l,\mathbf{k}}$ are the wavefunction and energy, respectively, of an eigenstate labeled by band index l and wavevector **k**, $V(\mathbf{r})$ is the crystal (periodic) potential, and m_0 is the free electron mass. Eq. (96) is the starting point for many types of BS calculations including pseudopotential and **k•p**, but has the limitation of the approximations we assumed above. Later we will extend our formalism to account for important excitonic effects within the effective mass approximation. The lattice periodicity requires the solution of Eq. (96) to be Bloch functions,[57] that is

Reproduced with permission of the copyright owner. Further reproduction prohibited without permission.

$$\psi_{l,\mathbf{k}}(\mathbf{r}) = e^{i\mathbf{k}\bullet\mathbf{r}} u_{l,\mathbf{k}}(\mathbf{r}) \tag{97}$$

where $u_{l,\mathbf{k}}(\mathbf{r})$ is a periodic function with the same periodicity as $V(\mathbf{r})$ (that is of the lattice). Thus, $u_{l,k}(\mathbf{r}+\mathbf{R}) = u_{l,k}(\mathbf{r})$, where $\mathbf{R}$ is a lattice vector. We will use the reduced zone scheme to denote our BS. In this scheme, we take advantage of the fact that due to the translational symmetry of the crystal, both $\mathbf{k}$ and $\mathbf{k} + \mathbf{G}$ will satisfy Eq. (97) where $\mathbf{G}$ is a reciprocal lattice vector ($e^{i\mathbf{G}\bullet\mathbf{R}} = 1$). Thus, in the reduced zone scheme we replace $\mathbf{k}$ by $\mathbf{k}' = \mathbf{k} - \mathbf{G}$ where $\mathbf{G}$ is chosen to limit $\mathbf{k}'$ to the first Brillouin zone. Each $\mathbf{G}$ therefore corresponds to a different band which is indicated by the band index l.

In semi-empirical approaches, experimental data such as energy gaps and oscillator strength are used as input parameters to find approximate solutions to Eq. (96). In the semi-empirical pseudopotential method, $V(\mathbf{r})$ (which is a periodic function and thus can have only Fourier components corresponding to reciprocal lattice vectors) is expressed in terms of a few Fourier coefficients corresponding to the shortest reciprocal lattice vectors. This is a reasonable approximation since the valence electrons, which we are most interested, are expelled from regions near the nuclei by Pauli's exclusion principle. Thus we can approximate the potential with a weak slow varying "effective potential" or Pseudopotential for the valence electrons. This method beaks down for the core electron states. In the $\mathbf{k}\bullet\mathbf{p}$ method (which we will explain in some detail later in this section), the BS near a CP is treated by perturbation theory for small $\mathbf{k}$. The electronic BS is the plot of the electron energies in Eq. (96) as a function of $\mathbf{k}$.

Reproduced with permission of the copyright owner. Further reproduction prohibited without permission.

We display a typical zincblende-type BS in Fig. 19, which shows the BS of GaAs as calculated by the semi-empirical pseudopotential method.[56] Bands which are occupied in the ground state are termed valence bands, while the excited states of the system are termed conduction bands. The zero of energy is placed at the top of the highest valence bands. Γ, X, and L are used to denote the center, edge at $\mathbf{k} = 2\pi/a$ [100], and edge at $\mathbf{k} = \pi/a$ [111] of the Brillouin zone respectively where a is the lattice constant. The direction from Γ to X is denoted as Δ, while the direction from Γ to L is denoted Λ. The subscripted letters (i.e. Γ_1) denote the symmetry of the wave function at the corresponding point of the BZ, which can be obtained from group theory. We note that the condition of standing waves at the edge of the BZ (that is $\mathbf{k} = \mathbf{G}/2$) or at the Γ point requires that the non-degenerate BS curves at these points have zero slope. In the case of degenerate BS curves, the curves must still have zero slope at the Γ point, but at the edge of the BZ ($\mathbf{k} = \mathbf{G}/2$) only the average slope of the BS curves must be zero.

Most of the structure of the optical functions is related to direct optical interband transitions, that is an excitation of an electron from a valence band to a conduction band involving only an electron and a photon. Since visible light carries little momentum compared to the size of the BZ, the electron and hole states involved in a direct transitions have nearly identical values of **k** and are therefor called vertical transitions. We will also consider indirect transitions arising from electron, photon, phonon interactions. These indirect transitions have a smaller effect on the dielectric function than direct transitions since they are three-particle interactions and can involve electron states of different **k** since phonons can have momentum similar to the size of the BZ.

Reproduced with permission of the copyright owner. Further reproduction prohibited without permission.

Figure 19. Band structure of GaAs (Ref. 56) showing the E_0, $E_0+\Delta_0$, E_1, $E_1+\Delta_1$, E_2, E_0', and E_{ind} interband CPs.

Reproduced with permission of the copyright owner. Further reproduction prohibited without permission.

Low energy optical transitions near CP's are labeled in Fig. 19 with the notation due to Cardona.[58] For many zincblende materials (including the ZnCdSe and InGaAs presented in this study) the fundamental absorption edge corresponds to three-dimensional (3D) M_0 direct transitions from the highest valence band to the lowest conduction band at the Γ point (i.e. $\Gamma_{15}^{v} - \Gamma_{1}^{c}$, in single group notation). The spin-orbit interaction splits the Γ_{15}^{v} valence band into Γ_{8}^{v} and Γ_{7}^{v} (splitting energy Δ_0). The corresponding transitions at **k**=0 are labeled E_0 $[\Gamma_8^v(\Gamma_{15}^v) - \Gamma_6^c(\Gamma_1^c)]$ and $E_0+\Delta_0$ $[\Gamma_7^v(\Gamma_{15}^v) - \Gamma_6^c(\Gamma_1^c)]$, respectively. The spin-orbit interaction also splits the $L_3^v(\Lambda_3^v)$ valence band into $L_{4,5}^v(\Lambda_{4,5}^v)$ and $L_6^v(\Lambda_6^v)$. The corresponding 2D M_0 transitions are labeled E_1 $[L_{4,5}^v(L_3^v) - L_6^c(L_1^c)$ or $\Lambda_{4,5}^v(\Lambda_3^v) - \Lambda_6^c(\Lambda_1^c)]$ and $E_1+\Delta_1$ $[L_6^v(L_3^v) - L_6^c(L_1^c)$ or $\Lambda_6^v(\Lambda_3^v) - \Lambda_6^c(\Lambda_1^c)]$, respectively. The E_2 CP is due to transitions along [110] (Σ) or near the X point. The E_0' feature is due to transitions at the Γ point $[\Gamma_8^v(\Gamma_{15}^v) - \Gamma_7^c(\Gamma_{15}^c)]$. We have also labeled the $\Gamma_8^v - L_6^c$ indirect transition. More will be said about the relationship between these CPs and the dielectric function in sections 1.6.4 and 1.7.

For illustration of BS calculations and to derive some simplified results we will use later, we outline the **k•p** formalism. Substituting Eq. (97) into Eq. (96), we obtain

$$\left[\frac{p^2}{2m_0} + V(\mathbf{r}) + \frac{\hbar}{m_0}\mathbf{k}\bullet\mathbf{p}\right]u_{l,k}(\mathbf{r}) = \left[E_l(\mathbf{k}) - \frac{\hbar^2 k^2}{2m_0}\right]u_{l,k}(\mathbf{r}) \tag{98}$$

Reproduced with permission of the copyright owner. Further reproduction prohibited without permission.

where $\mathbf{p} = -i\hbar\nabla$. We treat the term proportional to **k•p** as a perturbation, that is

$$H = H_0 + H_1 \quad \text{where} \quad H_0 = \frac{p^2}{2m_0} + V(\mathbf{r}) \quad \text{and} \quad H_1 = \frac{\hbar}{m_0}\mathbf{k}\bullet\mathbf{p} \tag{99}$$

At $\mathbf{k}_0 = (0,0,0)$, Eq. (98) reduces to

$$\left[\frac{p^2}{2m_0} + V(\mathbf{r})\right] u_{l,0}(\mathbf{r}) = \left[E_l(0)\right] u_{l,0}(\mathbf{r}) \tag{100}$$

Using the orthonormality of the states $u_{l,\mathbf{k}}$ and Eq. (100), Eq. (98) becomes the secular equation for the system.

$$\langle u_{l',\mathbf{k}} | H_1 | u_{l,\mathbf{k}} \rangle = \left[E_l(\mathbf{k}) - E_l(0) - \frac{\hbar^2 k^2}{2m_0} \right] \delta_{l,l'} \tag{101}$$

where we have used Dirac bra-ket notation for simplicity. In order to have solutions for Eq. (101), the secular determinant must be zero. This leads to the standard perturbation result

$$E_l(\mathbf{k}) - E_l(0) - \frac{\hbar^2 k^2}{2m_0} = \langle u_{l,0} | H_1 | u_{l,0} \rangle + \frac{\hbar^2}{{m_0}^2} \sum_{n'} \frac{\left\| \langle u_{l',0} | H_1 | u_{l,0} \rangle \right\|^2}{E_{l'}(0) - E_l(0)} + \cdots \tag{102}$$

Reproduced with permission of the copyright owner. Further reproduction prohibited without permission.

The first term on the right side of Eq. (102) is zero because H_1 has odd parity. This leads to final results for the energy and effective mass.

$$E_l(\mathbf{k}) = E_l(0) + \frac{\hbar^2 k^2}{2m_0} + \frac{\hbar^2}{m_0^2} \sum_{l'} \frac{\left\| \langle u_{l',0} | H_1 | u_{l,0} \rangle \right\|^2}{E_{l'}(0) - E_l(0)} + \ldots \tag{103}$$

The effective mass tensor is defined as the curvature of the E versus $\mathbf{k}$ dispersion curve.

$$\left(\frac{1}{m^*}\right)_{ij} \equiv \frac{1}{\hbar^2} \frac{\partial^2 E}{\partial k_i \partial k_j} = \frac{1}{m_0} \left[\delta_{ij} + \frac{2}{m_0} \sum_{l'} \frac{\langle u_{l,0} | p_i | u_{l',0} \rangle \langle u_{l',0} | p_j | u_{l,0} \rangle}{E_{l'}(0) - E_l(0)} \right] \tag{104}$$

We note in passing two key results from Eqs. (103) and (104). First, a wave function $u_{l,0}$ can only couple to another wavefunction $u_{l',0}$ if the matrix element $\langle u_{l',0} | H_1 | u_{l,0} \rangle$ is nonzero. Thus some of the terms in Eq. (104) which reduce the effective mass will be zero due to symmetry. Second, The energy separation $E_{l'}(0) - E_l(0)$ determines the relative importance of the contribution of the l' state to the effective mass of the l state. Eq. (104) defining an effective mass is very suggestive. We will show in section 1.6.3 that the effects of a perturbation to the crystal potential near a CP can be treated by considering the Schrödinger equation for a particle of mass m^* under the influence of the perturbing potential only.

Reproduced with permission of the copyright owner. Further reproduction prohibited without permission.

To go a little further, we consider a simplified two-band model. That is two bands that only interact with each other. Labeling the states 1 and 2, Eq. (101) leads to the secular determinant

$$\det\begin{vmatrix} E_1(0)+\dfrac{\hbar^2k^2}{2m_0}-E & \dfrac{\hbar}{m_0}Pk \\ \dfrac{\hbar}{m_0}Pk & E_2(0)+\dfrac{\hbar^2k^2}{2m_0}-E \end{vmatrix}=0 \tag{105}$$

where

$$P=\langle u_{2,k}|-i\hbar\nabla|u_{1,k}\rangle . \tag{106}$$

Letting $E_g = E_1(0)$-$E_2(0)$, we find for $\dfrac{4\hbar^2P^2k^2}{{m_0}^2E_g} << 1$, Eq. (105) reduces to

$$E_{\substack{1\\2}}(k)=E_{\substack{1\\2}}(0)\frac{\hbar^2k^2}{2m_0}\pm\frac{2\hbar^2P^2k^2}{{m_0}^2E_g} \tag{107}$$

From this we see that the interaction has the important effect that the effective mass of the two states is now

$$\left(\frac{1}{m^*}\right)_{\substack{1\\2}}=\frac{1}{m_0}\left(1\pm\frac{4P^2}{m_0E_g}\right) \tag{108}$$

Reproduced with permission of the copyright owner. Further reproduction prohibited without permission.

Thus, the higher lying state has a lower effective mass while the lower lying state has an increased and possibly negative effective mass. In addition, the effect on m^* is greater for small E_g.

As can be seen by the above simplified example, BS calculations are not easy. It is crucial to use the symmetry of the crystal to help simplify the calculations. Early empirical BS calculations relied heavily on experimentally determined data to obtain realistic results.[56] Recently, realistic first principles calculations of band structures have been carried out, which even account for the many-bodied nature of the problem, [11,12] but only by using long computer calculations.

1.6.3 Effective Mass Approximation-Envelope Function

In our section on band structures, we have already defined the effective mass in Eqs. (103) and (95). In this section we will show how this definition can be made useful. Namely that this definition along with some approximations leads to a simple way of evaluating the effects near BS CPs of a small perturbation with envelope functions.

The envelope function formalism applies to small local perturbations to the crystal potential.

Reproduced with permission of the copyright owner. Further reproduction prohibited without permission.

$$H = \frac{-i\hbar^2\nabla^2}{2m_0} + V(r) + V_p(r) = H_0 + V_p(r) \tag{109}$$

where $V_p(\mathrm{r})$ is some local perturbation of the crystal potential. Since the Bloch functions are a complete orthonormal set, a superposition of them can be used to represent the final state.

$$\Psi(\mathbf{r}) = \sum_{l,\mathbf{k}} A_l(\mathbf{k})\psi_{l,\mathbf{k}}(\mathbf{r}) = \sum_{l,\mathbf{k}} A_l(\mathbf{k})e^{i\mathbf{k}\bullet\mathbf{r}}u_{l,\mathbf{k}}(\mathbf{r}) \tag{110}$$

where $\psi_{l,\mathbf{k}}(\mathbf{r})$ is a Bloch function and we are using the reduced zone scheme, that is the summation in $\mathbf{k}$ is over the first Brillouin zone and the various zone-folded bands are referenced by the index l.

We wish to consider a state near a CP in the BS, $\mathbf{k} = \mathbf{k}_0$. Also, In the limit $V_p(\mathbf{r}) = 0$, the state would be a single Bloch state at $\mathbf{k}_0$ in the band which we label with index l=0. For small $V_p(\mathbf{r})$, we anticipate these statements will approximately hold. That is

$$\begin{gathered} \mathbf{k} - \mathbf{k}_0 << \frac{\pi}{a} \\ A_l(\mathbf{k}) \approx \delta_{l,0}\delta_{\mathbf{k},\mathbf{k}_0} \end{gathered} \quad . \tag{111}$$

The second line of Eq. (111) that the wavefunction $\Psi(\mathbf{r})$ is sharply peaked in $\mathbf{k}$ space and thus spread out in $\mathbf{r}$ space, which is what we expect for weak $V_p(\mathbf{r})$. In the case of a

Reproduced with permission of the copyright owner. Further reproduction prohibited without permission.

shallow dopant, the band 0 would be the lowest lying conduction band in the case of a donor or the highest lying valence band in the case of an acceptor. For an exciton, the state of interest will be the state in which a single electron has been excited from the conduction to the valence band. That is the index 0 will refer to the electron hole state near the CP $\mathbf{k} = \mathbf{k}_0$.

In the Dirac bra-ket notation, Eq. (110) becomes

$$\left|\Psi(\mathbf{r})\right\rangle = \sum_{l,\mathbf{k}} A_l(\mathbf{k})\left|\psi_{l,\mathbf{k}}(\mathbf{r})\right\rangle = \sum_{l,\mathbf{k}} A_l(\mathbf{k}) e^{i\mathbf{k}\bullet\mathbf{r}}\left|u_{l,\mathbf{k}}(\mathbf{r})\right\rangle \tag{112}$$

Using the Hamiltonian in Eq. (109) and the wavefunction in Eq. (112), the Schrödinger equation becomes

$$\left(\frac{-\hbar^2\nabla^2}{2m_0} + V(\mathbf{r}) + V_p(\mathbf{r})\right)\sum_{l,\mathbf{k}} A_l(\mathbf{k})\left|\psi_{l,\mathbf{k}}(\mathbf{r})\right\rangle = E\sum_{l,\mathbf{k}} A_l(\mathbf{k})\left|\psi_{l,\mathbf{k}}(\mathbf{r})\right\rangle \tag{113}$$

Taking the scalar product with $\left\langle\psi_{l',\mathbf{k}'}(\mathbf{r})\right|$ from the right and using Eq. (109), this becomes

$$\begin{gathered}\left\langle\psi_{l',\mathbf{k}'}(\mathbf{r})\right|\left(H_0 + V_p(\mathbf{r})\right)\sum_{l,\mathbf{k}} A_l(\mathbf{k})\left|\psi_{l,\mathbf{k}}(\mathbf{r})\right\rangle = E\left\langle\psi_{l',\mathbf{k}'}(\mathbf{r})\right|\sum_{l,\mathbf{k}} A_l(\mathbf{k})\left|\psi_{n,\mathbf{k}}(\mathbf{r})\right\rangle \\ \sum_{l,\mathbf{k}}\left\langle\psi_{l',\mathbf{k}'}(\mathbf{r})\right|\left(E_{l'}(\mathbf{k}') + V_p(\mathbf{r})\right)A_l(\mathbf{k})\left|\psi_{l,\mathbf{k}}(\mathbf{r})\right\rangle = \sum_{l,\mathbf{k}} E\left\langle\psi_{l',\mathbf{k}'}(\mathbf{r})\right|A_l(\mathbf{k})\left|\psi_{l,\mathbf{k}}(\mathbf{r})\right\rangle\end{gathered} \tag{114}$$

Reproduced with permission of the copyright owner. Further reproduction prohibited without permission.

where $H_0 = \frac{-\hbar^2\nabla^2}{2m_0} + V(\mathbf{r})$

This reduces to

$$\sum_{l,\mathbf{k}} A_l(\mathbf{k})E_l(\mathbf{k})\delta_{l,l'}\delta_{\mathbf{k},\mathbf{k}'} + \sum_{l,\mathbf{k}} \langle \psi_{l',\mathbf{k}'}(\mathbf{r}) | V_p(\mathbf{r}) | \psi_{l,\mathbf{k}}(\mathbf{r}) \rangle A_l(\mathbf{k}) = \sum_{l,\mathbf{k}} EA_l(\mathbf{k})\delta_{l,l'}\delta_{\mathbf{k},\mathbf{k}'} \tag{115}$$

evaluating the sums over the delta functions and exchanging $\mathbf{k}$ and $\mathbf{k}'$, we obtain

$$\sum_{l',\mathbf{k}'} \langle \psi_{l,\mathbf{k}}(\mathbf{r}) | V_p(\mathbf{r}) | \psi_{l',\mathbf{k}'}(\mathbf{r}) \rangle A_{l'}(\mathbf{k}') = [E - E_l(\mathbf{k})]A_l(\mathbf{k}) . \tag{116}$$

Keeping in mind Eq. (111), we rewrite Eq. (116) to emphasize the importance of the l=0 band

$$\sum_{\mathbf{k}'} \langle \psi_{0,\mathbf{k}}(\mathbf{r}) | V_p(\mathbf{r}) | \psi_{0,\mathbf{k}'}(\mathbf{r}) \rangle A_0(\mathbf{k}') + \sum_{l'\neq 0,\mathbf{k}'} \langle \psi_{0,\mathbf{k}}(\mathbf{r}) | V_p(\mathbf{r}) | \psi_{l',\mathbf{k}'}(\mathbf{r}) \rangle A_{l'}(\mathbf{k}') = [E - E_0(\mathbf{k})]A_0(\mathbf{k}) \qquad (l = 0) \tag{117a}$$

$$\sum_{\mathbf{k}'} \langle \psi_{l,\mathbf{k}}(\mathbf{r}) | V_p(\mathbf{r}) | \psi_{0,\mathbf{k}'}(\mathbf{r}) \rangle A_0(\mathbf{k}') + \sum_{l'\neq 0,\mathbf{k}'} \langle \psi_{l,\mathbf{k}}(\mathbf{r}) | V_p(\mathbf{r}) | \psi_{l',\mathbf{k}'}(\mathbf{r}) \rangle A_{l'}(\mathbf{k}') = [E - E_l(\mathbf{k})]A_l(\mathbf{k}) \qquad (l \neq 0) \tag{117b}$$

Reproduced with permission of the copyright owner. Further reproduction prohibited without permission.

We examine the second term in Eq. (117a) more closely

$$\langle \psi_{l,\mathbf{k}}(\mathbf{r}) | V_p(\mathbf{r}) | \psi_{l',\mathbf{k}'}(\mathbf{r}) \rangle = \frac{1}{\Omega} \int u_{l,\mathbf{k}}^* u_{l',\mathbf{k}'} e^{i(\mathbf{k}'-\mathbf{k})\bullet\mathbf{r}} V_p(\mathbf{r}) d^3r \tag{118}$$

where Ω is the volume of the crystal. Since $u_{l,\mathbf{k}}^* u_{l',\mathbf{k}'}$ is a periodic function, it can be written as

$$u_{l,\mathbf{k}}^* u_{l',\mathbf{k}'} = \sum_{\mathbf{G}} C_{l,\mathbf{k};l',\mathbf{k}'}^{\mathbf{G}} e^{i\mathbf{G}\bullet\mathbf{r}} \tag{119}$$

where **G** are the reciprocal lattice vectors. For later purposes, we note that from orthonormality, for $\mathbf{k}' = \mathbf{k}$

$$C_{l,\mathbf{k};l',\mathbf{k}}^{\mathbf{G}} = \delta_{l,l'} \tag{120}$$

Using Eq. (119), Eq. (118) becomes

$$\langle \psi_{l,\mathbf{k}}(\mathbf{r}) | V_p(\mathbf{r}) | \psi_{l',\mathbf{k}'}(\mathbf{r}) \rangle = \frac{1}{\Omega} \int \sum_{\mathbf{G}} C_{l,\mathbf{k};l',\mathbf{k}'}^{\mathbf{G}} e^{i(\mathbf{G}+\mathbf{k}'-\mathbf{k})\bullet\mathbf{r}} V_p(\mathbf{r}) d^3r \tag{121}$$

We define the Fourier transform of $V_p(\mathbf{r})$ as

Reproduced with permission of the copyright owner. Further reproduction prohibited without permission.

$$V_p(\mathbf{k}) = \frac{1}{\Omega}\int e^{-i\mathbf{k}\bullet\mathbf{r}}V_p(\mathbf{r})d^3r$$
$$V_p(\mathbf{r}) = \sum_{\text{all }\mathbf{k}} e^{i\mathbf{k}\bullet\mathbf{r}}V_p(\mathbf{k}) \qquad (122)$$

then

$$\sum_{\mathbf{k}'}\langle\psi_{0,\mathbf{k}}(\mathbf{r})|V_p(\mathbf{r})|\psi_{0,\mathbf{k}'}(\mathbf{r})\rangle A_0(\mathbf{k}') \approx \sum_{\mathbf{k}'}\sum_{\mathbf{G}} C^G_{l,\mathbf{k};l',\mathbf{k}'}V_p(\mathbf{k}-\mathbf{k}'-\mathbf{G})A_0(\mathbf{k}') \qquad (123)$$

We make the further assumption that $V_p(\mathbf{r})$ is a slowly varying function on the order of the lattice constant a, that is

$$a\|\nabla V_p(\mathbf{r})\| << V_p(\mathbf{r}) \qquad (124)$$

then $V_p(\mathbf{k})$ will be negligible for $\mathbf{k} \sim \mathbf{G}$. Therefore, taking $\mathbf{k}$ is near the center of the Brillouin zone, we only expect the terms on the left side of Eq. (123) to be negligible unless $\mathbf{G}=0$ since $\mathbf{k}'$ is restricted to the first Brillouin zone. (If $\mathbf{k}$ is near the edge of the Brillouin zone, a similar argument holds since one can simply translate the first Brillouin zone to create a new unit cell in reciprocal lattice space.) Remembering that $A_0(\mathbf{k}')$ is sharply peaked near $\mathbf{k}' = \mathbf{k}_0$, and that we are considering the effects near $\mathbf{k} = \mathbf{k}_0$ along with Eqs. (120) and (123), we can write

Reproduced with permission of the copyright owner. Further reproduction prohibited without permission.

$$\sum_{\mathbf{k}'} \left\langle \psi_{0,\mathbf{k}}(\mathbf{r}) \middle| V_p(r) \middle| \psi_{0,\mathbf{k}'}(\mathbf{r}) \right\rangle \approx \sum_{\mathbf{k}'} V_p(\mathbf{k}-\mathbf{k}') \tag{125}$$

Using this and according to Eq. (111) letting $A_l(\mathbf{k}) = 0$ for $l \neq 0$, Eq. (117a) becomes

$$\sum_{\mathbf{k}'} V_p(\mathbf{k}-\mathbf{k}')A_0(\mathbf{k}') = [E - E_0(\mathbf{k})]A_0(\mathbf{k}) . \tag{126}$$

For $\mathbf{k} \approx \mathbf{k}_0$, we can use Eq. (103) to find

$$E_0(\mathbf{k}) \approx E_0(\mathbf{k}_0) + \frac{\hbar^2(\mathbf{k}-\mathbf{k}_0)^2}{2m^*} . \tag{127}$$

For simplicity, we let $\mathbf{k}_0 = 0$. Then Eq. (126) becomes

$$\frac{\hbar^2\mathbf{k}^2}{2m^*} A_0(\mathbf{k}) + \sum_{\mathbf{k}'} V_p(\mathbf{k}-\mathbf{k}')A_0(\mathbf{k}') = [E - E_0(0)]A_0(\mathbf{k}) . \tag{128}$$

Since by our assumption of Eq. (124) $V_p(\mathbf{k}\text{-}\mathbf{k}')$ is nearly zero outside the first BZ, we can let the sum in Eq. (126) run over all $\mathbf{k}'$. Then Eq. (126) is the Schrödinger equation in momentum space of an electron of mass m^* moving in the potential V_p. with the energy relative to $E_0(0)$. To transform this to coordinate space, we introduce the Fourier transform of $A_l(\mathbf{k})$,

Reproduced with permission of the copyright owner. Further reproduction prohibited without permission.

$$A_l(\mathbf{k}) = \frac{1}{\Omega}\int e^{-i\mathbf{k}\bullet\mathbf{r}} F_l(\mathbf{r}) d^3r$$
$$F_l(\mathbf{r}) = \sum_k e^{i\mathbf{k}\bullet\mathbf{r}} A_l(\mathbf{k}) \tag{129}$$

Then multiplying Eq. (126) by $e^{i\mathbf{k}\bullet\mathbf{r}}$ and summing over **k**, we obtain

$$\frac{-\hbar^2\nabla^2}{2m^*} F_l(\mathbf{r}) + V_p(\mathbf{r})F_l(\mathbf{r}) = [E - E_0(0)]F_l(\mathbf{r}) \tag{130}$$

This is known as the effective mass approximation. It is useful for both shallow dopants and weakly bound (Wannier) excitons. Eq. (130) is the Schrödinger equation for a particle of mass m^* moving in a potential $F_l(\mathbf{r})$. Also, since the wavefunction is spread out in space compared to the lattice constant, the potential an electron feels is screened by the static dielectric constant ε_0, so we write the Coulomb potential as

$$V_p(\mathbf{r}) = -\frac{e^2}{\varepsilon_0 r} \tag{131}$$

According to Eqs. (129) and (112), the total wavefunction becomes

$$|\Psi(\mathbf{r})\rangle = \sum_{\mathbf{k}} A_0(\mathbf{k})|\psi_{0,\mathbf{k}}(\mathbf{r})\rangle = \sum_{\mathbf{k}} A_0(\mathbf{k})e^{i\mathbf{k}\bullet\mathbf{r}}u_{0,\mathbf{k}}(\mathbf{r}) \tag{132}$$

Since $A_0(\mathbf{k})$ is sharply peaked around $\mathbf{k} = \mathbf{k}_0$, we make a Taylor series expansion

Reproduced with permission of the copyright owner. Further reproduction prohibited without permission.

$$u_{0,\mathbf{k}}(\mathbf{r}) \approx u_{0,\mathbf{k}_0}(\mathbf{r}) + (\mathbf{k}-\mathbf{k}_0) \bullet \nabla u_{0,\mathbf{k}}(\mathbf{r}) + \cdots \tag{133}$$

Neglecting all but the first term, we obtain

$$|\Psi(\mathbf{r})\rangle = u_{0,\mathbf{k}_0}(\mathbf{r}) \sum_{\mathbf{k}} A_0(\mathbf{k}) e^{i\mathbf{k}\bullet\mathbf{r}} = u_{0,\mathbf{k}_0}(\mathbf{r}) F(\mathbf{r}) \tag{134}$$

In order for this approximation to be valid, we must show that the wavefunction $F_l(\mathbf{r})$ is spread out in space compared to the size of a unit cell, or equivalently the Fourier transform $A_l(\mathbf{k})$ is extends over only a small fraction of the first Brillouin zone and that the amplitudes $A_{l'}(\mathbf{k})$ ($l' \neq l$) are in fact negligible compared to $A_l(\mathbf{k})$. Also, $V_p(\mathbf{r})$ should be a slowly varying function. To be more exact, we must in order for the effective mass approximation to be valid, the following must hold:

$$\begin{aligned} &A_l(\mathbf{k}) \approx \frac{1}{E - E_l(\mathbf{k})} \sum_{\mathbf{k}'} \langle \psi_{l,\mathbf{k}}(\mathbf{r}) | V_p(\mathbf{r}) | \psi_{0,\mathbf{k}'}(\mathbf{r}) \rangle A_0(\mathbf{k}') << A_0(\mathbf{k}_0) \\ &A_0\left(\mathbf{k}_0 + \frac{1}{a}\right) >> A_0(\mathbf{k}_0) \\ &V_p(\mathbf{k}=0) >> V_p\left(\mathbf{k} \sim \frac{1}{a}\right) \end{aligned} \tag{135}$$

where a is the lattice constant, so that $1/a$ is of order of the size of the first Brioullin zone.

Reproduced with permission of the copyright owner. Further reproduction prohibited without permission.

1.6.4 Relation of Dielectric Function To Quantum Transitions

The dielectric function is primarily due to direct and indirect interband transitions, exciton interactions, phonons, and free electron effects. In the energy range of our measurements, the first two are the most important, with most of the observed structure coming near interband critical points (CP's) (extrema of the interband energy levels of the band structure). In an interband transition, an electron from a valence band is excited into a conduction band, leaving behind a positively charged hole in the valence band. Direct transitions involve only the photon and the electron, while indirect transitions also involve scattering a phonon. Since visible light carries little momentum compared to the size of the BZ, the electron and hole states involved in a direct transitions have nearly identical values of **k** and are therefor called vertical transitions. Indirect transitions, which can involve electron states of different **k** since phonons carry momentum of the order of the BZ, have a much smaller effects on the optical structure than direct transitions since they involve three particle interactions. The electron-hole pair formed in an interband transition interact via the Coulomb potential with two main effects on the optical function: (1) resonance peaks occur below interband CP's due to discrete bound two-particle states formed by the Coulomb attraction called bound excitons (BE's) and (2) an enhancement of interband transition probability for transition energies at or above the CP's called band to band Coulomb enhancement (BBCE) or sometimes continuum exciton (CE). Both of these effects vary depending on the nature of the CP and will be discussed in more detail in sections 1.6.5 and 1.7.

Reproduced with permission of the copyright owner. Further reproduction prohibited without permission.

In this section, we relate the imaginary part of the dielectic function to transitions between BS states caused by an oscillating transverse electric field (light). We leave the details of specific critical points in the band structure and excitonic effects within the envelope function approximation to section 1.7.

To describe the electromagnetic fields, we introduce the vector potential, $\mathbf{A}(\mathbf{r}, t)$, and a scalar potential defined, $\Phi(\mathbf{r}, t)$. The form of these potentials will depend on the gauge we select. For simplicity, we choose the Coulomb gauge

$$\Phi = 0 \quad \text{and} \quad \nabla \bullet \mathbf{A} = 0 \tag{136}$$

Then

$$\mathbf{E} = -\frac{1}{c}\frac{\partial \mathbf{A}}{\partial t} \quad \text{and} \quad \mathbf{B} = \nabla \times \mathbf{A} \tag{137}$$

The Hamiltonian describing the motion of a charge $-e$ in an external electromagnetic field is obtained by making the substitution for the electron momentum operator

$$-i\hbar\nabla \rightarrow -i\hbar\nabla + \frac{e\mathbf{A}}{c} \tag{138}$$

With this substitution, the Hamiltonian becomes

Reproduced with permission of the copyright owner. Further reproduction prohibited without permission.

$$\begin{aligned} H &= \frac{1}{2m_0}\left(-i\hbar\nabla + \frac{e\mathbf{A}}{c}\right)^2 + V(\mathbf{r}) \\ &= \frac{1}{2m_0}\left(-\hbar^2\nabla^2 - \frac{e}{c}\mathbf{A}\bullet i\hbar\nabla - \frac{e}{c}i\hbar\nabla\bullet\mathbf{A} + \frac{e^2\mathbf{A}^2}{2c^2}\right) + V(\mathbf{r}) \\ &= \frac{1}{2m_0}\left(-\hbar^2\nabla^2 - \frac{2e}{c}\mathbf{A}\bullet i\hbar\nabla + \frac{e^2\mathbf{A}^2}{2c^2}\right) + V(\mathbf{r}) \\ &\approx \frac{1}{2m_0}\left(-\hbar^2\nabla^2 - \frac{2e}{c}\mathbf{A}\bullet i\hbar\nabla\right) + V(\mathbf{r}) \end{aligned} \tag{139}$$

where we have used Eq. (136) between the second and third lines and have neglected the quadratic term $e^2\mathbf{A}^2/(2m_0c^2)$ since we are interested in the linear (low field) optical properties. We will treat the term $e/(m_0c)\ \mathbf{A}\bullet i\hbar\nabla$ as a perturbation. For electric field of magnitude $\mathscr{E}$, wavevector $\mathbf{k}^\mathbf{L}$, frequency ω, and polarization vector $\hat{\mathbf{e}}$, the vector potential takes the form

$$\mathbf{A}(\mathbf{r},t) = -\frac{\mathscr{E}c}{2\omega}\hat{\mathbf{e}}\left(e^{i(\mathbf{k}^\mathbf{L}\bullet\mathbf{r}-\omega t)} + e^{-i(\mathbf{k}^\mathbf{L}\bullet\mathbf{r}-\omega t)}\right) \tag{140}$$

so that $\mathbf{A}(\mathbf{r},t)$ is a real function. The term containing $e^{i(\mathbf{k}^\mathbf{L}\bullet\mathbf{r}-\omega t)}$ corresponds to the absorption process we are interested in, while the one containing $e^{-i(\mathbf{k}^\mathbf{L}\bullet\mathbf{r}-\omega t)}$ corresponds to stimulated emission in the presence of an electric field. For such a time dependent perturbation, the probability of transition per unit time is

Reproduced with permission of the copyright owner. Further reproduction prohibited without permission.

$$P_{v,c} = \left\| \int_{-\infty}^{\infty} \left\langle \psi_{c,\mathbf{k}_c} \middle| \mathbf{A}(\mathbf{r},t) \bullet i\hbar\nabla \middle| \psi_{v,\mathbf{k}_v} \right\rangle e^{i\omega_{cv}t} dt \right\|^2 \qquad (141)$$

where

$$\omega_{cv} = \frac{E_c - E_v}{\hbar} \qquad (142)$$

and the time independent Bloch functions are

$$\begin{aligned} \left| \psi_{v,\mathbf{k}_v} \right\rangle &= e^{i\mathbf{k}_v \bullet \mathbf{r}} u_{v,\mathbf{k}_v} \\ \left| \psi_{c,\mathbf{k}_c} \right\rangle &= e^{i\mathbf{k}_c \bullet \mathbf{r}} u_{c,\mathbf{k}_c} \end{aligned} \qquad (143)$$

and the subscripts c and v correspond to the conduction and valence bands respectively. Equation (141) is valid so long as $P_{c,v} << 1$. That is the normal linear optic regime where most of the electrons are in their ground states. The integration over time of Eq. (141) for the term corresponding to absorption contributes a factor of

$$\int_{-\infty}^{\infty} e^{i\omega_{cv}t} e^{-i\omega t} dt = \frac{2\pi}{\hbar} \delta[E_c(\mathbf{k}_c) - E_v(\mathbf{k}_v) - \hbar\omega] \qquad (144)$$

Reproduced with permission of the copyright owner. Further reproduction prohibited without permission.

That is the energy of the photon must be exactly the energy difference between the conduction and valence bands as expected from conservation of energy. Evaluating the time independent part of Eq. (141), we obtain

$$\begin{aligned}\left\langle \psi_{c,\mathbf{k}_c} \middle| \mathbf{A}(\mathbf{r},t) \bullet i\hbar\nabla \middle| \psi_{v,\mathbf{k}_v} \right\rangle &= -\frac{\mathscr{E} i\hbar}{2k_R} \int u^*_{c,\mathbf{k}_c} e^{i(\mathbf{k}^{\mathbf{L}} - \mathbf{k}_c)\bullet\mathbf{r}} (\hat{\mathbf{e}} \bullet \nabla) e^{i\mathbf{k}_v \bullet \mathbf{r}} u_{v,\mathbf{k}_v} d\mathbf{r} \\ &= -\frac{\mathscr{E} i\hbar}{2k_R} \hat{\mathbf{e}} \bullet \int u^*_{c,\mathbf{k}_c} e^{i(\mathbf{k}^{\mathbf{L}} - \mathbf{k}_c)\bullet\mathbf{r}} (e^{i\mathbf{k}_v \bullet \mathbf{r}} \nabla u_{v,\mathbf{k}_v} + \hbar \mathbf{k}_v u_{v,\mathbf{k}_v} e^{i\mathbf{k}_v \bullet \mathbf{r}}) d\mathbf{r}\end{aligned} \tag{145}$$

The second term on the last line of Eq. (145) vanishes because $u_{v,\mathbf{k}_v}$ and $u_{c,\mathbf{k}_c}$ are orthogonal. Continuing, because of the periodicity of $u_{v,\mathbf{k}_v}$ and $u_{c,\mathbf{k}_c}$ we can rewrite the integral of the first term in the last line of Eq. (145) by using $\mathbf{r} = \mathbf{R}_j + \mathbf{r}'$ where $\mathbf{r}'$ lies within one unit cell and $\mathbf{R}_j$ is a reciprocal lattice vector. Therefore,

$$\begin{aligned}&\int u^*_{c,\mathbf{k}_c} e^{i(\mathbf{k}^{\mathbf{L}} + \mathbf{k}_v - \mathbf{k}_c)\bullet\mathbf{r}} \nabla u_{v,\mathbf{k}_v} d\mathbf{r} \\ &= \left(\sum_j e^{i(\mathbf{k}^{\mathbf{L}} + \mathbf{k}_v - \mathbf{k}_c)\bullet\mathbf{R}_j} \right) \int_{\substack{\text{unit} \\ \text{cell}}} u^*_{c,\mathbf{k}_c} e^{i(\mathbf{k}^{\mathbf{L}} + \mathbf{k}_v - \mathbf{k}_c)\bullet\mathbf{r}'} \nabla u_{v,\mathbf{k}_v} d\mathbf{r}' \\ &= \delta(\mathbf{k}^{\mathbf{L}} + \mathbf{k}_v - \mathbf{k}_c) \int_{\substack{\text{unit} \\ \text{cell}}} u^*_{c,\mathbf{k}_c} e^{i(\mathbf{k}^{\mathbf{L}} + \mathbf{k}_v - \mathbf{k}_c)\bullet\mathbf{r}'} \nabla u_{v,\mathbf{k}_v} d\mathbf{r}' \\ &= \int_{\substack{\text{unit} \\ \text{cell}}} u^*_{c,\mathbf{k}_v + \mathbf{k}^{\mathbf{L}}} \nabla u_{v,\mathbf{k}_v} d\mathbf{r}'\end{aligned} \tag{146}$$

In addition, we can simplify the expression further because for visible light, $\mathbf{k}^L$ is three to four orders of magnitude smaller than the size of the Brillouin zone, so

Reproduced with permission of the copyright owner. Further reproduction prohibited without permission.

$$u_{\mathbf{k}_v+\mathbf{k}^L} = u_{\mathbf{k}_v} + \mathbf{k}^L \bullet \nabla_{\mathbf{k}} u_{\mathbf{k}_v} + \cdots \approx u_{\mathbf{k}_v} \tag{147}$$

and we can rewrite Eq. (146) as

$$\int u^*_{c,\mathbf{k}_c} e^{i(\mathbf{k}_R+\mathbf{k}_v-\mathbf{k}_c)\bullet\mathbf{r}} \nabla u_{v,\mathbf{k}_v} d\mathbf{r} = \int_{\substack{\text{unit}\\\text{cell}}} u^*_{c,\mathbf{k}} \nabla u_{v,\mathbf{k}} d\mathbf{r}' \tag{148}$$

where $\mathbf{k} = \mathbf{k}_v = \mathbf{k}_c$. If we consider three particle electron-phonon-photon interactions, the phonon can contribute momentum of order the size of the Brioullin zone, making Eq. (148) invalid. This low probability case will be considered in section 1.6.6.

Finally, combining Eqs. (140), (141), (144), (145), and (148), we obtain the final expression for the transition probability per unit time.

$$P_{v,c} = \frac{2\pi}{\hbar}\left(\frac{e}{m_0\omega}\right)^2 \left\|\frac{\mathscr{E}(\omega)}{2}\right\|^2 \sum_{\mathbf{k}} \|\mathbf{M}_{cv}(\mathbf{k})\|^2 \delta[E_c(\mathbf{k}) - E_v(\mathbf{k}) - \hbar\omega] \tag{149}$$

where

Reproduced with permission of the copyright owner. Further reproduction prohibited without permission.

$$\|\mathbf{M}_{cv}(\mathbf{k})\|^2 = \hbar^2 \left\| \langle \psi_{c,\mathbf{k}} | \hat{\mathbf{e}} \bullet \nabla | \psi_{v,\mathbf{k}} \rangle \right\|^2 = \left(\hbar \int_{\substack{\text{unit}\\\text{cell}}} u_{\mathbf{k}}^* \hat{\mathbf{e}} \bullet \nabla u_{\mathbf{k}} d\mathbf{r}' \right)^2 \qquad (150)$$

If we restrict the summation over **k** in Eq. (149) to only those **k**'s allowed per unit volume of the crystal, then Eq. (149) gives the absorption transition rate per unit volume of the crystal. The power loss per unit volume (which can be expressed in terms of the imaginary dielectric function) then is this probability times the energy for each photon.

$$\text{Power loss} = P_{v,c}\hbar\omega = -\frac{dI}{dt} = -\left(\frac{dI}{dx}\right)\left(\frac{dx}{dt}\right) = (I\alpha)\left(\frac{c}{n}\right) = \frac{\alpha c I}{n} = \frac{\varepsilon_i \omega I}{n^2} \qquad (151)$$

where I is the intensity of the incident beam

$$I = \frac{n^2}{8\pi}\|\mathscr{E}(\omega)\|^2 \qquad (152)$$

Using these, we find

$$\varepsilon_2(E) = \left(\frac{2\pi e\hbar}{m_0 E}\right)^2 \sum_{c,v}\sum_{\mathbf{k}} \|\mathbf{M}_{cv}(\mathbf{k})\|^2 \delta[E_c(\mathbf{k}) - E_v(\mathbf{k}) - E]. \qquad (153)$$

where $E = \hbar\omega$ is the photon energy. Although $\mathbf{M}_{cv}$ is a function of **k**, it typically does not have much structure. In addition, for allowed transitions, it usually is nearly constant

Reproduced with permission of the copyright owner. Further reproduction prohibited without permission.

near a CP $\mathbf{k} \approx \mathbf{k}_0$. Thus, since we are considering the contribution to the dielectric function near a CP, we can let $\mathbf{M}_{cv}(\mathbf{k}) = \mathbf{M}_{cv}(\mathbf{k}_0)$. Then the structure of the dielectric function is seen to simply come from the sum over the allowed transition energies otherwise known as the interband or joint density of states (JDOS), which will be different depending on the nature of the critical point.

$$\varepsilon_2(E) = \left(\frac{2\pi e\hbar}{m_0 E}\right)^2 \|\mathbf{M}_{cv}(\mathbf{k}_0)\|^2 \sum_{c,v} \sum_{\mathbf{k}} \delta[E_c(\mathbf{k}) - E_v(\mathbf{k}) - E]. \tag{154}$$

The real part of the dielectric function can then be found using the Kramers Kronig relation [Eq. (199)]. Applying this to Eq. (153), we find the correct, but difficult to work with, form of the real dielectric function.

$$\varepsilon_1(E) = 1 + \frac{8\pi e\hbar^2}{m_0{}^2} \sum_{\mathbf{k}} \frac{\|\mathbf{M}_{cv}\|^2}{[E_c(\mathbf{k}) - E_v(\mathbf{k})]\{[E_c(\mathbf{k}) - E_v(\mathbf{k})]^2 - E^2\}} \tag{155}$$

The JDOS term in Eq. (154) is often expressed using the quasi-continuous approximation as the integral

$$\sum_{\mathbf{k}} \delta[E_c(\mathbf{k}) - E_v(\mathbf{k}) - E] \rightarrow D(E)dE. \tag{156}$$

where

Reproduced with permission of the copyright owner. Further reproduction prohibited without permission.

$$\int D(E)dE = 2\int \frac{d^3k}{(2\pi)^3} = \frac{2}{(2\pi)^3}\int \frac{dS_{\mathbf{k}}}{\|\nabla_{\mathbf{k}}E\|}dE\,. \tag{157}$$

where $D(E)dE$ is the JDOS as a function of energy and $S_{\mathbf{k}}$ is the constant energy surface defined by $E(\mathbf{k})$ = constant. This can be evaluated for several types of CPs. For a 3D M_0 type CP (parabolic E vs. **k** bands in all three directions), the energy as a function of **k** is

$$E(\mathbf{k}) = \frac{\hbar^2\mathbf{k}^2}{2\mu^*} + E_g \tag{158}$$

where μ^* is the reduced interband effective mass and E_g is the bandgap of interest. Then the JDOS is

$$D_{3D}(E) = \begin{cases} \dfrac{\mu^{*3/2}\sqrt{2(E-E_g)}}{\pi^2\hbar^3} & E > E_g \\ 0 & E < E_g \end{cases} \tag{159}$$

For a 2D M_0 type critical point (parabolic E vs. **k** bands in two directions and no dispersion in the third), we have

$$E(\mathbf{k}) = E_g + \frac{\hbar^2\mathbf{k}^2}{2\mu_\perp^*} \tag{160}$$

Reproduced with permission of the copyright owner. Further reproduction prohibited without permission.

where $\mu_\perp^*$ is the reduced effective mass in the direction perpendicular to the direction with no dispersion (which has infinite effective mass) and E_g is the bandgap of interest. Now the JDOS is

$$D_{2D}(E) = \begin{cases} \dfrac{\mu_\perp^*}{\pi\hbar^3} & E > E_g \\ 0 & E < E_g \end{cases} \tag{161}$$

1.6.5 Relation of Dielectric Function To Quantum Transitions Considering Excitonic Effects

When we wish to consider excitonic effects on the absorption coefficient, we make a few changes to the formalism given above. First of all, instead of considering a transition of an electron from a valence state to a conduction state, we consider that a photon excites the crystal from its ground state to a state with one hole in the valence band and one electron in the conduction band. In the case of no electron-hole interaction, we can write this as

$$|0\rangle \xrightarrow[photon]{} |\mathbf{k}_e, \mathbf{k}_h, \mathbf{r}\rangle = \left|\psi^e_{c,\mathbf{k}_e}(\mathbf{r})\right\rangle \left|\psi^h_{v,\mathbf{k}_h}(\mathbf{r})\right\rangle . \tag{162}$$

where $\left|\psi^e_{c,\mathbf{k}_e}(\mathbf{r})\right\rangle$ represents an electron in the conduction band with a Bloch function of wavevector $\mathbf{k}_e$ and $\left|\psi^h_{v,\mathbf{k}_h}(\mathbf{r})\right\rangle$ represents an electron missing from the valence band (a

Reproduced with permission of the copyright owner. Further reproduction prohibited without permission.

hole) with a Bloch function of wavevector $\mathbf{k}_h$. Up to this point, this new notation is equivalent to that in the previous section. However, once we add the Coulomb attraction, following the envelope function formalism we see that the excited state will not be given by the right side of Eq. (162) (which is constructed from Bloch functions), but rather we can expand the state as a superpostion of the states given in Eq. (162). If we let the total wavevector of the electron-hole pair be $\mathbf{k}_{ex} = \mathbf{k}_e + \mathbf{k}_h$, then we can expand the exciton state as

$$\left|\Psi_{ex}(\mathbf{r})\right\rangle = \sum_{\mathbf{k}} A(\mathbf{k}) \left|\psi^{e}_{c,\mathbf{k}+\mathbf{k}_{ex}}(\mathbf{r}_e)\right\rangle \left|\psi^{h}_{v,\mathbf{k}-\mathbf{k}_{ex}}(\mathbf{r}_h)\right\rangle. \tag{163}$$

As mentioned earlier, the momentum of the photon is negligible compared to the size of the first Brioullin zone, so we can take $k_{ex} \approx 0$. Since we have a two particle state, we must consider the two particle Hamiltonian

$$\begin{aligned} H &= -\frac{i\hbar^2 \nabla_e^{\;2}}{2m} + \frac{i\hbar^2 \nabla_h^{\;2}}{2m} + V_c(\mathbf{r}_e) - V_c(\mathbf{r}_h) - \frac{e^2}{\varepsilon_0 \left|\mathbf{r}_e - \mathbf{r}_h\right|} \\ &= H_0^e(\mathbf{r}_e) - H_0^h(\mathbf{r}_h) + V_p(r) \end{aligned} \tag{164}$$

where e and h are used to denote symbols that pertain to the electron and the hole, respectively and $r = |\mathbf{r}_e - \mathbf{r}_h|$ and we have defined the free electron Hamiltonian, free hole Hamiltonian and Coulomb potential as

Reproduced with permission of the copyright owner. Further reproduction prohibited without permission.

$$
\begin{aligned}
H_0^e(\mathbf{r}_e) &= -\frac{i\hbar^2 \nabla_e{}^2}{2m} + V_c(\mathbf{r}_e) \\
H_0^h(\mathbf{r}_h) &= -\frac{i\hbar^2 \nabla_h{}^2}{2m} + V_c(\mathbf{r}_h) \\
V_p(r) &= -\frac{e^2}{\varepsilon_0 |\mathbf{r}_e - \mathbf{r}_h|}
\end{aligned}
\tag{165}
$$

respectively.

Note that the energy of a hole is negative as it represents the absence of the electron's energy for that state. Also, the perturbative Coulomb potential is attractive and thus lowers the energy.

In our present notation, the Schrödinger equation for the exciton is

$$
H_0^e(\mathbf{r}_e) - H_0^h(\mathbf{r}_h) + V_p(r) |\Psi_{ex}(\mathbf{r})\rangle = E|\Psi_{ex}(\mathbf{r})\rangle \tag{166}
$$

Multiplying by $\langle \psi_{v,\mathbf{k}-\mathbf{k}_{ex}}^h(\mathbf{r}_h) | \langle \psi_{c,\mathbf{k}+\mathbf{k}_{ex}}^e(\mathbf{r}_e) |$ on the right, and summing over $\mathbf{k}$, we obtain the equation that corresponds to Eq. (117a)

$$
\sum_{\mathbf{k}'} \langle \psi_{0,\mathbf{k}}(\mathbf{r}) | V_p(r) | \psi_{0,\mathbf{k}'}(\mathbf{r}) \rangle A_0(\mathbf{k}') = \{E - [E_c(0) - E_v(0)]\} A(\mathbf{k}) \tag{167}
$$

Reproduced with permission of the copyright owner. Further reproduction prohibited without permission.

which leads to the effective mass approximation just as for Eq. (116). In this case, it takes the form

$$\left[-\frac{i\hbar^2\nabla^2}{2\mu *}-\frac{e^2}{\varepsilon_0 r}\right]F(\mathbf{r})=\{E-[E_c(0)-E_v(0)]\}F(\mathbf{r})=E_{ex}F(\mathbf{r}) \tag{168}$$

where we have explicitly labeled the energy as the exciton energy.

where μ^* is the reduced effective mass tensor and the CP of interest is at $\mathbf{k} = \mathbf{k}_0$ and we have defined an exciton energy, which is referenced to the bandgap energy, $E_{ex} = E - [E_c(0)-E_v(0)] = E - E_g$.

With this knowledge, we see that we must reevaluate the dipole transition matrix to account for the modified wavefunction. Now, in the vicinity of a CP

$$\|\mathbf{M}_{cv}(\mathbf{k})\|^2 \longrightarrow \left\|\sum_{\mathbf{k}} A(\mathbf{k})\mathbf{M}_{cv}(\mathbf{k})\right\|^2 \tag{169}$$

If we argue as we did for Eq. (154) that $\mathbf{M}_{cv}(\mathbf{k}) \approx \mathbf{M}_{cv}(\mathbf{k}_0)$ in the vicinity of a CP at $\mathbf{k} = \mathbf{k}_0$, this evaluates to

$$\left\|\sum_{\mathbf{k}} A(\mathbf{k})\mathbf{M}_{cv}(\mathbf{k})\right\|^2 \approx \left\|\mathbf{M}_{cv}(\mathbf{k}_0)\sum_{\mathbf{k}} A(\mathbf{k})\right\|^2 = \|\mathbf{M}_{cv}(\mathbf{k}_0)\|^2 \|F(0)\|^2 \tag{170}$$

Reproduced with permission of the copyright owner. Further reproduction prohibited without permission.

Thus our final expression for the imaginary part of the dielectric function is given by multiplying Eq. (154) by the square of the magnitude of the envelope function at **r**=0. Thus we have

$$\varepsilon_2^{exciton}(E) = \|F(0)\|^2 \varepsilon_2^{SP}(E). \tag{171}$$

where $\varepsilon_2^{SP}(E)$ is the single particle function defined in Eq. (154) and $\varepsilon_2^{exciton}(E)$ is the form for the imaginary dielectric function including the exciton interaction. Thus we arrive at

$$\varepsilon_2^{exciton}(E) = \|F(0)\|^2 \left(\frac{2\pi e}{m_0 E}\right)^2 \|\mathbf{M}_{cv}(\mathbf{k}_0)\|^2 \sum_{\substack{\text{all}\\\text{states}}} \delta(E_{ex} + E_g - E). \tag{172}$$

The sum in the density of states term must now run over all allowed energies. For photon energies below the bandgap ($E_{ex} < 0$) we will have discrete bound states, while above the bandgap ($E_{ex} > 0$) we will have the original interband density of states given by Eq. (159) or Eq. (161) since the exciton interaction is assumed to be small.

1.6.6 Indirect Transitions

In the previous section, we found that since a visible wavelength photon carries very little momentum compared to the size of the BZ, photon-induced transitions between valence

Reproduced with permission of the copyright owner. Further reproduction prohibited without permission.

and conduction states are nearly vertical ($\mathbf{k}_v \approx \mathbf{k}_c$). However, if we consider the interaction of the electrons with the vibrations of the lattice (phonons), this situation is changed. A photon can excite an electron from valence to conduction band with the assistance of a phonon. The wavevector difference between the electrons in the two bands is now supplied by the phonon. Since this is a three particle interaction, the probability of transition will be much lower than that for direct transitions.

The two likely indirect gap absorption processes are shown in Fig. 20. In the path labeled 1, an electron is excited via a virtual (non-energy conserving) transition by absorption of a photon. This transition still conserves momentum due to the translation symmetry of the crystal. A second virtual transition, 1′, takes the electron from this state to the final state at a different **k** vector, $\mathbf{q} = \mathbf{k}_c - \mathbf{k}_v$ through the absorption or emission of a phonon. A second possible phonon assisted indirect optical transition is labeled 2 in Fig. 20.

To handle this situation analytically, we start with a Hamiltonian which is perturbed by both an electric field and a phonon interation.

$$H = H_0 + H_{eR} + H_{ep} \,. \tag{173}$$

Reproduced with permission of the copyright owner. Further reproduction prohibited without permission.

Figure 20. The two likely indirect gap absorption processes. In the path labeled 1, an electron is excited via a virtual (non-energy conserving) transition by absorption of a photon (1). This transition still conserves momentum due to the translation symmetry of the crystal. A second virtual transition takes the electron from this state to the final state at a different **k** vector, $\mathbf{q} = \mathbf{k}_c - \mathbf{k}_v$ through the absorption or emission of a phonon(1'). A second possible phonon assisted indirect optical transition is labeled 2.

Reproduced with permission of the copyright owner. Further reproduction prohibited without permission.

where H_0 is the unperturbed Hamiltonian whose eigenfunctions are Bloch states, H_{eR} is the perturbation due to the electromagnetic radiation field as given by Eq. (139)

$$H_{eR} = -\frac{e}{mc}\mathbf{A} \bullet i\hbar\nabla \tag{174}$$

and H_{ep} is the electron-phonon interaction. We start with the perturbation H_{ep}, which has the effect of mixing Bloch states at **k** and **k′**. So our new states are given by second order perturbation theory by

$$\left|l,\mathbf{k}\right\rangle = \left|l^0,\mathbf{k}\right\rangle + \sum_{m\neq l}\frac{\left|m^0,\mathbf{k}'\right\rangle\left\langle m^0,\mathbf{k}'\right|H_{ep}\left|l^0,\mathbf{k}\right\rangle}{E_0(l^0,\mathbf{k}) - E_0(m^0,\mathbf{k}') \pm \hbar\omega_p} \tag{175}$$

where $\left|l,\mathbf{k}\right\rangle$ is the new perturbed wavefunction, $\left|l^0,\mathbf{k}\right\rangle$ denotes an unperturbed Bloch function of wavevector **k** and band index l, $E_0(l^0,\mathbf{k})$ is the energy of the unperturbed state $\left|l^0,\mathbf{k}\right\rangle$, and $E_0(m^0,\mathbf{k}')$ is the energy of the unperturbed intermediate (virtual) state $\left|m^0,\mathbf{k}'\right\rangle$. This is valid if

$$\frac{\left\langle m^0,\mathbf{k}'\right|H_{ep}\left|l^0,\mathbf{k}\right\rangle}{E_0(l^0,\mathbf{k}) - E_0(m^0,\mathbf{k}') \pm \hbar\omega_p} << 1 \tag{176}$$

Then,

Reproduced with permission of the copyright owner. Further reproduction prohibited without permission.

$$\langle c,\mathbf{k}'|e\bullet\mathbf{p}|v,\mathbf{k}\rangle = \sum_{m\neq v}\sum_{\mathbf{k}_m}\frac{\langle c^0,\mathbf{k}'|e\bullet\mathbf{p}|m^0,\mathbf{k}_m\rangle\langle m^0,\mathbf{k}_m|H_{ep}|v^0,\mathbf{k}\rangle}{E_0(v^0,\mathbf{k})-E_0(m^0,\mathbf{k}_m)\pm\hbar\omega_p} + \sum_{l\neq v}\sum_{\mathbf{k}_l}\frac{\langle c^0,\mathbf{k}'|H_{ep}|l^0,\mathbf{k}_l\rangle\langle l^0,\mathbf{k}_l|e\bullet\mathbf{p}|v^0,\mathbf{k}\rangle}{E_0(v^0,\mathbf{k})-E_0(l^0,\mathbf{k}_l)\pm\hbar\omega_p} \tag{177}$$

where the sums in **k** are over the first BZ. From Eq. (148), we know that the perturbation $e\bullet\mathbf{p}$ preserves **k**; therefore, $\mathbf{k}_m = \mathbf{k}'$ and $\mathbf{k}_l = \mathbf{k}$. Also, using our definition from Eq. (150), we can write

$$\mathbf{M}_{eR,ep}(\mathbf{k},\mathbf{k}') \equiv \langle c,\mathbf{k}'|e\bullet\mathbf{p}|v,\mathbf{k}\rangle = \sum_{m\neq v}\frac{e\bullet\mathbf{M}_{cm}(\mathbf{k}')\langle m^0,\mathbf{k}'|H_{ep}|v^0,\mathbf{k}\rangle}{E_0(v^0,\mathbf{k})-E_0(m^0,\mathbf{k}')\pm\hbar\omega_p} + \sum_{l\neq v}\frac{\langle c^0,\mathbf{k}'|H_{ep}|l^0,\mathbf{k}\rangle e\bullet\mathbf{M}_{lv}(\mathbf{k})}{E_0(v^0,\mathbf{k})-E_0(l^0,\mathbf{k})\pm\hbar\omega_p} \tag{178}$$

Finally, following the logic leading up to Eq. (153) and summing the contributions from all possible transitions within the first BZ, we find an expression for the imaginary part of the dielectric function due to indirect transitions.

$$\varepsilon_2(E) = \left(\frac{2\pi e\hbar}{m_0 E}\right)^2 \sum_{\mathbf{k}}\sum_{\mathbf{k}'}\left\|\mathbf{M}_{eR,ep}(\mathbf{k},\mathbf{k}')\right\|^2 \delta\left[E_c(\mathbf{k}')-E_v(\mathbf{k})-E\pm\hbar\omega_p\right]. \tag{179}$$

Reproduced with permission of the copyright owner. Further reproduction prohibited without permission.

In many semiconductors, the matrix elements $\mathbf{M}_{eR,ep}(\mathbf{k},\mathbf{k}')$ can be assumed to be constant in the vicinity of the indirect bandgap. Then we can find the structure of the indirect gap by converting the sums in Eq. (179) to integrals over the density of states

$$\sum_{\mathbf{k}}\sum_{\mathbf{k}'}\delta\left[E_c(\mathbf{k}') - E_v(\mathbf{k}) - E \pm \hbar\omega_p\right] = \iint D_v(E_v)D_c(E_c)\delta\left[E_c - E_v - E \pm \hbar\omega_p\right]dE_c dE_v \tag{180}$$

For the case of parabolic bands,

$$\begin{aligned} E_c(\mathbf{k}') &= E_{ind} + \frac{\hbar^2\mathbf{k}'^2}{2m_c^*} \\ E_v(\mathbf{k}) &= -\frac{\hbar^2\mathbf{k}^2}{2m_v^*} \end{aligned} \tag{181}$$

where we have put the zero of energy at the top of the valence band, $\mathbf{k}$ and $\mathbf{k}'$ are referenced to their respective extrema, and the effective masses are also the values for the extrema. Then using Eq. (159), the densities of states are

Reproduced with permission of the copyright owner. Further reproduction prohibited without permission.

$$D_v(E_v) = \begin{cases} \dfrac{m_v^{*3/2}\sqrt{-2E_v}}{\pi^2\hbar^3} & E_v < 0 \\ 0 & E_v > 0 \end{cases}$$
$$D_c(E_c) = \begin{cases} \dfrac{m_c^{*3/2}\sqrt{2(E_c - E_{ind})}}{\pi^2\hbar^3} & E_c > E_{ind} \\ 0 & E_c < E_{ind} \end{cases} \tag{182}$$

Then returning to our integral we have

$$\begin{aligned} &\iint D_v(E_v)D_c(E_c)\delta\left[E_c - E_v - E \pm \hbar\omega_p\right]dE_c dE_v \\ &= \frac{2\left(m_c^* m_v^*\right)^{3/2}}{\pi^4\hbar^6}\iint\sqrt{-E_v}\sqrt{E_c - E_{ind}}\,\delta\left[E_c - E_v - E \pm \hbar\omega_p\right]dE_c dE_v \\ &= \frac{2\left(m_c^* m_v^*\right)^{3/2}}{\pi^4\hbar^6}\int_{E_g}^{\hbar\omega \mp \hbar\omega_p}\sqrt{E \mp \hbar\omega_p - E_c}\sqrt{E_c - E_{ind}}\,dE_c \end{aligned} \tag{183}$$

by changing the variable of integration to

$$x = \frac{E_c - E_{ind}}{E \mp \hbar\omega_p - E_c} \tag{184}$$

Then the integral becomes

Reproduced with permission of the copyright owner. Further reproduction prohibited without permission.

$$\iint D_v(E_v)D_c(E_c)\delta\left[E_c - E_v - E \pm \hbar\omega_p\right]dE_c dE_v$$
$$= \frac{2\left(m_c^* m_v^*\right)^{3/2}}{\pi^4 \hbar^6}\left(E - E_{ind} \mp \hbar\omega_p\right)^2 \int_0^1 \sqrt{x}\sqrt{1-x}\,dx \tag{185}$$
$$= \frac{\left(m_c^* m_v^*\right)^{3/2}}{4\pi^3 \hbar^6}\left(E - E_{ind} \mp \hbar\omega_p\right)^2$$

Using this result, Eq. (178) becomes

$$\varepsilon_2(E) =$$
$$\left(\frac{2\pi e\hbar}{m_0 E}\right)^2 \frac{\left(m_c^* m_v^*\right)^{3/2}}{4\pi^3 \hbar^6}\left\|\mathbf{M}_{eR,ep}(\mathbf{k}_{0,v},\mathbf{k}_{0,c})\right\|^2 \left(E - E_{ind} \mp \hbar\omega_p\right)^2 \theta\left(1 - \frac{E_{ind} \pm \hbar\omega_p}{E}\right). \tag{186}$$

where $\mathbf{k}_{0,v}$ and $\mathbf{k}_{0,c}$ are the $\mathbf{k}$ vectors at the CP extrema of the conduction and valence band, respectively, and θ is the unit step function. As a final comment, we note that although $\mathbf{M}_{eR,ep}(\mathbf{k},\mathbf{k}')$ does not have a strong $\mathbf{k}$ dependence in the region of the CP, it does have a temperature dependence since it incorporates H_{ep}. Thus it will be proportional to n_p and $n_p + 1$ for phonon absorption and emission, respectively, where n_p is the phonon occupancy number given by the Bose-Einstein distribution

$$n_p = \frac{1}{e^{\hbar\omega_p / k_B T} - 1}. \tag{187}$$

Reproduced with permission of the copyright owner. Further reproduction prohibited without permission.

where T is temperature and k_B is the Boltzman constant. Since the work for this dissertation was all done at room temperature, n_p was taken to be constant.

1.6.7 The Krammers Kronig Relation and Dielectric Function Symmetries

For most of this section, we follow the presentation of Jackson.[51] We begin with the defining equation for the dielectric function

$$\mathbf{D}(\mathbf{r},\omega) = \tilde{\varepsilon}(\omega)\mathbf{E}(\mathbf{r},\omega) = \mathbf{E}(\mathbf{r},\omega) + 4\pi\tilde{\chi}(\omega)\mathbf{E}(\mathbf{r},\omega) \tag{188}$$

where $\tilde{\varepsilon}(\omega)$ and $\tilde{\chi}(\omega)$ are the complex frequency dependent dielectric function and polarizability respectively. $\mathbf{D}(\mathbf{r},\omega)$ and $\mathbf{E}(\mathbf{r},\omega)$ are related to the time dependent expressions via Fourier transformations

$$\begin{aligned} \mathbf{D}(\mathbf{r},t) &= \frac{1}{\sqrt{2\pi}}\int_{-\infty}^{\infty}\mathbf{D}(\mathbf{r},\omega)e^{-i\omega t}\,d\omega \\ \mathbf{D}(\mathbf{r},\omega) &= \frac{1}{\sqrt{2\pi}}\int_{-\infty}^{\infty}\mathbf{D}(\mathbf{r},t)e^{i\omega t}\,dt \end{aligned} \tag{189}$$

and corresponding equations for **E**. Using these expressions, we find

Reproduced with permission of the copyright owner. Further reproduction prohibited without permission.

$$\mathbf{D}(\mathbf{r},t) = \mathbf{E}(\mathbf{r},t) + \frac{1}{\sqrt{2\pi}} \int_{-\infty}^{\infty} 4\pi\tilde{\chi}(\omega)\mathbf{E}(\mathbf{r},\omega)e^{-i\omega t}d\omega$$
$$= \mathbf{E}(\mathbf{r},t) + 2\int_{-\infty}^{\infty} \tilde{\chi}(\omega)e^{-i\omega t}\int_{-\infty}^{\infty}\mathbf{E}(\mathbf{r},t')e^{i\omega t'}dt'd\omega \tag{190}$$

Interchanging the order of integration above, making the substitution $\tau = t\text{-}t'$, and performing the integral over ω, we obtain

$$\mathbf{D}(\mathbf{r},t) = \mathbf{E}(\mathbf{r},t) + \frac{1}{2\pi}\int_{-\infty}^{\infty} G(\tau)\mathbf{E}(\mathbf{r},t-\tau)d\tau \tag{191}$$

where $G(\tau)$ is the Fourier transform of $4\pi\tilde{\chi}(\omega) = \tilde{\varepsilon}(\omega) - 1$

$$G(\tau) = \frac{1}{2\pi}\int_{-\infty}^{\infty}[\tilde{\varepsilon}(\omega) - 1]e^{-i\omega\tau}d\omega$$
$$\tilde{\varepsilon}(\omega) = 1 + \int_{-\infty}^{\infty} G(\tau)e^{i\omega\tau}d\tau \tag{192}$$

We now apply the argument of causality to Eq. (191). That is the electric displacement **D** at a time t is only determined by electric fields that have occurred up to the that time. Thus, $G(\tau) = 0$ for $\tau < 0$. Therefore, we can rewrite Eq. (191) as

Reproduced with permission of the copyright owner. Further reproduction prohibited without permission.

$$\mathbf{D}(\mathbf{r},t) = \mathbf{E}(\mathbf{r},t) + \frac{1}{2\pi}\int_0^\infty G(\tau)\mathbf{E}(\mathbf{r},t-\tau)d\tau \tag{193}$$

Correspondingly, the second line of Eq. (192) becomes

$$\tilde{\varepsilon}(\omega) = 1 + \int_0^\infty G(\tau)e^{i\omega\tau}d\tau \tag{194}$$

This is an important result because of what it tells us about the dielectric function. First of all, $G(\tau)$ must be real due to the reality of $\mathbf{D}(\mathbf{r},t)$ and $\mathbf{E}(\mathbf{r},t)$ and Eq. (193). Thus we can deduce from Eqs. (189) and (194) that

$$\begin{aligned} \mathbf{D}(-\omega) &= \mathbf{D}^*(\omega^*) \\ \mathbf{E}(-\omega) &= \mathbf{E}^*(\omega^*) \\ \tilde{\varepsilon}(-\omega) &= \tilde{\varepsilon}^*(\omega^*) \end{aligned} \tag{195}$$

For real ω, this means that the real part and the imaginary part of the dielectric function are even and odd respectively. Further, Eq. (193) shows that $\tilde{\varepsilon}(\omega)$ is an analytic function in the complex upper half plane (Im $\omega > 0$) provided $G(\tau)$ is finite. Along the real axis, we also find that $\tilde{\varepsilon}(\omega)$ is analytic, so long as $G(\tau) \to 0$ as $\tau \to \infty$. For conductors, this last requirement is not met since an electric field even in the remote past generates a polarization in the present. That is $G(\tau \to \infty) \to 4\pi\sigma$ and thus, the imaginary dielectric function has a pole at $\omega = 0$ in agreement with Eq. (94) which we restate here.

Reproduced with permission of the copyright owner. Further reproduction prohibited without permission.

$$\varepsilon_i(\omega \approx 0) = \frac{4\pi\sigma}{\omega} \tag{94}$$

The analyticity of $\tilde{\varepsilon}(\omega)$ in the upper half plane leads to the important Kramers-Kronig (KK) relation, which relates the real and imaginary parts of $\tilde{\varepsilon}(\omega)$. For any point ω in the upper half plane, Cauchy's theorem states

$$\tilde{\varepsilon}(\omega) - 1 = \frac{1}{2\pi i}\oint_C \frac{\tilde{\varepsilon}(\omega') - 1}{\omega' - \omega} d\omega' \tag{196}$$

We choose the contour to consist of the real ω axis and a great semicircle at infinity in theupper half plane. $\tilde{\varepsilon}(\omega)$ vanishes sufficiently fast for $\|\omega\| \to \infty$ that there is no contribution to the integral from the greal semicircle. Thus Eq. (196) becomes

$$\tilde{\varepsilon}(\omega) - 1 = \frac{1}{2\pi i}\int_{-\infty}^{\infty} \frac{\tilde{\varepsilon}(\omega') - 1}{\omega' - \omega} d\omega' \tag{197}$$

Temporarily neglecting the possible simple pole for a conductor, Eq. (197) has only a single pole at $\omega = \omega'$. Thus Eq. (197) can be written as

$$\tilde{\varepsilon}(\omega) - 1 = \frac{1}{\pi i} P \int_{-\infty}^{\infty} \frac{\tilde{\varepsilon}(\omega') - 1}{\omega' - \omega} d\omega' \tag{198}$$

Reproduced with permission of the copyright owner. Further reproduction prohibited without permission.

Where the P indicates the Cauchy principal part of the integral (that is when performing the contour integration, one takes half the value of a residue on the contour). To be consistent with other sections, we use $E = \hbar\omega$ The real and imaginary parts of Eq. (198) then are

$$\varepsilon_1(E) - 1 = \frac{1}{\pi} P \int_{-\infty}^{\infty} \frac{\varepsilon_2(E')}{E' - E} dE'$$
$$\varepsilon_2(E) = \frac{1}{\pi} P \int_{-\infty}^{\infty} \frac{\varepsilon_1(E') - 1}{E' - E} dE' \tag{199}$$

Using the symmetry property of the dielectric function in Eq. (195) [that is $\varepsilon_1(E)$ even and $\varepsilon_2(E)$ odd], this can be rewritten

$$\varepsilon_1(E) - 1 = \frac{2}{\pi} P \int_{0}^{\infty} \frac{E'\varepsilon_2(E')}{E'^2 - E^2} dE'$$
$$\varepsilon_2(E) = \frac{2E}{\pi} P \int_{0}^{\infty} \frac{\varepsilon_1(E') - 1}{E'^2 - E^2} dE' \tag{200}$$

The relations in Eq. (199) or Eq. (200) are known as the KK relations.

Reproduced with permission of the copyright owner. Further reproduction prohibited without permission.

1.7 Modeling – lineshape

The dielectric properties of a crystal are known to be strongly connected with its energy BS. Transitions involving these energy bands, including relevant excitonic effects, are responsible for the structure in the optical constants in the region of this thesis (MIR-UV), as discussed in sections 1.6.2 and 1.6.4. (We note that in the far infrared, the dielectric function is dominated by contributions from phonons and free carrier absorption.) For illustration, we display in Fig. 21 the dielectric function of $In_{0.66}Ga_{0.34}As$ along with a model fit developed in this thesis. The main structures correspond to the energy-band structure interband critical points (CPs) denoted E_0, E_0+Δ_0, E_1, E_1+Δ_1, E_0', and E_2. The features near E_1 and E_1+Δ_1 are labeled by their exciton energies E_1-R_1 and E_1+Δ_1-R_1 (R_1 being the exciton binding energy) since the excitons are the major feature for these CPs, as will be shown in sections 1.7.2 and 1.7.3. The fact that the main feature is lower than the CP and even the well known excitonic nature of theses CPs[2-7] is usually neglected in the literature, even when it is important as for semi-empirical band structure calculations. For this material, the E_0' and E_2 CPs are at nearly the same energy and were not resolved, so they were treated as a single structure.

In this section, we present a new comprehensive model dielectric function for diamond- and zincblende-type semiconductors. Ours is the first correct modeling of the dielectric for diamond and zincblende-type semiconductors including discrete as well as band-to-band Coulomb enhanced (BBCE) effects, i.e., continuum exciton at the CPs denoted E_0,

Reproduced with permission of the copyright owner. Further reproduction prohibited without permission.

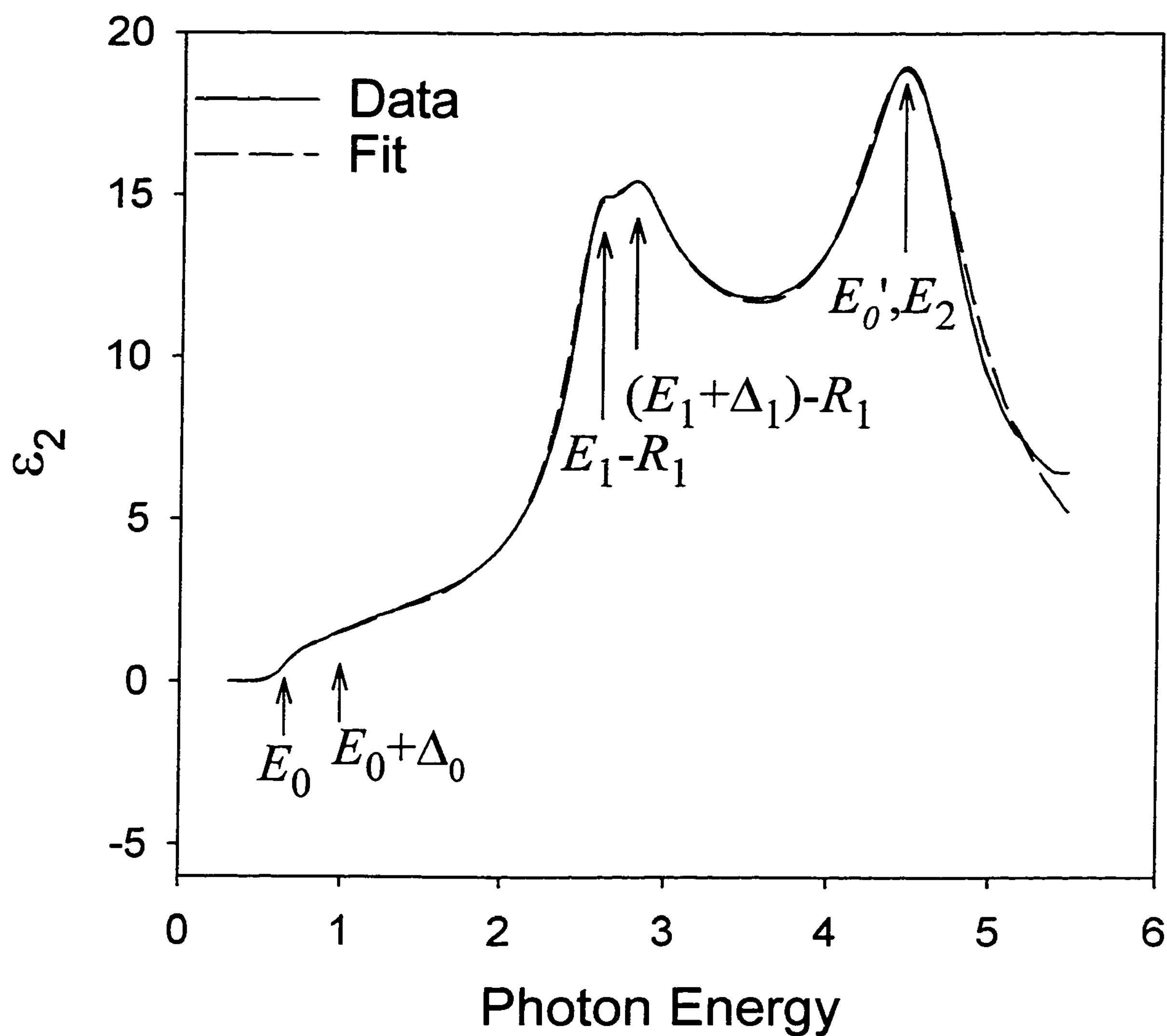

Figure 21. Dielectric Function of $In_{0.66}Ga_{0.34}As$ showing major features at E_0, $E_0+\Delta_0$, E_1-R_1, $E_1+\Delta_1$-R_1, E_2, and E_0' along with the fit developed in this section. For this material, the E_2 and E_0' CPs are at nearly the same energy and were not resolved, so a they were treated as a single structure.

Reproduced with permission of the copyright owner. Further reproduction prohibited without permission.

$E_0+\Delta_0$, E_1, and $E_1+\Delta_1$.[1] Because of the inclusion of these effects, we are able to obtain an excellent fit to the experimental data yielding several physically important parameters such as energy gaps, oscillator strength, broadening, and exciton binding energies, including the first evaluation of the exciton binding energy at the E_1, $E_1+\Delta_1$ CP, R_1. Our results, particularly for exciton continuum effects at E_1, have considerable implications for recent first-principles band structure calculations which include exciton effects.[11,12]

Previous work on modeling dielectric functions have been incomplete, in particular prior to this work, no one has correctly accounted for excitonic effects in modeling an experimentally determined dielectric function. Aspnes who was the first to obtain high quality visible range dielectric function data chose not to model his data,[47] or used third derivative Lorentzian lineshapes to fit the third derivative of the dielectric function in order to extract bandgap energies and broadening parameters.[59] Erman *et al.*[60] used a model of several harmonic oscillators to fit the dielectric function. Although the data can be fit well given enough oscillators, no physical information is obtain from this phenomenological fit. Lautenschlager *et al.*[61] used second derivative Lorentzian lineshapes to fit the second derivative of the dielectric function in order to extract bandgap energies of GaAs for several temperatures. Adachi and his collaborators[62] have probably done the most fitting of ellipsometric data to date. They used a model similar to ours based on a sum of contributions from the various CPs in the band structure. Their model takes the nature of each CP into account and includes terms for the bound exciton states; However, it fails to take into account the Coulomb enhancement to the continuum states, which must be present along with the bound exciton as shown by Elliot.[63] The

Reproduced with permission of the copyright owner. Further reproduction prohibited without permission.

University of Illinois-Chicago group[64] have used a model similar to Adachi's and introduced both Lorentzian and Gaussian broadening terms into their expressions, but they have, like Adachi, failed to include Coulomb enhancement to the continuum states.

Absorption data near the fundamental bandgap has been modeled using the correct Elliot formulation with great success at least for the E_0, $E_0+\Delta_0$ transitions.[65] In particular, Goñi *et. al.*[66] found a closed form for the Lorentzian broadened Elliot formula for the absorption coefficient near the fundamental bandgap.

In the model that we have employed, the dielectric function is approximated as a sum of several components, each of which is an explicit function of energy and represents a contribution from the neighborhood of a CP in the joint density of states (JDOS). For the E_0, $E_0+\Delta_0$ and E_1, $E_1+\Delta_1$ features we have explicitly taken exciton effects into account. As required ε_1 and ε_2 are KK transforms [Eq. (199)] of each other.

Using the model explained in this section, we have performed the first fitting of both the real and imaginary parts of the dielectric function explicitly taking both bound exciton states and continuum Coulomb enhancement into account at the E_0, $E_0+\Delta_0$ and E_1, $E_1+\Delta_1$ CPs. To represent actual dielectric function data, we have performed two integrals on each of the expressions given by Elliot[63] for the 3D features, E_0, $E_0+\Delta_0$ and Shinada and Sugano[67] for the 2D and E_1, $E_1+\Delta_1$ features: 1) the probability per unit time of electron transitions is Lorenzian broadened and then 2) the resulting imaginary part of the dielectric function is analytically KK transformed to obtain the real part. Tanguy has

Reproduced with permission of the copyright owner. Further reproduction prohibited without permission.

developed similar expressions for the dielectric function including bound and continuum excitonic effects near both 3D[68] and 2D[5] type CPs, but has not used his expressions to fit measured data. Our expressions differ from his in two main ways. First, he Lorentzian broadens the entire dielectric function while we only Lorentzian broaden the electron transition probability, which in our case corresponds to a lifetime effect for the electronic energy states. Secondly, our expressions involve only simple functions while his involve the more complicated digamma function.

1.7.1 E_0 and $E_0+\Delta_0$ Features

The E_0 band gap is a 3D M_0 type CP at the center (Γ point) of the BZ. This means that the BS has positive interband effective mass in all directions for this CP. To calculate the contribution to the dielectric function near the E_0 CP, we begin with Eq. (172) for the imaginary part of the dielectric function including exciton interactions applied at a CP with $\mathbf{k}_0 = 0$.

$$\varepsilon_{2,E_0^{CP}}(E) = \|F(0)\|^2 \left(\frac{2\pi e\hbar}{mE}\right)^2 \|\mathbf{M}_{cv}(0)\|^2 \sum_{\substack{\text{all} \\ \text{states}}} \delta(E_{ex} + E_0 - E) . \qquad (201)$$

where E_0 is the direct bandgap energy. According to Eq. (168), the envelope function $F(\mathbf{r})$ refers to the solution of the hydrogen atom-type Schrödinger equation

Reproduced with permission of the copyright owner. Further reproduction prohibited without permission.

$$\left[-\frac{\hbar^2\nabla^2}{2\mu^*}-\frac{e^2}{\varepsilon_0 r}\right]F(\mathbf{r})=E_{ex}F(\mathbf{r}) \tag{202}$$

where μ^* is the (3D) reduced interband effective mass at $\mathbf{k} = 0$ and ε_0 is the static dielectric constant of the material. This equation has well known solutions.[63]

For the bound states, $F(0)$ is non-zero only for s states, where we have

$$F_{q_n q_l q_m}(0)=F_{q_n 00}(0)=\frac{1}{\sqrt{\pi a_{ex}^3 q_n^3}} \tag{203}$$

at the doubly degenrate (spin up/spin down) eigenenergies

$$E_{q_n,0}^{ex}=-\frac{R}{q_n^2} \tag{204}$$

where q_n is the energy quantum number, q_l is the orbital angular momentum quantum number, q_m is the magnetic quantum number, R is the ground state exciton binding energy (the Rydberg), and a_{ex} is the effective Bohr radius of the exciton. These last two are given by

Reproduced with permission of the copyright owner. Further reproduction prohibited without permission.

$$R = \frac{\mu^* e^4}{2\hbar^2 \varepsilon_0^2}$$
$$a_{ex} = \frac{\hbar^2 \varepsilon_0}{\mu^* e^2} \tag{205}$$

where e is the electron charge.

For unbound states, the wavefunction gives a factor of[63]

$$\|F(0)\|^2 = \frac{\pi z(E) e^{\pi z(E)}}{\sinh[\pi z(E)]} \tag{206}$$

where $z(E) = \sqrt{\frac{R}{E - E_0}}$.

The density of states in the continuum is given by Eq. (159) to be

$$\sum_{\mathbf{k}} \delta(E_c - E_v - E) = \begin{cases} \frac{\mu^{*3/2} \sqrt{2(E - E_0)}}{\pi^2 \hbar^3} & E > E_0 \\ 0 & E < E_0 \end{cases}. \tag{207}$$

where $E_0 = E_c(0) - E_v(0)$ is the bandgap energy.

Reproduced with permission of the copyright owner. Further reproduction prohibited without permission.

Substituting Eqs. (203)-(207) into Eq. (201), one obtains for the unbroadened imaginary part of the dielectric function for positive energy

$$\varepsilon_{2,E_0^{CP}}(E)=\frac{\pi A}{E^2}\left[\sum_{q_n=1}^{\infty}\frac{4R}{q_n^3}\delta(E_0-\frac{R}{q_n^2}-E)+\frac{e^{\pi z}\theta(E-E_0)}{\sinh[\pi z(E)]}\right] \tag{208}$$

where

$$A=\|\mathbf{M}_{cv}(0)\|^2\,\frac{2e^2\sqrt{2\mu^{*3}R}}{m^2\hbar} \tag{209}$$

Next, following Goñi *et al*,[66] we convolute the term in brackets (and not the $1/E^2$) of Eq. (208) with a Lorentzian function. Since the term in brackets comes from the transition probability of the quantum states [Eq. (141)], this corresponds to a finite lifetime of these states. When we broaden the dielectric function, we must remember Eq. (195) which states that the imaginary dielectric function must be odd. Although this seems to be a small correction, it is crucial if one wants to use the KK transform to determine the real part of the dielectric function (as we will later). With these considerations, we find the imaginary dielectric function to be

Reproduced with permission of the copyright owner. Further reproduction prohibited without permission.

$$\varepsilon_{2,E_0^{CP}}(E) = \text{Im}\left\{\frac{2A}{E^2}\left[\begin{array}{l}\displaystyle\sum_{q_n=1}^{\infty}\frac{2R}{q_n^3}\left(\frac{1}{E_{q_n,0}^{ex} - E - i\Gamma_{q_n,0}^{ex}} + \frac{1}{E_{q_n,0}^{ex} + E + i\Gamma_{q_n,0}^{ex}}\right) \\ \displaystyle + \int_{-\infty}^{\infty}\left(\frac{\theta(E' - E_0)}{1 - e^{-2\pi z(E')}} - \frac{\theta(-E' - E_0)}{1 - e^{-2\pi z(-E')}}\right)\frac{dE'}{E' - E - i\Gamma_0}\end{array}\right]\right\} \tag{210}$$

where $E_{q_n,0}^{ex}$ are the bound exciton energy defined by Eq. (204), $\Gamma_{q_n,0}^{ex}$ are the broadening parameters for the exciton states, E_0 is the CP energy, and Γ_0 is the broadening parameter for the continuum states.

Since Eq. (210) is the imaginary part of a real function, one might be tempted to assume that the expression in curly brackets is also good for the real part of the dielectric function. We will see later that this is not quite correct, and the KK transform will give us an additional real term that will cancel a singularity in the real part of the term in curly brackets at E=0.

To evaluate the integral Eq. (210) we follow the method presented in Goñi *et al.*[66] Focusing on the first term, we simplify it as

$$\begin{aligned}\int_{-\infty}^{\infty}\frac{\theta(E' - E_0)}{1 - e^{-2\pi z(E')}}\frac{dE'}{E' - E - i\Gamma_0} &= \frac{1}{2}\int_{E_0}^{\infty}\frac{1 + \coth[\pi z(E')]}{E' - E - i\Gamma_0}dE' \\ &= -\frac{1}{2}\text{Im}[\ln(E_0 - E - i\Gamma)] + \int_{E_0}^{\infty}\frac{\coth[\pi z(E')]}{E' - E - i\Gamma_0}dE'\end{aligned} \tag{211}$$

Reproduced with permission of the copyright owner. Further reproduction prohibited without permission.

To evaluate the part containing coth(πz), we make the substitutions

$$x^2 = \frac{1}{z^2} = \frac{E - E_0}{R} \qquad \xi^2 = \frac{E_0 - E - i\Gamma_0}{R} \tag{212}$$

Then we find

$$\int_{E_0}^{\infty} \frac{\coth[\pi z(E')]}{E' - E - i\Gamma_0} dE' = \int_0^{\infty} \frac{x}{x^2 + \xi^2} \coth\left(\frac{\pi}{x}\right) dx = \frac{1}{2} \int_{-\infty}^{\infty} \frac{x}{x^2 + \xi^2} \coth\left(\frac{\pi}{x}\right) dx \tag{213}$$

The last step is valid since the integrand is an even function of x. The poles for this expression in the upper hemisphere are at

$$x = i\xi \qquad \text{and} \qquad x = \frac{i}{m}, \qquad m = 1, 2, 3, ... \tag{214}$$

Thus, integrating Eq. (213) along the real axis and half-circle in the upper half plane,

$$\int_{E_0}^{\infty} \frac{\coth[\pi z(E')]}{E' - E - i\Gamma_0} dE' = -\pi \cot\left(\frac{\pi}{\xi}\right) - \sum_{n=1}^{\infty} \frac{2}{n^3} \frac{1}{\xi^2 - 1/n^2} \tag{215}$$

Using Eqs. (211) and (215) in Eq. (210), we find the broadened expression for the imaginary dielectric function

Reproduced with permission of the copyright owner. Further reproduction prohibited without permission.

$$\varepsilon_{2,E_0^{CP}}(E) = \mathrm{Im}\left\{ \frac{A}{E^2} \left[\begin{array}{l} \sum_{q_n=1}^{\infty} \{ gb_{q_n}[\xi(E + i\Gamma_{q_n}^{ex})] + gb_{q_n}[\xi(-E - i\Gamma_{q_n}^{ex})] \} \\ + gu[\xi(E + i\Gamma_0)] + gu[\xi(-E - i\Gamma_0)] \end{array} \right] \right\} \tag{216}$$

where

$$\begin{aligned} \xi^2(X) &= \frac{E_0 - X}{R} \\ gb_{q_n}(\xi) &= \frac{4}{q_n} \frac{1}{\xi^2 - q_n^{-2}} \\ gu(\xi) &= -\ln(\xi^2) - \pi\cot\left(\frac{\pi}{\xi}\right) - \sum_{q_n=1}^{\infty} \frac{2}{q_n} \frac{1}{\xi^2 - q_n^{-2}} \end{aligned} \tag{217}$$

with *gb* corresponding to the bound excitonic states and *gu* to the unbound band to band continuum excitonic states (BBCE). At this point, because Eq. (216) is the imaginary part of a complex function, it is tempting to simply take the expression in Eq. (216) as the complex dielectric function. However, one needs to use the KK relation to insure the correct result. In particular, the real part of the expression in Eq. (216) has a singularity at E=0 that goes as $1/E^2$. To perform the integration we start with Eq. (200)

$$\varepsilon_1(E) - 1 = \frac{2}{\pi} P \int_0^{\infty} \frac{E'\varepsilon_2(E')}{E'^2 - E^2} dE' \tag{218}$$

Reproduced with permission of the copyright owner. Further reproduction prohibited without permission.

where now we must take the contour around the upper half plane that includes the pole at $E = E'$. Using the odd symmetry of ε_i, we can transform this to

$$\varepsilon_1(E) - 1 = \frac{1}{\pi} P \int_{-\infty}^{\infty} \frac{E'\varepsilon_2(E')}{E'^2 - E^2} dE' \tag{219}$$

For simplicity, we examine this integral for the $n = 1$ bound state

$$\varepsilon_{1,E_0^{CP},1b}(E) - 1$$
$$= \frac{2}{\pi} P \int_{-\infty}^{\infty} \frac{AR}{E'(E'^2 - E^2)} \mathrm{Im}\left(\frac{1}{E_{1,0}^{ex} - E' - i\Gamma_{1,0}^{ex}} + \frac{1}{E_{1,0}^{ex} + E' + i\Gamma_{1,0}^{ex}} \right) dE' \tag{220}$$

By partial fraction decomposition, we get

$$\varepsilon_{1,E_0^{CP},1b}(E) - 1$$
$$= \frac{AR}{\pi E^2} P \int_{-\infty}^{\infty} \left(\frac{1}{E' + E} + \frac{1}{E' - E} - \frac{2}{E'} \right) \mathrm{Im}\left(\frac{1}{E_{1,0}^{ex} - E' - i\Gamma_{1,0}^{ex}} + \frac{1}{E_{1,0}^{ex} + E' + i\Gamma_{1,0}^{ex}} \right) dE' \tag{221}$$

Since we are taking the principle values for the singularities at $E' = \pm E$ we must do the same for the singularity at $E' = 0$ in our contour. This can be seen by letting $E' \to E' - i\delta$ (δ being infinitesimal) to include the first two singularities explicitly, and noting that in this case, the third term singularity is also included. By symmetry, the $(E' + E)^{-1}$ and $(E'$

Reproduced with permission of the copyright owner. Further reproduction prohibited without permission.

- $E)^{-1}$ terms must give the same contribution. We further note that each term in the integral of Eq. (221) is simply the expression for the KK transform of a Lorentzian function. Thus we obtain

$$\begin{aligned}&\varepsilon_{1,E_0^{CP},1b}(E)-1\\&=\frac{AR}{E^2}\mathrm{Re}\left(\frac{1}{E_{1,0}^{ex}-E'-i\Gamma_{1,0}^{ex}}+\frac{1}{E_{1,0}^{ex}+E'+i\Gamma_{1,0}^{ex}}-\frac{1}{E_{1,0}^{ex}-i\Gamma_{1,0}^{ex}}-\frac{1}{E_{1,0}^{ex}+i\Gamma_{1,0}^{ex}}\right)\end{aligned} \tag{222}$$

The other terms in Eq. (216) likewise only have residues at $E' = \pm E$, 0 and thus transform similarly. The final expression for the E0 contribution to the complex dielectric function then is

$$\begin{aligned}&\tilde{\varepsilon}_{E_0^{CP}}(E)\\&=\frac{A}{E^2}\left[\begin{matrix}\sum_{q_n=1}^{\infty}\left\{\begin{matrix}gb_{q_n}[\xi(E+i\Gamma_{q_n}^{ex})]+gb_{q_n}[\xi(-E-i\Gamma_{q_n}^{ex})]\\-gb_{q_n}[\xi(i\Gamma_{q_n}^{ex})]-gb_{q_n}[\xi(-i\Gamma_{q_n}^{ex})]\end{matrix}\right\}\\+gu[\xi(E+i\Gamma_0)]+gu[\xi(-E-i\Gamma_0)]-gu[\xi(i\Gamma_0)]-gu[\xi(-i\Gamma_0)]\end{matrix}\right]\end{aligned} \tag{223}$$

This expression has the properties one expects for the dielectric function as discussed in section 1.6.7. The real part is even, the imaginary part is odd, there are no singularities in the upper half plane, and of course it satisfies the KK relation. The imaginary part of Eq. (223) does have one singularity along the real energy axis at $E = 0$. This singularity at $E = 0$ goes as 1/E and thus corresponds to a DC conductivity as discussed in the paragraph after Eq. (195) and given in Eq. (94). It results from the Lorentzian broadening in that at

Reproduced with permission of the copyright owner. Further reproduction prohibited without permission.

zero energy there is still a small probability of producing transitions. This singularity and others like it will be discussed below the section 1.7.6.

The first and second derivatives of Eq. (223) can be written as

$$\frac{d\left[\tilde{\varepsilon}_{E_0^{CP}}(E)\right]}{dE}=\frac{-2}{E}\tilde{\varepsilon}_{E_0^{CP}}(E)$$
$$+\frac{A}{E^2R}\left\{\begin{array}{l}\sum_{q_n=1}^{\infty}\frac{4}{q_n}\left[\frac{1}{\left(\xi_{b+}^2-q_n^{-2}\right)^2}-\frac{1}{\left(\xi_{b-}^2-q_n^{-2}\right)^2}\right]+\pi^2\left[\frac{\csc^2\left(\frac{\pi}{\xi_{u+}}\right)}{\xi_{u+}^4}-\frac{\csc^2\left(\frac{\pi}{\xi_{u-}}\right)}{\xi_{u-}^4}\right]\\ +\frac{1}{\xi_{u+}^2}-\frac{1}{\xi_{u-}^2}-\sum_{q_n=1}^{\infty}\frac{2}{n}\left[\frac{1}{\left(\xi_{u+}^2-q_n^{-2}\right)^2}-\frac{1}{\left(\xi_{u-}^2-q_n^{-2}\right)^2}\right]\end{array}\right\}$$

(224)

and

Reproduced with permission of the copyright owner. Further reproduction prohibited without permission.

$$\frac{d^2\left[\tilde{\varepsilon}_{E_0^{CP}}(E)\right]}{dE^2}=\frac{-2}{E^2}\tilde{\varepsilon}_{E_0^{CP}}(E)-\frac{4}{E}\frac{d\left[\tilde{\varepsilon}_{E_0^{CP}}(E)\right]}{dE}$$

$$+\frac{A}{E^2R^2}\left\{\begin{array}{l}\displaystyle\sum_{q_n=1}^{\infty}\frac{8}{q_n}\left[\frac{1}{\left(\xi_{b+}^2-q_n^{-2}\right)^3}+\frac{1}{\left(\xi_{b-}^2-q_n^{-2}\right)^3}\right]\\ \displaystyle+2\pi^2\left[\frac{\csc^2\left(\frac{\pi}{\xi_{u+}}\right)}{\xi_{u+}^6}\left(\frac{\pi\cot\left(\frac{\pi}{\xi_{u+}}\right)}{\xi_{u+}^2}-1\right)+\frac{\csc^2\left(\frac{\pi}{\xi_{u-}}\right)}{\xi_{u-}^6}\left(\frac{\pi\cot\left(\frac{\pi}{\xi_{u-}}\right)}{\xi_{u-}^2}-1\right)\right]\\ \displaystyle+\frac{1}{\xi_{u+}^4}+\frac{1}{\xi_{u-}^4}-\sum_{q_n=1}^{\infty}\frac{4}{q_n}\left[\frac{1}{\left(\xi_{u+}^2-q_n^{-2}\right)^3}+\frac{1}{\left(\xi_{u-}^2-q_n^{-2}\right)^3}\right]\end{array}\right\} \quad (225)$$

where

$$\begin{aligned}\xi_{b+}&=\xi(E+i\Gamma_b)\\ \xi_{b-}&=\xi(-E-i\Gamma_b)\\ \xi_{u+}&=\xi(E+i\Gamma_u)\\ \xi_{u-}&=\xi(-E-i\Gamma_u)\end{aligned} \quad (226)$$

The $E_0+\Delta_0$ feature has also been described by broadened excitonic and BBCE components, with parameters similar to those used for the E_0 feature, i.e. Eq. (223) with $\tilde{\varepsilon}_{E_0^{CP}}(E)\rightarrow\tilde{\varepsilon}_{E_0^{CP}+\Delta_0}(E)$, $A\rightarrow B$, $E_0\rightarrow E_0+\Delta_0$, $R\rightarrow R_{so}$,

$$\Gamma_{q_n}^{ex}\rightarrow\Gamma_{q_n,so}^{ex},\ \text{and}\ \Gamma_0\rightarrow\Gamma_{so} \quad (227)$$

Reproduced with permission of the copyright owner. Further reproduction prohibited without permission.

1.7.2 E_1 and $E_1+\Delta_1$ Features

For diamond and zincblende materials, the E_1 and $E_1+\Delta_1$ CPs are generally accepted to be M_1 type, but with a very large mass along the <111> direction compared to the mass perpendicular to this direction. We take the approximation that the interband mass along the <111> direction is infinite. Then the CP is of the 2D M_0 type. The form of the unbroadened absorption spectrum was worked out by Shinada and Sugano.[67]

As at E_0 we begin with Eq. (172), only now we apply it at a CP near $\mathbf{k}_0 = \mathrm{L} = \pi/a\,[111]$.

$$\varepsilon_{2,E_1^{CP}}(E) = \left(\frac{2\pi e\hbar}{mE}\right)^2 \|\mathbf{M}_{cv}(\mathrm{L})\|^2 \|F(0)\|^2 \sum_{\substack{\text{all} \\ \text{states}}} \delta(E_{ex} + E_1 - \hbar\omega) . \tag{228}$$

where E_1 is the CP energy. The envelope function is now the solution to the 2D hydrogen atom-type Schrödinger equation

$$\left[-\frac{\hbar^2}{2\mu_\perp^*}\left(\frac{\partial^2}{\partial x^2}+\frac{\partial^2}{\partial y^2}\right)-\frac{e^2}{\varepsilon_0 r}\right]F(\mathbf{r}) = E_{ex}F(\mathbf{r}) \tag{229}$$

where $\mu_\perp^*$ is the (2D) reduced interband effective mass perpendicular to the <111> direction at $\mathbf{k} = \mathrm{L}$ and ε_0 is the static dielectric constant of the material. This equation has well known solutions.[67]

Reproduced with permission of the copyright owner. Further reproduction prohibited without permission.

$F(0)$ is non-zero only for s-type states. For the bound states, we have

$$F_{q_n q_l q_m}(0) = F_{q_n 00}(0) = \sqrt{\frac{8}{\pi a_{ex}^2 (2q_n - 1)^3}} \tag{230}$$

at the doubly degenerate (spin up/spin down) eigenenergies

$$E_{q_n,1}^{ex} = -\frac{R_1}{(2q_n - 1)^2} \tag{231}$$

where q_n is the energy quantum number, q_l is the orbital angular momentum quantum number, q_m is the magnetic quantum number, R_1 is the ground state exciton binding energy (the 2D Rydberg), and a_{ex} is the effective Bohr radius of the exciton. These last two are given by

$$\begin{aligned} R_1 &= \frac{2\mu_\perp^* e^4}{\hbar^2 \varepsilon_0^2} \\ a_{ex} &= \frac{\hbar^2 \varepsilon_0}{\mu_\perp^* e^2} \end{aligned} \tag{232}$$

where e is the electron charge. Note that in some literature, the Rydberg is defined as ¼ the value given here.

Reproduced with permission of the copyright owner. Further reproduction prohibited without permission.

For unbound states, the wavefunction gives a factor of[67]

$$\|F(0)\|^2 = \frac{e^{2\pi z(E)}}{\cosh[2\pi z(E)]} \tag{233}$$

where $z(E) = \sqrt{\dfrac{R_1}{E - E_1}}$

The density of states in the continuum is given by Eq. (161) to be

$$\sum_{\mathbf{k}} \delta(E_c - E_v - E) = \begin{cases} \dfrac{\mu_\perp^*}{\pi\hbar^3} & E > E_1 \\ 0 & E < E_1 \end{cases} \tag{234}$$

where $E_1 = E_c(\mathrm{L}) - E_v(\mathrm{L})$ is the CP energy.

Substituting Eqs. (230)-(234) into Eq. (228), one obtains for the unbroadened imaginary part of the dielectric function for positive energy

$$\varepsilon_{2,E_1^{CP}}(E) = \frac{\pi C_1}{E^2}\left[\sum_{q_n=1}^{\infty} \frac{8R_1}{(2q_n-1)^3}\delta\left(E_1 - \frac{R_1}{(2q_n-1)^2} - E\right) + \frac{e^{2\pi z(E)}\theta(E-E_1)}{\cosh[2\pi z(E)]}\right] \tag{235}$$

where

Reproduced with permission of the copyright owner. Further reproduction prohibited without permission.

$$C_1 = \|\mathbf{M}_{cv}(\mathrm{L})\|^2 \frac{4\mu_\perp^* e^2}{m^2} \tag{236}$$

Next as we did for E_0, we convolute the term in brackets of Eq. (234) with a Lorentzian function. We find the imaginary dielectric function to be

$$\varepsilon_{2,E_1^{CP}}(E) = \mathrm{Im}\left\{ \frac{2C_1}{E^2} \left[\sum_{q_n=1}^{\infty} \frac{4R_1}{(2q_n-1)^3} \left(\frac{1}{E_{q_n,1}^{ex} - E - i\Gamma_{q_n,1}^{ex}} + \frac{1}{E_{q_n,1}^{ex} + E + i\Gamma_{q_n,1}^{ex}} \right) + \int_{-\infty}^{\infty} \left(\frac{\theta(E'-E_1)}{1-e^{-4\pi z(E')}} - \frac{\theta(-E'-E_1)}{1-e^{-4\pi z(-E')}} \right) \frac{dE'}{E'-E-i\Gamma_1} \right] \right\} \tag{237}$$

where $E_{q_n,1}^{ex}$ are the bound exciton energy defined by Eq. (231), $\Gamma_{q_n,1}^{ex}$ are the broadening parameters for the exciton states, E_1 is the CP energy, and Γ_1 is the broadening parameter for the continuum states.

To evaluate the integral Eq. (237) we are guided by the method we used for E_0. Focusing on the first term, we simplify it as

Reproduced with permission of the copyright owner. Further reproduction prohibited without permission.

$$\int_{-\infty}^{\infty} \frac{\theta(E'-E_1)}{1+e^{-4\pi z(E')}} \frac{dE'}{E'-E-i\Gamma_1} = \frac{1}{2}\int_{E_0}^{\infty} \frac{1+\tanh[2\pi z(E')]}{E'-E-i\Gamma_1} dE'$$
$$= -\frac{1}{2}\mathrm{Im}[\ln(E_1-E-i\Gamma)] + \int_{E_0}^{\infty} \frac{\tanh[2\pi z(E')]}{E'-E-i\Gamma_1} dE' \quad (238)$$

To evaluate the part containing $\tanh(2\pi z)$, we make the substitutions

$$x^2 = \frac{1}{z^2} = \frac{E-E_1}{R_1} \qquad \xi^2 = \frac{E_1-E-i\Gamma_1}{R_1} \quad (239)$$

Then we find

$$\int_{E_0}^{\infty} \frac{\tanh[2\pi z(E')]}{E'-E-i\Gamma_1} dE' = \int_0^{\infty} \frac{x}{x^2+\xi^2} \tanh\left(\frac{2\pi}{x}\right) dx = \frac{1}{2}\int_{-\infty}^{\infty} \frac{x}{x^2+\xi^2} \tanh\left(\frac{2\pi}{x}\right) dx \quad (240)$$

The last step is valid since the integrand is and even function of x. The poles for this expression in the upper hemisphere are at

$$x = i\xi \qquad \text{and} \qquad x = \frac{4i}{2m-1}, \qquad m = 1, 2, 3, \ldots \quad (241)$$

Thus, integrating Eq. (240) along the real axis and half-circle in the upper half plane,

Reproduced with permission of the copyright owner. Further reproduction prohibited without permission.

$$\int_{E_0}^{\infty} \frac{\tanh[\pi z(E')]}{E' - E - i\Gamma_0} dE' = \pi \tan\left(\frac{\pi}{\xi}\right) - \sum_{q_n=1}^{\infty} \frac{2}{q_n^3} \frac{1}{\xi^2 - q_n^{-2}} \tag{242}$$

The rest of the analysis follows exactly as for the E_1 transition with the final result for the E_1 transition contribution to the dielectric function of

$$\tilde{\varepsilon}_{E_1}^{CP}(E) = \frac{C_1}{E^2} \left[\sum_{q_n=1}^{\infty} \begin{Bmatrix} gb_{q_n}[\xi(E + i\Gamma_{q_n}^{ex})] + gb_{q_n}[\xi(-E - i\Gamma_{q_n}^{ex})] \\ -gb_{q_n}[\xi(i\Gamma_{q_n}^{ex})] - gb_{q_n}[\xi(-i\Gamma_{q_n}^{ex})] \end{Bmatrix} \\ + gu[\xi(E + i\Gamma_1)] + gu[\xi(-E - i\Gamma_1)] - gu[\xi(i\Gamma_1)] - gu[\xi(-i\Gamma_1)] \right] \tag{243}$$

where now,

$$\begin{aligned} \xi^2(X) &= \frac{E_1 - X}{R_1} \\ gb_{q_n}(\xi) &= \frac{8}{2q_n - 1} \frac{1}{\xi^2 - 1/(2q_n - 1)^2} \\ gu(\xi) &= -\ln(4\xi^2) + \pi \tan\left(\frac{\pi}{2\xi}\right) - \sum_{q_n=1}^{\infty} \frac{4}{2q_n - 1} \frac{1}{\xi^2 - 1/(2q_n - 1)^2} \end{aligned} \tag{244}$$

with gb corresponding to the bound excitonic states and gu to the unbound band to band continuum excitonic states (BBCE).

Reproduced with permission of the copyright owner. Further reproduction prohibited without permission.

Like Eq. (223), Eq. (243) has the properties one expects for the dielectric function as discussed the section 1.6.7. The real part is even, the odd part is odd, there are no singularities in the upper half plane, and of course it satisfies the KK relation. The imaginary part of Eq. (243) does have one singularity along the real energy axis at $E = 0$. This singularity at $E = 0$ goes as 1/E and thus corresponds to a DC conductivity as discussed in the paragraph after Eq. (195) and given in Eq. (94). It results from the Lorentzian broadening in that at zero energy there is still a small probability of producing transitions. This singularity and others like it will be discussed below in section 1.7.6.

The first and second derivatives of Eq. (223) can be written as

$$\frac{d\left[\tilde{\varepsilon}_{E_1^{CP}}(E)\right]}{dE} = \frac{-2}{E}\tilde{\varepsilon}_{E_1^{CP}}(E) + \frac{C_1}{E^2 R_1}\left\{\begin{aligned}&\sum_{q_n=1}^{\infty}\frac{8}{2q_n-1}\left[\frac{1}{\left(\xi_{b+}^2-\frac{1}{(2q_n-1)^2}\right)^2}-\frac{1}{\left(\xi_{b-}^2-\frac{1}{(2q_n-1)^2}\right)^2}\right]\\&+\frac{\pi^2}{2}\left[\frac{\sec^2\left(\frac{\pi}{2\xi_{u+}}\right)}{\xi_{u+}^4}-\frac{\sec^2\left(\frac{\pi}{2\xi_{u-}}\right)}{\xi_{u-}^4}\right]+\frac{1}{\xi_{u+}^2}-\frac{1}{\xi_{u-}^2}\\&-\sum_{q_n=1}^{\infty}\frac{4}{2q_n-1}\left[\frac{1}{\left(\xi_{b+}^2-\frac{1}{(2q_n-1)^2}\right)^2}-\frac{1}{\left(\xi_{b-}^2-\frac{1}{(2q_n-1)^2}\right)^2}\right]\end{aligned}\right\} \quad (245)$$

and

Reproduced with permission of the copyright owner. Further reproduction prohibited without permission.

$$\frac{d^2\left[\tilde{\varepsilon}_{E_1}^{CP}(E)\right]}{dE^2}=\frac{-2}{E^2}\tilde{\varepsilon}_{E_1}^{CP}(E)-\frac{4}{E}\frac{d\left[\tilde{\varepsilon}_{E_1}^{CP}(E)\right]}{dE}$$

$$+\frac{A}{E^2R^2}\left\{\begin{array}{l}\displaystyle\sum_{q_n=1}^{\infty}\frac{16}{2q_n-1}\left[\frac{1}{\left(\xi_{b+}^2-\frac{1}{(2q_n-1)^2}\right)^3}+\frac{1}{\left(\xi_{b-}^2-\frac{1}{(2q_n-1)^2}\right)^3}\right]\\ \displaystyle+\pi^2\left[\frac{\sec^2\left(\frac{\pi}{2\xi_{u+}}\right)}{\xi_{u+}^6}\left(\frac{\pi\tan\left(\frac{\pi}{2\xi_{u+}}\right)}{2\xi_{u+}^2}+1\right)+\frac{\sec^2\left(\frac{\pi}{2\xi_{u-}}\right)}{\xi_{u-}^6}\left(\frac{\pi\tan\left(\frac{\pi}{2\xi_{u-}}\right)}{2\xi_{u-}^2}+1\right)\right]\\ \displaystyle+\frac{1}{\xi_{u+}^4}+\frac{1}{\xi_{u-}^4}-\sum_{q_n=1}^{\infty}\frac{8}{2q_n-1}\left[\frac{1}{\left(\xi_{u+}^2-\frac{1}{(2q_n-1)^2}\right)^3}+\frac{1}{\left(\xi_{u-}^2-\frac{1}{(2q_n-1)^2}\right)^3}\right]\end{array}\right\} \quad (246)$$

where

$$\begin{aligned}\xi_{b+}&=\xi(E+i\Gamma_b)\\ \xi_{b-}&=\xi(-E-i\Gamma_b)\\ \xi_{u+}&=\xi(E+i\Gamma_u)\\ \xi_{u-}&=\xi(-E-i\Gamma_u)\end{aligned} \quad (247)$$

The $E_1+\Delta_1$ feature has also been described by broadened excitonic and BBCE components, with parameters similar to those used for the E_1 feature, i.e. Eq. (243) with

Reproduced with permission of the copyright owner. Further reproduction prohibited without permission.

$$\tilde{\varepsilon}_{E_1^{CP}}(E) \rightarrow \tilde{\varepsilon}_{E_1^{CP}+\Delta_1}(E), C_1 \rightarrow C_2, E_1 \rightarrow E_1+\Delta_1, R_1 \rightarrow R_{1\Delta},$$

$$\Gamma_{q_n}^{ex} \rightarrow \Gamma_{q_n,\Delta}^{ex}, \text{and } \Gamma_1 \rightarrow \Gamma_{1\Delta} \quad (248)$$

1.7.3 Discussion of E_1 Exciton Binding Energies

We pause the development of the dielectric function model, to discuss the significance of the 2D exciton at E_1 and $E_1+\Delta_1$, R_1. Fits based on our model (presented in section 1.8.1 for $Zn_{0.53}Cd_{0.47}Se$ and section 1.8.2 for $In_{0.66}Ga_{0.34}As$) have yielded the only experimental evaluation of the exciton binding energies at the E_1, $E_1+\Delta_1$ CP's, R_1, except for one study based on low temperature (10 K) reflectivity which measured R_1 for CdTe and ZnTe.[2] The contribution to the dielectric function of $\tilde{\varepsilon}_{E_1^{CP}}(E)$ and $\tilde{\varepsilon}_{E_1^{CP}+\Delta_1}(E)$ based on Eqs. (243) and (248) and the fit parameters for $Zn_{0.53}Cd_{0.47}Se$ from Table III is given in Fig. 22. The solid, dotted, and dashed lines represent the total, bound exciton, and BBCE contributions to the dielectric function. The arrows at the bottom of the figure denote the values of E_1, E_1-R_1, $E_1+\Delta_1$, and $E_1+\Delta_1$-R_1.

It is clear from the figure that the main structural features in the vicinity of the E_1, $E_1+\Delta_1$ CP's are actually due to the bound exciton, which in this case is 270 meV below these CP's. Although the excitonic nature of the E_1, $E_1+\Delta_1$ CP's is well established,[2-7] all but a few papers label the main BE features as the E_1, $E_1+\Delta_1$ CP energies rather than as the exciton energy.

Reproduced with permission of the copyright owner. Further reproduction prohibited without permission.

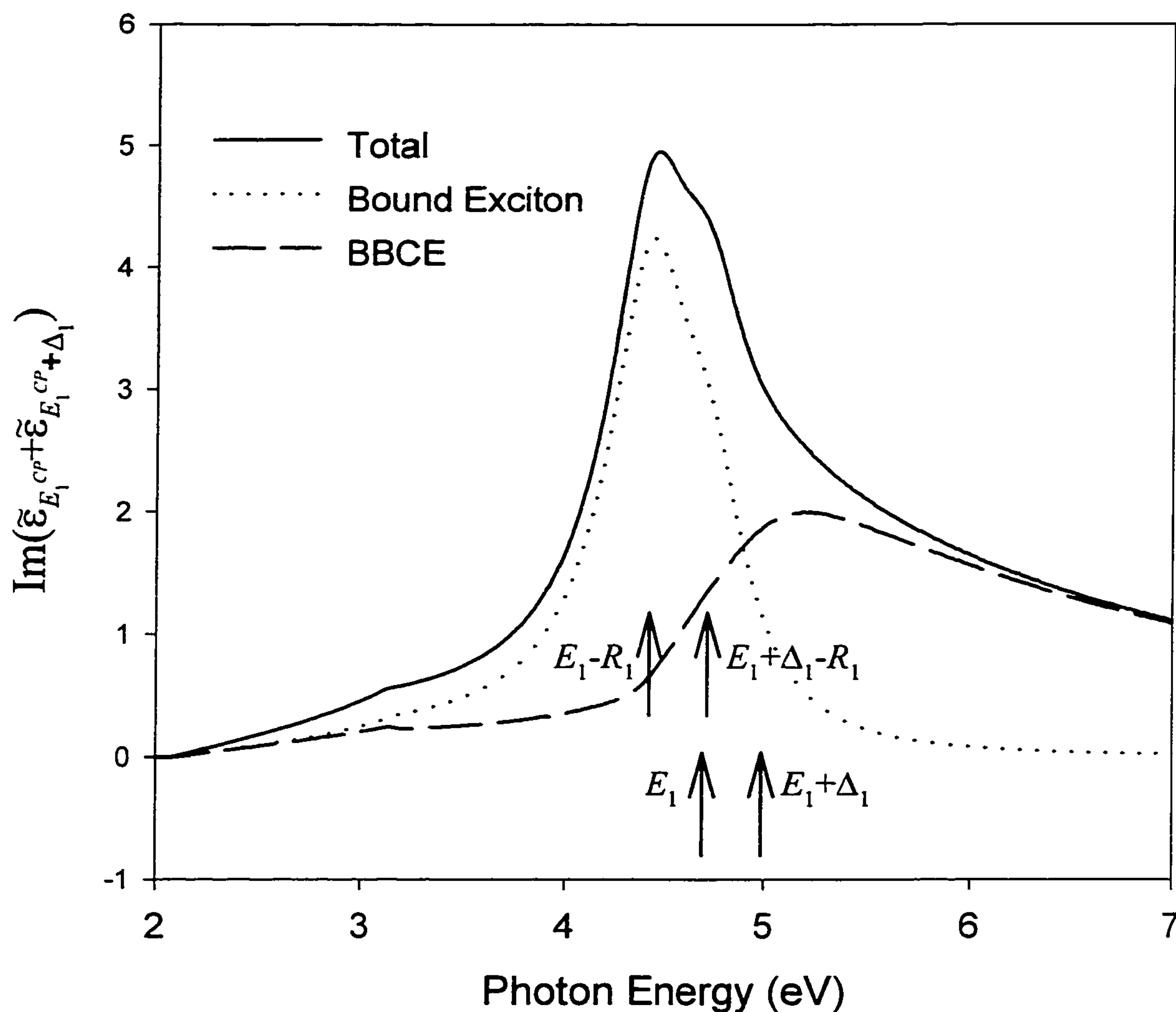

Figure 22. Contribution to the dielectric function of $\tilde{\varepsilon}_{E_1^{CP}}(E)$ and $\tilde{\varepsilon}_{E_1^{CP}+\Delta_1}(E)$ based on Eqs. (243) and (248) and the fit parameters for $Zn_{0.53}Cd_{0.47}Se$ from Table xxx. The solid, dotted, and dashed lines represent the total, bound exciton, and BBCE contributions to the dielectric function. The arrows at the bottom of the figure denote the values of E_1, E_1-R_1, E_1+Δ_1, and E_1+Δ_1-R_1.

Reproduced with permission of the copyright owner. Further reproduction prohibited without permission.

To verify the validity of our experimentally determined values of R_1, we can use a simple three-band **k•p** as pointed out by Kane.[69] (Basic **k•p** theory was discussed in section 1.6.2.) Due to symmetry, there is no **k•p** interaction between the lowest lying conduction band and the highest lying valence band along the [111] (Λ) direction (which is the reason for the large effective mass along this direction and the 2D nature of the E_1 and $E_1+\Delta_1$ CPs). The expression for the conduction and valence band effective masses perpendicular to [111] at E_1 ($m^*_{c\perp}$ and $m^*_{v\perp}$ repectively) from three-band **k•p** are

$$\begin{aligned} \frac{1}{m^*_{c\perp}} &= \frac{1}{m_0} + \frac{\hbar^2 P^2}{m_0}\left(\frac{1}{E_1} + \frac{1}{E_1+\Delta_1}\right) \\ \frac{1}{m^*_{v\perp}} &= \frac{1}{m_0} + \frac{\hbar^2 P^2}{m_0}\left(-\frac{1}{E_1}\right) \\ P &= \langle u_v | -i\hbar\nabla | u_c \rangle \end{aligned} \tag{249}$$

where m_0 is the free electron mass and u_v and u_c are the valence and conduction band wave functions, respectively. We can obtain an estimate of P by applying the three-band **k•p** model at the center of the BZ for the conduction band effective mass, m^*_c, at the Γ point.

$$\frac{1}{m^*_c} = \frac{1}{m_0} + \frac{2\hbar^2 P^2}{{m_0}^2}\left(\frac{2}{3E_0} + \frac{1}{3(E_0+\Delta_0)}\right) \tag{250}$$

Reproduced with permission of the copyright owner. Further reproduction prohibited without permission.

Using Eqs. (249) and (250), we can determine $m^*_{c\perp}$ and $m^*_{v\perp}$ from m^*_c, E_0, $E_0+\Delta_0$, E_1, and $E_1+\Delta_1$. The theory is not exact since the values of P at the Γ and L points of the BZ should be somewhat different. Also it only considers interactions between the lowest lying conduction band and the two highest lying valence bands. Finally, using Eqs. (249), (250) and (232), we can evaluate R_1 as

$$R_1 = \frac{2\mu^*_\perp e^4}{\hbar^2 \varepsilon_0^2}$$
$$\frac{1}{\mu^*_\perp} = \frac{1}{m^*_{c\perp}} - \frac{1}{m^*_{v\perp}} \qquad (251)$$

Our extracted R_1 values for $Zn_{0.53}Cd_{0.47}Se$ and $In_{0.66}Ga_{0.34}As$ and those of GaSb,[8] $Ga_{1-x}In_xAs_ySb_{1-y}$ ($x\approx0.15$, $y\approx0.15$),[9] CdTe,[10] and CdS[10] determined by others using our model are listed in Table II along with the theoretical values given by Eq. (251). It can be seen from the table that the values obtained by fitting the dielectric function to our model are in good agreement with the value predicted by Eq. (251) and show the correct general trend.

Reproduced with permission of the copyright owner. Further reproduction prohibited without permission.

Table II. Extracted R_1 values for several materials using our model and theoretical values given by Eq. (251).

Material	Experimental R_1	Theoretical R_1
$Zn_{0.53}Cd_{0.47}Se$[a]	270±50	300
CdS[b]	205±30	290
CdTe[b]	145±40	150
$In_{0.66}Ga_{0.34}As$[c]	92±20	55
GaSb[d]	32±2	25
$Ga_{1-x}In_xAs_ySb_{1-y}$[e] (x≈0.15, y≈0.15)	30±5	26

[a] determined in section 1.8.1
[b] from ref. 10
[c] determined in section 1.8.2
[d] from ref. 8
[e] from ref. 9

Our model treats the E_1 and $E_1+\Delta_1$ CPs as purely 2D. That is we have assumed the reduced interband effective mass to be infinite along the [111] direction for these CPs. Clearly this can only be an approximation. This approximation is somewhat validated by the Kane's study of the Coulomb interactions at CPs with large mass in one direction. His numerical simulations using the effective-mass approximation and the adiabatic method show a dominant peak in the dielectric function near the 2D exciton binding energy. He also finds the E_1-R_1 peak should be asymmetrical, dropping more sharply on the high energy side for a negative heavy mass (M_1) CP and more sharply on the low energy side for a positive heavy mass (M_0) CP.

Reproduced with permission of the copyright owner. Further reproduction prohibited without permission.

1.7.4 E_0' and E_2 Features

The E_0' triplet features come from transitions at the center of the BZ between the highest lying valence band and the second lowest lying conduction bands, including spin-orbit split bands, while the E_2 feature comes from transitions near the X point ($2\pi/a$ [100]) and along the Σ ([110]) direction of the BZ. Often the E_0' triplet transitions cannot be resolved in the broad CP usually observed in optical measurements and can be modeled as a single transition.

The nature of these transitions are more complicated than the E_0 and E_1 transitions in that they do not correspond to a single, well-defined CP. Therefore, following Adachi[62,70] we model these with a damped harmonic oscillator (DHO) model.

$$\tilde{\varepsilon}_{E_2^{CP}}(E) = \frac{F}{\left(1-\chi^2\right)-i\chi\gamma_2} \tag{252}$$

where F is the oscillator strength parameter, $\chi = \frac{E}{E_2}$, E_2 is the interband energy gap for the E_2 CP, and γ_2 is a nondimensional broadening parameter. For the E_0' transition, we use Eq. (252), but with $\varepsilon_{E_2^{CP}}(E) \to \varepsilon_{E_0'^{CP}}(E), F \to G$, $E_2 \to E_0'$, and $\gamma_2 \to \gamma_0'$.

Reproduced with permission of the copyright owner. Further reproduction prohibited without permission.

We note in passing that these transitions probably have a strong excitonic component owing to their high interband effective mass. The DHO we are using is similar to a simple Lorentzian as would be expected for a broadened exciton state.

1.7.5 Indirect Transitions Features

The unbroadened expression for an indirect transition's contribution to the imaginary dielectric function of in the absence of excitonic effects is given by Eq. (186). We rewrite this as

$$\varepsilon_{2,E_{ind}^{CP}}(E) = \frac{\pi D}{E^2}\left(E \mp \hbar\omega_p - E_{ind}\right)^2 \theta\left(1 - \frac{E_{ind} \pm \hbar\omega_p}{E}\right) \tag{253}$$

where

$$D = \left(\frac{2e}{m}\right)^2 \frac{\left(m_c^* m_v^*\right)^{3/2}}{4\pi^2\hbar^4} \left\| \mathbf{M}_{eR,ep}(\mathbf{k}_{0,v}, \mathbf{k}_{0,c}) \right\|^2 . \tag{254}$$

and E is the photon energy, $\hbar\omega_p$ is the energy of the phonons involved, and E_{ind} is the indirect gap energy. From here, we follow the procedure of Adachi for getting a broadened dielectric function for this expression.[70] First we note a problem with the expression in Eq. (253) in that it does not converge to 0 as $E \to \infty$. This is due to the

Reproduced with permission of the copyright owner. Further reproduction prohibited without permission.

nonphysical assumtion of parabolic bands extending to infinite energies. On must, therefore, modify the model by applying a cutoff at energy E_c to the expression in Eq. (253), obtaining

$$\varepsilon_{2,E_{ind}}(E) = \frac{\pi D}{E^2}\left(E \mp \hbar\omega_p - E_{ind}\right)^2 \theta(1 - \frac{E_g^{ID} \pm \hbar\omega_p}{E})\theta(1 - \frac{E}{E_c}). \tag{255}$$

We have assumed D is independent of energy. We make the further simplification of letting $\hbar\omega_p = 0$. Then the KK transformation of Eq. (255) is

$$\varepsilon_{1,E_{ind}}(E) = D\begin{Bmatrix} -2\left(\frac{E_{ind}}{E}\right)^2 \ln\left(\frac{E_c}{E_{ind}}\right) + \left(1 + \frac{E_{ind}}{E}\right)^2 \ln\left(\frac{E + E_c}{E + E_{ind}}\right) \\ + \left(1 - \frac{E_{ind}}{E}\right)^2 \ln\left(\frac{E - E_c}{E - E_{ind}}\right) \end{Bmatrix} \tag{256}$$

We now introduce broadening effects by introducing a phenomenologic damping by replacing E by $E+i\Gamma$. Thus the contribution of the indirect transitions to the dielectric function is given by

$$\tilde{\varepsilon}_{E_{ind}}(E) = D\begin{Bmatrix} -2\left(\frac{E_{ind}}{E + i\Gamma}\right)^2 \ln\left(\frac{E_c}{E_{ind}}\right) + \left(1 + \frac{E_{ind}}{E + i\Gamma}\right)^2 \ln\left(\frac{E + i\Gamma + E_c}{E + i\Gamma + E_{ind}}\right) \\ + \left(1 - \frac{E_{ind}}{E + i\Gamma}\right)^2 \ln\left(\frac{E + i\Gamma - E_c}{E + i\Gamma - E_{ind}}\right) \end{Bmatrix} \tag{257}$$

Reproduced with permission of the copyright owner. Further reproduction prohibited without permission.

Equation (257) is not as carefully derived as our expressions for the E_0 and E_1 transitions. Excitonic effects have been neglected; however, since we are not concerned with indirect gap semiconductors, we have not observed this structure anyway. The broadening is phenomenological and approximates Lorentzian broadening. Equation (257) does incorporate the proper symmetry of the dielectric function [Eq. (195)] and is obeys the KK relation. In addition as $\Gamma \rightarrow 0$. the imaginary part of Eq. (257) agrees exactly with Eq. (255). Also, one should be careful with this expression to make sure that it does not introduce unwanted structure at E_c, that is that it is broad enough to not give structure at E_c.

1.7.6 Total Dielectric Function/Other Considerations

The model presented above can be used to fit the experimental dispersion of $\varepsilon(E)$ over the entire range of measurement presented in this document. The total dielectric function was found by summing the expressions given in the previous four sections, i.e., Eqs. (223), (243), (252), and (208). A constant, $\varepsilon_{1\infty}$, was added to the real part of the dielectric function to account for the vacuum plus contributions from higher-lying energy gaps. The various strength parameters (A, B, ...), bandgap energies, and exciton binding energies were used as adjustable constants for the calculation of both $\varepsilon_1(E)$ and $\varepsilon_2(E)$. That is

Reproduced with permission of the copyright owner. Further reproduction prohibited without permission.

$$\tilde{\varepsilon}(E) = \tilde{\varepsilon}_{E_0^{CP}}(E) + \tilde{\varepsilon}_{E_0^{CP}+\Delta_0}(E) + \tilde{\varepsilon}_{E_{ind}^{CP}}(E) + \tilde{\varepsilon}_{E_1^{CP}}(E) + \tilde{\varepsilon}_{E_1^{CP}+\Delta_1}(E) + \tilde{\varepsilon}_{E_2^{CP}}(E) + \tilde{\varepsilon}_{E_0'^{CP}}(E) + \varepsilon_{1\infty} \quad (258)$$

After initial fitting to the data, it was noted that model $\varepsilon_2(E)$ had a small but significant value below the E_0 gap. This is due to the fact that the broadening of the various CPs is not exactly as we have assumed, that is Lorentzian. In particular we note that broadening terms tend to increase for higher energies because there are more decay channels for higher energy states.

For the high bandgap (2.08 eV) $Zn_{0.53}Cd_{0.47}Se$, this problem was relieved by introducing a simple linear cutoff for the low energy tail (well below the CP) for the E_{ind}, E_1, $E_1+\Delta_1$, and E_2 contributions to ε_2. That is a corrected imaginary dielectric $\varepsilon_{2,co}$ was calculated using

$$\varepsilon_{2,co}(E) = \varepsilon_2(E)\frac{E - E_0}{E_{co} - E_0} \quad (259)$$

where E_{co} is the cutoff energy and E_0 is the direct bandgap. ε_1 was corrected by a numerical KK analysis of Eq. (259).

For the low bandgap InGaAs (0.612 eV), The singular terms at E=0 in the expressions for ε_2 at E_0, $E_0+\Delta_0$, $E_1$and $E_1+\Delta_1$ [Eqs. (223) and (243)] made the above procedure untenable. In this case, we simply subtracted off the $1/E$ singularity from the imaginary parts of

Reproduced with permission of the copyright owner. Further reproduction prohibited without permission.

these terms. By examining these equations at E=0, one can find real expressions for the singularities to be subtracted as follows.

$$E_0: \qquad \varepsilon_{2,s}(E)=\frac{A}{E}\left\{\begin{array}{l}\dfrac{32\Gamma_0 n^3 R(E_0 n^2-R)}{\left[\left(E_0^2 n^2-R\right)^2+\Gamma_0^2 n^4\right]^2}+\dfrac{4\Gamma_0}{E_0^2+\Gamma_0^2} \\ +2\pi^2 R\,\mathrm{Im}\left[\dfrac{\xi(i\Gamma_0)\left(1+\cot^2\left[\dfrac{\pi}{\xi(i\Gamma_0)}\right]\right)}{\left(E_0-i\Gamma_0\right)^2}\right]\end{array}\right\} \tag{260a}$$

$$E_1: \qquad \varepsilon_{2,s}(E)=\frac{C_1}{E}\left\{\begin{array}{l}\dfrac{64\Gamma_1 R_1(2n-1)^3\left[E_1(2n-1)^2-R_1\right]}{\left[\left(E_1^2(2n-1)^2-R_1\right)^2+\Gamma_1^2(2n-1)^4\right]^2} \\ +\dfrac{4\Gamma_1}{E_1^2+\Gamma_1^2}+\dfrac{\pi^2}{R}\mathrm{Im}\left[\dfrac{1+\tan^2\left[\dfrac{\pi}{\xi(i\Gamma_1)}\right]}{\xi(i\Gamma_1)^{3/2}}\right]\end{array}\right\} \tag{260b}$$

and corresponding expressions for the spin orbit split components. We note that the KK relation tells us that subtracting a term proportional to $1/E$ from ε_2 has no effect on ε_1, so after this subtraction, the expressions are still KK consistent.

As a final note, we discuss how the effects of a Burstien-Moss (BM) shift of the optical absorption edge due to heavy doping can be modeled in our formalism. For degenerately

Reproduced with permission of the copyright owner. Further reproduction prohibited without permission.

doped semiconductors, the optical absorption edge moves to higher energy due to the filling of states near the band edge. More will be said about BM shifts the section 1.8.2. For now, we simply wish to note that since this effect is simply the filling of the band to some Fermi level, the shifted imaginary dielectric function $\varepsilon_{2,BM}(E)$ should be simply a Fermi function times $\varepsilon_2(E)$ for doped material

$$\varepsilon_{2,BM}(E) = \varepsilon_2(E)\frac{1}{1+e^{(E_F-E)/k_BT}} \tag{261}$$

where k_B is the Boltzman constant, E_F is the Fermi energy, and T is the temperature. As will be seen later, when we used this to fit the dielectric function, we had to use a temperature much higher than the measurement temperature (room temperature). A better procedure would be to introduce Lorentzian (or Gaussian) broadening into the expression for the unbroadened dielectric function times the Fermi function; however, this proved too difficult to do analytically. In addition, the dopants should act as scattering centers causing mixing of states of slightly different **k**. This would thus allow slightly indirect transitions at the absorption edge, which would broaden the feature somewhat. We were also unable to obtain an analytic expression for the ε_1 corresponding to Eq. (261); however, the BBCE lineshape without an exciton could be made to closely resemble it.

Equation (261) neglects the reduction of exciton binding energy introduced by Coulomb screening by the free carriers. The free carriers should increase the static dielectric

Reproduced with permission of the copyright owner. Further reproduction prohibited without permission.

function and thus decrease the exciton binding energy [in accordance with Eqs. (205) and (232)]. For the exciton at E_0, this effect will be hard to observe since the lineshape is dominated by Fermi filling as given by Eq. (261). For higher lying transitions, such as the E_1, E_1+Δ_1 doublet, the reduction of the exciton binding energy will change the lineshape. In addition, the dopants can act as scattering centers and thus increase the contribution of indirect transitions to the dielectric function as well as the broadening parameters. While all of these effects should produce changes in the dielectric function, the Fermi filling (BM effect) was the most noticeable effect in the $In_{0.66}Ga_{0.34}As$ samples we measured.

1.8 Experimental Results

For this thesis two zincblende type crystals ($Zn_{0.53}Cd_{0.47}Se$ lattice matched to InP and *n*- and *p*-type $In_{0.66}Ga_{0.34}As$ grown on InP) were measured by spectral ellipsometry and modeled according to the procedures laid out in the preceding sections.

1.8.1 $Zn_{0.53}Cd_{0.47}Se$ Lattice Matched to InP

Spectral ellipsometry at 300 K, in the range 0.8-5.5 eV was used to study the bulk and surface oxide properties of a molecular-beam-expitaxy (MBE) grown $Zn_{0.53}Cd_{0.47}Se$/InP film (≈ 1 μm thick). We observed the direct gap E_0, which exhibits a well defined excitonic structure, its spin orbit split component E_0+Δ_0, as well as the spin-orbit split E_1,

Reproduced with permission of the copyright owner. Further reproduction prohibited without permission.

$E_1+\Delta_1$ doublet. The experimental data over the entire measured spectral range (after oxide removal) were well fit by the model discussed in section 1.7. Because of the quality of the data and the comprehensiveness of the model from the previous section, we are able to extract several physically relevant parameters from the fit, such as bandgap energies, oscillator strengths, broadening parameters, and exciton binding energies, including the first extraction of the 2D exciton binding energy at the E_1 transition, R_1, from ellipsometric data. The influence of a native oxide on the optical properties also was investigated.

1.8.1.1 Introduction

ZnSe based semiconductor alloys are important materials from both fundamental and applied perspectives, due to their potential in the fabrication of blue-green laser devices.[71] Currently, the only reported cw blue-green laser involved ZnSe-based alloys grown nearly lattice matched to GaAs substrates, which contained a strained layer $Zn_xCd_{1-x}Se$ active region.[72] Laser diodes with lifetimes over 400 hours have been demonstrated.[73] This development has largely relied on the reduction of defect density such as stacking faults and dislocation,[74-76] which occur at the interface of GaAs and ZnSe. The degradation most likely still remains defects at the II-VI/III-V interface that propagate into the active region, aided by the presence of strain in the $Zn_xCd_{1-x}Se$ quantum well. Entirely lattice matched structures can be fabricated on InP substrates, thus possibly improving the reliability of the devices.

Reproduced with permission of the copyright owner. Further reproduction prohibited without permission.

A detailed understanding of the bulk and surface optical properties of these materials is essential in order to make the best selection. However, in spite of its significance, very little work has been done on the optical properties of $Zn_{0.53}Cd_{0.47}Se$ lattice matched to InP.[77,1] Several authors have reported ellipsometric studies on closely related materials such as ZnSe (bulk),[78,79] ZnSe/GaAs(001),[80-82] $Zn_xCd_{1-x}Se$/GaAs (001),[83-85] and zincblende CdSe.[52,83] The work by the author and collaborators (presented in more detail in this thesis) was the first ellipsometric study of $Zn_{0.53}Cd_{0.47}Se$/InP(001).[1] Fits to various models have been presented in Refs. 79-81 and 83-84. However, none of these investigations accounted for the data around the fundamental direct gap (E_0) with the correct exciton plus band-to-band Coulomb enhanced (BBCE) line shape but rather used an exciton plus a one-electron band-to-band parabolic form. Indeed, nobody used the correct exciton plus BBCE line shape to fit ellipsometric data prior to our work.[1,86] Also, in Refs. 79, 80, and 91 the E_1, $E_1+\Delta_1$ doublet was not resolved. The measurements of Refs. 80, 81, and 91 were performed without removal of the native oxide.

Spectral ellipsometry in the range 0.8-5.5 eV was used to study the bulk complex dielectric function $\varepsilon(E)$ [$= \varepsilon_1(E) + i\,\varepsilon_2(E)$] of a MBE grown $Zn_{0.53}Cd_{0.47}Se$/InP film (≈ 1 μm thick). We have investigated films both as received and after a HF etch to remove the native oxide. The experimentally measured dielectric function (after oxide removal) was fit over the entire range of measurement using a model based on the electronic energy-band structure near critical points. Excitonic and Coulomb enhancement effects were included not only at the fundamental gap E_0, but also its spin-orbit split component

Reproduced with permission of the copyright owner. Further reproduction prohibited without permission.

$E_0+\Delta_0$ as well as the spin-orbit split E_1, $E_1+\Delta_1$ doublet. In addition, the effects of the native oxide on the optical properties has been evaluated.

1.8.1.2 Experimental Details

The sample was fabricated in two Riber 2300P MBE chambers, one for II-VI growth and the other of III-V growth, connected by UHV modules. The films were grown on a not intentionally doped (NID) ($n \approx 5 \times 10^{17}$ cm^{-3}) InP buffer layer (500 Å) on an n^+-type InP(001) substrate. Details about the growth are described elsewhere.[87]

The data were taken as described in section 1.3. Several samples were measured and the best was selected for etching and detailed analysis. The sample was etched in a 10% solution of HF in H_2O, as suggested by Liu *et al.*,[88] then transferred to the instrument for measurement at three angles of incidence (65°, 70°, and 75°) under flowing N_2 as described in section 1.3.3.1.

Figure 23 shows the room-temperature ellipsometric data for (a) cos(Δ) and (b) tan(ψ) of $Zn_{0.53}Cd_{0.47}Se$/InP (oxide removed) measured at an angle of incidence of 70° in the range 0.8-5.5 eV. The large oscillations below the fundamental band gap E_0 (about 2 eV) are interference fringes. Interference effects above the band gap become negligible as the penetration depth is much less than the film thickness.

Reproduced with permission of the copyright owner. Further reproduction prohibited without permission.

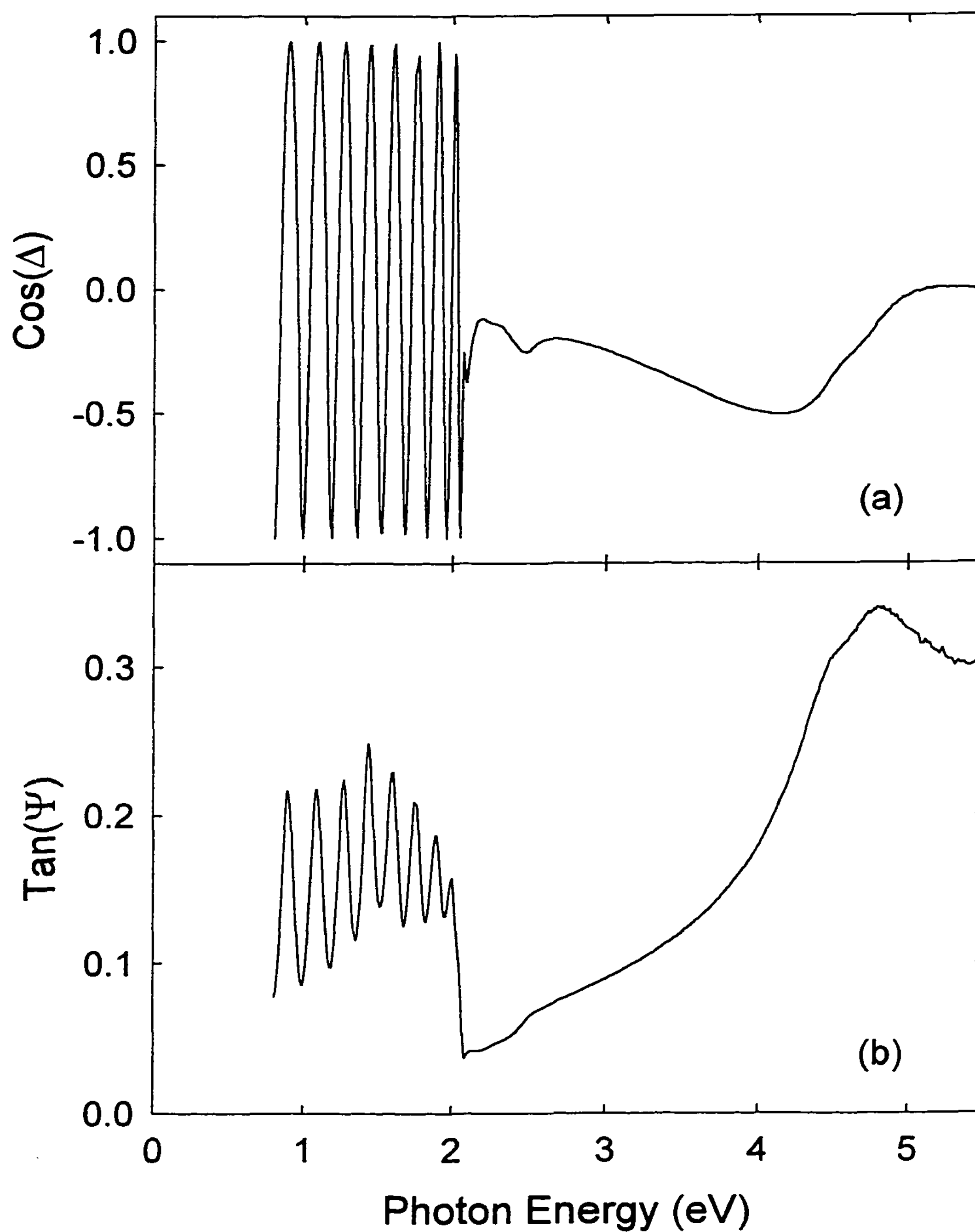

Fig. 23. The ellipsometric data (a) cos(Δ) and (b) tan(ψ) of $Zn_{0.53}Cd_{0.47}Se/InP$ (oxide removed) measured at an angle of incidence of 70° in the range 0.8-5.5 eV.

Reproduced with permission of the copyright owner. Further reproduction prohibited without permission.

The data was analyzed according to the formalism in section 1.5 in several steps. The first step was to determine the layer thickness. This value was determined from the large interference fringes below the fundamental band gap, which are periodic in the product of the refractive index times the layer thickness divided by the wavelength. While we do not know *a priori* either the index or the thickness, we begin by assuming that the index is a constant; since the thickness is also constant, this means that at least six periods of the interference fringes must be explained for the measured wavelength variation by only two parameters: a fixed index of refraction and the inferred layer thickness. This treatment was then refined by using a Sellmeier model[89] for the behavior of the index of refraction (or ε_1) in the transparent region below the band gap:

$$\varepsilon_1(E) = n_0^2 + \frac{bE_a^2}{E_a^2 - E^2}. \tag{262}$$

This appraisal adds two more free parameters that must be obtained. A least-squares analysis leads to the following best fit parameters: n_0^2 (=5.4), b (=0.81), and E_a (=2.5 eV), which yielded a thickness of 1.34±0.02 μm. Using a Philtec Instruments sectioner, the dimension of the epilayer was found to be 1.30±0.1 μm.

Next, using the multilayer model detailed in section 1.5.3, the system was modeled using this thickness to find the real and imaginary components of the dielectric function that best explained the experimental data for all three angles; this analysis was performed sequentially for each wavelength. This process was repeated for different assumed

Reproduced with permission of the copyright owner. Further reproduction prohibited without permission.

thickness, and a range of thickness was found that minimized the residual error. The final obtained thickness was 1.31 μm, in good agreement with the physical determination of the layer dimension. For the energy range at the onset of absorption, where the absorption coefficient cannot be presumed zero but the optical response still must account for the substrate, further ambiguity arose in that more than one combination of real and imaginary dielectric functions were equally consistent with the data. We chose the pair most consistent with the less ambiguous results from higher and lower energies. Although more complicated interface structures could have been analyzed, the samples discussed here were grown on InP buffer layers and no need for an extra interface layer was found.

1.8.1.3 Results and Analysis

For the purposes of discussion, we consider the band structures of ZnSe[90] and zincblende CdSe,[83] which are reproduced in Figs. 24 and 25, respectively, since the band structure of $Zn_{0.53}Cd_{0.47}Se$/InP has not been calculated. The CPs are labeled according to the notation discussed in section 1.6.2.

Reproduced with permission of the copyright owner. Further reproduction prohibited without permission.

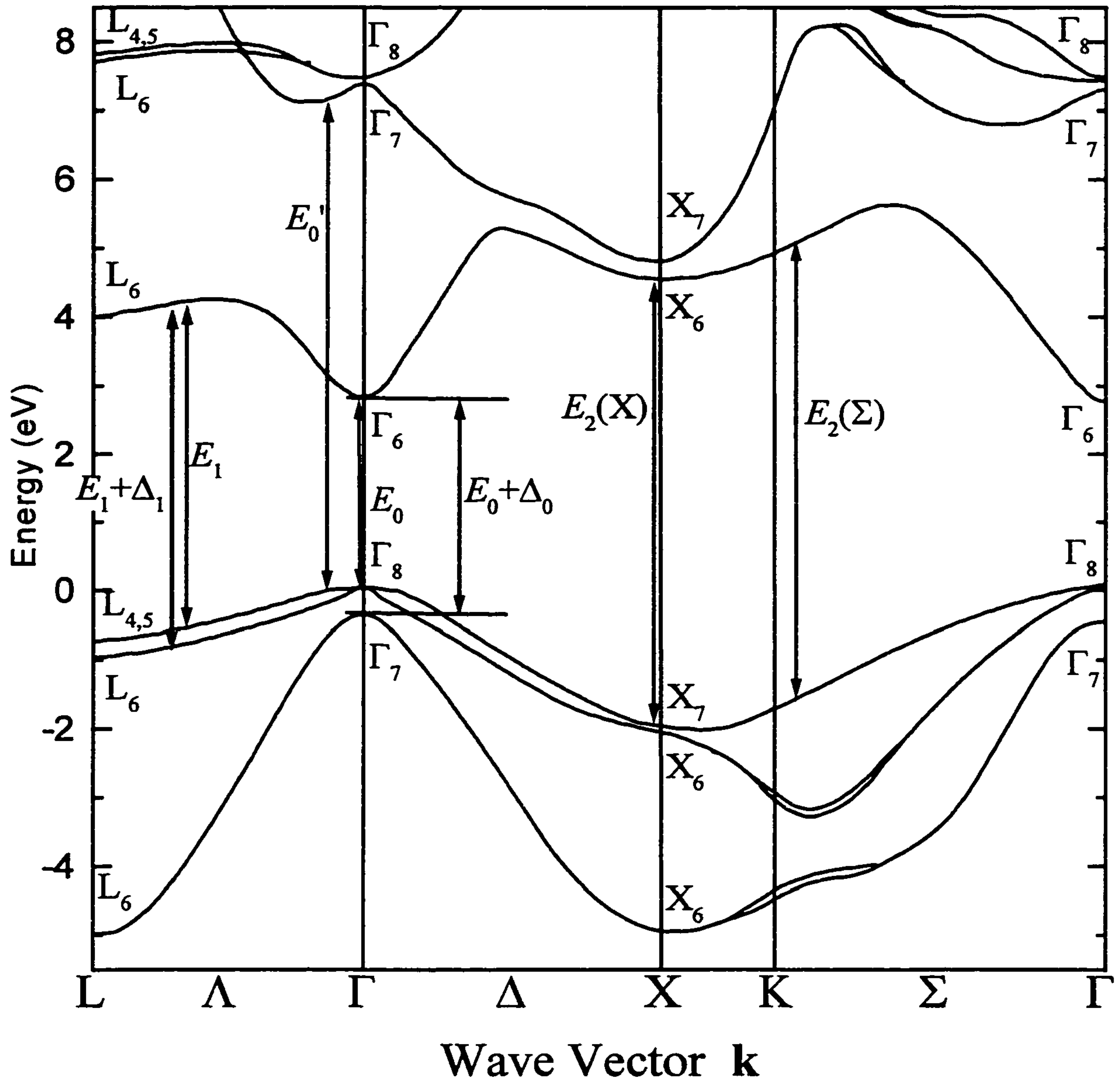

Fig. 24. Electronic energy-band structure of zincblende ZnSe calculated by nonlocal empirical pseudopotential method after Ref. 56.

Reproduced with permission of the copyright owner. Further reproduction prohibited without permission.

Fig. 25. Electronic energy-band structure of zincblende CdSe calculated by nonlocal empirical pseudopotential method, showing the main interband critical points after Ref. 83.

Reproduced with permission of the copyright owner. Further reproduction prohibited without permission.

Shown by the solid lines in Figs. 26 and 27 are values of ε_1, ε_2 and n (real), k (imaginary) components of the complex index of refraction, respectively, as a function of photon energy E obtained from an analysis of the data of Fig. 23. Displayed by the solid line in Fig. 28 is ε_2 in the vicinity of E_0. The direct gap exhibits a very well-defined excitonic structure even at 300 K. In Figs. 26 and 27 the spin-orbit split component $E_0+\Delta_0$ also is seen. There is a very well-resolved E_1, $E_1+\Delta_1$ doublet in the region around 4.5 eV.

The dashed lines in Figs. 26-28 are the fits to the model in the previous section (1.7). Specifically, we have used Eq. (258) with no contribution from the E_0' CP.

$$\tilde{\varepsilon}(E) = \tilde{\varepsilon}_{E_0^{CP}}(E) + \tilde{\varepsilon}_{E_0^{CP}+\Delta_0}(E) + \tilde{\varepsilon}_{E_{ind}^{CP}}(E) + \tilde{\varepsilon}_{E_1^{CP}}(E) + \tilde{\varepsilon}_{E_1^{CP}+\Delta_1}(E) + \tilde{\varepsilon}_{E_2^{CP}}(E) + \varepsilon_{1\infty} \tag{263}$$

The E_0' and E_2 CPs were not observed in our spectrum and should be at higher energies; however, there appears to be the tail of one or both of these transitions at the high energy side of our spectrum. Since the effect of these transitions on our spectrum is small, we used only the term for the E_2 CP and dropped the term for the E_0' CP. Although the E_2 feature was not observed, it was expected to lie between the E_2 structure of ZnSe near 6.7 eV[79] and that of zincblende CdSe near 6.0 eV.[83] The energy of E_2 was taken to be 6.35 for the fit. For the E_1 and $E_1+\Delta_1$, only a single broadening parameter Γ_1 was used for the excitonic as well as the BBCE components, and also the same effective 2D Rydberg (R_1) was used for both features.

Reproduced with permission of the copyright owner. Further reproduction prohibited without permission.

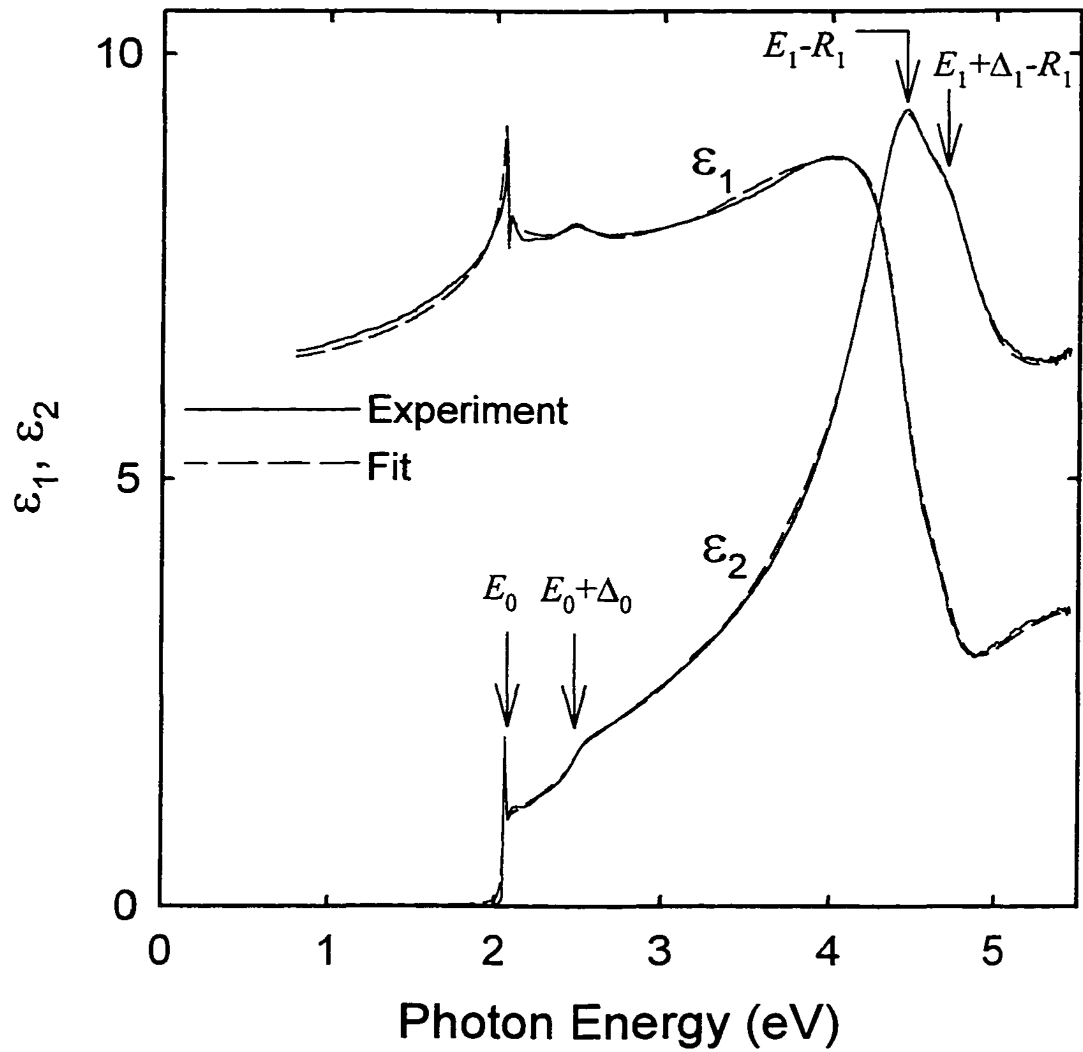

Fig. 26. The solid lines are the experimental values of ε_1 and ε_2 (oxide removed) in the range 0.8-5.5 eV. The dashed lines are the fits to Eq. (263).

Reproduced with permission of the copyright owner. Further reproduction prohibited without permission.

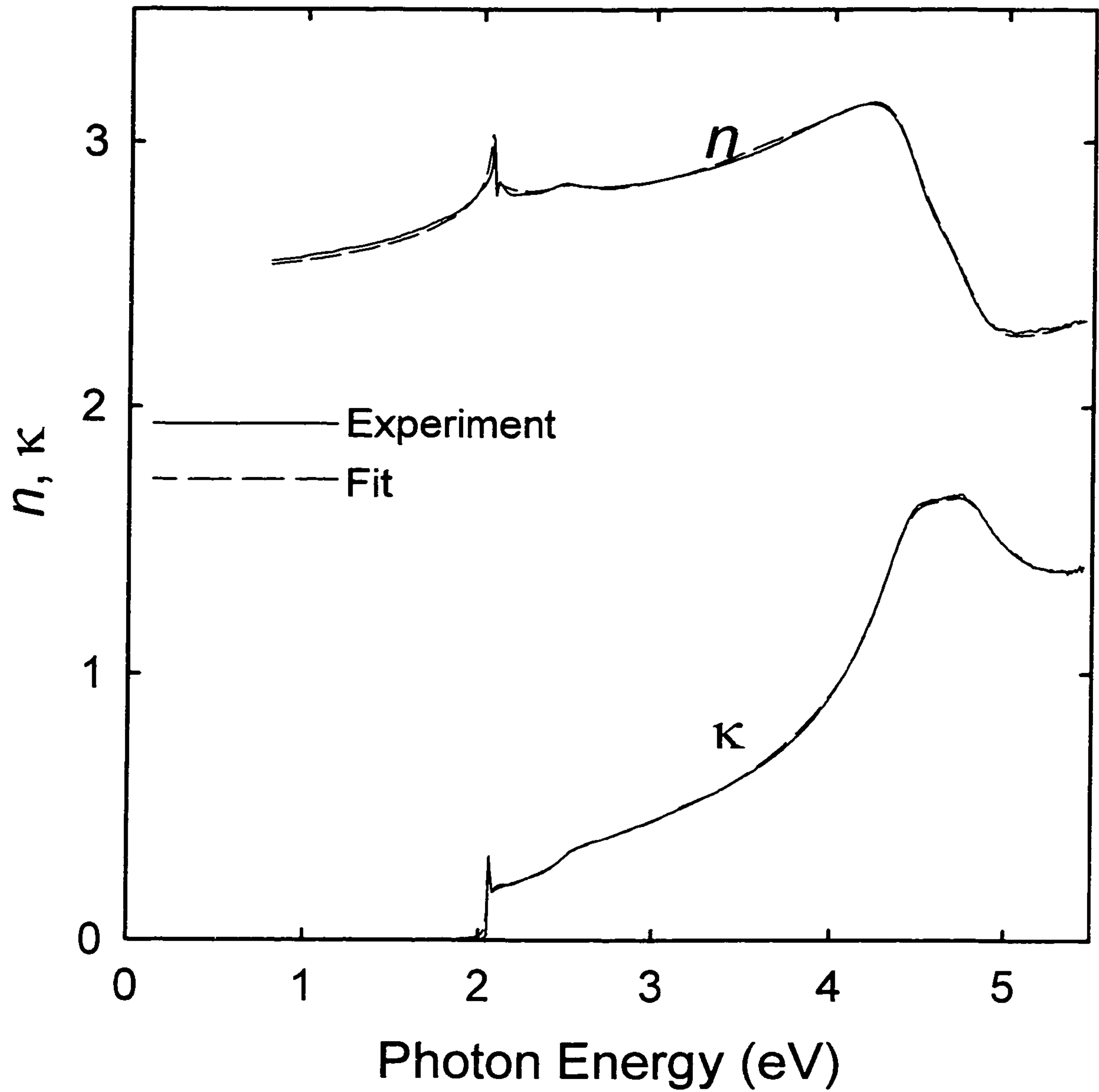

Fig. 27. The solid lines are the experimental values of *n* and κ (oxide removed) in the range 0.8-5.5 eV. The dashed lines are the fits.

Reproduced with permission of the copyright owner. Further reproduction prohibited without permission.

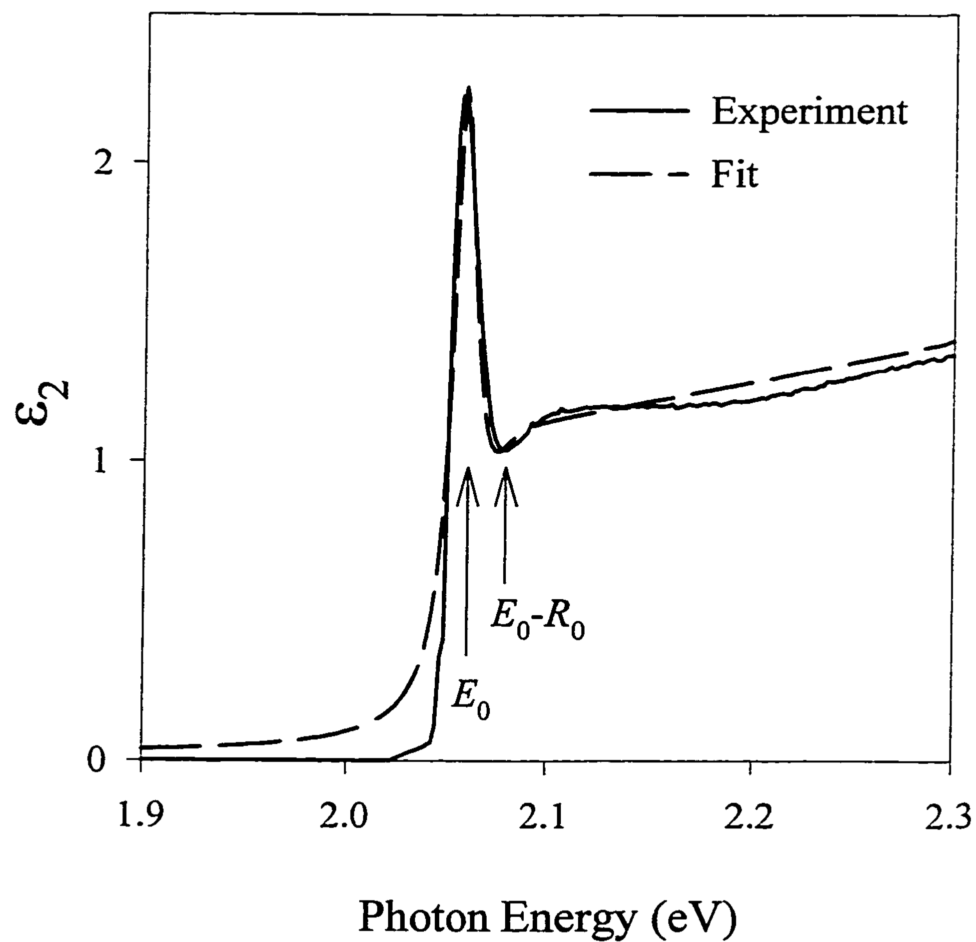

Fig. 28. The solid line is the experimental value of ε_2 (oxide removed) in the region of E_0. The dashed line is the fit Eq. (263)

Reproduced with permission of the copyright owner. Further reproduction prohibited without permission.

After the initial fitting it was noted that ε_2 still had a significant value below the E_0 gap, so a linear cutoff given by Eq. (259) was introduced for the E_{ind}, E_1, $E_1+\Delta_1$, and E_2 contributions to ε_2. The quantity ε_1 corresponding to the cutoff was obtained by numerical KK analysis of Eq. (259).

The parameters obtained by the fit are given in Table III. For comparison purposes, we have also listed in Table III the numbers for ZnSe from Ref. 79.

Table III. Material parameters used in the calculation of the optical constants of $Zn_{0.53}Cd_{0.47}Se$/InP. Values for ZnSe from Ref. 79 also are listed.

Parameter	$Zn_{0.53}Cd_{0.47}Se$	ZnSe
E_0 (eV)	2.078 ± 0.003	2.69
A (eV^2)[(a)]	0.78 ± 0.04	3.2/3.05[(b)]
R_0 (meV)	20 ± 2	17
Γ_0 (meV)	10 ± 2	30
$\Gamma_{0,ex}$ (meV)	7.5 ± 1	30
$E_0+\Delta_0$ (eV)	2.52 ± 0.02	3.10
B (eV^2)[(a)]	0.52 ± 0.05	1.6/1.52[(b)]
R_{so} (meV)	20 ± 6	17
$\Gamma_{so}/\Gamma_{so,ex}$ (meV)	70 ± 6	30
E_1-R_1 (eV)	4.42 ± 0.01	4.75
C_1 (eV^2)	14.8 ± 1	48.3[(c)]
R_1 (meV)	270 ± 50	
Γ_1 (meV)	245 ± 5	370

Reproduced with permission of the copyright owner. Further reproduction prohibited without permission.

Parameter	$Zn_{0.53}Cd_{0.47}Se$	ZnSe
$E_1+\Delta_1-R_1$ (eV)	4.72 ± 0.02	5.05
C_2 (eV^2)	9.0 ± 1	27.4[c]
E_{ind} (eV)	3.9[d]	
F_{ind}	730 ± 70	
Γ_{ind} (meV)	650 ± 70	
E_c (eV)	4.42[e]	
E_2 (eV)	6.35[d]	6.7
D_2	1/55 ± 0.15	1.6
γ_2	0.24 ± 0.07	0.2
$\varepsilon_{1\infty}$	1.53 ± 0.15	1.2

[a]Reference 79 used different amplitude constants for the BE and band-to-band features
[b]Parabolic band-to-band transition, not BBCE
[c]Exciton only; evaluated using our value of R_1
[d]Fixed
[e]Set equal to E_1-R_1

The E_1 and $E_1+\Delta_1$ features were more difficult to model than the E_0 and $E_0+\Delta_0$ due to the significant overlap and larger broadening of the E_1 and $E_1+\Delta_1$ features. In practice, only a single broadening parameter Γ_1 was used for the excitonic as well as the BBCE components for both the E_1 and $E_1+\Delta_1$, and also the same effective 2D Rydberg (R_1) was used for both features.

In order to initialize the parameters for the E_1 and $E_1+\Delta_1$ features, the first ($d\varepsilon/dE$) and second ($d^2\varepsilon/dE^2$) derivatives of the experimental dielectric function with respect to the

Reproduced with permission of the copyright owner. Further reproduction prohibited without permission.

energy were calculated numerically. These results are shown by the solid lines in Figs. 29 and 30, respectively.

The first and second derivatives of our expressions for the delectric function for the E_1 and $E_1+\Delta_1$ CPs were obtained analytically [Eqs. (245) and (246), respectively] and fit to the relevant numerical derivative of the data as displayed by the dashed lines in Figs. 29 and 30, respectively. The fit to $d^2\varepsilon/dE^2$ allowed us to determine the broadening parameter (Γ_1) and exciton energies (E_1- R_1 and $E_1+\Delta_1$- R_1) as well as the products C_1R_1 and C_2R_1. However, due to the large exciton binding energy, the BBCE contribution to $d^2\varepsilon/dE^2$ was small making it difficult to determine R_1 from this data. The quantity $d\varepsilon/dE$ is more sensitive to the Rydberg enabling us to obtain an initial value of $R_1 \approx 250$ meV. This is in reasonable agreement with a theoretical value of 300 meV for ZnSe.[2]

The first derivative spectrum (Fig. 29) shows a significant background that can be seen on the low-energy side of E_1 and also a small background on the high-energy side. As will be discussed in more detail below, these differences have been ascribed to the influence of the $\Gamma_8^v - L_6^c$ indirect band gap (E_{ind}) and the E_2 transitions, respectively.

Reproduced with permission of the copyright owner. Further reproduction prohibited without permission.

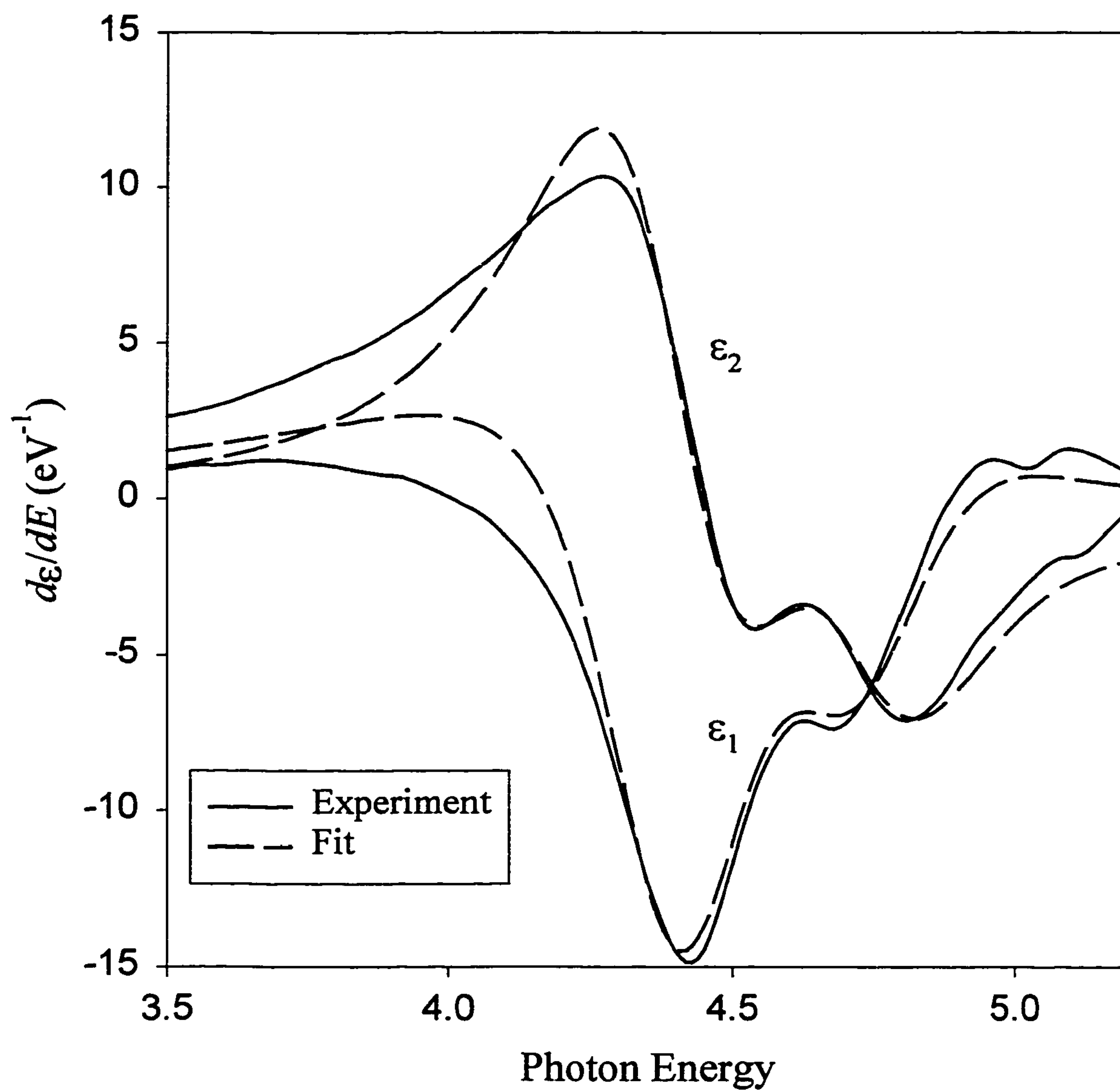

Fig. 29. The solid lines are the experimental values of $d\varepsilon_1/dE$ and $d\varepsilon_2/dE$. The dashed lines are the fits to Eq. (245).

Reproduced with permission of the copyright owner. Further reproduction prohibited without permission.

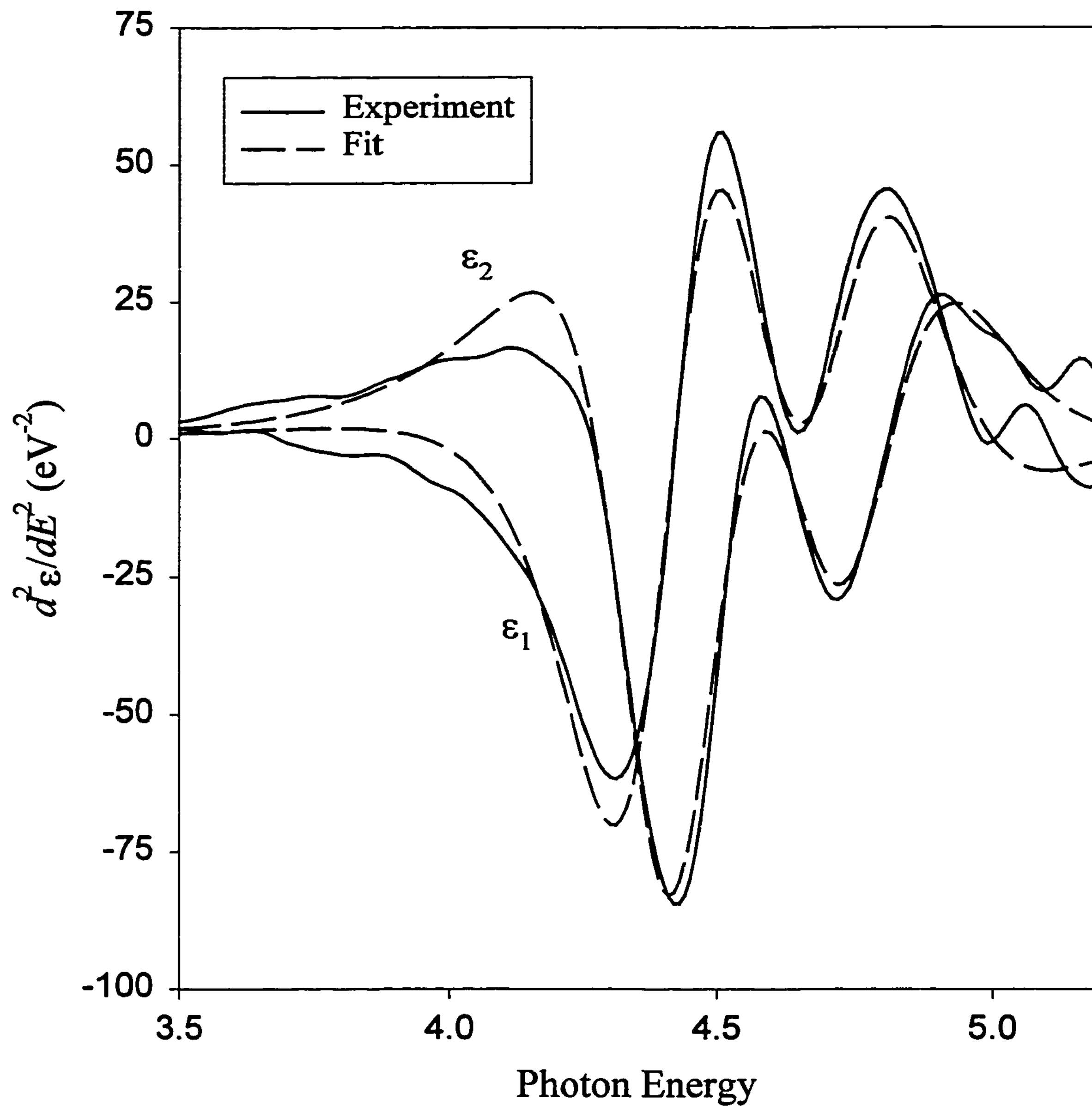

Fig. 30. The solid lines are the experimental values of $d^2\varepsilon_1/dE^2$ and $d^2\varepsilon_2/dE^2$. The dashed lines are the fits to Eq. (246).

Reproduced with permission of the copyright owner. Further reproduction prohibited without permission.

Displayed in Figs. 31 and 32 are the individual contributions to ε_1 and ε_2, respectively, of the various transitions. They were obtained from Eq. (263).

1.8.1.4 Oxide Effects

The effect of oxide formation on the optical functions also has been observed. Oxide thickness and surface roughness have a large effect on the pseudodielectric function, as discussed in section 1.5.2. The measured pseudodielectric function $\langle\tilde{\varepsilon}\rangle$ of an as-received sample (with oxide) is compared to an etched sample (without oxide) in Fig. 33. The effect of the oxide is (a) to lower $<\varepsilon_2>$ in the region around E_1, $E_1+\Delta_1$ and to increase it at lower energies and (b) to diminish $<\varepsilon_1>$ for all photon energies in our spectral range.[52]

To gain further information about the native oxide, we have taken the values of $\tilde{\varepsilon}$ (without the oxide) and added the effects of this layer by means of a three-phase model (section 1.5.2). The only relevant oxide optical constants available are for ZnO, which were employed. Shown by the solid lines in Fig. 34 are the experimental values of $\langle\tilde{\varepsilon}\rangle$ for the as received sample. The dashed lines are a least-squares fit simulation yielding a 20 Å thickness of ZnO. Lee *et al.*[85] have reported a similar oxide thickness in their study of $Zn_xCd_{1-x}Se$/GaAs. Despite the small thickness obtained for the oxide layer, it should be noted that it appears to be a very robust and stable covering, as evidenced by its relative lack of reactivity to various etchants.

Reproduced with permission of the copyright owner. Further reproduction prohibited without permission.

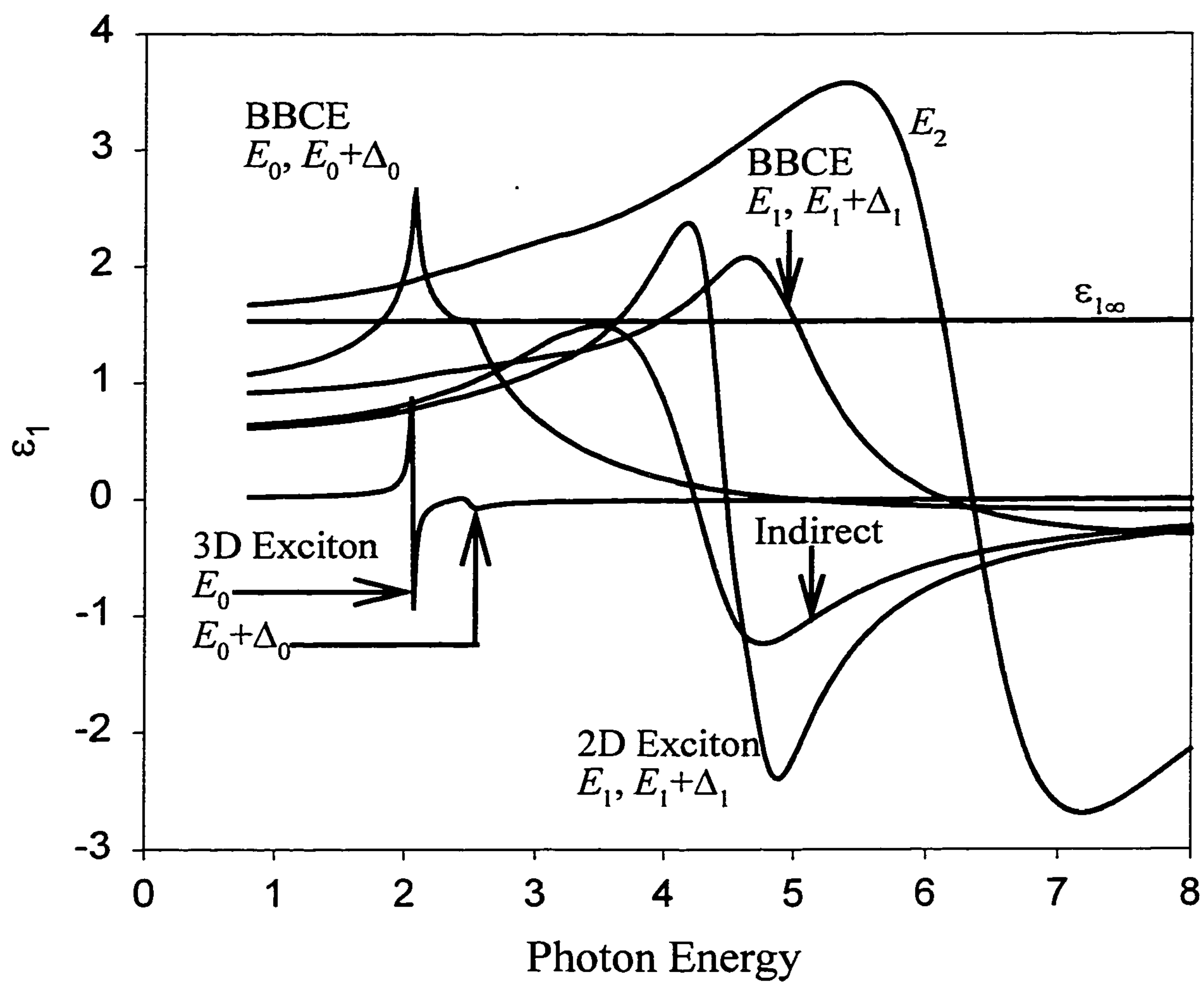

Fig. 31. Individual contributions of the various transitions to ε_1.

Reproduced with permission of the copyright owner. Further reproduction prohibited without permission.

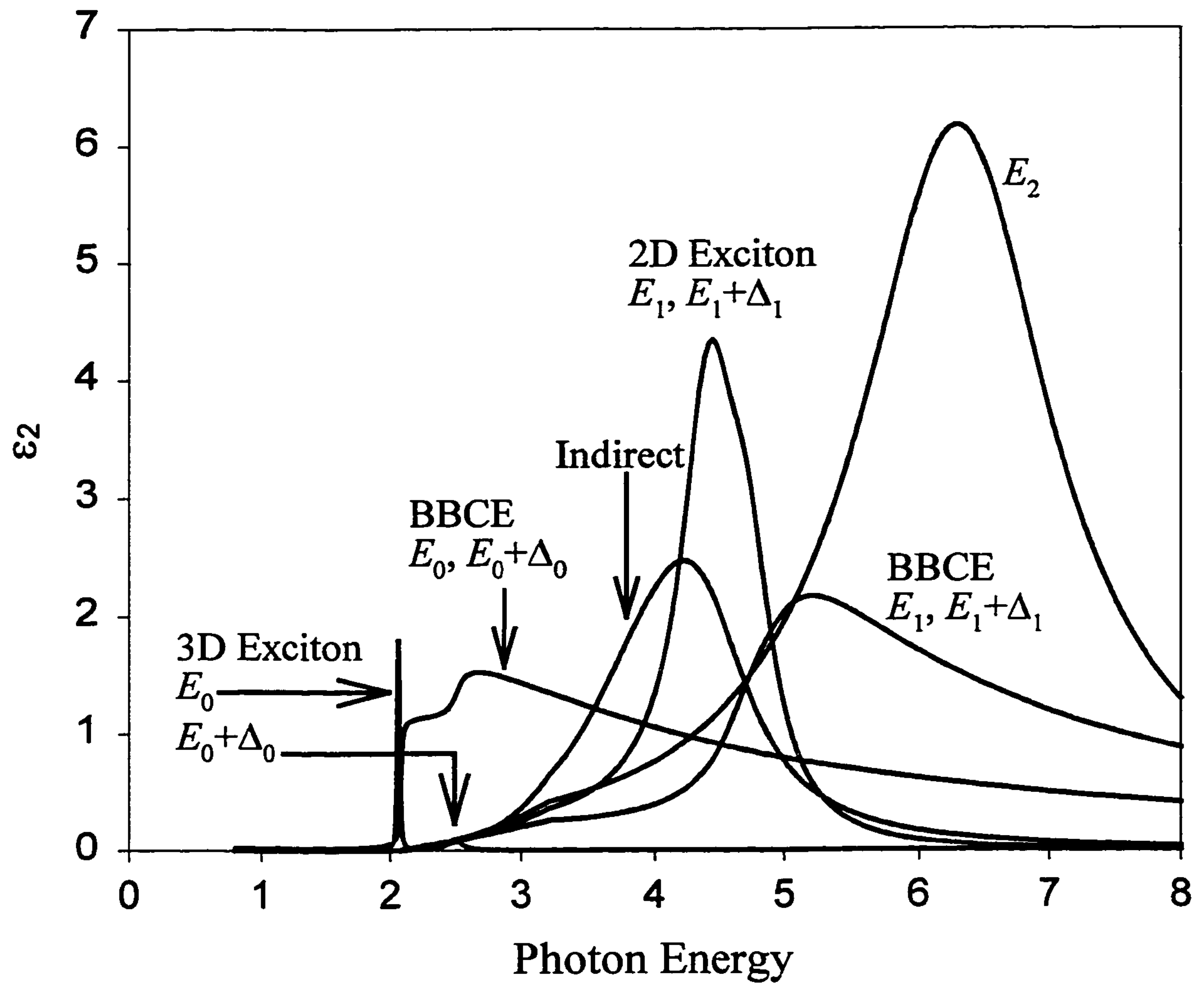

Fig. 32. Individual contributions of the various transitions to ε_2.

Reproduced with permission of the copyright owner. Further reproduction prohibited without permission.

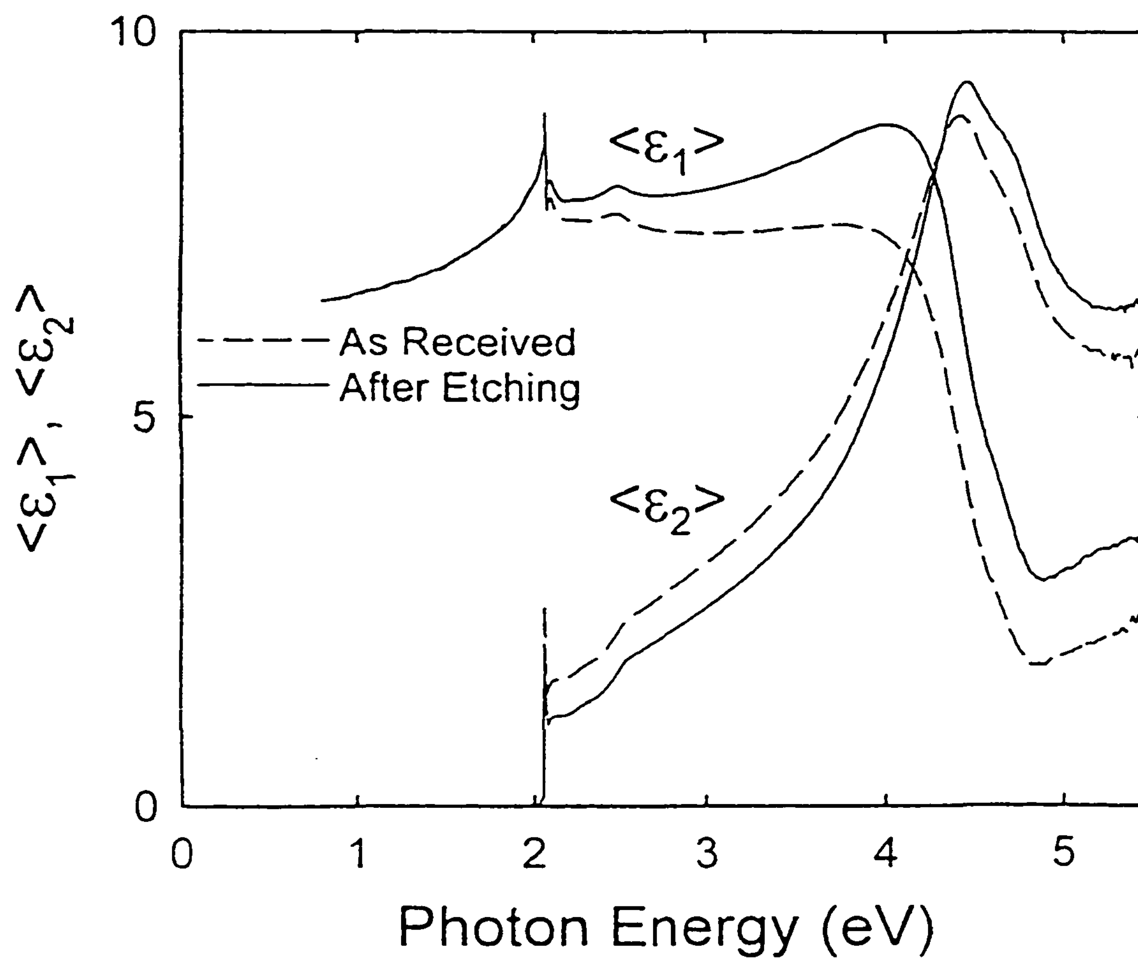

Fig. 33. The dashed lines are $<\varepsilon_1>$ and $<\varepsilon_2>$ for the as-received sample (native oxide). The solid lines are ε_1 and ε_2 after removal of the oxide.

Reproduced with permission of the copyright owner. Further reproduction prohibited without permission.

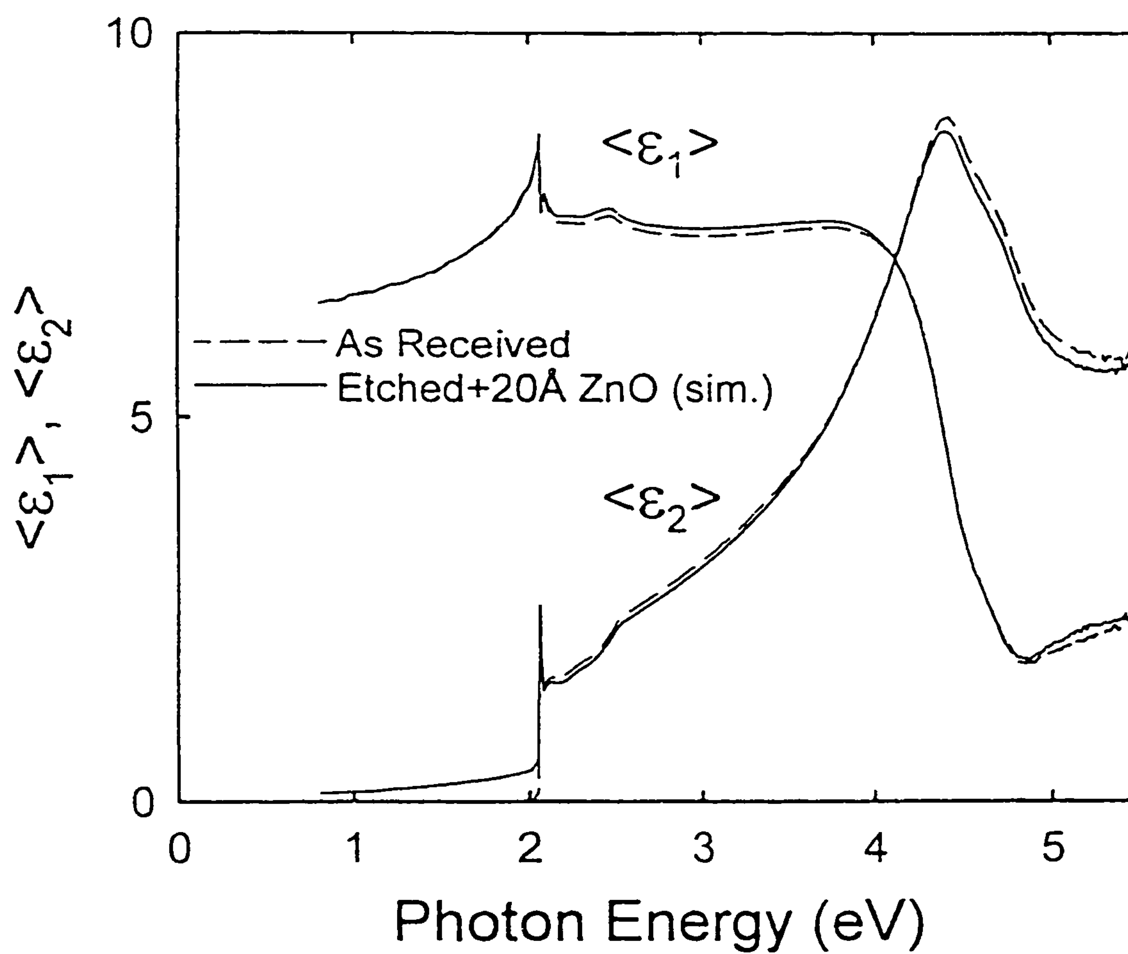

Fig. 34. The dashed lines are $<\varepsilon_1>$ and $<\varepsilon_2>$ for the as-received sample (native oxide). The solid lines are ε_1 and ε_2 after removal of the oxide.

Reproduced with permission of the copyright owner. Further reproduction prohibited without permission.

1.8.1.5 Discussion

In Fig. 26, we have the experimentally determined $\tilde{\varepsilon}(E)$ along with fits based on Eq. (258). Note there is excellent agreement over the entire spectral range of the measurement. These fits yielded the values of the relevant parameters listed in Table III. For comparison purposes we also present in Table III numbers for ZnSe from Ref. 79.

In contrast to other ellipsometric studies of related materials such as ZnSe (bulk),[78,79] ZnSe/GaAs(001),[80-82] $Zn_xCd_{1-x}Se$/GaAs(001),[83-85] and zincblende CdSe[83,91] we have used a Lorentzian broadened (a) excitonic and (b) relevant BBCE profiles for E_0, $E_0+\Delta_0$ and E_1, $E_1+\Delta_1$. This approach has enabled us to extract the relevant Rydbergs for the exciton associated with these various transitions. Although Kim and Sivananthan[81] took into account excitons for these four features in ZnSe they used only a one-electron expression for the band-to-band transitions. To improve their fit the authors of Ref. 81 added a Gaussian term to the broadening. Adachi and Taguchi[79] used only an excitonic profile for E_1, $E_1+\Delta_1$. References 79 and 81 did not extract the Rydberg R_1. In Ref. 83 the effects of the exciton at both E_0, $E_0+\Delta_0$ and E_1, $E_1+\Delta_1$ were accounted for an the basis of a Slater-Koster "contact" potential, which results in a phase shift between the real and imaginary components of the complex dielectric function and their derivatives. The discrete nature of the excitons was not considered. In Refs. 80, 84, and 85 the data were fit with a simple harmonic-oscillator model.

Reproduced with permission of the copyright owner. Further reproduction prohibited without permission.

Our value for R_0 = 20 meV (Table III) is somewhat larger than that reported for ZnSe. Based on the smaller band gap of $Zn_xCd_{1-x}Se$/InP in relation to ZnSe, one would have expected a somewhat smaller exciton binding energy. The value of $R_1 = 270 \pm 50$ meV is in good agreement with the theoretical calculation of 300 meV in Ref. 2.

The nature of the E_1, $E_1+\Delta_1$ transitions in diamond- and zincblende-type semiconductors has been the subject of considerable investigation. It is well known that these features contain not only a band-to-band component but also a strong excitonic contribution, even at room temperature.[2-7] Efforts to fit the optical and derivative optical properties with an exciton plus a one-electron band-to-band profile, without taking into account the proper BBCE form, has necessitated the addition of *ad hoc* terms, such as a Gaussian broadening (in addition to the Lorentzian),[81,92] in order to properly account for the experimental data.

In particular, our analysis has yielded the only experimental evaluation of the exciton binding energies at the E_1, $E_1+\Delta_1$ CP's, R_1, except for one study based on low temperature (10 K) reflectivity which measured R_1 for CdTe and ZnTe.[2] Our analysis shows that the features in the vicinity of the E_1, $E_1+\Delta_1$ CP's are actually due to the bound exciton, which can be several hundred meV below the these CP's. Although the excitonic nature of the E_1, $E_1+\Delta_1$ CP's is well established,[2-7] all but a few papers label the main BE features as the E_1, $E_1+\Delta_1$ CP energies rather than as the exciton energy. The extracted R_1 values for $Zn_{0.53}Cd_{0.47}Se$ and $In_{0.66}Ga_{0.34}As$ and those of GaSb,[8] $Ga_{1-x}In_xAs_ySb_{1-y}$ ($x\approx0.15$, $y\approx0.15$),[9] CdTe,[10] and CdS[10] determined by others using our

Reproduced with permission of the copyright owner. Further reproduction prohibited without permission.

model are in good agreement with effective-mass **k•p** theory as discussed in section 1.7.3.

The small feature at about 2.1 eV in the data of Fig. 28 is possibly due to an exciton logitudinal-optical phonon resonance, as discussed by Trallero-Giner *et al.*[93] It was not explicitly included in our calculation.

The broadening parameter for both the exciton and band-to-band E_0 transition is comparable to that reported by Kim and Sivananthan[81] for ZnSe data of Ref. 79. This is evidence for the high quality of our alloy sample.

In order to fit the data between E_0, $E_0+\Delta_0$ and E_1, $E_1+\Delta_1$ we added the contribution of the $\Gamma_8^v - L_6^c$ indirect transition. Although most authors have not used the $\Gamma_8^v - L_6^c$ indirect transition to fit their data for direct bandgap materials, such as ZnSe, Adachi did employ it for his analysis of InP.[70] It should be mentioned that in $Zn_{0.53}Cd_{0.47}Se$/InP the separation between E_0, $E_0+\Delta_0$ and E_1, $E_1+\Delta_1$ is about 300 meV larger than in ZnSe (see Table III). Therefore, any deficiencies in the model dielectric function, such as the assumption of parabolic bands, are more likely to appear in this material. This may also be the reason why it was necessary to add another oscillator in the region between these major spectral structures.

Reproduced with permission of the copyright owner. Further reproduction prohibited without permission.

1.8.2 *n*- and *p*-Type $In_{0.66}Ga_{0.34}As$ on InP

The complex dielectric function (ε_1 and ε_2) in the range 0.3-5.45 eV have been evaluated at 300K using spectral ellipsometry for a series of *n*-(5.7×10^{17} cm^{-3} $< n <$ 5.5×10^{19} cm^{-3}) and *p*-($6.5 \times 10^{17} < p < 5.0 \times 10^{19}$ cm^{-3}) doped relaxed $In_{0.66}Ga_{0.34}As$ grown by Metal-Organic Chemical Vapor Deposition (MOCVD) on InP (001). We have observed the fundamental absorption edge, spin-orbit split excitonic and E_1-R_1, E_1+Δ_1-R_1 doublet, and a feature corresponding to the E_0' and E_2 CPs. (All of these CPs are discussed in section 1.6.2.) The experimental data in the vicinity of the direct gap has been fit using the model of section 1.7. The intrinsic band gap of 0.612 ± 0.01 eV corresponds to an In composition of 66 ± 1 %. The Burstein-Moss (BM) shift was taken into account using a Fermi level filling factor in addition to the excitonic and BBCE terms according to Eq. (261). While the BM shift for the *p*-type samples exhibited no nonparabolic effects, the *n*-type samples had pronounced nonparabolicity at the highest doping level. These observations for the *n*-type material are in agreement with a recent bandstructure calculation based on the Full Potential Linear Augmented Plane Wave Method.[94,95] The shift of E_1-R_1, E_1+Δ_1-R_1 with doping density also was evaluated, an effect which is related to surface electric fields.

Reproduced with permission of the copyright owner. Further reproduction prohibited without permission.

1.8.2.1 Introduction

Thermophotovoltaic (TPV) generation of electricity is attracting attention due to a number of factors including advances in materials and designs, as well as a widening appreciation of the large number of applications that can be addressed using TPV-based generators. The attractions include the wide range of fuel sources and the potentially high power density outputs. One main approach to TPV generation is broad band radiation coupled with converters with bandgaps in the range 0.4-0.7 eV.[96]

Degenerately-doped (> 10^{19} cm^{-3}) *n*-type $In_xGa_{1-x}As$ possesses a number of intriguing electrical and optical properties relevant to electro-dptic devices and thermophotovoltaic devices in particular. Due to the low electron effective mass of these materials ($m^* < 0.2$) and the demonstrated ability to incorporate *n*-type dopants into the high-10^{19} cm^{-3} range, both the BM bandgap shift and plasma reflection characteristics are particularly dramatic.

Using spectral ellipsometry in the range 0.3-5.45 eV we have evaluated the complex dielectric function at room temperature for a series of *n*-(5.7×10^{17} cm^{-3} $< n < 5.5 \times 10^{19}$ cm^{-3}) and *p*-($6.5 \times 10^{17} < p < 5.0 \times 10^{19}$ cm^{-3}) doped relaxed $In_{0.66}Ga_{0.34}As$ grown by Metal-Organic Chemical Vapor Deposition (MOCVD) on InP (001). We have also observed the fundamental absorption edge, spin-orbit split excitonic and E_1-R_1, E_1+Δ_1-R_1 doublet [<111> directions of the BZ] and E_2 feature [<100> BZ edge]. The experimental data has been fit using the model of the previous section. The intrinsic band gap of 0.612 ± 0.01 eV corresponds to an In composition of 66 ± 1 %. The Burstein-Moss (BM) shift

Reproduced with permission of the copyright owner. Further reproduction prohibited without permission.

was taken into account using a Fermi level filling factor in addition to the excitonic and BBCE terms using Eq. (261). While for the p-type samples the BM shift exhibited no nonparabolic effects, the n-type samples had pronounced nonparabolicity at the highest doping level. These observations for the n-type material are in agreement with a recent bandstructure calculation based on the Full Potential Linear Augmented Plane Wave Method.[94,95] By accounting for the BBCE term we obtained the binding energy, R_1 ($\approx$ 90 meV), of the 2D exciton associated with E_1- R_1. The shift of E_1-R_1, E_1+Δ_1-R_1 with doping density also was evaluated, an effect which is related to surface electric fields.

1.8.2.2 Experimental Details

The samples used in this study were a series of n- and p-doped relaxed In0.66Ga0.34As grown by MOCVD on InP (001) substrates. The epitaxial layers were $\approx$ 1 micron thick. The carrier concentrations were determined by room temperature Hall measurements. The characteristics of the p- and n-type samples are listed in Table IV. The data in the range 0.75-5.45 eV (UV/VIS/NIR) was taken using the Instruments SA variable angle ellipsometer (described in section 1.3), while for the interval 0.3-1.0 eV (MIR) a Sentech variable angle instrument was employed (described in section 1.4). Thus there was some overlap between the two intervals.

Reproduced with permission of the copyright owner. Further reproduction prohibited without permission.

Table IV. Doping levels and fitting parameters for the fundamental absorption edge. Γ_0 was 60 meV for all samples.

Sample	Doping (x 10^{17} cm^{-3})	E_{abs} (eV)[c]	"$k_B T$" (meV)
A	6.5[a]	0.612[d]	60
B	9.4[a]	0.622	57
C	55[a]	0.658	52
D	87[a]	0.693	52
E	500[a]	0.739	44
F	5.7[b]	0.636	49
G	13[b]	0.660	55
H	28[b]	0.772	53
I	77[b]	0.833	47
J	106[b]	0.955	42
K	550[b]	1.270	50

[a] *p*-type.
[b] *n*-type.
[c] error bars of ± 0.01 eV.
[d] $E_{abs} = E_0$

The UV/VIS/NIR measurements were done with 70° incidence angle and the IR measurements were done with 60° and 70° incidence angles. The etching was done on the samples mounted on the sample stand as described in section 1.3.3.2. Several etchants were tried on these samples, including KOH/Methanol, HCl/Methanol, and HCl/water. The effectiveness of the etchant was evaluated by the strength of the imaginary dielectric function at the E_2 CP as discussed in section 1.3.3 and 1.5.2. The best procedure found consisted of four 1 second sprays of 50% concentrated HCl + 50% Methanol followed by a rinse consisting of 5 one second sprays of Methanol and 5 one second sprays of de-ionized water. After the UV/VIS/NIR measurement, the sample was transferred in the dry nitrogen atmosphere etching cell to the FTIR ellipsometer as described in section 1.4.4.2. In all cases, the inferred oxide growth during measurement (based on a three phase model applied to the UV/VIS/NIR data near E_2 before and after the FTIR run) was less than 3 Å.

Reproduced with permission of the copyright owner. Further reproduction prohibited without permission.

1.8.2.3 Results and Analysis

Displayed in Figs. 35 and 36 are the real (ε_1) and imaginary (ε_2) components of the complex dielectric function of the *p*-type InGaAs/InP samples A-E in the range 0.3-5.5 eV. Displayed in Figs. 37 and 38 are the real (ε_1) and imaginary (ε_2) components of the complex dielectric function of the *n*-type InGaAs/InP samples F-K in the range 0.3-5.5 eV. In these four figures, the dielectric function is displaced in increments of two units for clarity.

The solid lines in Figs. 39 and 40 are the experimental values of ε_2 for *p*-type samples A and E and *n*-type samples F and K, respectively, in the region of the fundamental absorption edge. Note that for the highly *n*-type samples, there is a small finite value of ε_2 (Figs. 38 and 40) and a drop off in ε_1 (Fig. 37) below ~ 0.5 eV due to free carrier absorption.

Reproduced with permission of the copyright owner. Further reproduction prohibited without permission.

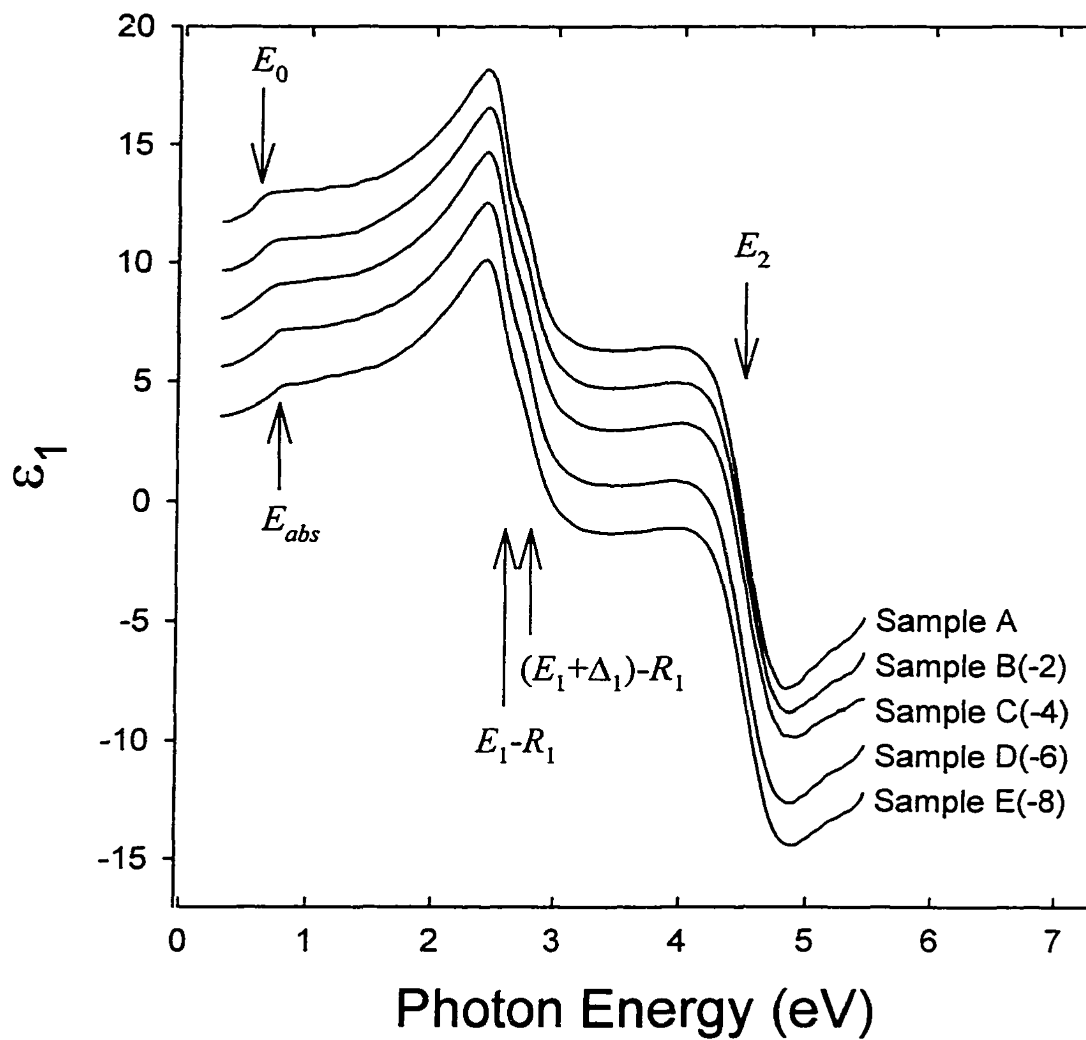

Fig. 35. Experimental values of ε_1 for *p*-type samples A-E. ε_1 for samples B, C, D, and E are displaced in increments of two units for clarity.

Reproduced with permission of the copyright owner. Further reproduction prohibited without permission.

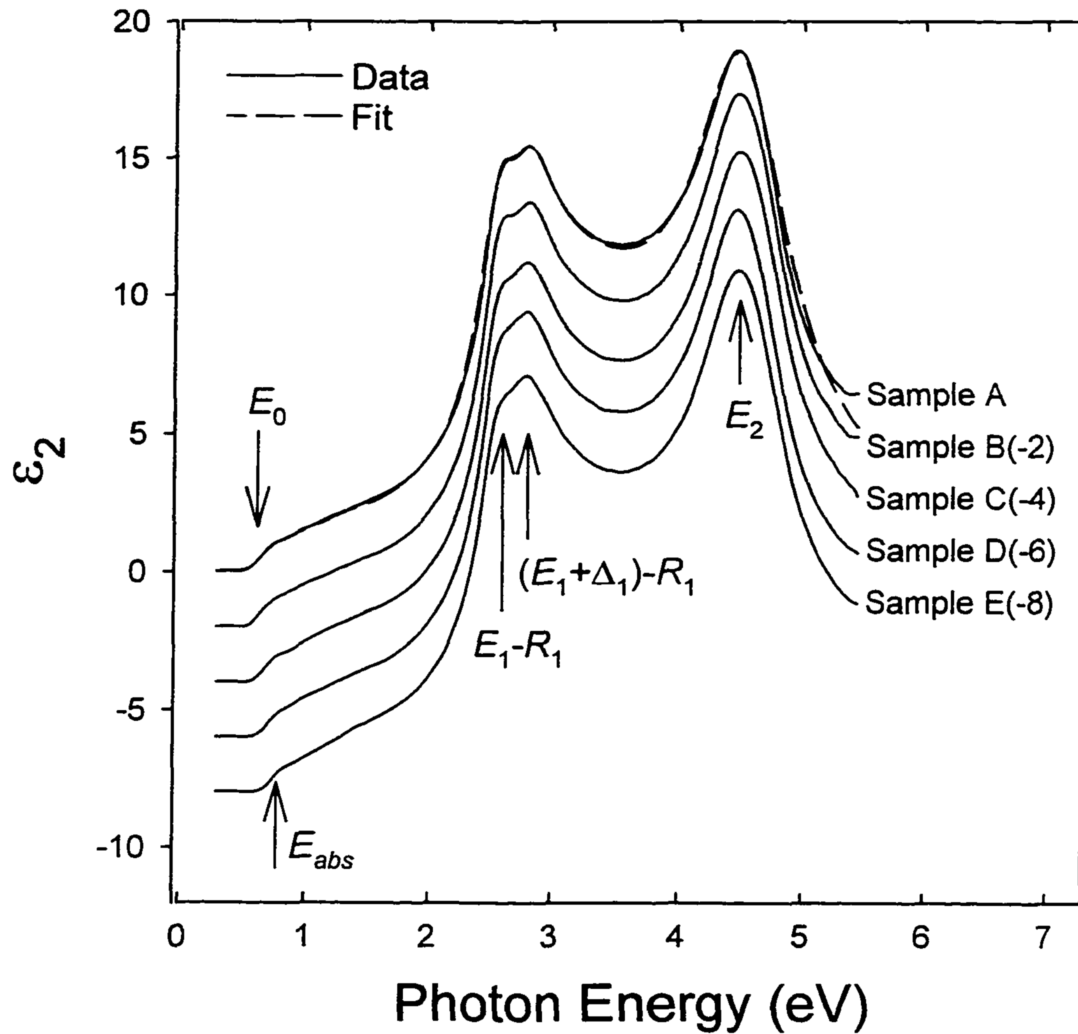

Fig. 36. Experimental values of ε_2 for *p*-type samples A-E. ε_2 for samples B, C, D, and E are displaced in increments of two units for clarity. The dashed line is a fit to sample A based on Eq. (264).

Reproduced with permission of the copyright owner. Further reproduction prohibited without permission.

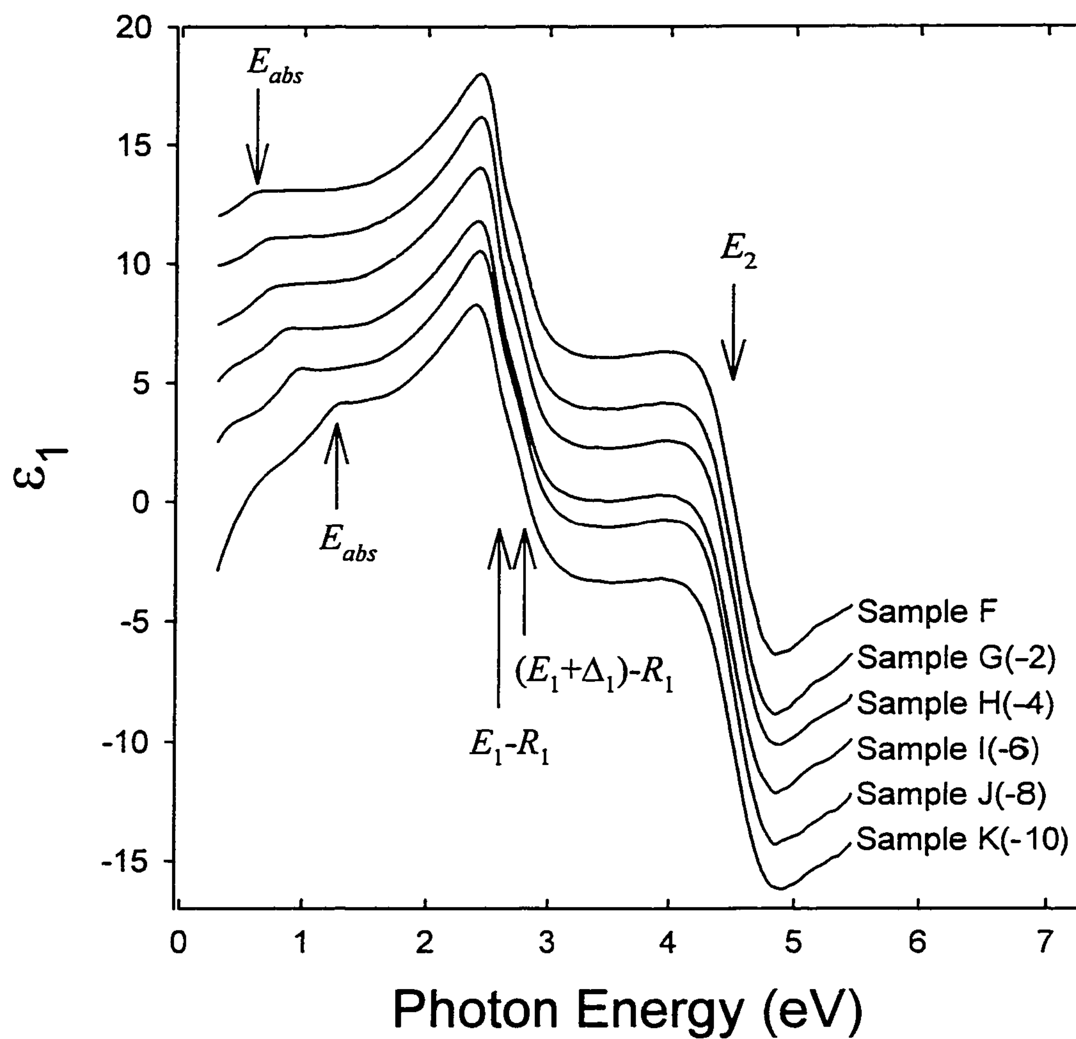

Fig. 37. Experimental values of ε_1 for n-type samples F-K. ε_1 for samples G, H, I, J, and K are displaced in increments of two units for clarity.

Reproduced with permission of the copyright owner. Further reproduction prohibited without permission.

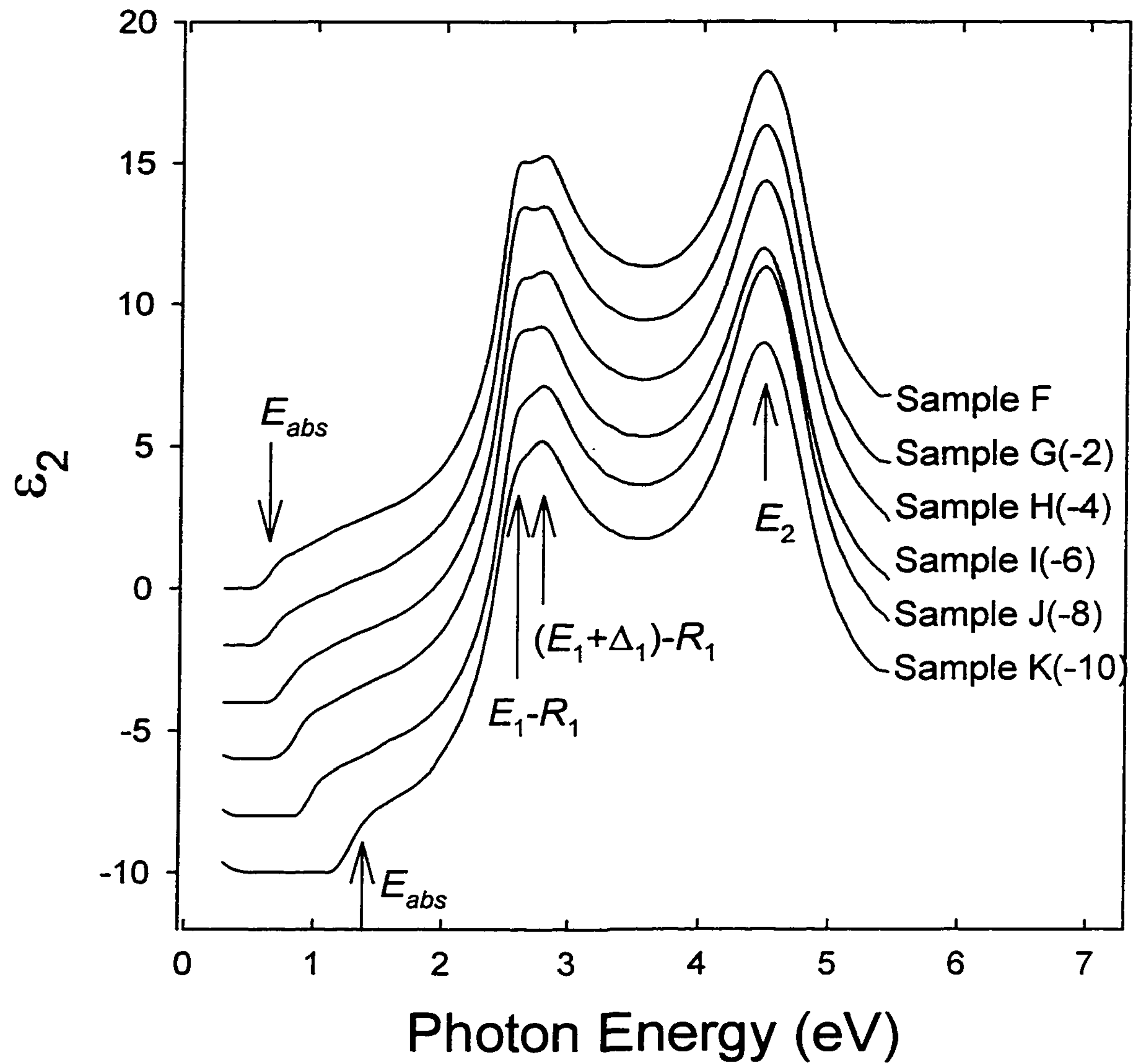

Fig. 38. Experimental values of ε_2 for *n*-type samples F-K. ε_2 for samples G, H, I, J, and K are displaced in increments of two units for clarity.

Reproduced with permission of the copyright owner. Further reproduction prohibited without permission.

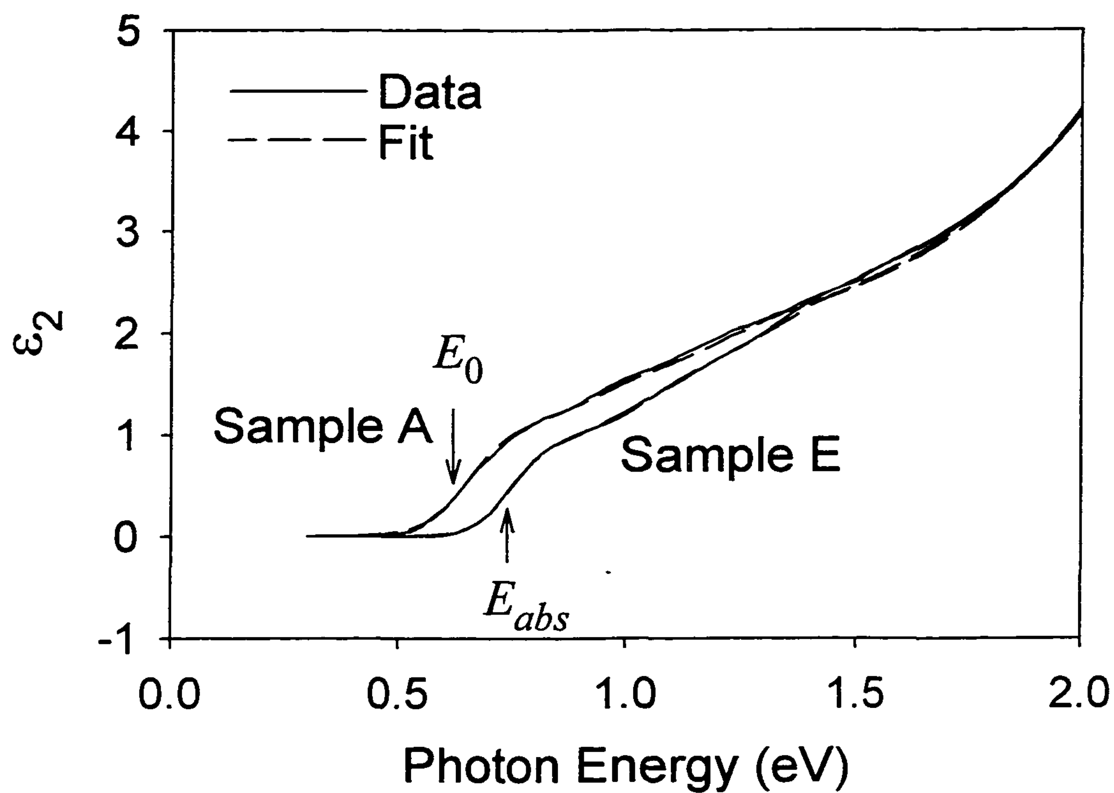

Fig. 39. Experimental values (solid lines) of ε_2 in the region of the fundamental absorption edge for *p*-type samples A and E. Dashed lines are the fits.

Reproduced with permission of the copyright owner. Further reproduction prohibited without permission.

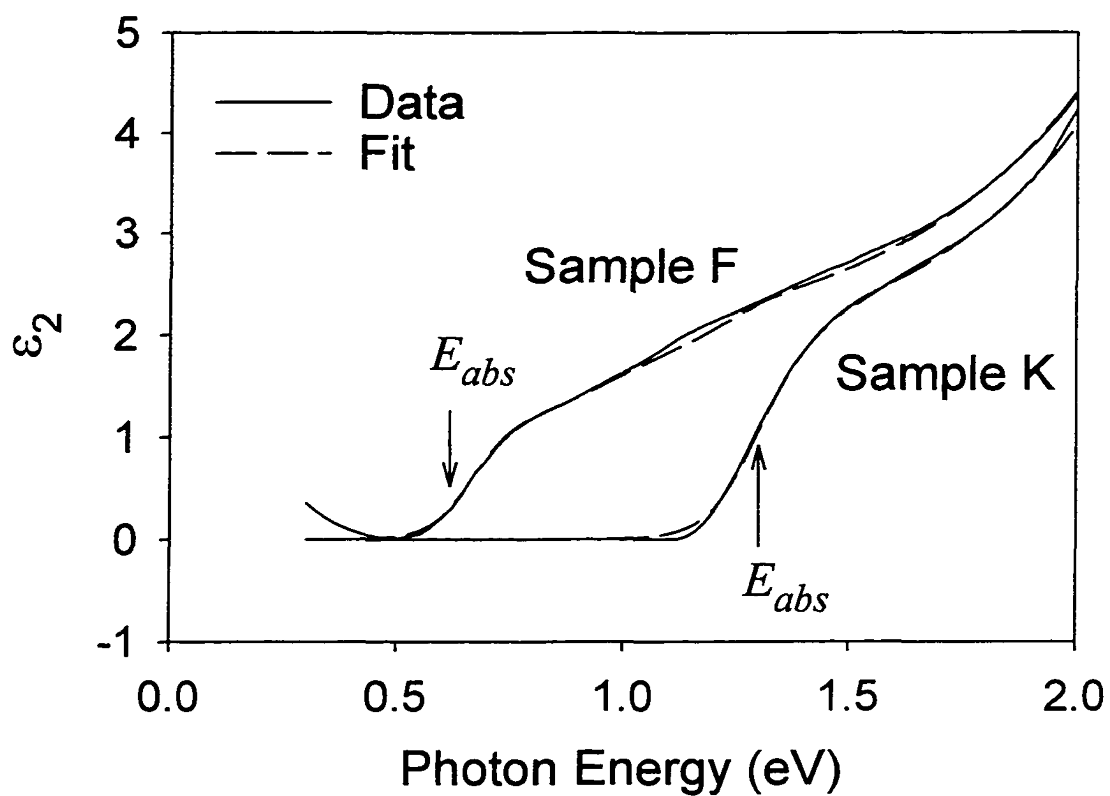

Figure 40. Experimental values (solid lines) of ε_2 in the region of the fundamental absorption edge for *n*-type samples F and K. Dashed lines are the fits.

Reproduced with permission of the copyright owner. Further reproduction prohibited without permission.

For the purposes of discussion, we consider the band structures of InAs and GaAs which are reproduced in Figs. 41 and 19 respectively, since the band structure of $In_{0.66}Ga_{0.34}As/InP$ has not been calculated. The CPs are labeled according to the notation discussed in section 1.6.2.

The presence of the exciton at the fundamental gap affects the band-to-band component of the absorption. Thus even though the exciton is not resolved, the Coulomb interaction still affects the band-to-band lineshape. We have fit the data using a slight modification of Eq. (258). Since the E_0' transition is not resolved from the E_2 transition, we have used the E_2 expression to model the contributions from both of the CPs. In addition, for doped samples the Fermi level filling factor and related BM shift have to be taken into account by Eq. (261). Thus the final expression for the imaginary part of the dielectric function is

$$\varepsilon_2(E) = \frac{1}{1+e^{(E_F-E)/\text{"}k_BT\text{"}}} \mathrm{Im}\begin{bmatrix} \tilde{\varepsilon}_{E_0}(E) + \tilde{\varepsilon}_{E_0+\Delta_0}(E) + \tilde{\varepsilon}_{E_{ind}}(E) + \tilde{\varepsilon}_{E_1}(E) \\ + \tilde{\varepsilon}_{E_1+\Delta_1}(E) + \tilde{\varepsilon}_{E_2}(E) \end{bmatrix} \tag{264}$$

ε_1 was not fit because we could not find an analytic form for the KK transform of Eq. (264).

The term $\frac{1}{1+e^{(E_F-E)/\text{"}k_BT\text{"}}}$ in Eq. (264) is the Fermi level filling factor. For undoped (or lightly p-doped) samples, $E_{abs} = E_0$. The fact that "k_BT" is in quotation marks will be explained in the next section.

Reproduced with permission of the copyright owner. Further reproduction prohibited without permission.

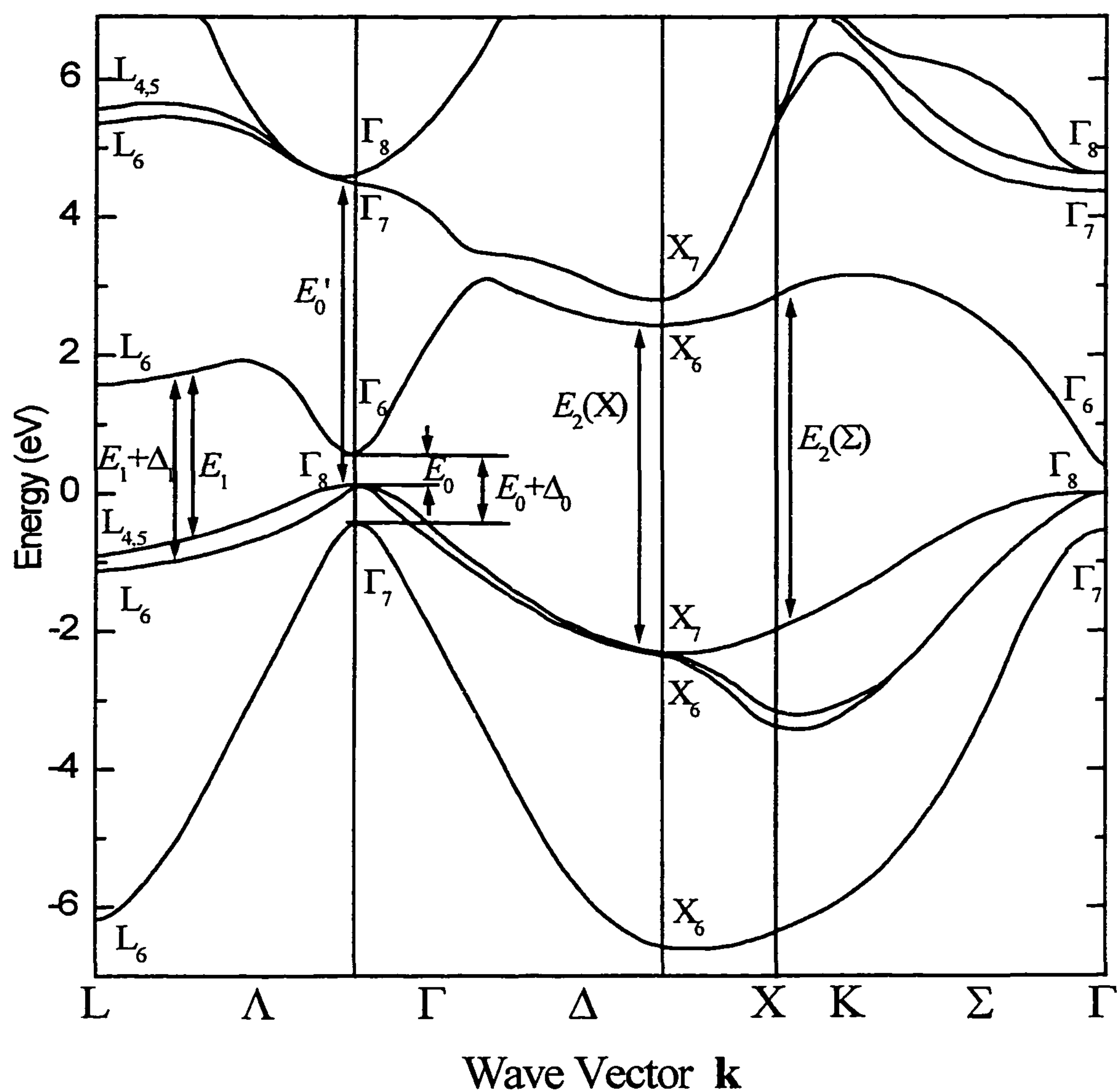

Fig. 41. Electronic energy-band structure of zincblende InAs calculated by nonlocal empirical pseudopotential method after Ref. 56.

Reproduced with permission of the copyright owner. Further reproduction prohibited without permission.

In Figs. 35-38 the E_1-R_1 and E_1+Δ_1-R_1 optical features are superimposed on a large "background" due to the residual effects of the other transitions. In order to eliminate this "background" we have numerically taken the second derivative of ε_1 and ε_2. This is shown by the solid lines in Fig. 42 for sample F. In order to compare our results with previous studies,[97,98] lineshape has been fit with the second derivative of an excitonic feature, i.e.,

$$\frac{d^2\tilde{\varepsilon}}{dE^2} \propto \frac{d^2}{dE^2}\frac{1}{E - E_{ex} + i\Gamma} \tag{265}$$

where E_{ex} = E_1-R_1 or E_1+Δ_1-R_1. This fit is shown by the dashed lines in the figure. The obtained values of the energies of E_1-R_1 and E_1+Δ_1-R_1 (2.551 eV and 2.805 eV) are indicated by the arrows.

1.8.2.3 Discussion of Results

Shown by the dashed lines in Figs. 36, 39, and 40 are the least-square fits to Eq. (264). The obtained values of E_{abs} (=E_0) for sample A and E_{abs} for samples E, F, and K are denoted by arrows in these figures. E_{abs} values for all samples are listed in Table IV. The value of E_0 = 0.612±0.01 eV corresponds to an In composition of (66±1)%.[99] In all cases we used Γ_0 = 60 meV.

Reproduced with permission of the copyright owner. Further reproduction prohibited without permission.

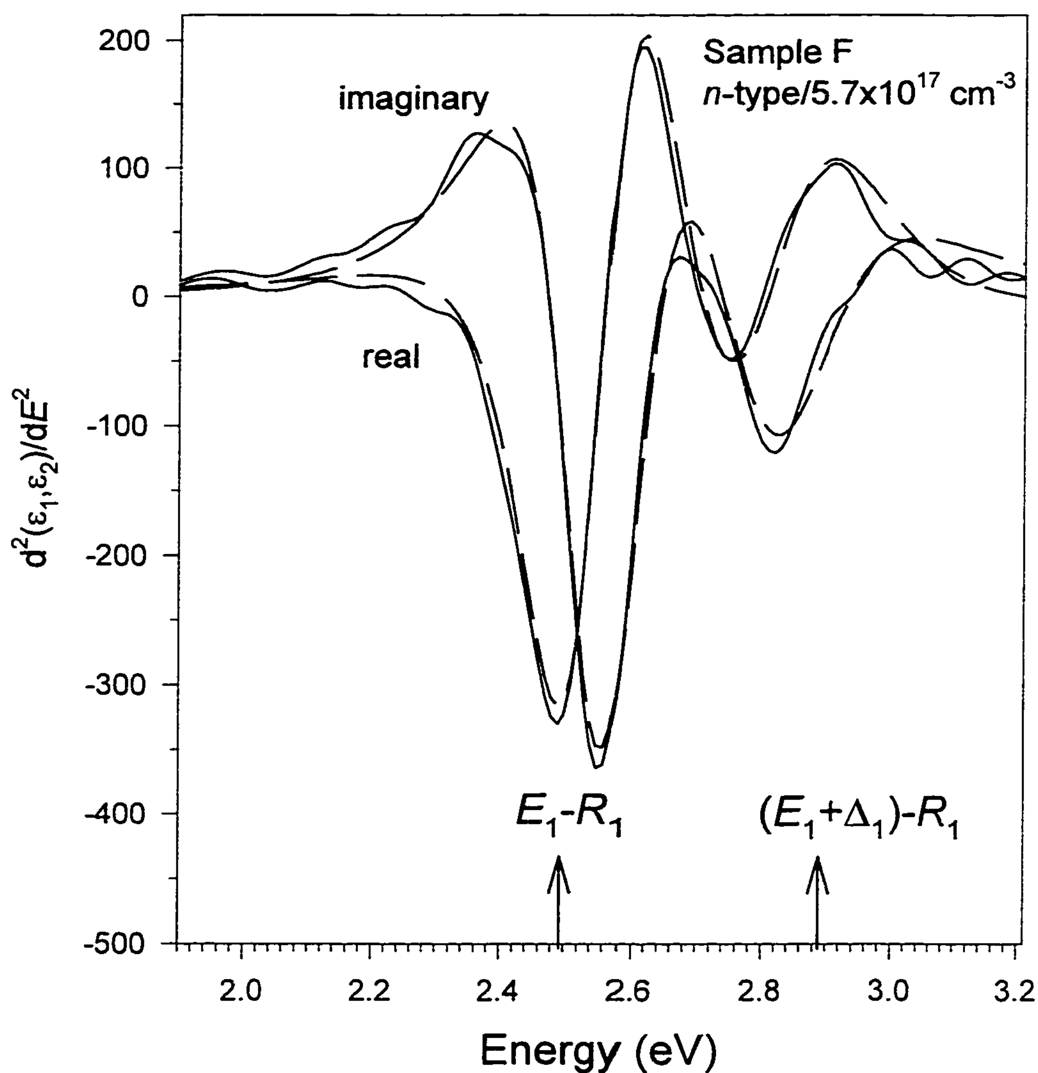

Figure 42. The solid lines are the numerical values of the second derivative of ε_1 and ε_2 for sample F (from Figs. 37 and 38). The dashed lines are fits to Eq. (265) yielding the values of E_1-R_1 and of E_1+Δ_1-R_1 indicated by the arrows.

Reproduced with permission of the copyright owner. Further reproduction prohibited without permission.

Also listed in Table IV are the deduced values for "k_BT". In order to take into account inhomogeneous broadening, Eq. (264) (with "k_BT" set equal to its room temperature value of 26 meV) should be convoluted with a Gaussian. However, this is very difficult to do analytically, so to "simulate" inhomogeneous broadening we have used "k_BT" as an adjustable parameter.

In Fig. 43 the solid squares and triangles are the values of the absorption edge (from Table IV) for the *n*- and *p*-type samples, respectively, as a function of (dopant concentration)$^{2/3}$. Representative error bars are shown. For the case of parabolic bands we should have:

$$E_F - E_0 = \frac{\hbar^2}{2m^*_{c(h)}}[3\pi^2 n(p)]^{2/3} - E_{BGR} \tag{266}$$

where $m^*_{c(h)}$ is the effective mass of the electron (hole), and $n(p)$ is the electron (hole) carrier density, and E_{BGR} includes any band gap reduction effects.

Note that in Fig. 43 for the first five *n*-type samples the relation is linear, as one would expect for parabolic band filling. The solid line is a least-squares fit to a linear function (neglecting the highest doped sample) yielding an intercept (E_0) of 0.599±0.01 eV and a slope of 7.3x10^{-14} eV•cm^2. For the *p*-type samples a least squares fit to a linear function yields E_0 = 0.605±0.01 eV and a slope of 1.12x10^{-14} eV•cm^2. Note that there is no evidence for nonparabolic effects. Within experimental error the values of E_0 for the *n*-

Reproduced with permission of the copyright owner. Further reproduction prohibited without permission.

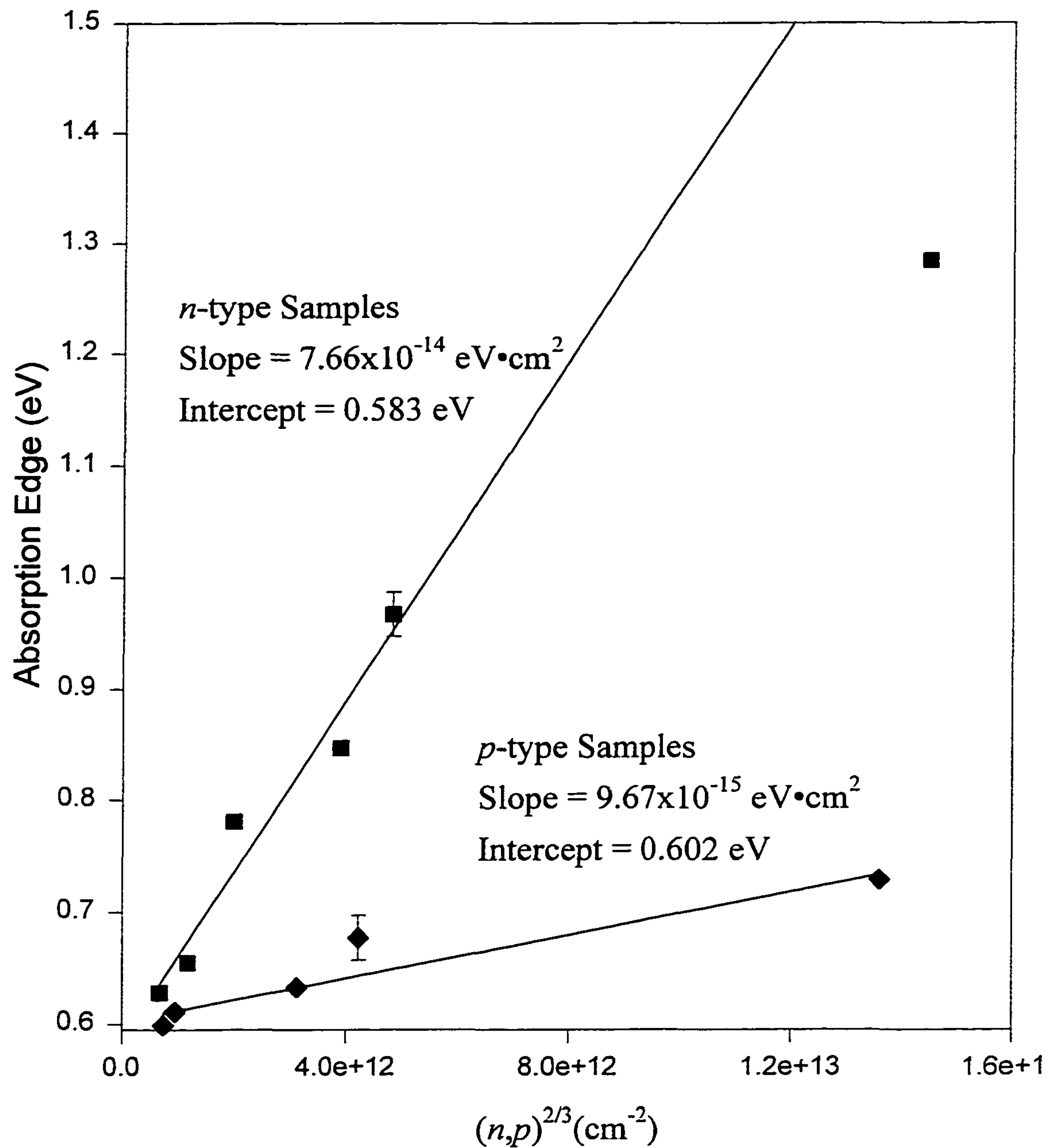

Figure 43. Solid squares and triangles are E_{abs} for n- and p-type samples, respectively, as a function of (dopant concentration)$^{2/3}$. The solid lines are fits to a linear function.

Reproduced with permission of the copyright owner. Further reproduction prohibited without permission.

and p-type samples in Fig. 43 are the same, and are in good agreement with the value in Table V.

These non-parabolic effects have been accounted for based on electronic band structure calculation using the Full Potential Linearized Augmented Plane Wave method which accounts for non-local exchange and spin orbit effects.[95,100] Good agreement is found between this experiment and theory for the n-type samples.

Recently Charache *et al.*[101] reported on the optical (absorption) and electrical properties of doped n-$In_xGa_{1-x}As$ ($x = 0.67$ and 0.53). The former samples are the same as the n-type samples used in this study. Their obtained value of 0.6 eV for E_0 is very close to our value. However, they found deviations from the parabolic band calculations at a doping density of about 7×10^{18} cm^{-3}, while we find that this approximation is still valid for densities as high as $\sim 1.0 \times 10^{19}$ (see Fig. 43).

Note that for the highly n-type samples, there is a small finite value of ε_2 (Figs. 38 and 40) and a drop off in ε_1 (Fig. 37) below ~ 0.5 eV. This is due to free carrier plasma absorption observed for these samples.[101] From Drude theory, the contribution of free carrier absorption to the dielectric function is:

$$\tilde{\varepsilon}_{FC}(E) = \varepsilon_{1\infty} - \frac{E_p^2}{E^2 + iE\gamma_{FC}}, \qquad E_p^2 = \frac{ne^2}{m_c^*} \tag{267}$$

Reproduced with permission of the copyright owner. Further reproduction prohibited without permission.

where $\varepsilon_{1\infty}$ is the high energy (high energy compared to photons, but still below our energy range) dielectric function, γ_{FC} is a phenomenological broadening parameter, and e is the charge on an electron. For sample K the quantity $E_p \approx 0.22$ eV[101] an so according to Eq. (267) a rise in ε_2 and a drop off in ε_1 are expected below the fundamental absorption edge.

The dashed line in Fig. 36 is a least-squares fit over the entire spectral range for sample A using Eq. (264). Since we have not resolved the $E_0+\Delta_0$ feature, the value for this gap for $x = 0.66$ was taken from Ref. 99. For E_{ind} we empoyed a number using E_0 (0.612 eV) plus the $\Gamma_6^c - L_6^c$ separation (0.81 eV), the latter being obtained from x-ray absorption measurements from core levels to the conduction bands.[95] Only a single broadening parameter, Γ_1, was used for the excitonic as well as the BBCE components for both the E_1 and $E_1+\Delta_1$ transitions, and the same 2D Rydberg (R_1) was used for both features. The parameters obtained by the fit for the lightest p-doped sample (sample A) are listed in Table V.

Table V. Materials parameters for the fit of ε_2 for sample A.

Parameter	$In_{0.66}Ga_{0.34}As$
E_0 (eV)	0.612±0.01
A (eV^2)	0.056±0.003
R_0/R_{so} (meV)	3.5
Γ_0 (meV)	60±12
$E_0+\Delta_0$ (eV)	0.95[(a)]

Reproduced with permission of the copyright owner. Further reproduction prohibited without permission.

Parameter	$In_{0.66}Ga_{0.34}As$
B (eV^2)	0.046±0.01
Γ_{so}	100
E_1-R_1 (eV)	2.56±0.01
C_1 (eV^2)	11.4±1
R_1 (meV)	92±20
Γ_1 (meV)	200±10
E_1+Δ_1-R_1 (eV)	2.82±.0.01
C_2 (eV^2)	7.5±0.5
E_{ind} (eV)	1.42[b]
F_{ind}	3±0.5
Γ_{ind} (meV)	400±100
E_c (eV)	4
E_2 (eV)	4.51±0.02
D_2	3.1±0.1
γ_2	0.21±0.02
$\varepsilon_{1\infty}$	1.4

[a]Ref. 99 for $x = 0.66$.
[b]From E_0+($\Gamma_6^c - L_6^c$) Ref. 95

Our value of the 2D exciton binding energy R_1 (~ 90 meV) is in good agreement with the general consideration of Ref. 2, based on effective mass and **k•p** theories as discussed in section 1.6.3.

Reproduced with permission of the copyright owner. Further reproduction prohibited without permission.

In Fig. 42 is a least squares fit (dashed line) to the numerical second derivative of ε_1 (solid line) and ε_2 for sample F using the expression in Eq. (265). Listed in Table VI are the obtained values of the energies and broadening parameters for the E_1-R_1 and E_1+Δ_1-R_1 transitions. Note that for both *n*- and *p*-type samples there is a red shift of both E_1-R_1 and E_1+Δ_1-R_1 with increased doping level. Also listed in Table VI are the values of the energy shift compared to the lightest doped samples, $|\Delta(E_1\text{-}R_1)|$ and $|\Delta(E_1+\Delta_1\text{-}R_1.)|$.

Table VI. Energies and broadening parameters for the E_1-R_1 and E_1+Δ_1-R_1 transitions obtained from a fit to Eq. (265).

Sample	E_1-R_1 (eV)	Γ_1 (meV)	$\|\Delta(E_1\text{-}R_1)\|$ (meV)	E_1+Δ_1-R_1 (eV)	$\Gamma_{1+\Delta 1}$ (meV)	$\|\Delta(E_1+\Delta_1\text{-}R_1)\|$ (meV)
A	2.551	163	0	2.805	239	0
B	2.549	169	1.8	2.804	238	0.5
C	2.534	180	16.9	2.790	256	14.8
D	2.531	174	20.2	2.781	285	24.1
E	2.529	173	21.5	2.780	278	25
F	2.548	157	0	2.793	256	0
G	2.541	168	7.3	2.788	239	4.9
H	2.541	176	7	2.794	253	-0.9
I	2.537	173	10.5	2.783	281	9.3
J	2.533	187	14.7	2.786	275	6.4
K	2.515	202	32.7	2.770	273	23.1

Pickering *et al.*[97] have reported an ellipsometric study of strained and relaxed $In_xGa_{1-x}As$ for $0 \leq x \leq 0.53$ as well as InAs in the region of the E_1-R_1 and E_1+Δ_1-R_1 features. Note:

Reproduced with permission of the copyright owner. Further reproduction prohibited without permission.

as with most other optical studies they refer to these observed excitonic resonances as E_1 and $E_1+\Delta_1$. They have presented quadratic relationships for the energies of these features as a function of composition:

$$\begin{aligned}[E_1 - R_1](x) &= 2.91 - 0.91x + 0.50x^2 \\ [E_1 + \Delta_1 - R_1](x) &= 3.13 - 0.83x + 0.47x^2\end{aligned} \tag{268}$$

This yields 2.53 eV and 2.79 eV for the energies of these structures for $x = 0.66$. Thus our values for the energies of the E_1-R_1 and $E_1+\Delta_1$-R_1 peaks are consistent with their data.

Plotted in Fig. 44 are $|\Delta(E_1\text{-}R_1)|$ and $|\Delta(E_1+\Delta_1\text{-}R_1.)|$ as a function of doping concentration for the *n*- and *p*-type samples. Representative error bars are shown.

Kubal *et al.*[98] have reported an ellipsometric study of the doping dependence of the E_1-R_1 and $E_1+\Delta_1$-R_1 features (which they refer to as E_1 and $E_1+\Delta_1$) in *n*- and *p*-doped GaAs. These authors also have observed a red shift of these features with increasing doping level for both types of carriers that is linear with the logarithm of the doping density as in Fig. 44. They ascribe this effect to band bending and carrier depletion in the surface region.

Reproduced with permission of the copyright owner. Further reproduction prohibited without permission.

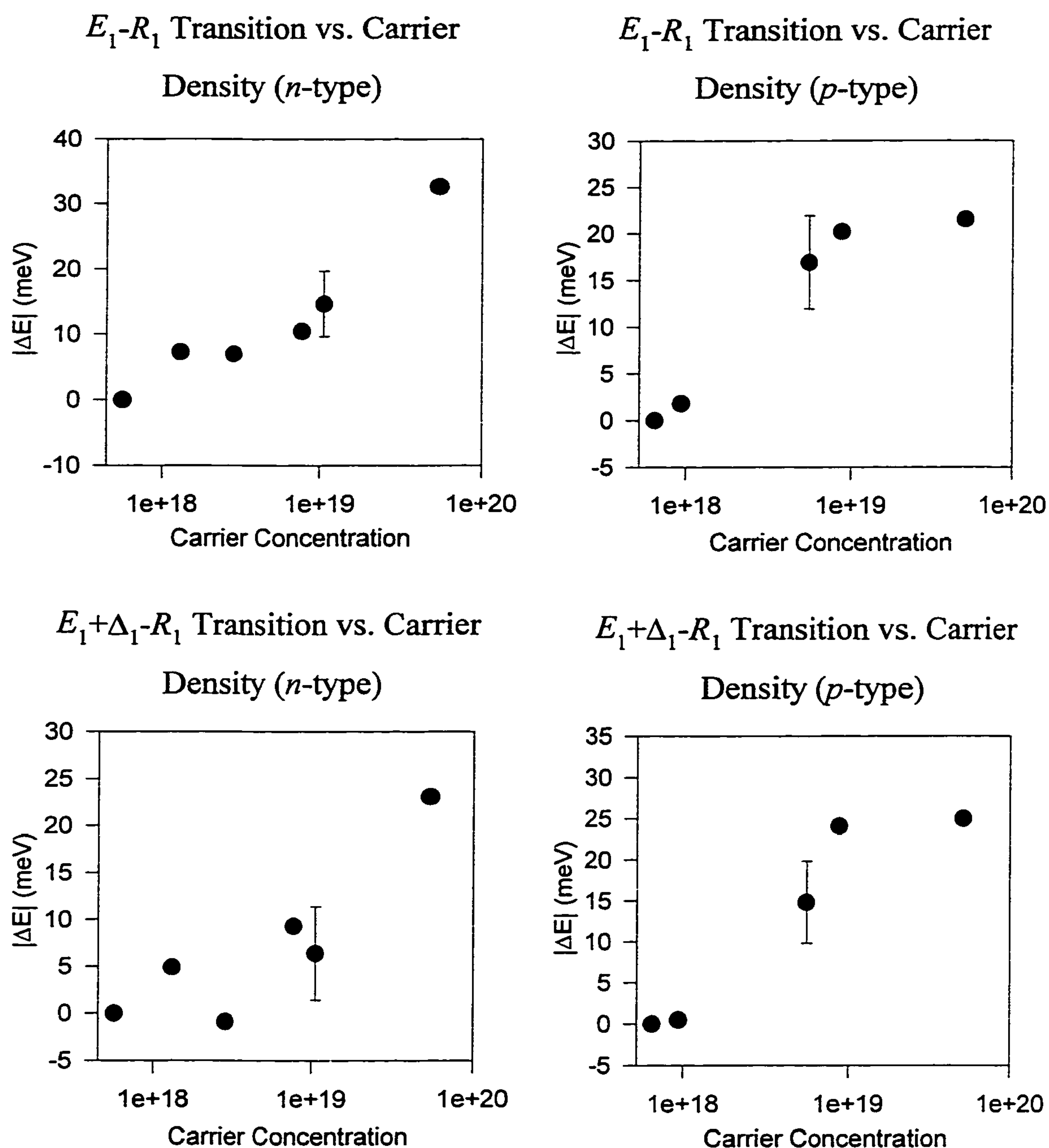

Figure 44. $|\Delta(E_1\text{-}R_1)|$ and $|\Delta(E_1\text{+}\Delta_1\text{-}R_1.)|$ as a function of doping concentration for the *n*- and *p*-type samples. Representative error bars are shown.

Reproduced with permission of the copyright owner. Further reproduction prohibited without permission.

Chapter 2. Reflection Difference Anisotropy

2.1 Historical Overview

Figure 45 illustrates the basic principle of RDA. Near-normal incident polarized light is reflected off a sample, and the difference between the reflectances for light polarized along two orthogonal principal axes (normalized to the reflectivity) is measured. For example for zincblende- and diamond-type semiconductors one often looks at the difference in near normal reflectivity between light polarized along the [110] and [$1\bar{1}0$] principal axes in the plane of the (001) surface. Since materials with full cubic symmetry have no RDA signal (that is the [110] and [$1\bar{1}0$] directions are equivalent in the bulk of a perfect cubic crystal), RDA signals come only from regions that do not have full cubic symmetry. To date, RDA has been used in several studies of optical anisotropies due to surfaces,[13-17] buried heterojunctions,[32-34] strain fields (including those arising from dislocations),[30,31] ordering,[26-29] and near-surface electric fields (zincblende only).[18-25]

The technique was first used in a preliminary study on (110) Si in 1966 by Cardona, Pollak, and Shaklee.[102] The technique was originally termed rotoreflectance because the signal was generated by directly rotating the sample and holding the polarizer fixed. After this, the field lay dormant for nearly twenty years until Aspnes and Studna reported

Reproduced with permission of the copyright owner. Further reproduction prohibited without permission.

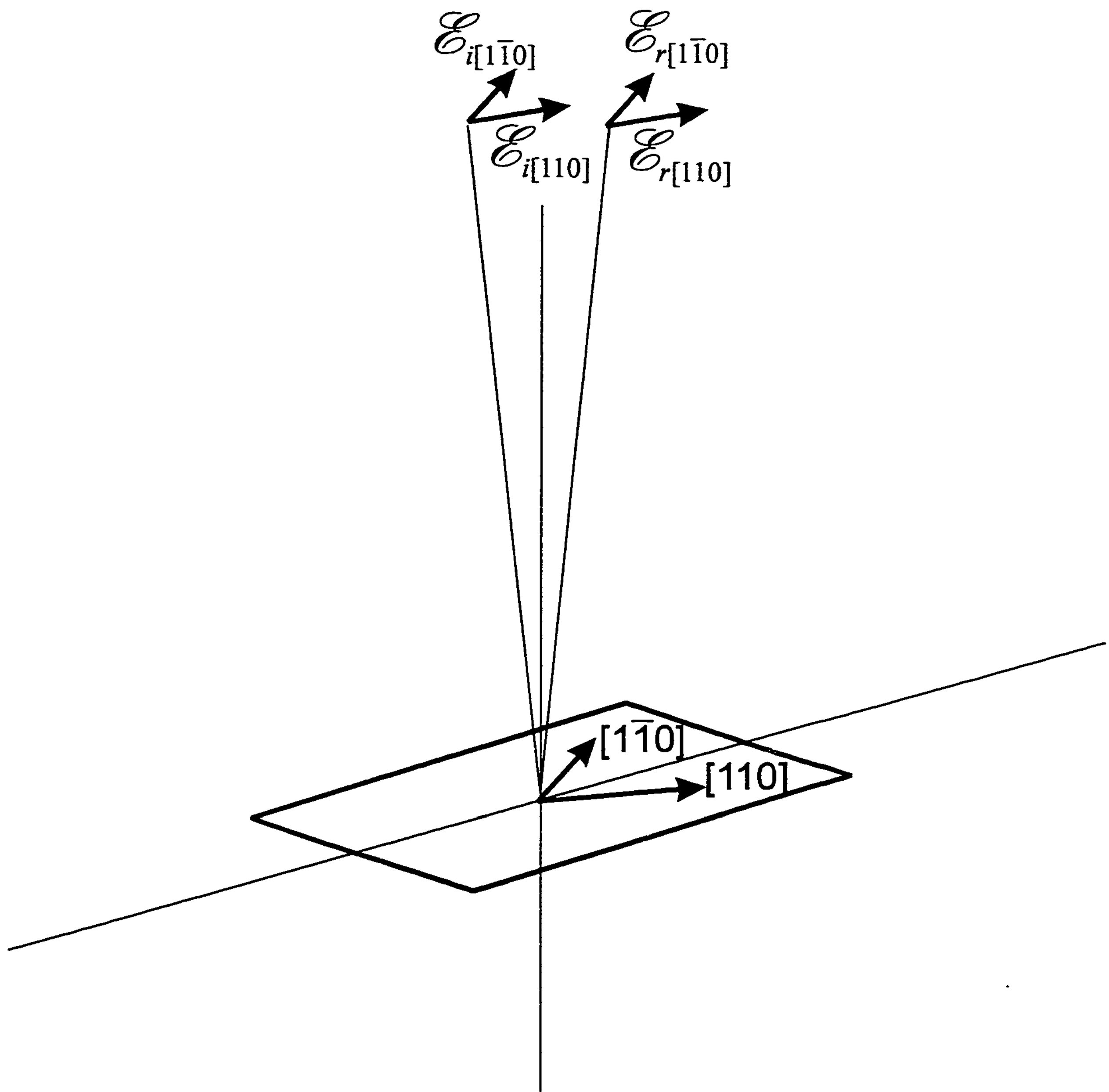

Figure 45 RDA meaurement. Light reflecting off a surface at near-normal incidence. The difference between reflectance for light polarized along the two principal axes measures the optical anisotopy of the sample.

Reproduced with permission of the copyright owner. Further reproduction prohibited without permission.

RDA studies on variously prepared Si and Ge samples.[17] In the study, they extracted both the real and imaginary parts of the RDA signal and proposed several mechanisms for the signal.

The study of electric fields with RDA began with Berkovits *et al.*,[103] who investigated relectance anisotropies in (110) surfaces of InSb and GaAs and concluded that they are partially due to the electric field induced by the pinning of the Fermi level at the oxidized surface of the semiconductor. In 1989, Acosta-Ortiz and Lastras-Martínez compared the RDA signal for doped GaAs with electroreflectance signal and showed that the RDA signal is due to the linear electro-optic (LEO) effect. In 1998, Chen and Yang were able to explain the LEO signal in GaAs based on deformation potential and **k•p** theory and the converse piezoelectric effect.

In the mean time, RDA had been employed as a surface monitor during growth.[104] This is due to RDA's sensitivity to surface reconstruction.[13] In 1996, Lastras-Martínez and Lastras-Martínez reported both RDA signals due to strain fields induced by the presence of dislocations and a theoretical model to explain these signals.[30]

2.2 Overview of the Measurement Technique

RDA[105] is an optical technique that measures the difference between the reflectances for light polarized along two orthogonal principal axes (normalized to the reflectivity) for

Reproduced with permission of the copyright owner. Further reproduction prohibited without permission.

near-normal incident light (Fig. 45). The technique takes advantage of crystal symmetry in that the dominant, but unwanted, nominally isotropic optical contribution from the bulk is subtracted out of the signal.

For our purposes, we measured the (001) face of zincblende type semiconductors. Thus the principal axes were along the [110] and $[1\bar{1}0]$ directions. Then the complex RDA signal is:

$$\Delta\tilde{r}_{RDA} = \frac{\Delta R}{R} + i\Delta\theta = 2\frac{\tilde{r}_{[110]} - \tilde{r}_{[1\bar{1}0]}}{\tilde{r}_{[110]} + \tilde{r}_{[1\bar{1}0]}} \tag{269a}$$

where $\frac{\Delta R}{R}$ and $\Delta\theta$ are the real and imaginary components of the RDA signal, respectively. $\tilde{r}_{[110]}$ and $\tilde{r}_{[1\bar{1}0]}$ are the complex Fresnel reflection coefficients along the [110] and $[1\bar{1}0]$ directions, respectively, and defined as

$$\tilde{r}_{[110]} = \frac{\mathscr{E}_{r[110]}}{\mathscr{E}_{i[110]}} \qquad \tilde{r}_{[1\bar{1}0]} = \frac{\mathscr{E}_{r[1\bar{1}0]}}{\mathscr{E}_{i[1\bar{1}0]}} \tag{269b}$$

where $\mathscr{E}_{i[110]}$, $\mathscr{E}_{r[110]}$, $\mathscr{E}_{i[1\bar{1}0]}$, and $\mathscr{E}_{r[1\bar{1}0]}$ are the complex electric field magnitudes for incident and reflected light along the [110] and $[1\bar{1}0]$ directions as defined in Fig.

Reproduced with permission of the copyright owner. Further reproduction prohibited without permission.

45. $\frac{\Delta R}{R}$ and $\Delta\theta$ are related by the KK relation. The RDA signal can be related to the normal incidence (ϕ=0) ellipsometric signal, $\tilde{\rho}(0)$, by noting that

$$\Delta\tilde{r}_{RDA} = 2\frac{\tilde{r}_{[110]} - \tilde{r}_{[1\bar{1}0]}}{\tilde{r}_{[110]} + \tilde{r}_{[1\bar{1}0]}} = 2\frac{\frac{\tilde{r}_{[110]}}{\tilde{r}_{[1\bar{1}0]}} - 1}{\frac{\tilde{r}_{[110]}}{\tilde{r}_{[1\bar{1}0]}} + 1} = \frac{\tilde{\rho}(0) - 1}{\tilde{\rho}(0) + 1} \tag{270}$$

where $\tilde{\rho}(0)$ is the measured ellipsometric signal as defined by Eq. (1) with ϕ=0, $\tilde{r}_p = \tilde{r}_{[110]}$, and $\tilde{r}_s = \tilde{r}_{[1\bar{1}0]}$.

Thus it is seen that RDA and SE can be measured by the same apparatus except that RDA is done at near-normal incidence and SE is done at oblique incidence. However as mentioned above, SE is best suited to measure isotropic optical properties while RDA is sensitive only to anisotropic optical properties. We also point out that although SE and RDA can have the same basic measurement apparatus, because RDA measures a difference, it is a modulation spectroscopy whereas SE is not.

Reproduced with permission of the copyright owner. Further reproduction prohibited without permission.

2.3 Experimental Details (Phase Modulated RDA)

According to Eq. (270), the RDA signal can be measured using the same apparatus as SE.

The instrument configuration is shown in Fig. 46. This is identical to the setup for ellipsometry in Fig. 3 except the analyzer of interest is mounted inside the modulator head at a fixed angle of incidence of 2.8° for the measurement.

Since the RDA signal is small, the value of $\tilde{\rho}(0)$ in Eq. (270) is near 1. For this reason, maximum sensitivity is achieved with the polarizer angle equal to the analyzer angle [P=A in Eqs. (A14), (A15), and (3c)].

Since the angle of incidence is not exactly 0°, we can have not only the desired signal due to in-plane anisotropy but also the SE signal from isotropic properties. We can eliminate the unwanted SE signal from isotropic properties by using the configuration P=A=0° so that the light polarization is modulated symmetrically with respect to the sample surface and rotating the sample so that the principal axes ($[110]$ and $[1\bar{1}0]$) are at ±45°. In order to understand this, it is necessary to understand to which principal axes the reflectances in Eq. (270) refer. For SE the principal axes are parallel and perpendicular to the plane of incidence of the light, while for RDA they are the principal anisotropy axes of the sample. According to Eq. (A15), the SE signal should be 0 for P=A=0°. On the other hand, since the sample is rotated 45° with respect to the polarizer, we can use Eq. (3c) for

Reproduced with permission of the copyright owner. Further reproduction prohibited without permission.

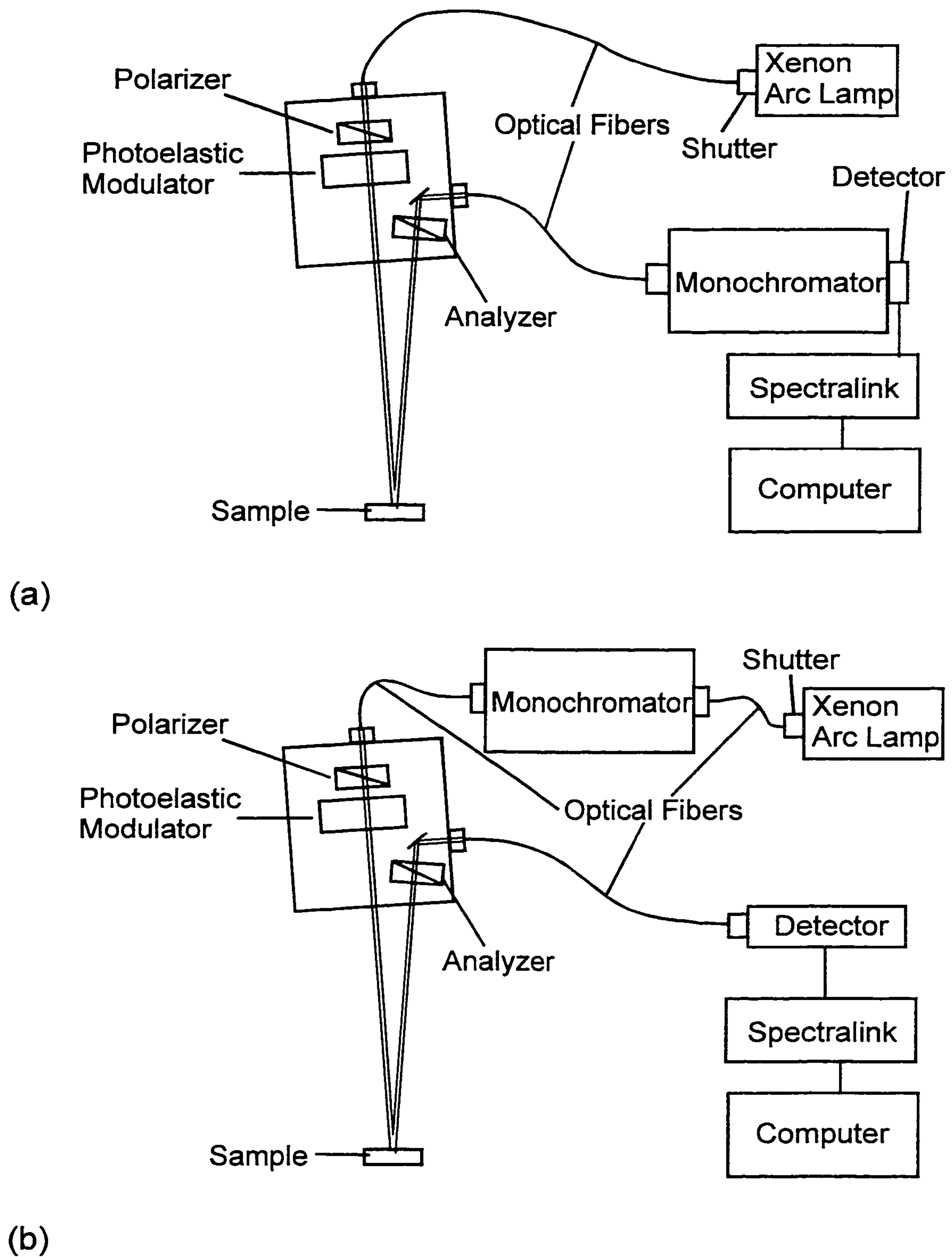

Figure 46. RDA setup. (a) is configuation used above 1.5 eV. (b) shows the configuation used in below 1.5 eV, which has three fiber optic cables in the light path instead of two.

Reproduced with permission of the copyright owner. Further reproduction prohibited without permission.

the anisotropic part of the signal given in Eq. (270) (that is the polarizer and analyzer are at 45° when referenced to the eigen-axes of the sample.

The rest of the experimental setup is identical to the PME experimental setup given in section 1.3, including the detectors, light source, and monochromators.

2.3.1 Elimination of Background

In spite of the configuration mentioned in the previous section, which should eliminate the SE portion of the signal, we typically still have a background (of about 1%) in our RDA signal most likely due small misalignment of the modulator, analyzer, and sample or a small residual birefringence of the optical components. Because the RDA signal is small, we need to eliminate this background even though it is basically featureless. To do this we first measure $\left(\frac{\Delta R}{R}+i\Delta\theta\right)_1$, defined as:

$$\left(\frac{\Delta R}{R}+i\Delta\theta\right)_1 = 2\frac{\tilde{r}_{[011]}-\tilde{r}_{[0\bar{1}1]}}{\tilde{r}_{[011]}+\tilde{r}_{[0\bar{1}1]}} \tag{272}$$

Then we rotate the sample by 90° and measure $\left(\frac{\Delta R}{R}+i\Delta\theta\right)_2$ defined as:

Reproduced with permission of the copyright owner. Further reproduction prohibited without permission.

$$\left(\frac{\Delta R}{R}+i\Delta\theta\right)_2 = 2\frac{\tilde{r}_{[0\bar{1}1]}-\tilde{r}_{[0\bar{1}\bar{1}]}}{\tilde{r}_{[0\bar{1}1]}+\tilde{r}_{[0\bar{1}\bar{1}]}} \tag{272}$$

The signal, aside from background terms, given in Eq. (272) should be the negative of that given by Eq. (271). The RDA spectrum of interest $\left(\frac{\Delta R}{R}+i\Delta\theta\right)$ is then obtained by taking the difference between these two signals to eliminate any background terms, i.e.

$$\frac{\Delta R}{R}+i\Delta\theta = \frac{1}{2}\left[\left(\frac{\Delta R}{R}+i\Delta\theta\right)_1 - \left(\frac{\Delta R}{R}+i\Delta\theta\right)_2\right] \tag{273}$$

2.3.2 Alignment of the Apparatus

Compared to SE, the interpretation of the RDA signal is less well understood. For this reason, the alignment of the modulator and analyzer positions and the modulation amplitude calibration were done in the SE configuration (section 1.3.2). Then the angle of incidence was changed to 2.8° for RDA measurement. Also, the sample stand was lowered to its lowest position.

Reproduced with permission of the copyright owner. Further reproduction prohibited without permission.

2.3.2.1 Sample Leveling

A small difficulty arose in the tilt alignment of the sample with the instrument in RDA configuration since the modulator head was in the way of the autocolumnator. There are two ways around this problem. The first is simply to move the modulator head to 45°, align the tilt as described in section 1.3.2.1, and then move the modulator head back to 2.8°. Alternatively, the sample could be rotated and the level adjusted until the DC signal (s_0) showed less than 1% variation for all orientations. This second method proved to be faster after enough experience had been gained and also could be used when the surface was too rough to use the autocolumnator (which was not the case for the data presented in this thesis). It also has the advantage that no movement of the modulator head was required. This was important for some of the time when movement of the modulator head was causing the system to crash due to a weak power supply in the spectralink controller. Both of the methods lead to the same alignment of the sample.

For samples with very rough backsides, small paper wedges under the sample were sometimes used to make the initial tilt of the sample surface small enough to be within the range of the adjustment screws.

2.3.2.2 Sample Alignment

Reproduced with permission of the copyright owner. Further reproduction prohibited without permission.

In addition to the above leveling procedure, a few other steps were taken to maximize signal. As previously mentioned, the sample stand was positioned at its lowest position. Only in this position is maximum throughput achieved for 2.8° incidence angle. In addition, 2.7° and 2.9° angle of incidence were tested for maximum intensity after the sample was leveled as our goniometer was only calibrated to a precision of about 0.1° (section 1.3.2.2). Finally, small shims were used to slightly change the height of the modulator head to maximize signal. This last step was done infrequently as it required loosening the screws that fix the modulator head to the goniometer, and thus required a new goniometer (angle of incidence) calibration (section 1.3.2.2).

2.3.3 Signal to Noise Ratio Problems in the IR

The signal to noise ratio below 1.5 eV (0.8-1.5 eV) was not good on our system. We attribute this to the poor signal to noise characteristics of the InGaAs detector as compared to the photomultiplier tube and the fact that we have three (rather than two for $E > 1.5$ eV) fiber optic cables in the configuration for this energy range.

Up to now, the problem has been addressed simply by taking many scans with long integration times in this regime. In the future the situation could be improved by using a better detector (perhaps a cooled detector) or by mounting the InGaAs detector directly on the exit port of the monochromator. This second option would eliminate our current

Reproduced with permission of the copyright owner. Further reproduction prohibited without permission.

ability to remove the photoluminescence signal by using monochromatic rather than white light incidence on the sample.

2.3.4 Etching Procedures

Although etching was not found to significantly change the RDA signal for the samples in this study, other etches and certainly surface passivation might be expected to yield interesting results.

Etching on the sample stand can be done using the procedure given in section 1.3.3.2, except the hole in the top of the cover must be left open for the light to reach the sample and the exit slit should be covered during the entire etching process.

2.3.5 Extension to FTIR-based RDA

RDA signal can also be obtained from the FTIR based ellipsometer. Up to now, we have only used this to measure the anisotropy of a polarizer. To use the instrument for RDA, we simply take advantage of Eq. (270) and perform a normal SE measurement at 5° or even 10° incidence. Most of the spectral structure of such a run comes from the RDA signal. Since for this configuration there is still a small SE signal, the sample must be rotated by 90° re-leveled and re-measured. Then a subtraction can be done using Eq.

Reproduced with permission of the copyright owner. Further reproduction prohibited without permission.

(273). This eliminates the SE signal as well as other possible background terms. Shown in Fig. 47 is the RDA signal obtained for a polarizer using this method at 5° incidence angle. Figure 48 shows the same polarizer as measured on our normal phase modulation RDA setup for comparison.

All other samples tested on the FTIR based instrument showed no RDA structure in the measured spectral range. Elimination of the SE signal in the range could also be accomplished by using a polarizer angle of 0°, but this would require new software to take and analyze the data. The other samples tested were 5×10^{19} cm^{-3} *p*-doped $In_{0.66}Ga_{0.34}As$ grown on InP, bulk GaSb, one of the Au mirrors, low temperature grown (LTG) GaAs, and the p^+-doped Si reference sample.

Reproduced with permission of the copyright owner. Further reproduction prohibited without permission.

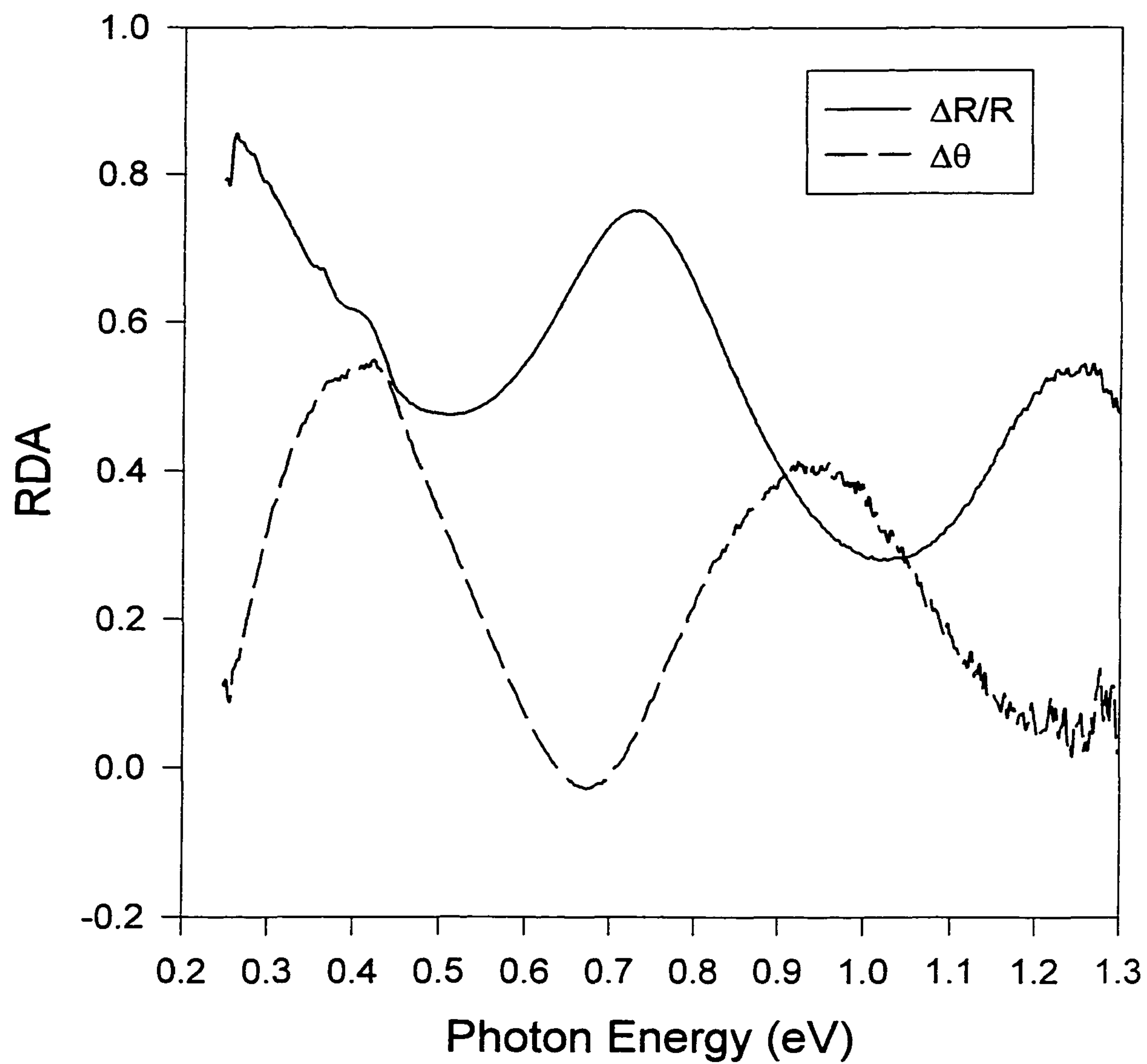

Figure 47. RDA data taken for a polarizer using the FTIR based ellipsometer.

Reproduced with permission of the copyright owner. Further reproduction prohibited without permission.

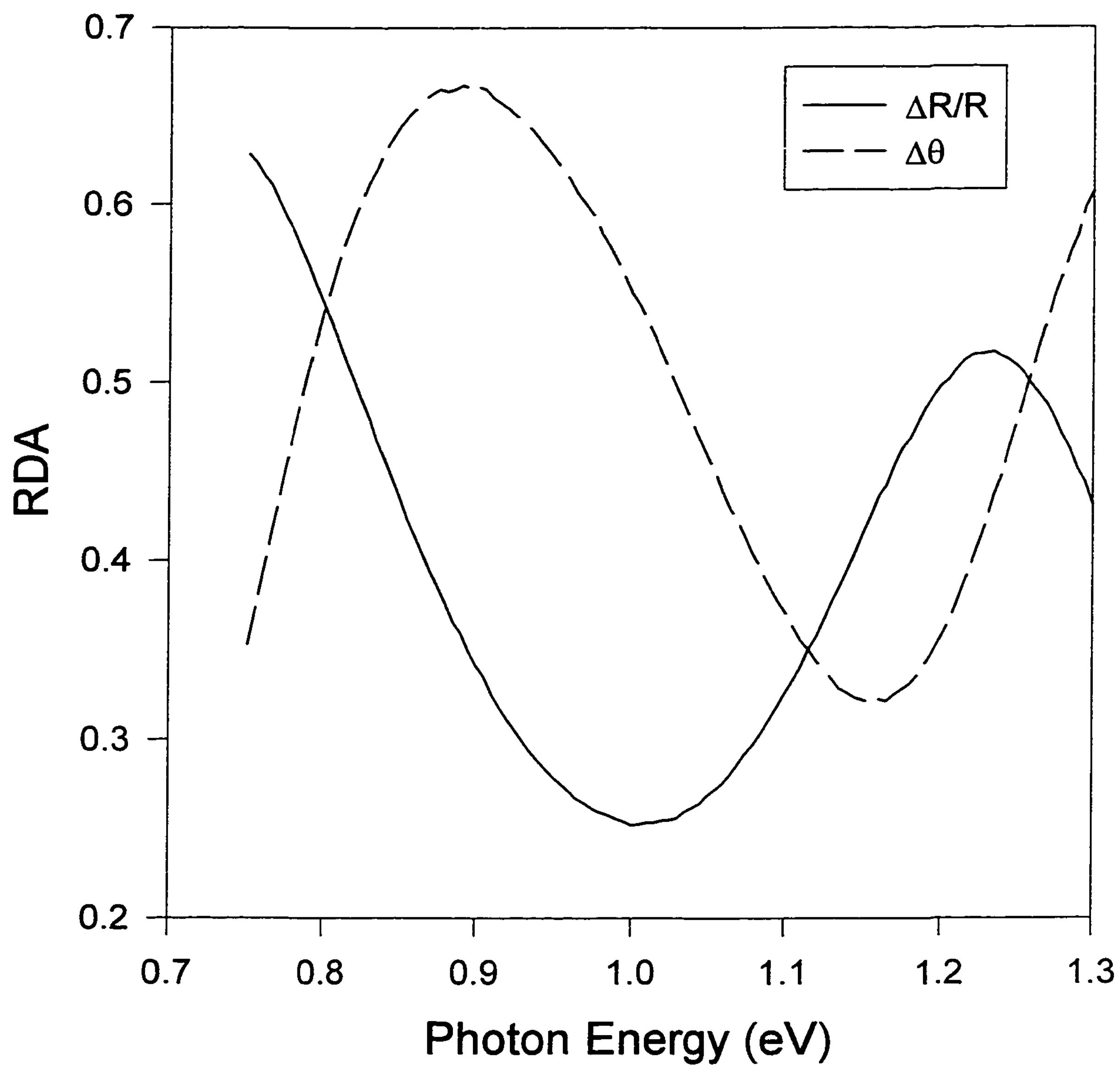

Figure 48. RDA data taken for a polarizer using the phase modulation based (ISA) ellipsometer.

Reproduced with permission of the copyright owner. Further reproduction prohibited without permission.

Theory of Selected RDA signals

In this section, we discuss the theory of the RDA signals due to near surface electric fields in zincblende materials, strain fields due to 60° (misfit) dislocations, and ordering.

2.4.1 Linear Electro-Optic Effect Near E_1 and $E_1+\Delta_1$ Transitions

An electric field in zincblende semiconductors will produce an RDA signal due to the linear electro-optic (LEO) effect. This effect is most pronounced at the exciton energies E_1-R_1 and $E_1+\Delta_1$-R_1 corresponding to the E_1 and $E_1+\Delta_1$ BS CPs discussed in section 1.6.2. In this section, we will denote these exciton energies as "E_1" and "$E_1+\Delta_1$", respectively, to be consistent with the notation in the literature. Since the signal varies linearly with the electric field, it can be used to gain information about the sign and magnitude of near surface electric fields, and thus the band bending, in these semiconductors. For example, it has been shown that for a conventional space charge region (SCR), i.e., linear variation of the electric field with distance from the surface, the RDA signal is a direct measure of the surface electric field if the width of the SCR is much larger that the penetration depth of the light.[23] RDA experiments have been used to study the SCR in *n*- and *p*- doped GaAs (001),[22,23,106,107] ZnSe (001)[108,107] and InGaAs/InP (001)[109] as well as InSb (110)[110] and GaAs (110).[32] Paget *et al* have used this method to investigate sulfur-passivated

Reproduced with permission of the copyright owner. Further reproduction prohibited without permission.

GaAs (001).[111] In this thesis we discuss the use of RDA to investigate the properties of undoped, *n*-, and *p*-doped LTG:GaAs.[18-21]

The basic idea of the LEO effect can be seen by examining the zincblende structure. For concreteness, we show the structure of zincblende GaAs in Fig. 49. The Ga atoms (shown as white) occupy the sites of an FCC lattice, while the As atoms (shown in black) occupy another FCC lattice offset from the Ga lattice by $a/4[111]$ where a is the lattice constant. Note that the bonds in the $[\bar{1}11]$ and $[1\bar{1}1]$ directions (shown as white) all have As on the bottom and Ga on top, while the bonds in the $[111]$ and $[\bar{1}\bar{1}1]$ directions (shown as black) have Ga on the bottom and As on top. Therefore any affect that distinguishes top from bottom can create anisotropies along these direction. An electric field along [001] is just such an effect, since the partially ionic character of the bonding causes the positively (negatively) charged Ga (As) to move in (against) the direction of the electric field. (Note, a uniaxial stress would not give an effect since it doesn't distinguish top from bottom, *i.e.* stress has even parity.) The projection of these bonds into the (001) plane give the measured anisotropy between the reflectivity along the [110] and $[1\bar{1}0]$ directions. In Fig. 49(b) the structure is shown looking down the [001] direction. This argument explains why there is no LEO effect in diamond-type materials, since if the atoms of both of the sublattices are the same, the sublattices will not be displaced with respect to one another. Additional symmetries also eliminate the LEO effect at the E_0 transition, so we look for the effect at the "E_1" and "E_1+Δ_1" transitions.

Reproduced with permission of the copyright owner. Further reproduction prohibited without permission.

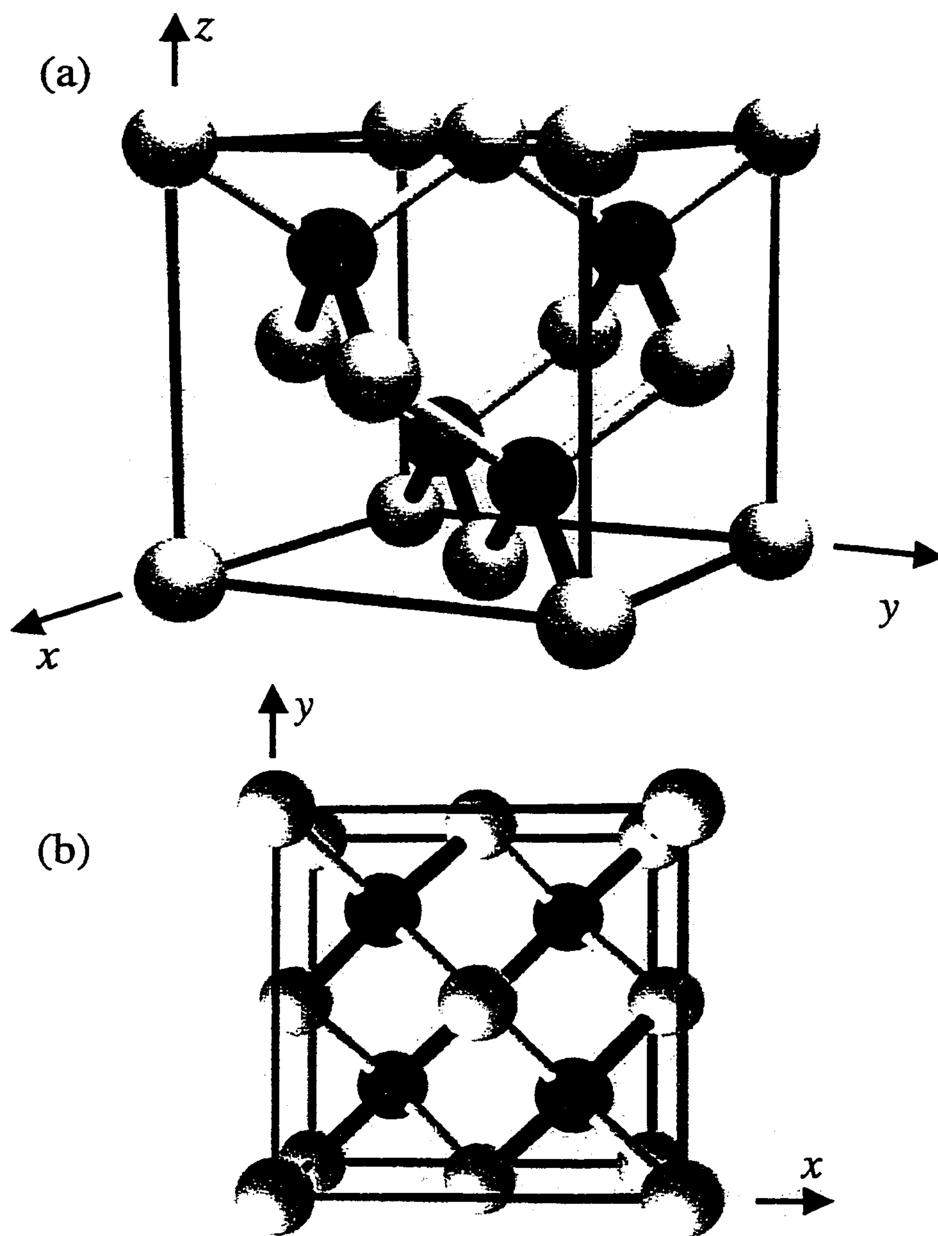

Figure 49. Zincblende structure. Bonds in the [$\bar{1}$11] and [1$\bar{1}$1] directions (shown as white) all have As on the bottom and Ga on top, while bonds in the [111] and [$\bar{1}\bar{1}$1] directions (shown as black) have Ga on the bottom and As on top. (a) shows the conventional zincblende cell. (b) shows the same conventional cell looking down in the [001] direction.

Reproduced with permission of the copyright owner. Further reproduction prohibited without permission.

Recently, Chen and Yang have developed a theory of how the inverse piezoelectric effect creates the LEO RDA signal.[21] Their method is outlined below.

Referring to the GaAs BS shown in Fig. 19, we denote the top two valence bands and the lowest conduction band along the Λ (<111>) direction as V_1, V_2, and C. According to the theory, we will find that the RDA signal is created by two strain effects: (1) a transfer of oscillator strength from V_1 to the V_2 valence band and (2) a smaller effect due to the interband splitting of the V_1 and V_2 bands.

Along the Λ direction, the wave functions V_1, V_2, and C bands can be expressed as linear combinations of the **k**=0 wave functions as[112]

$$
\begin{aligned}
C &= A\left|\bar{S}\uparrow\right\rangle + B\left|\bar{z}\uparrow\right\rangle \\
V_1 &= \frac{1}{\sqrt{2}}\left|\left(\bar{X}+i\bar{Y}\right)\uparrow\right\rangle \\
V_2 &= \frac{1}{\sqrt{2}}\left|\left(\bar{X}-i\bar{Y}\right)\uparrow\right\rangle
\end{aligned}
\tag{274}
$$

For GaAs A=-0.56 and B=0.56. Also,

$$
\begin{aligned}
\bar{z} &= \frac{1}{\sqrt{3}}(hx+ky+lz) && \leftarrow \text{from } \Gamma_{15}^{c} \\
\bar{X} &= \frac{1}{\sqrt{2}}(hX-kY) && \\
\bar{Y} &= \frac{1}{\sqrt{6}}(hX+kY-2lZ) && \Big\} \leftarrow \text{from } \Gamma_{15}^{v}
\end{aligned}
\tag{275}
$$

Reproduced with permission of the copyright owner. Further reproduction prohibited without permission.

where h, k, and l are ±1 and given by the first, second, and third component, respectively, of the **k** vector for the given band ($[hkl] = [111]$, $[\bar{1}\bar{1}1]$, $[\bar{1}1\bar{1}]$, or $[1\bar{1}\bar{1}]$). X, Y, and Z are the p-like wave functions at the top of the valence band. x, y, and z are the wave functions of the Γ_{15} conduction band at **k**=0. The X, Y, and Z wave functions, which we are most interested in because they make up the V_1 and V_2 bands, are related to the $P_{3/2}$ multiplet (J=3/2, M_J = ±3/2, ±1/2 in sphereical notation) and $P_{1/2}$ multiplet (J=1/2, M_J = ±1/2) and thus to the spherical harmonics (Y_1^1, Y_1^{-1}, Y_1^0) as[113]

$$
\begin{aligned}
\left|\frac{3}{2},\frac{3}{2}\right\rangle &= \frac{1}{\sqrt{2}}\left(|X\rangle + i|Y\rangle\right)\uparrow \propto Y_1^1\uparrow \\
\left|\frac{3}{2},\frac{1}{2}\right\rangle &= \frac{1}{\sqrt{6}}\left(|X\rangle + i|Y\rangle\right)\downarrow - \sqrt{\frac{2}{3}}|Z\rangle\uparrow \propto \frac{1}{\sqrt{3}}Y_1^1\downarrow - \sqrt{\frac{2}{3}}Y_1^0\uparrow \\
\left|\frac{3}{2},-\frac{1}{2}\right\rangle &= -\frac{1}{\sqrt{6}}\left(|X\rangle - i|Y\rangle\right)\uparrow - \sqrt{\frac{2}{3}}|Z\rangle\downarrow \propto -\frac{1}{\sqrt{3}}Y_1^{-1}\uparrow - \sqrt{\frac{2}{3}}Y_1^0\downarrow \\
\left|\frac{3}{2},\frac{3}{2}\right\rangle &= -\frac{1}{\sqrt{2}}\left(|X\rangle - i|Y\rangle\right)\downarrow \propto Y_1^{-1}\downarrow \\
\left|\frac{1}{2},\frac{1}{2}\right\rangle &= \frac{1}{\sqrt{3}}\left(|X\rangle + i|Y\rangle\right)\downarrow + \frac{1}{\sqrt{3}}|Z\rangle\uparrow \propto \sqrt{\frac{2}{3}}Y_1^1\downarrow + \frac{1}{\sqrt{3}}Y_1^0\uparrow \\
\left|\frac{1}{2},-\frac{1}{2}\right\rangle &= \frac{1}{\sqrt{3}}\left(|X\rangle - i|Y\rangle\right)\uparrow - \frac{1}{\sqrt{3}}|Z\rangle\downarrow \propto \sqrt{\frac{2}{3}}Y_1^{-1}\uparrow - \frac{1}{\sqrt{3}}Y_1^0\downarrow
\end{aligned}
\qquad (276)
$$

Now that the wave functions are known, the anisotropy of the optical transitions between the $[110]$ and $[1\bar{1}0]$ directions can be calculated. We denote the optical transition strengths for transitions from the V_1 and V_2 states to the C state for light polarized along

Reproduced with permission of the copyright owner. Further reproduction prohibited without permission.

the [110] and [1$\bar{1}$0] directions as $M_{[110]}$ and $M_{[1\bar{1}0]}$, respectively. Then the anisotropy between the 110] and [1$\bar{1}$0] directions is

$$\frac{\Delta M}{M} = \frac{M_{[110]} - M_{[1\bar{1}0]}}{M_{[110]} + M_{[1\bar{1}0]}} \tag{277}$$

where $M = M_{[110]} + M_{[1\bar{1}0]}$.

Figure 50 shows a diagram of the <111> valence band states under the influence of an electric field along the [001] direction. In the absence of an electric field, $\frac{\Delta M}{M}$ is 0.5 for the [111] and [$\bar{1}\bar{1}$1] directions, while it is –0.5 for the [$\bar{1}$1$\bar{1}$] and [1$\bar{1}\bar{1}$] directions. Since the bands corresponding to these four directions are degenerate in the absence of an electric field, the total $\frac{\Delta M}{M}$ is zero.

The right side of Fig. 50 shows the effects of an electric field along the [001] direction on the valence band states. When the crystal is subjected to an electric field along the [001] direction, a shear strain $e_{xy} = d_{14}\,\mathscr{E}$ is developed in the material due to the converse piezoelectric effect,[114] where e_{xy} is a shear strain for the x = [100] and y = [010]

Reproduced with permission of the copyright owner. Further reproduction prohibited without permission.

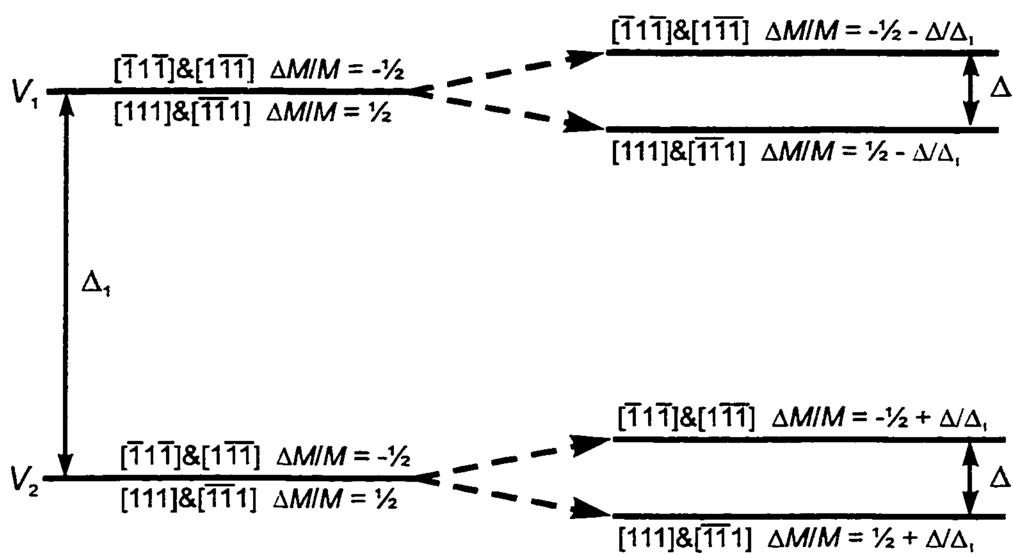

Figure 50 Diagram of the <111> states under the influence of an electric field along the [001] direction.

Reproduced with permission of the copyright owner. Further reproduction prohibited without permission.

directions, d_{14} is the piezoelectric constant, and $\mathscr{E}$ is the electric field. This strain causes a coupling between the V_1 and V_2 states through the Hamiltonian for a shear strain.[113]

$$H_{e_{xy}} = Dd_{14}\mathscr{E}(\hat{L}_x\hat{L}_y + \hat{L}_y\hat{L}_x) \tag{278}$$

where $\hat{L}_x$ and $\hat{L}_y$ are the usual angular momentum operators for the X, Y, and Z states at the top of the valence band and D is the deformation potential.

The strain Hamiltonian between V_1 and V_2 for the [111] and $[\bar{1}\,\bar{1}\,1]$ bands is

$$\begin{array}{cc} V_1 & V_2 \end{array}$$
$$\begin{bmatrix} -E-\dfrac{\Delta}{2} & -\Delta \\ -\Delta & -E-\Delta_1-\dfrac{\Delta}{2} \end{bmatrix} \tag{279}$$

and for the [111] and $[\bar{1}\,\bar{1}\,1]$ bands is

$$\begin{array}{cc} V_1 & V_2 \end{array}$$
$$\begin{bmatrix} -E+\dfrac{\Delta}{2} & \Delta \\ \Delta & -E-\Delta_1+\dfrac{\Delta}{2} \end{bmatrix} \tag{280}$$

where $\Delta = 2Dd_{14}\mathscr{E}/\sqrt{3}$. The coupling between V_1 and V_2 leads to a splitting of Δ in these levels, due to the $\pm\Delta/2$ terms in the diagonals of the matrices. In addition, the off

Reproduced with permission of the copyright owner. Further reproduction prohibited without permission.

diagonal matrix elements lead to a mixing of the valence states. The new valence states have optical transition anisotropies changes of $\Delta M / M = -\Delta / \Delta_1$ for the V_1 states and $\Delta M / M = \Delta / \Delta_1$ for the V_2 states. These changes are noted in the right side of Fig. 50.

Reference 21 calculates the RDA signal for GaAs based on the parameters, Adachi's model for GaAs near "E_1", and an assumed Gaussian distribution of spin orbit splitting, Δ_1, for the states contributing to the "E_1", "E_1+Δ_1" features. Their calculation is in good agreement with experiment and shows that most of the RDA signal comes from the transfer in interband oscillator strength from the V_1 to the V_2 state and that the RDA lineshape is dominated by the exciton contribution to the dielectric function. The anisotropy introduced by the splitting of the V_1 and V_2 bands produces a small feature which is not observed in the experiment. The simulation also shows that the observed peaks in the RDA spectra are separated by less that Δ_1 since the shift in oscillator strength is inversely proportional to Δ_1 and is thus is dominated by the states with small Δ_1 (in the Gaussian distribution).

It can be shown using the above formalism that an (001) electric field does not produce a RDA signal at E_0.

Reproduced with permission of the copyright owner. Further reproduction prohibited without permission.

2.4.2 Strain Field Associated with Misfit Dislocations

When a film with an unstrained lattice constant a_f is deposited on a substrate with a different lattice constant, a_s [Fig. 51(a)], it initially grows with a lattice constant equal to that of the substrate. The mismatch (misfit strain), $([a_f\text{-}a_s])/a_{avg}$, is accommodated by a biaxial strain in the layer [Fig. 51(b)]. This is known as pseudomorphic film. This continues until the film reaches some critical thickness h_c (see figure). When the film thickness exceeds h_c, the misfit is accommodated by the formation of misfit dislocations, and the lattice constant of the film relaxes toward the unstrained value [Fig. 51(c)].

In zincblende type materials, these misfit dislocations take the form of 60° dislocations. Such dislocations, which are characterized by the fact that the Burgers vector makes an angle of 60° with the dislocation core (which lies along any of six equivalent <110> directions), have both screw and edge components that are directed along the <110> and <112> directions, respectively.

The theory of how the near-surface strain fields of 60° dislocations affect the RDA signal has been worked out in Ref. 30. Below, we follow their work to find the RDA signal near E_0. We are interested in E_0 because an electric field does not produce a signal at E_0.

There are 48 types of 60° dislocations,[115,116] but following Ref. 30 we only consider the 16 dislocations with cores oriented along $[110]$ or $[1\bar{1}0]$, since they are the only ones

Reproduced with permission of the copyright owner. Further reproduction prohibited without permission.

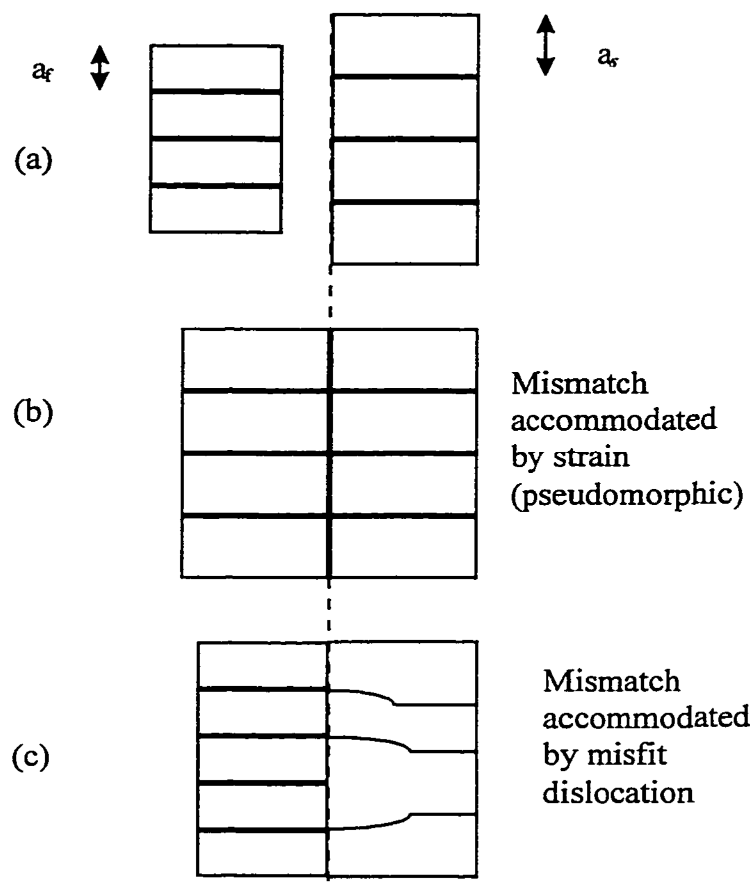

Figure 51 Schematic representation of the formation of misfit dislocations. (a) unstrained lattice, (b) thickness of the film less than the critical thickness, h_c, and (c) thickness of the film greater than h_c – misfit dislocations are generated.

Reproduced with permission of the copyright owner. Further reproduction prohibited without permission.

leading to an optical anisotropy for normal incidence on the (001) surface. Burgers vectors for these sixteen dislocations are given by

$$\mathbf{b}^{(ijkmn)} = \mathbf{b}_e^{(ijk)} + \mathbf{b}_s^{mn} = -\frac{a}{4}[ijk] + \frac{a}{4}[mn0] \tag{281}$$

where a is the lattice constant and the subscripts e and s stand for the edge and screw components of the Burgers vector, respectively. Index k takes values ±2, while i, j, m, and n take values ±1, with the condition $|\boldsymbol{l}\bullet\mathbf{b}| = lb\cos(\pi/3)$ (the core is 60° from the Burgers vector). In Table VI we list the possible values of i, j, k, m, and n and the direction of the dislocation cores for the sixteen 60° dislocations we are considering, according to dislocation type as follows. 60° dislocations are termed α or β according to whether their cores are composed of arsenic or gallium atoms, respectively.[115] Furthermore, 60° dislocations are termed negative or positive depending on whether the dislocation extra half plane is introduced from the surface toward the interior of the crystal or in the opposite direction.

Reproduced with permission of the copyright owner. Further reproduction prohibited without permission.

Table VI. Conventions used for the indices i, j, k, m, and n and direction of the dislocation cores for the sixteen 60° dislocations with cores parallel to the (001) surface. Indices (i, j, k) and (m, n) determine the orientations of the edge and screw components of the Burgers vector, respectively.

Dislocation Type	i	j	k	m	n	Core Direction (l)
α^+	1	1	2 -2	±1 ∓1	∓1 ±1	$[1\bar{1}0]$
α^-	1	-1	2 -2	±1 ∓1	±1 ∓1	[110]
β^+	-1	1	2 -2	±1 ∓1	±1 ∓1	[110]
β^-	-1	-1	2 -2	±1 ∓1	∓1 ±1	$[1\bar{1}0]$

The strain tensor for the edge components of the dislocations can be obtained by the procedure outlined by Eshelby, Read, and Shockley to be[117]

$$\mathbf{e}_e^{ijk} = \frac{1}{2}\begin{bmatrix} 2i\delta_{ij}e_{11} & 0 & ik\delta_{ij}e_{13} \\ 0 & 2i(\delta_{ij}-1)e_{11} & ik(\delta_{ij}-1)e_{13} \\ ik\delta_{ij}e_{13} & ik(\delta_{ij}-1)e_{13} & 2je_{33} \end{bmatrix} \tag{282a}$$

where e_{11}, e_{13}, and e_{33} are magnitudes of the only independent strain components and δ_{ij} is the Kronecker delta function.

The screw component tensor is a function of two independent strain components, e_{12} and e_{23} and is written as

Reproduced with permission of the copyright owner. Further reproduction prohibited without permission.

$$\mathbf{e}_s^{mn} = \begin{bmatrix} 0 & -ne_{12} & \delta_{mn}e_{23} \\ -ne_{12} & 0 & (1-\delta_{mn})e_{23} \\ \delta_{mn}e_{23} & (1-\delta_{mn})e_{23} & 0 \end{bmatrix} \tag{282b}$$

Since we are only considering in the linear piezo-optic contributions to the RDA spectra, we may average the strain tensors over the (100) surface. In addition, since we have a free surface, the average stress components $<\sigma_{33}> = <\sigma_{23}> = 0$, leading to the relations

$$\begin{aligned} &< e_{33} > = -\frac{c_{12}}{c_{11}} < e_{11} > \\ &< e_{23} > = < e_{32} > = 0 \end{aligned} \tag{283}$$

where c_{ij} are the conventional components of the elastic stiffness tensor (Young's modulus)[114]

This leads to the average strain tensors[30]

$$\left\langle \mathbf{e}_e^{ijk} \right\rangle = \left\langle e_{11} \right\rangle \begin{bmatrix} i\delta_{ij} & 0 & 0 \\ 0 & i(\delta_{ij}-1) & 0 \\ 0 & 0 & -j\frac{c_{12}}{c_{11}} \end{bmatrix} \tag{284a}$$

and

Reproduced with permission of the copyright owner. Further reproduction prohibited without permission.

$$\left\langle \mathbf{e}_s^{mn} \right\rangle = -n\langle e_{12}\rangle \begin{bmatrix} 0 & 1 & 0 \\ 1 & 0 & 0 \\ 0 & 0 & 0 \end{bmatrix} \tag{284b}$$

which depend only on the parameters e_{11} and e_{12}.

The tensor in Eq. (284a) leads to an anisotropically stressed surface layer of thickness $\approx l$ if the density of α and β dislocations is different.

The Hamiltonian for the combined spin-orbit and dislocation-induced strain interactions can be written as[112]

$$\begin{aligned} H = & -a\langle e_{11}\rangle j\left(1-\frac{c_{12}}{c_{11}}\right)-\frac{3}{2}b\langle e_{11}\rangle j\left[\hat{L}_x^2+\hat{L}_y^2-2\frac{c_{12}}{c_{11}}\hat{L}_z^2+\frac{2}{3}\left(\frac{c_{12}}{c_{11}}-1\right)\hat{\mathbf{L}}^2\right] \\ & -\frac{\sqrt{3}}{2}d\langle e_{11}\rangle j(\hat{L}_x\hat{L}_y+\hat{L}_y\hat{L}_x)+\frac{\Delta_0}{3}\hat{\mathbf{L}}\bullet\hat{\mathbf{S}} \end{aligned} \tag{285}$$

where $\hat{\mathbf{L}}$ is the angular momentum operator, $\hat{\mathbf{S}}$ is the spin operator, and a, b, and d are the deformation potentials for hydrostatic, tetragonal, and orthorhombic deformations, respectively.

Using the Hamiltonian in Eq. (285) along with the valence band wavefunctions at the Γ point of the BZ given in Eq. (276), one finds that the E_0 is split and anisotropic. That is the highest lying valence band is split by an amount[30]

Reproduced with permission of the copyright owner. Further reproduction prohibited without permission.

$$\Delta_{E_0} = \pm j\langle e_{11}\rangle\sqrt{b^2\left(1+2\frac{c_{12}}{c_{11}}\right)^2 + d^2} \tag{286}$$

and the interband transition matrix anisotropy is defined by

$$\frac{\Delta M^{\pm}}{M} = \frac{M_{[110]} - M_{[1\bar{1}0]}}{M_{[110]} + M_{[1\bar{1}0]}} = \pm\frac{3}{8}(2\delta_{ij} - 1) \tag{287}$$

where $M_{[110]}$ and $M_{[1\bar{1}0]}$ are optical transition strengths for light polarized along the $[110]$ and $[1\bar{1}0]$ directions, respectively. The ± refers to the upward shifted (+) or downward shifted (-) valence band states.

2.4.3 Ordering

In this section, we discuss the RDA signal of CuPt-type ordering, that is ordering along the $[111]$ direction of a zincblende alloy. Some insight into the problem can be gained by considering the completely ordered case. For example, if the structure of completely ordered GaInP along the $[111]$ direction would be repeated planes of Ga, P, In, P, …. Thus for a perfectly ordered sample, the crystal is no longer cubic, but can be considered as a lattice twice as long in one direction as the previous cubic lattice with a BZ half as

Reproduced with permission of the copyright owner. Further reproduction prohibited without permission.

long as the original in this direction. Points of the band previously corresponding to different **k** can now be folded upon each other. Figure 52(a) shows a schematic band for the zincblende structure along the Λ direction. Figure 52(b) shows the situation for an ordered material. The BZ now ends at $\mathbf{k} = \pi/2a[111]$ instead of $\pi/a[111]$, and the part of the band originally between $\mathbf{k} = \pi/2a[111]$ and $\pi/a[111]$ now shows up as a new band in the smaller BZ, which we call the zone-folded band.

The folded bands interact with the unfolded ones with several effects.[118] For example, E_0 transition is split, due to the splitting of the valence band ($\Gamma_{8v} \rightarrow \Gamma_{4v},\Gamma_{5v} + \Gamma_{6v}$). Also E_0 is reduced, due to the lowering of the lowest lying (Γ_{6c}) conduction band produced by its $\mathbf{k}\cdot\mathbf{p}$ interaction with the zone folded L_{6c} band. Fig. 53 shows the states at the center of the zincblende BZ plus a zone folded state from the lowest lying L_{6c} conduction band of the original zincblende BZ.

Reproduced with permission of the copyright owner. Further reproduction prohibited without permission.

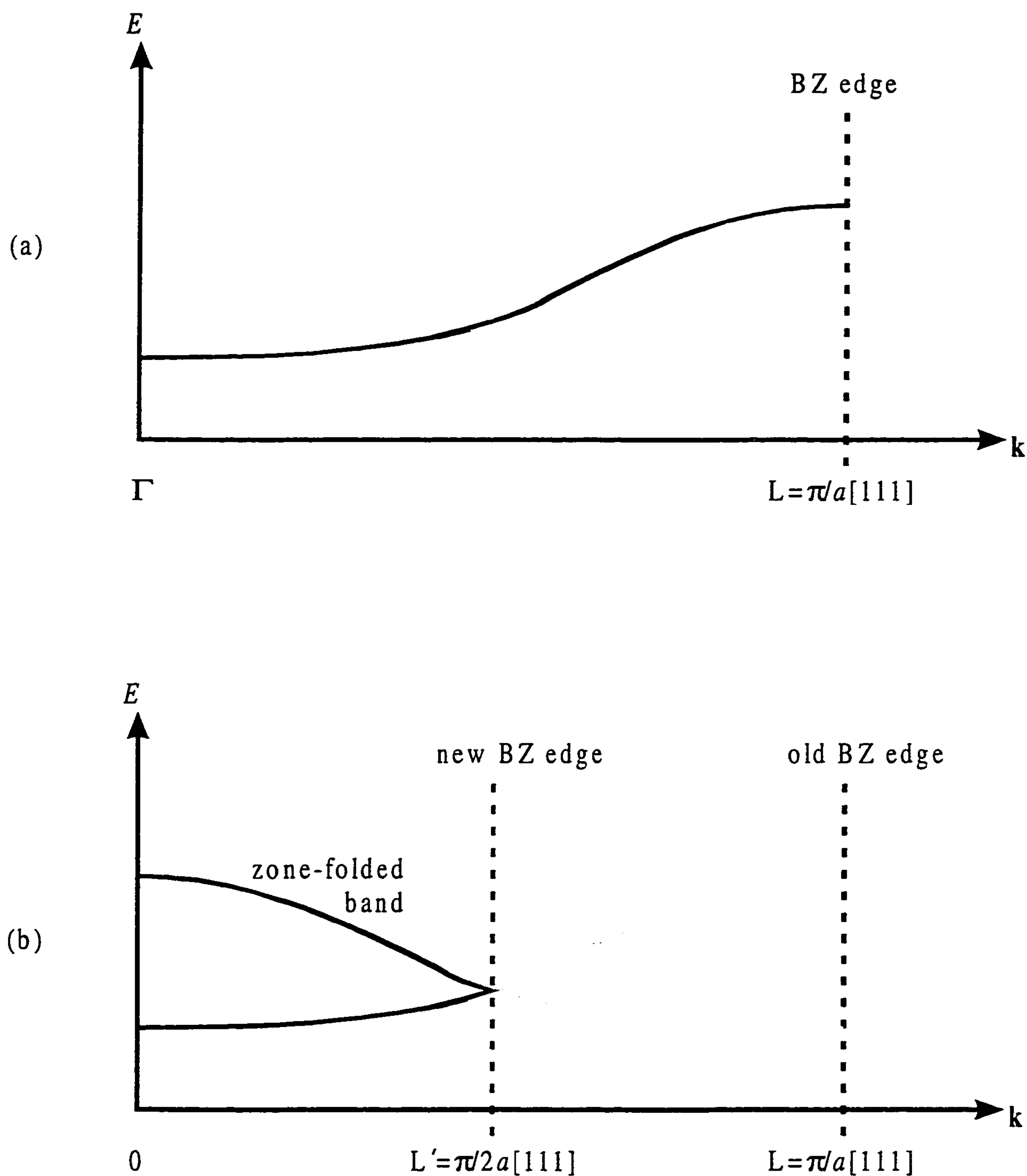

Figure 52. Illustration of zone folding due to complete CuPt-type ordering. (a) shows a schematic band for the zincblende structure along the Λ direction. (b) shows the situation for an ordered material. The BZ now ends at **k** = $\pi/2a[111]$ instead of $\pi/a[111]$, and the part of the band originally between **k** = $\pi/2a[111]$ and $\pi/a[111]$ now shows up as a new band in the smaller BZ, which we call the zone-folded band.

Reproduced with permission of the copyright owner. Further reproduction prohibited without permission.

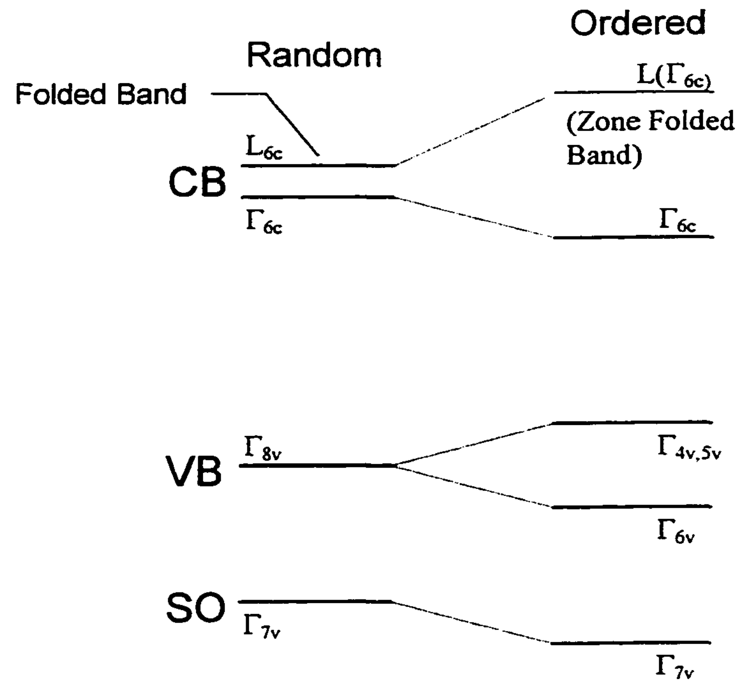

Figure 53. Schematic depiction of states for random and ordered alloys. Two major effects of the zone folding are the splitting of the E_0 transition due to the splitting of the valence band ($\Gamma_{8v} \rightarrow \Gamma_{4v},\Gamma_{5v} + \Gamma_{6v}$) and the reduction of E_0 due to the lowering of the lowest lying (Γ_{6c}) conduction band.

To be more precise, we follow the arguments given by Wei and Zunger.[119]

The Hamiltonian describing the valence band splitting due to atomic ordering is of the same form as that due to a [111] strain, which in our notation is written as[112]

$$H^O = \Delta^O(\eta)[\hat{L}_x\hat{L}_y + \hat{L}_y\hat{L}_x + \hat{L}_x\hat{L}_z + \hat{L}_z\hat{L}_x + \hat{L}_y\hat{L}_z + \hat{L}_z\hat{L}_y] \tag{288}$$

where $\Delta^O(\eta)$ is the crystal field splitting due to the atomic ordering and η is the ordering parameter (η=1 for complete ordering and η=0 for a random alloy). Using the

Reproduced with permission of the copyright owner. Further reproduction prohibited without permission.

Hamiltonian in Eq. (288) along with the valence band wavefunctions at the Γ point of the BZ given in Eq. (276), one finds that the E_0 is split and anisotropic. That is the highest lying valence band is split by $\Delta^{O}(\eta)$ and the interband transition matrix anisotropy defined in Eq. (277) is

$$\frac{\Delta M^{\pm}}{M} = \pm\frac{1}{2} \tag{289}$$

where the + and - refers to the upward and downward shifted valence band states, respectively. We note that the above result is only valid if $\Delta^{O}(\eta)$ is small enough that we don't need to consider other bands, that is $\Delta^{O}(\eta) << \Delta_0$. Reference 119 also considers the case of $\Delta^{O}(\eta) >> \Delta_0$.

Reproduced with permission of the copyright owner. Further reproduction prohibited without permission.

2.5 Experimental Results

2.5.1 Undoped *n*- and *p*-doped Low Temperature Grown GaAs

We have evaluated the "effective near surface electric fields", "effective depletion widths" and the sign (*n*-type/upward band bending) of the near surface electric fields in undoped as well as *n*-($5x10^{18}$ cm^{-3})-and *p*-($5x10^{18}$ cm^{-3}, $2x10^{19}$ cm^{-3} and $2x10^{20}$ cm^{-3}) doped low-temperature grown (LTG) GaAs (001) using the optical method of RDA in the vicinity of the spin-orbit split "E_1", "E_1+Δ_1" optical features. Even for the highest *p*-doping the surface band-bending is still *n*-type. Our results are in good agreement with a self-consistent Poisson's continuity calculation of the "effective near surface electric fields" assuming deep donor ($1x10^{20}$ cm^{-3}) and acceptor ($1x10^{19}$ cm^{-3}) trap densities and midgap surface Fermi level pinning except for the most heavily *p*-doped sample. In this case, the experiment and simulation can be brought into accord by assuming p=$4x10^{19}$ cm^{-3}, i.e., not all acceptors are electrically active. This experiment provides valuable information about the nature of the defects and surface Fermi level pinning in LTG:GaAs.

Reproduced with permission of the copyright owner. Further reproduction prohibited without permission.

2.5.1.1 Introduction

Low temperature grown (LTG) GaAs, i.e., layers grown by molecular beam epitaxy (MBE) at substrate temperatures between 250-300° C, possess many interesting electronic properties due to excess arsenic incorporated during growth.[120] In as-grown LTG:GaAs material, the excess arsenic results in a large concentration of point defects ($1x10^{20}$ cm^{-3}), due primarily to arsenic antisite defects. The pinning of the Fermi level near midgap in this material is generally associated with the point defects.[121,122] The stability of LTG:GaAs against oxidation in air recently has been demonstrated using scanning tunneling microscopy.[123]

LTG:GaAs has been employed in a number of important applications.[120] First, when LTG:GaAs is annealed at temperatures between 600-900° C, the excess As in the form of antisite defects coalesces into As precipitates, and, hence forms an elemental As phase of As clusters. These precipitates behave as buried Schottky barriers. As such, they exhibit 0.7 eV Schottky barrier heights and act as recombination centers for excess carriers. This property has resulted in realization of state of the art high speed photodetector devices, with responsivities of nearly 0.1 A/W and cut-off frequencies of 40 GHz. This material has been shown to have useful non-linear optical properties. Also, in the unannealed state, LTG:GaAs has been used to form excellent non-alloyed ohmic contacts when used in tandem with a thin layer of n^{++} GaAs.

Reproduced with permission of the copyright owner. Further reproduction prohibited without permission.

In order to gain more information about the nature of the surface and associated electric fields in this material, we have performed a RDA study of undoped, *n*-doped and *p*-doped LTG:GaAs (001). It has been demonstrated that RDA can be employed to determine the sign and magnitude of near surface electric fields in zincblende-type semiconductors (see section 2.4.1). By comparison of the experimental data with a self-consistent Poisson's, continuity calculation based on the defect properties and surface Fermi level pinning, we evaluated the "effective near surface electric field", $\mathscr{E}_{eff}$, and an "effective depletion width" of ≤ 22Å. The sign of the RDA signal shows that even in the most heavily *p*-doped sample, the electric field is still *n*-type (upward band bending).

2.5.1.2 Experimental Details

We measured five unannealed LTG:GaAs samples whose nominal dopings are given in Table VII. Sample #2 consisted of a not-intentionally doped (NID) LTG:GaAs film grown on a semi-insulating GaAs (001) substrate in a Gen II MBE system. A 2000 Å thick buffer layer was grown at 580° C prior to lowering the growth temperature to grow the LTG layer. A 5000 Å thick LTG layer was grown at a substrate temperature of 250° C as measured by a thermocouple. At this temperature the excess arsenic concentration is between 1 and 1.5 percent. The layers were grown at a rate of 1 μm/hr with As_2. Sample Nos. 1, 3, 4, and 5 were grown under similar conditions but were either *n*-doped at $5x10^{18}$ cm^{-3} (sample #1) or *p*-doped at levels of $5x10^{18}$ cm^{-3} (sample #3), $2x10^{19}$ cm^{-3} (sample #4), and $2x10^{20}$ cm^{-3} (sample #5).

Reproduced with permission of the copyright owner. Further reproduction prohibited without permission.

Table VII. Doping levels, $\mathscr{E}_{eff}$ (experiment and simulation), $\mathscr{E}(0)$, γ, $1/\alpha_{eff}$, and V_{BI} for the five LTG:GaAs samples

Sample	Doping (10^{18} cm^{-3})	$\mathscr{E}_{eff}$ (kV/cm)		$\mathscr{E}(0)$ (kV/cm)	γ	$1/\alpha_{eff}$ (Å)	V_{BI} (meV)
		Experiment	Simulation				
1	5 (n-type)	277	276	1550	17.8	22.2	344
2	undoped	220	230	1380	16.6	20.8	287
3	5 (p-type)	176	200	1240	16.1	20.4	253
4	20 (p-type)	150	135	850	16.1	20.0	170
5	200(p-type)[a]	60	-412[c]	-3660[c]	11.3[c]	13.7[c]	-500[c]
	40(p-type)[b]		50	350	14.3	18.0	63

[a] intended doping
[b] active doping
[c] *p*-type band bending

In addition to the LTG:GaAs, three normally grown GaAs samples were used in order to calibrate the RDA signal based on known electric fields. Sample #R1 consisted of 1000 Å of undoped GaAs fabricated on an *n*-type (Si=2×10^{18} cm^{-3}) buffer, 1 μm thick, on an n^+ (001) substrate. It has been shown that such a configuration has a uniform electric field in the undoped region due to Fermi level pinning at the surface.[111] The magnitude of this electric field (6.5×10^4 V/cm) was evaluated from the observed Franz-Keldysh oscillation (FKOs) using photoreflectance.[111] Sample Nos. R2 and R3 consisted of 0.5 μm 1×10^{18} cm^{-3} Si or Be doped layers on n^+ or p^+ substrates, respectively.

The RDA data was taken according to the procedure in section 2.3 and the background was eliminated using Eq. (273).

Reproduced with permission of the copyright owner. Further reproduction prohibited without permission.

Plotted in Fig. 54 by the dotted, solid, dashed, and dot-dashed curves are the RDA spectra of sample Nos. R1, 2, R2, and R3 respectively. The positions of the "E_1" (2.88 eV) and "E_1+Δ_1" (3.11 eV) features[61] are denoted by arrows at the bottom of the figure. It can be seen that the phases of R3 is opposed to the others. Thus the band bending of the NID LTG:GaAs material (sample #2) is clearly *n*-type (upward band bending). Also the amplitude of the RDA signal for sample #2 lies between that of sample Nos. R1 and R2.

Plotted in Fig. 55 by the solid, dotted, dashed, dot-dashed, and dot-dot-dashed curves are the RDA spectra of sample Nos. #1-#5, respectively, in the range 2.5-3.5 eV. The positions of the "E_1" (2.88 eV) and "E_1+Δ_1" (3.11 eV) features[61] are denoted by arrows at the bottom of the figure. It can be seen that the phases of all these samples are the same and correspond to an *n*-type (upward) band-bending.

2.5.1.2 Experimental Results and Discussion

In order to more accurately evaluate the amplitude of the linear electro-optic effect in the vicinity of the "E_1" and "E_1+Δ_1" features, we have taken the numerical derivative with respect to photon energy of the spectra [designated as $d(\Delta R/R)/dE$] of the LTG:GaAs (solid line) and samples R1 (dotted line) and R2 (dashed line). These results, which exhibit three extrema (A, B, and C) are shown in Fig. 56. As a measure of the amplitude of the linear eletro-optic effect, we have evaluated

Reproduced with permission of the copyright owner. Further reproduction prohibited without permission.

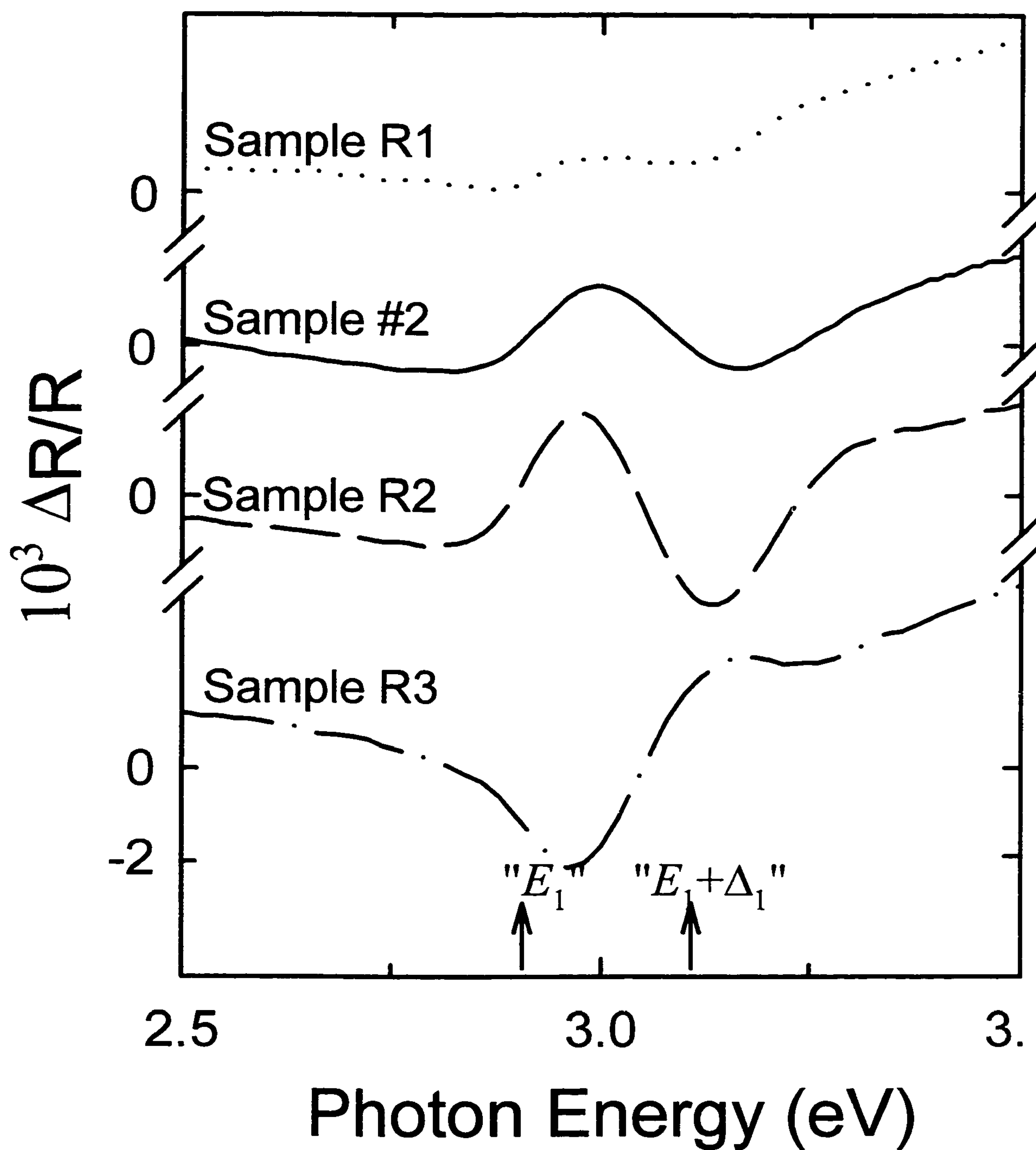

Figure 54. RDA spectra of sample Nos. R1 (dotted line), 2 (solid line), R2 (dashed line), and R3 (dot-dashed line). The positions of the "E_1" and "$E_1+\Delta_1$" features are denoted by arrows at the bottom of the figure.

Reproduced with permission of the copyright owner. Further reproduction prohibited without permission.

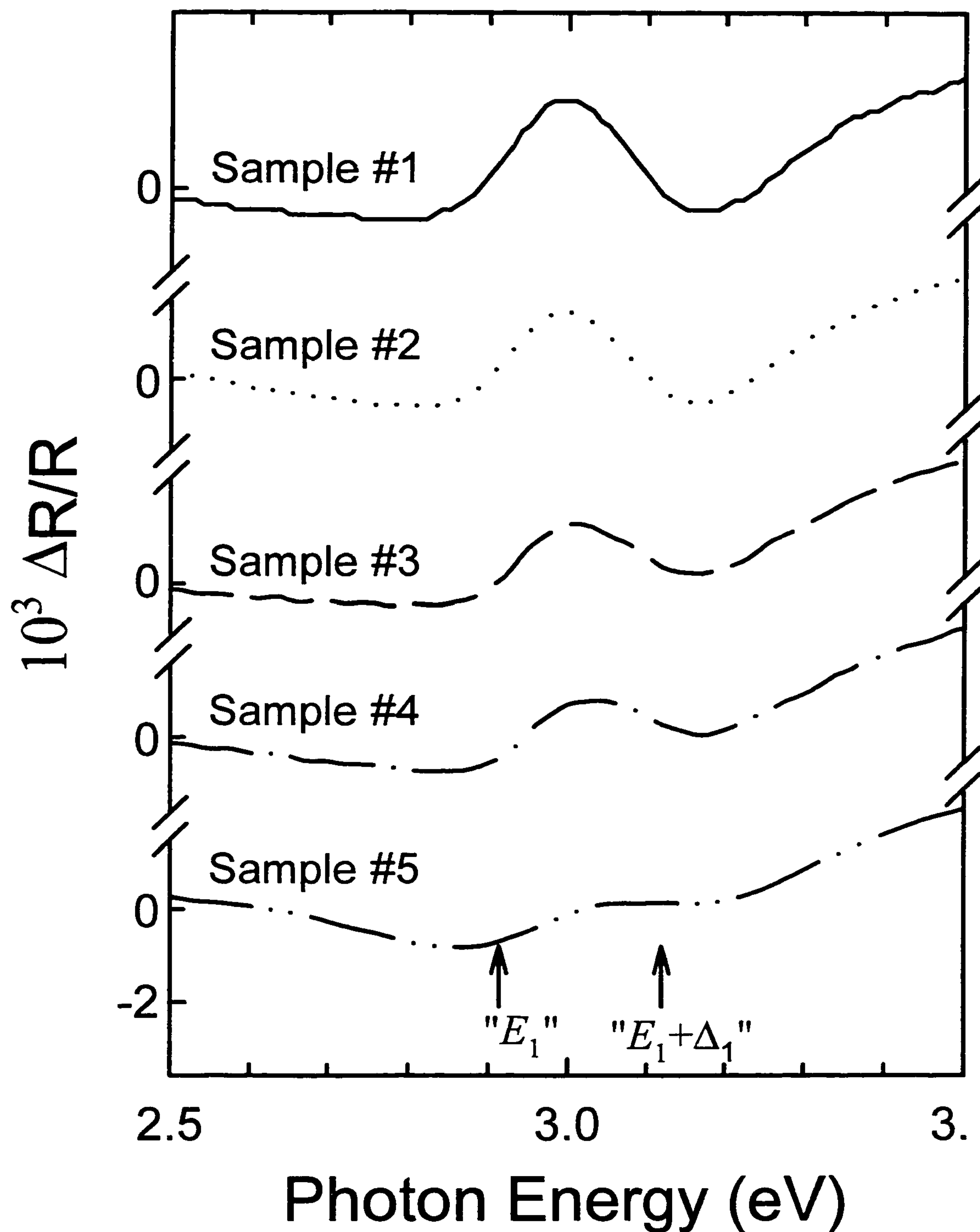

Figure 55. RDA spectra of sample Nos. 1 (solid line), 2 (dotted line), 3 (dashed line), 4 (dot-dashed line), and 5 (dot-dot-dashed line). The positions of the "E_1" and "E_1+Δ_1" features are denoted by arrows at the bottom of the figure.

Reproduced with permission of the copyright owner. Further reproduction prohibited without permission.

$$\frac{\left|\frac{d(\Delta R/R)}{dE}\right|_{AB} + \left|\frac{d(\Delta R/R)}{dE}\right|_{BC}}{2} \tag{290}$$

The ratios of the amplitudes of this signal for sample Nos. R1, 2, and R2 are 1:2.9:6, respectively.

Because of the high doping level in sample No. R2, it was not possible to observe FKOs.[111] Therefore, for conventional SCR sample No. 3 (with width of SCR ≫ penetration depth of the light), the surface electric field $\mathscr{E}_s$ = 4.6 x 10^5 V/cm) has been evaluated for the relation[124]

$$\mathscr{E}_s = \sqrt{\frac{8\pi q N_D}{\varepsilon_0}\left(V_{BI} - V_{pv} - \frac{k_B T}{q}\right)} \tag{291}$$
$$V_{BI} = V_{F,s}^{c} - V_{F,b}^{c}$$

where N_D is the donor concentration (1 x 10^{18} cm^{-3}), ε_0 (=13) is the static dielectric constant, V_{BI} is the built in voltage (that is the difference between surface and bulk potentials), V_{pv} is the reduction in the built in voltage due to the photovoltaic effect, and $V_{F,s}^{c}$ and $V_{F,b}^{c}$ are the surface and bulk Fermi levels (relative to the conduction band edge), respectively. It is well known that in as-grown *n*-type GaAs the Fermi level is pinned midgap[125] so that $V_{F,s}^{c} = 0.71$ V. For N_D = 1 x 10^{18} cm^{-3}, $V_{F,b}^{c}$ lies 0.075 eV above the conduction band edge.

Reproduced with permission of the copyright owner. Further reproduction prohibited without permission.

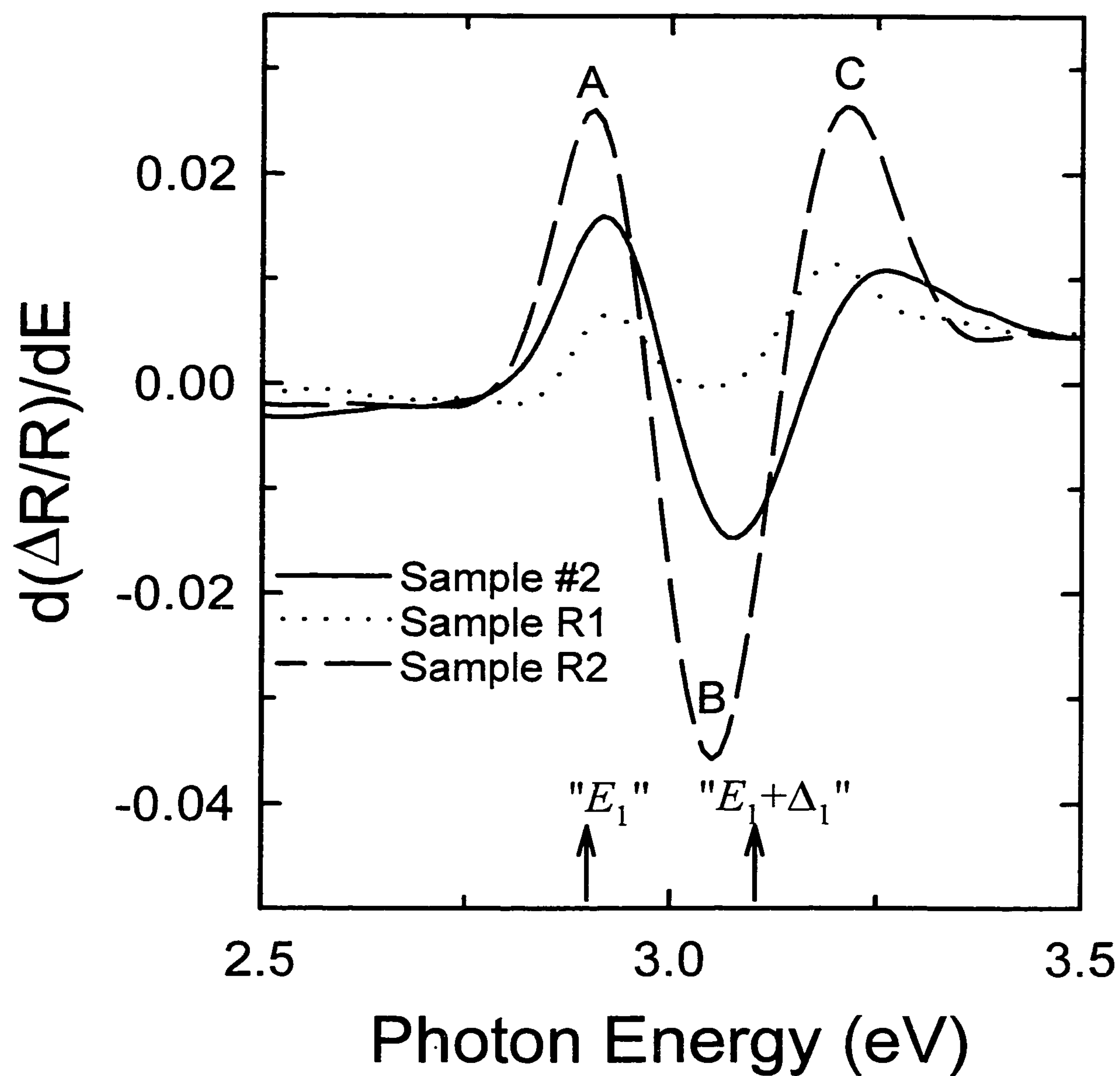

Figure 56. $d(\Delta R/R)/dE$ spectra of sample Nos. 2 (solid line), R1 (dotted line), and R2 (dashed line). The positions of the "E_1" and "$E_1+\Delta_1$" features are denoted by arrows at the bottom of the figure.

Reproduced with permission of the copyright owner. Further reproduction prohibited without permission.

From a linear interpolation between the fields of sample Nos. R1 and R2, we find an "effective near surface electric field", $\mathscr{E}_{eff} = 2.2 \times 10^5$ V/cm, in the NID LTG:GaAs material (sample #2). The interpretation of $\mathscr{E}_{eff}$ will be discussed below.

The numerical derivative of the signal ($\Delta R/R$) with respect to photon energy for sample Nos. 1-5 are shown in Fig. 57 by the dotted, solid, dashed, dot-dashed, and dot-dot-dashed curves, respectively. The ratios of the amplitude of the signal obtained from Eq. (290) for samples 1, 2, 3, 4, and 5 are 1.26:1.00:0.08:0.68:0.28, respectively. Sample #5 had a signal almost identical to undoped MBE GaAs grown at normal temperature (T ≈600 °C), i.e., near flatband and slightly *n*-type.

It has been shown that[23]

$$\frac{\Delta R}{R} = \mathrm{Re}\{\frac{<\Delta\tilde{\varepsilon}>}{\sqrt{\varepsilon}(\varepsilon-1)}\}$$
$$<\Delta\tilde{\varepsilon}> = 2i\kappa_L \int_0^\infty e^{2i\kappa_L z}\Delta\tilde{\varepsilon}(z)\mathrm{d}z \qquad (292)$$

where $\Delta\tilde{\varepsilon}(z)$ is the electric field induced perturbation of the dielectric function and κ_L is the unperturbed complex propagation vector of the light. At 3.0 eV for GaAs, the propagation vector, $\kappa_L = (6.85+i2.96)\times10^{-3}$ Å^{-1}.[47] For the LEO effect $\Delta\tilde{\varepsilon}(z) \propto \mathscr{E}(z)$ (see section 2.4.1), where $\mathscr{E}(z)$ is the electric field as a function of position, the surface being at z=0. So Eq. (292) becomes

Reproduced with permission of the copyright owner. Further reproduction prohibited without permission.

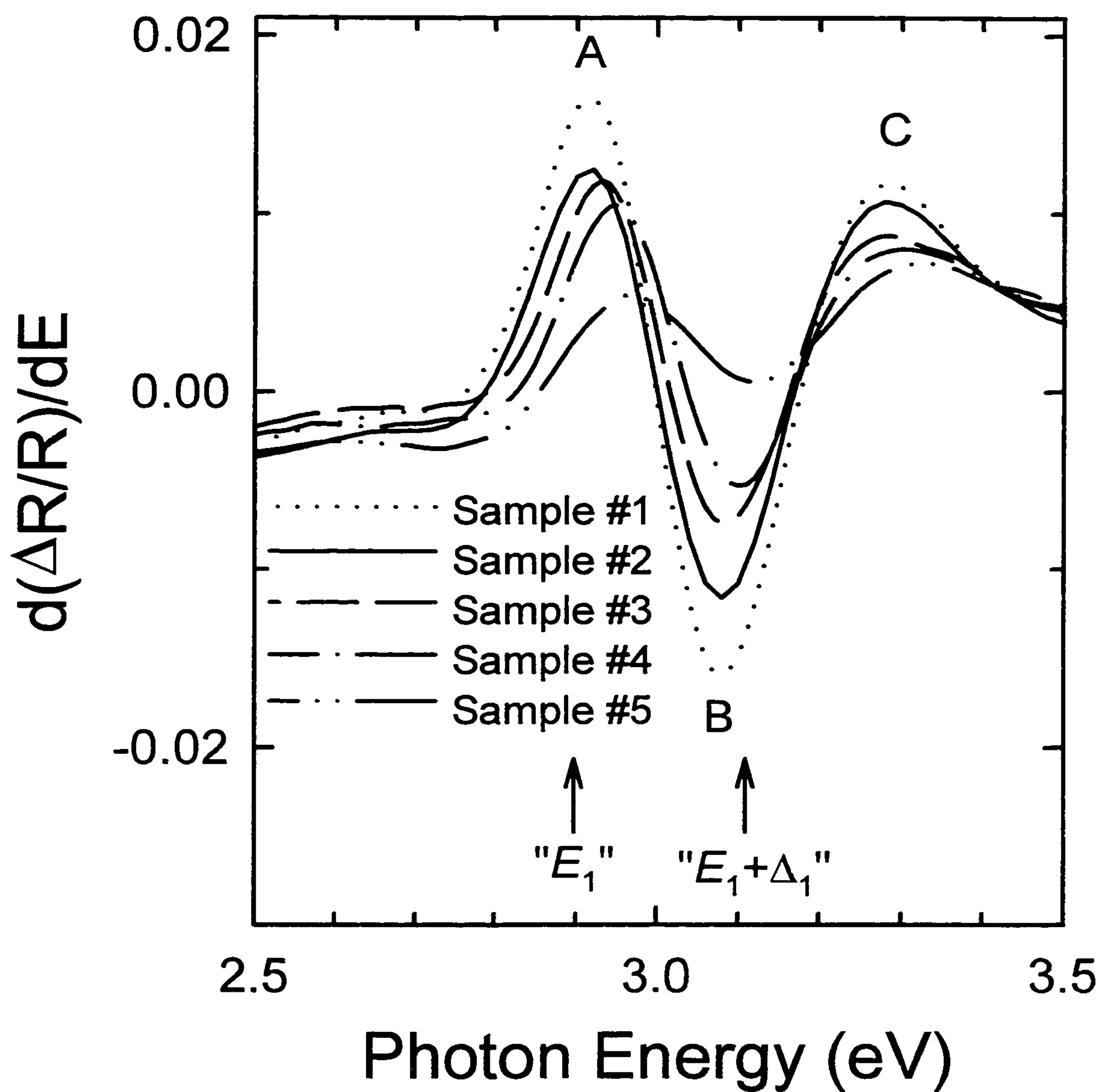

Figure 57. $d(\Delta R/R)/dE$ spectra of sample Nos. 1 (solid line), 2 (dotted line), 3 (dashed line), 4 (dot-dashed line), and 5 (dot-dot-dashed line). The positions of the E_1 and E_1+Δ_1 features are denoted by arrows at the bottom of the figure.

Reproduced with permission of the copyright owner. Further reproduction prohibited without permission.

$$< \Delta\tilde{\varepsilon} > \propto \kappa_L \int_0^\infty e^{2i\kappa_L z} \mathscr{E}(z) \mathrm{d}z \tag{293}$$

This states that the change in dielectric function due to the LEO effect for the field at each depth makes a contribution to the measured signal which depends on the electric field at the depth and the depth compared to the light penetration depth.

In contrast to previous experiments on semiconductors with conventional space charge regions (SCR), in LTG:GaAs there is no simple analytical expression for $\mathscr{E}(z)$. We define an "effective surface field", $\mathscr{E}_{\text{eff}} \propto \Delta R/R$ as the uniform electric field which would cause the given $\Delta R/R$ according to Eq. (293). The observed values of $\mathscr{E}_{\text{eff}}$ obtained from Eq. (1) are listed in Table VII.

In order to evaluate $\mathscr{E}$(z) we have performed a self-consistent Poisson's, continuity calculation[126] assuming (a) a donor trap density (N_{TD}) of $1\text{x}10^{20}$ cm^{-3} having a Gaussian distribution of states with width σ(= 0.2 eV), the peak of the Gaussian distribution occurring 0.45 eV below the conduction band, (b) an acceptor trap density (N_{TA}) of $1\text{x}10^{19}$ cm^{-3} having a Gaussian distribution of states with width σ(= 0.2 eV), the peak of the Gaussian distribution occurring 0.45 eV above the valence band, and (c) midgap surface Fermi level pinning.[127] Shown in Fig. 58 by the solid, dotted, dashed, dot-dashed, and dot-dot-dashed curves are the results of this calculation of $\mathscr{E}(z)$ for samples 1-5, respectively. The electric field does not vary linearly with position from the surface, as

Reproduced with permission of the copyright owner. Further reproduction prohibited without permission.

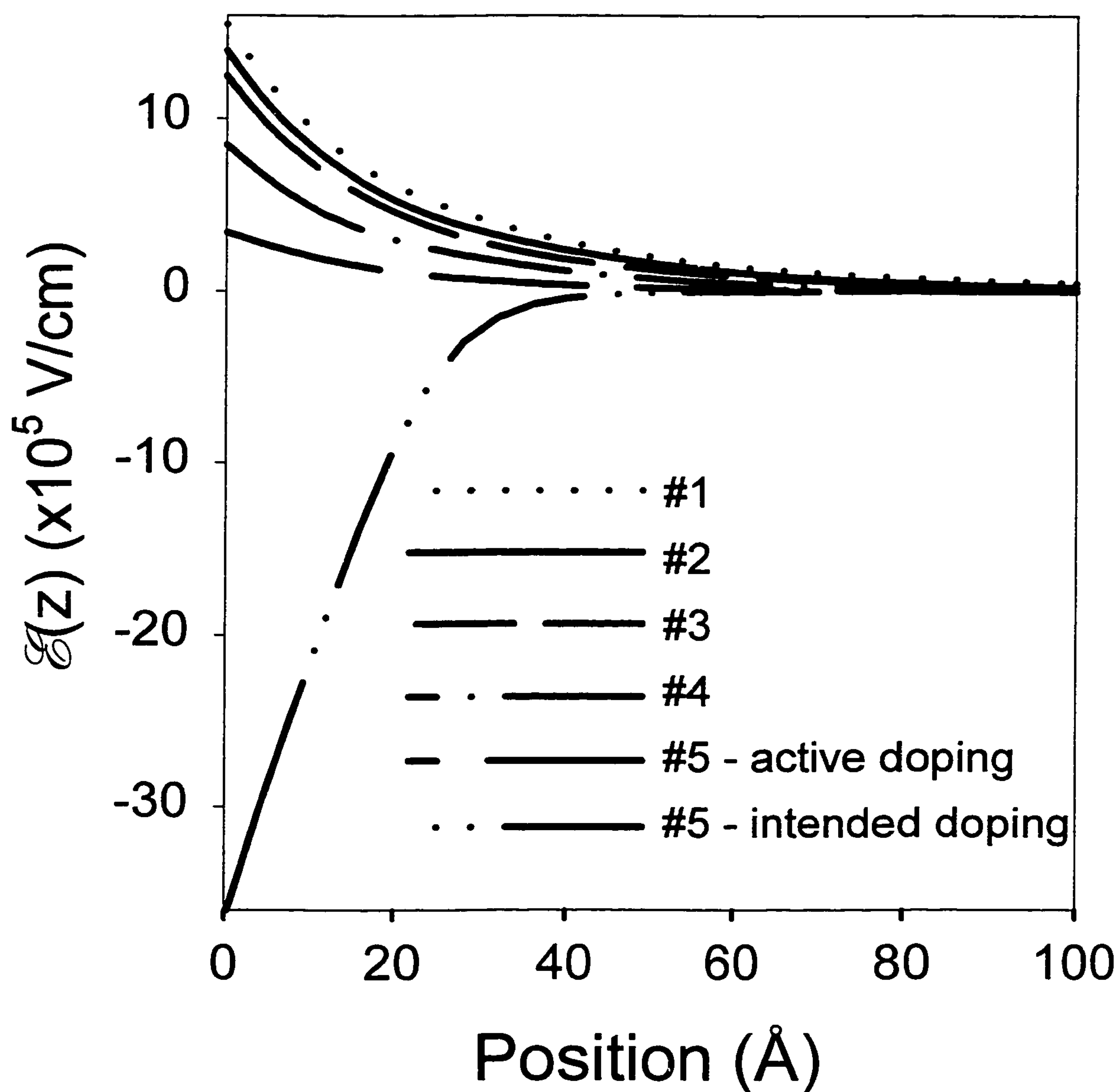

Figure 58. Self-consistent Poisson's, continuity calculation of the field distribution $\mathscr{E}(z)$ for sample Nos. 1 (solid line), 2 (dotted line), 3 (dashed line), 4 (dot-dashed line), 5 assuming complete doping (dot-dot-dashed line), and 5 assuming an incomplete doping of p=4x10^{19} cm^{-3} (long dashed line).

Reproduced with permission of the copyright owner. Further reproduction prohibited without permission.

would be the case for a fully depleted SCR. The values of the surface field $\mathscr{E}(0)$ are listed in Table VII.

For the first four samples, the simulation is in good agreement with experiment. For sample #5, based on the intended p-doping ($2\text{x}10^{20}$ cm^{-3}), the simulation exhibits p-type (downward) band bending and a large surface electric field, $\mathscr{E}(0)$, as shown by the dot-dot-dashed line in Fig. 58 (labeled p $2\text{x}10^{20}$). These effects are not observed in the data (see Fig. 1). Good agreement between the experiment and the simulation can be obtained if we assume p=$4\text{x}10^{19}$ cm^{-3}, i.e., not all the dopants are active. This result is displayed by the long dashed line in Fig. 58 (labeled p $4\text{x}10^{19}$).

We have numerically integrated Eq. (293) with the computed $\mathscr{E}(z)$ of Fig. 58 and find that

$$\text{Re} < \Delta\tilde{\varepsilon} > \propto \gamma \mathscr{E}(z) \tag{294}$$

The values of γ being listed in Table VII. This procedure also yields the simulation "effective near surface electric fields", $\mathscr{E}_{eff}$, given in Table VII. These values are in good agreement with our experimental results if we assume the maximum p-type doping is about 4 x 10^{19} cm^{-3} as mentioned in the previous paragraph.

Although $\mathscr{E}(z)$ does not have a simple analytical behavior, it is close to an exponential form (see Fig. 58). Thus, an effective depletion width can be evaluated if we assume that:

Reproduced with permission of the copyright owner. Further reproduction prohibited without permission.

$$\mathscr{E}(z) = \mathscr{E}(0)\, e^{-\alpha_{eff} z} \qquad (295)$$

where the quantity $1/\alpha_{eff}$ can be considered as the "effective depletion width". Using Eqs. (293) and (295) to yield $\mathscr{E}_{eff} = \gamma\, \mathscr{E}(0)$, we find the values of $1/\alpha_{eff}$ listed in Table VII. Note that all of these correspond to an "effective depletion width" of ≤ 22Å.

We can evaluate the built in field, V_{BI}, also listed in Table VII, as:

$$V_{BI} = \int_0^\infty \mathscr{E}(z)\,dz = \frac{\mathscr{E}(0)}{\alpha_{eff}} \qquad (296)$$

Chen *et al* also have recently reported a RDA spectroscopy study of LTG:GaAs (001), including the effects of post growth annealing.[25] These authors conclude that V_{BI} for unannealed NID material is about 0.1 V (relative to the conduction band). We find for our NID material $V_{BI} \approx 0.29$ V. However, Ref. 25 erroneously states that all the donor defects are ionized. Our result is consistent with a bulk Fermi level ≈ 0.45 V below the conduction band (as reported in Ref. [127] and also deduced from our simulation) and midgap surface Fermi-level pinning.

Reproduced with permission of the copyright owner. Further reproduction prohibited without permission.

2.5.2 High Electron Mobility Transistors Structures

In this section, we present a study of the RDA signal induced by the difference of misfit (60°) dislocation density along the [110] direction compared to the $[1\bar{1}0]$ in InGaAs/AlGaAs/GaAs high electron mobility transistors (HEMT) structures with InGaAs quantum well (QW) regions thicker than the critical thickness for strain relaxation. Although the theory of how such 60° dislocations create an RDA signal has been worked out (see section 2.4.2), to our knowledge, the technique has not been used to study misfit dislocations caused by strain relaxation. The effectiveness of RDA for this problem is made possible by the elimination of signal due to other effects at E_0. First there is no LEO effect (section 2.4.1) because of the symmetry at the Γ point of the BZ. Second there is no signal due to the biaxial (001) strain in the sample because both the [110] and $[1\bar{1}0]$ are perpendicular to the strain axis and thus have the same interband transition strength.[113] Meshkinpour *et al.*[128] have presented a study of how the number of threading dislocations and layer thickness affect the number of misfit dislocations in InGaAs/AlGaAs/GaAs HEMT's, similar to the ones used in this study using TEM. Since the system is already characterized, this allows us to correlate our RDA signal to the misfit dislocation densities.

Reproduced with permission of the copyright owner. Further reproduction prohibited without permission.

2.5.2.1 Introduction

Recent improvements in strained-layer epitaxy have provided improved electronic and optoelectronic systems and new wavelengths and frequencies are now at hand. For example, recent advances in the growth of stable strained-layer $Ga_{1-x}Al_xAs$ / $In_yGa_{1-y}As$ / GaAs QW's have produced HEMT structures with peak carrier velocities exceeding those of $Ga_{1-x}Al_xAs$ / GaAs alone.

In strained layer epitaxy, we can obtain two very different structures: (a) elastically strained (pseudomorphic) without the presence of unwanted effects such as misfit dislocations or (b) strain relief due to misfit dislocations if the strain goes beyond the limits of elastic deformation

In devices, it is desirable to prevent strain relieved structures as they carry defects and these defects degrade the performance of most devices by lowering the conductivity of the carriers. Particularly in HEMT's, the most important factor is the conductivity of the carriers, which influences the speed of response of a device.

A variety of methods are used to evaluate dislocation density and arrangement, such as etching, transmission electron microscopy (TEM),[129] scanning electron microscopy,[130,131] x-ray topography,[132] and x-ray diffractometry.[133,134]

Reproduced with permission of the copyright owner. Further reproduction prohibited without permission.

We have studied the RDA signal induced by the difference of misfit (60°) dislocation density along the [110] direction compared to the $[1\bar{1}0]$. The effectiveness of RDA for this problem is made possible by the elimination of signal due to other effects at E_0. First there is no LEO effect (section 2.4.1) because of the symmetry at the Γ point of the BZ. Second there is no signal due to the biaxial (001) strain in the sample because both the [110] and $[1\bar{1}0]$ are perpendicular to the strain axis and thus have the same interband transition strength. One also expects an anisotropy in light hole state of the QW due to the presence of the electric field there due to the Pockels effect.[135]

2.5.2.2 Experimental Details

Four HEMT structures, two on vertical gradient freeze (VGF) and two on liquid encapsulated Czochralski (LEC) semi-insulating substrates were grown by molecular beam epitaxy (MBE).[136] The reported etch pit density is ≤ 5000 cm^{-2} and ≤ 50 000 cm^{-2} for the VGF and LEC wafers, respectively. We will refer to these wafers as low (LTDD) and high threading dislocation density (HTDD) substrates rather than by their method of growth since other LEC-type wafers can have etch pit densities comparable to VGF substrates. The $Ga_{0.79}In_{0.21}As$ channel, which lies between the buffer layer and the 530 Å $Ga_{0.75}Al_{0.25}As$, (which includes a $\approx 5\times10^{12}$ cm^{-2} Si δ-doped layer) and a 50 Å GaAs capping layers, varies between 140 and 220 Å.[137] A schematic band diagram for these structures is given in Fig. 59. The Fermi level is pinned near the conduction band at the position of the planar Si δ-doping. The band offset between $Ga_{0.75}Al_{0.25}As$ and

Reproduced with permission of the copyright owner. Further reproduction prohibited without permission.

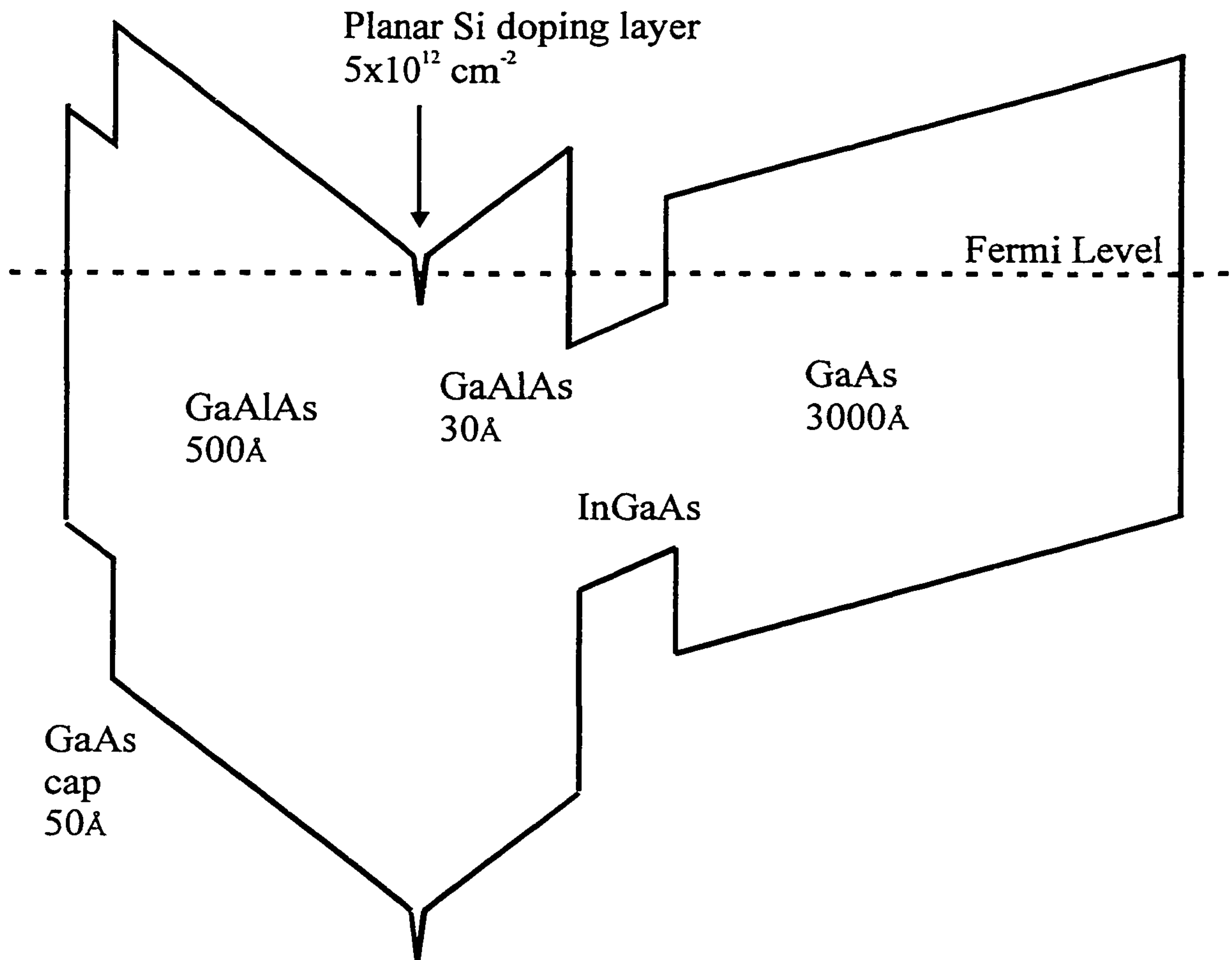

Figure 59. Schematic band diagram for HEMT structures.

Reproduced with permission of the copyright owner. Further reproduction prohibited without permission.

$Ga_{0.79}In_{0.21}As$ leads to a charge transfer to the $Ga_{0.79}In_{0.21}As$ QW region. Since the impurities are introduced outside the QW, this leads to the desired high electron mobility inside the QW, provided there are no dislocations or other defects introduced during growth.

The misfit dislocation densities along the [110] and $[1\bar{1}0]$ directions for different InGaAs channel thicknesses and different substrates were determined in Ref. 128 by plan view transmission electron microscopy. These values are listed in Table VIII.

Table VIII. Misfit dislocation densities along the [110] and $[1\bar{1}0]$ directions for different InGaAs channel thicknesses and different substrates.

Sample	Substrate	$In_{0.21}Ga_{0.79}As$ thickness (Å)	[110] misfits (μm^{-1})	$[1\bar{1}0]$ misfits (μm^{-1})	Relative Expected RDA Signal from Dislocations
#1	LTDD	140	0	0	0
#2	LTDD	160	0	0.2	0.2
#3	HTDD	160	0.2	1.1	0.9
#4	HTDD	220	0.7	2.6	1.9

RDA was performed on the samples by the method given in section 2.3. The back surfaces of all samples were roughened in order to eliminate the effects of back surface reflection.

Reproduced with permission of the copyright owner. Further reproduction prohibited without permission.

2.5.2.2 Experimental Results and Discussion

Since the strain in the QW is compressive, the misfit dislocations generated will all be positive type. These dislocations can then propagate both down into the GaAs and up into the $Ga_{0.75}Al_{0.25}As$. In addition, the $Ga_{0.75}Al_{0.25}As$ may develop its own negative misfit dislocations since its lattice constant is smaller than $Ga_{0.79}In_{0.21}As$. According to the theory in section 2.4.2, we should see an RDA signal at the E_0 for both GaAs and $Ga_{0.75}Al_{0.25}As$ which should scale approximately as the difference between the densities of misfit dislocations along the [110] and $[1\bar{1}0]$ directions. Thus we would expect the ration of signals for samples #1:#2:#3:#4 to be roughly 0:0.2:0.9:1.9, as listed in Table VIII.

Shown in Fig. 60 are the RDA spectra for samples #1-#4. The arrows at the bottom of the figure indicate the E_0 transitions for GaAs and $Ga_{0.75}Al_{0.25}As$. To more clearly see the signals associated with the misfit dislocations, we display in Fig. 61. the difference between the RDA signals for samples #2-#4 and sample #1, which we call ΔRDA.

Although we do not see quantitative agreement with the predicted signal ratios given in table VIII, we do see the features qualitatively. At the GaAs E_0, we see a general sharpening of the lineshape with increasing dislocation density and a peak forming for the highest dislocation densities. This shows up prominently in the ΔRDA spectra for samples #3 and #4 in Fig. 61. At the $Ga_{0.75}Al_{0.25}$ E_0, we see only subtle changes in lineshape except for sample #4 where we see a large peak. The lineshape in the 1.2-1.4

Reproduced with permission of the copyright owner. Further reproduction prohibited without permission.

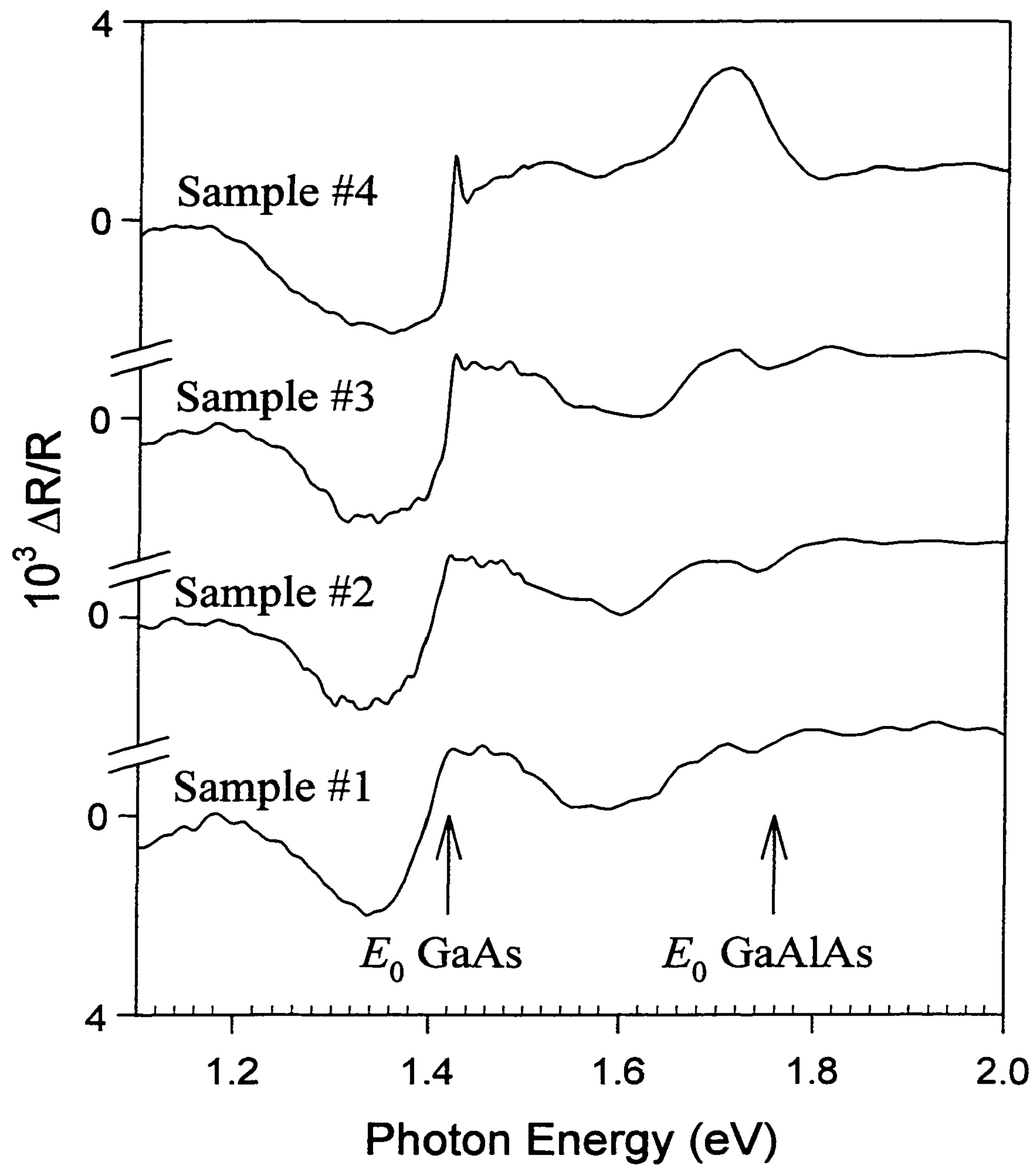

Figure 60. RDA signal for samples #1-#4. The arrows at the bottom of the figure indicate the E_0 transitions for GaAs and $Ga_{0.75}Al_{0.25}As$.

Reproduced with permission of the copyright owner. Further reproduction prohibited without permission.

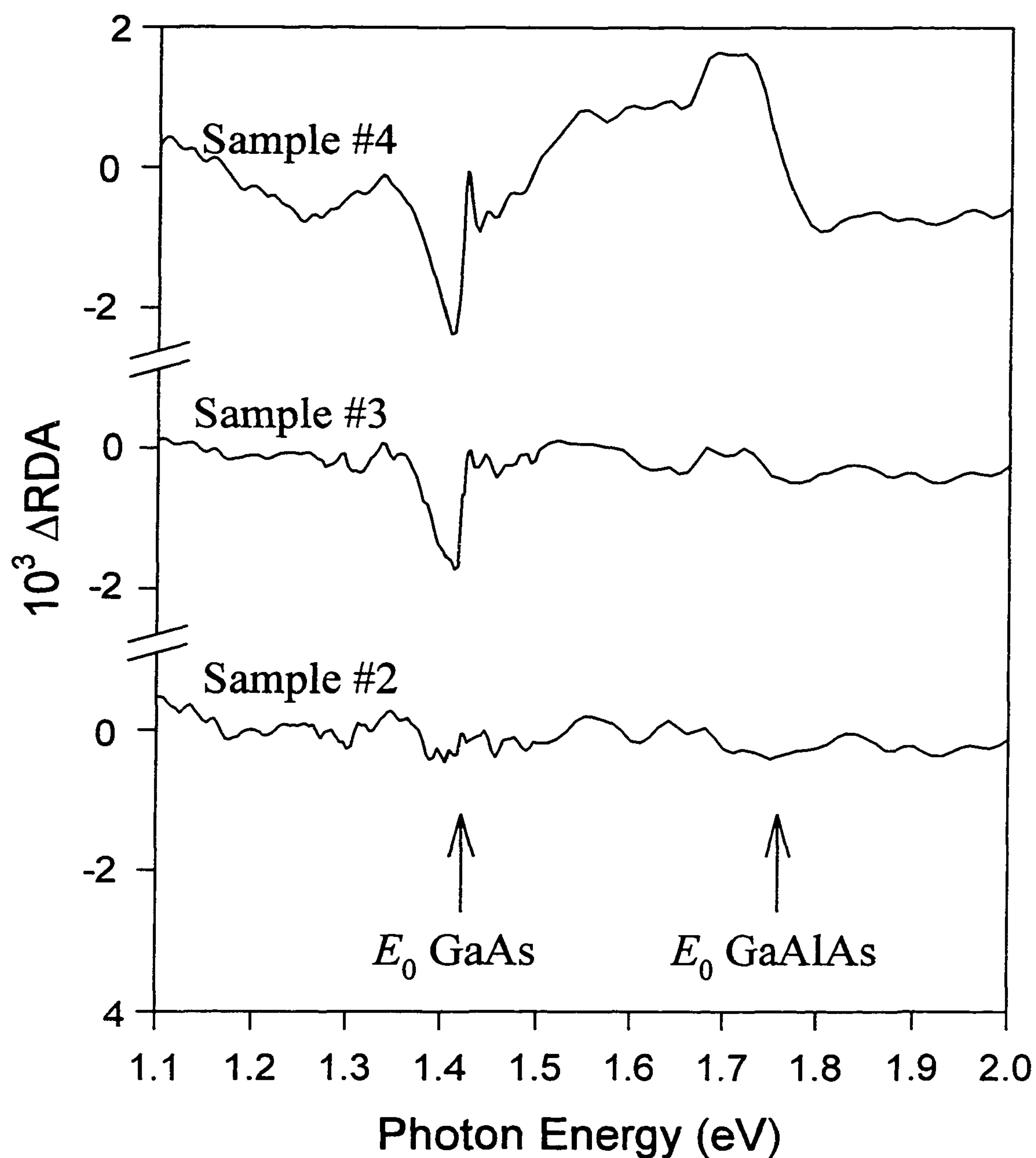

Figure 61. ΔRDA for samples #2-#4. ΔRDA is defined as the difference between the RDA signal for the sample and the RDA signal for sample #1. The arrows at the bottom of the figure indicate the E_0 transitions for GaAs and $Ga_{0.75}Al_{0.25}As$.

Reproduced with permission of the copyright owner. Further reproduction prohibited without permission.

eV region changes subtly, possibly due to the effects of the misfit dislocations on the states in the $Ga_{0.79}In_{0.21}As$ QW or to the Pockels effect. Some of the signal below E_0 for GaAs also may be due to the epilayer/substrate interface.

2.5.3 Ordered GaInP and InGaAsP

In this section we present an RDA study of partially ordered $Ga_{0.5}In_{0.5}P$/GaAs and $In_{0.48}(Ga_{1-x}Al_x)_{0.52}P$/GaAs grown by MOCVD. For the $Ga_{0.5}In_{0.5}P$/GaAs, we observed a strong signal near the E_0 CP, which is due to the valence band splitting discussed in section 2.4.3. We also observed a transition near 2.2 eV in this material, which is possibly due to transitions from the split valence band to a zone folded L conduction band. For the $In_{0.48}(Ga_{1-x}Al_x)_{0.52}P$/GaAs samples, we observed strong signals near the E_0 and "E_1" CPs for ordered samples but not for random samples.

2.5.3.1 Introduction

Atomic CuPt-type ordering on the {111} planes of the Group III sublattice has been observed in $Ga_{0.5}In_{0.5}P$/GaAs[138-141] and $In_{0.48}(Ga_{1-x}Al_x)_{0.52}P$/GaAs[27] grown by metalorganic chemical vapor deposition (MOCVD) on vicinal {001} substrates. As described in section 2.4.3, this creates a splitting of the highest lying valence band (creating two bands with polarization dependent transition matrices to the conduction

Reproduced with permission of the copyright owner. Further reproduction prohibited without permission.

bands) and a mixing between the states at the Γ and L points of the BZ due to the zone folding effect.

The GaInP/GaAs heterojunction system is considered an extremely attractive alternative to the widely used GaAlAs/GaAs couple for several micro- or optoelectronic devices.[142] $In_{0.48}(Ga_{1-x}Al_x)_{0.52}P/GaAs$ has a direct band gap transition in the wavelength range between green and red and is useful for optoelectronic applications such as visible laser diodes, light emitting diodes, and heterojunction bipolar transistors. These materials may be used to create better devices than those based on traditional semiconductors such as AlGaAs and GaAsP.[143]

Under appropriate growth conditions, $Ga_{0.5}In_{0.5}P$ has a strong tendency towards atomic ordering which leads to a bandgap reduction, valence-band splitting, and polarization effects.[144] In addition, the ordering creates electric field due to the piezoelectric effect.[145] This electric field can cause an RDA signal even at E_0, since it has a component along the [110] direction. To study the anisotropies introduced by the reduction of symmetry introduced by ordering, we have performed an RDA study of partially ordered $Ga_{0.5}In_{0.5}P/GaAs$ and $In_{0.48}(Ga_{1-x}Al_x)_{0.52}P/GaAs$ grown by MOCVD.

Reproduced with permission of the copyright owner. Further reproduction prohibited without permission.

2.5.3.2 Experimental Details

The expitaxial growth of the InGaAlP was performed by MOCVD using an EMCORE system E400. This system employs the vertical growth configuration and a high speed rotating disk reactor. High purity trimethyindium, trimethygallium, and trimethyaluminum metalorganic sources were used to supply In, Ga, and Al, respectively, and PH_3 was used for the P source. High purity H_2 was used as the carrier gas. Further details of the growth conditions can be found in Ref. [146]. The samples were grown on (100) n^+ GaAs substrates oriented 15° off towards (110), under different growth conditions. The amount of ordering was determined based on the RDA data presented here as well as photoluminescence, Raman scattering, photoreflectance, atomic force microscopy, and high resolution x-ray diffraction.[27]

The GaInP samples were grown by MOCVD on a 500 Å GaAs buffer layer on a GaAs (001) substrates oriented 2° off towards (110). The films were grown Si doped (n=3x10^{17} cm^{-3}) at a temperature of 630 °C.

RDA data was taken using the method described in section 2.3.

Reproduced with permission of the copyright owner. Further reproduction prohibited without permission.

2.5.3.3 Experimental Results and Discussion

Figure 62 displays the real and imaginary parts of the RDA signal for ordered (dashed lines) and random (solid lines) $In_{0.48}(Ga_{1-x}Al_x)_{0.52}P/GaAs$. The direct E_0 transitions as determined by photoreflectance are shown by the arrows. the position of "E_1" is also indicated by an arrow. The oscillations to the left of the figure are interference oscillations. While the ordered sample shows a sharp feature at E_0, there is no discernable signal at E_0 for the random sample, although a small signal might be masked by the interference oscillations. The signal at E_0 of the ordered sample can come from the valence band splitting of $\Delta^{O}(\eta)$ from Eq. (288) and the associated shift of oscillator strength given by Eq. (289) or from the order induced field along the [111] direction. The signal near "E_1" is also greatly enhanced in the ordered sample. This is also most likely due to the order induced splitting although electric fields (order-induced or related to a space charge region) can also affect the RDA signal near "E_1" through the LEO effect (section 2.4.1). The strong anisotropy near the top of the spectral range is probably due to similar effects at the E_2 and/or E_0' transitions.

Some RDA signal is expected from the interface between the GaAs substrate and the $In_{0.48}(Ga_{1-x}Al_x)_{0.52}P$ epilayer since the substrate is offcut 15° toward (110). However, this must be small since the random sample also has an offcut substrate and does not display strong RDA signal.

Reproduced with permission of the copyright owner. Further reproduction prohibited without permission.

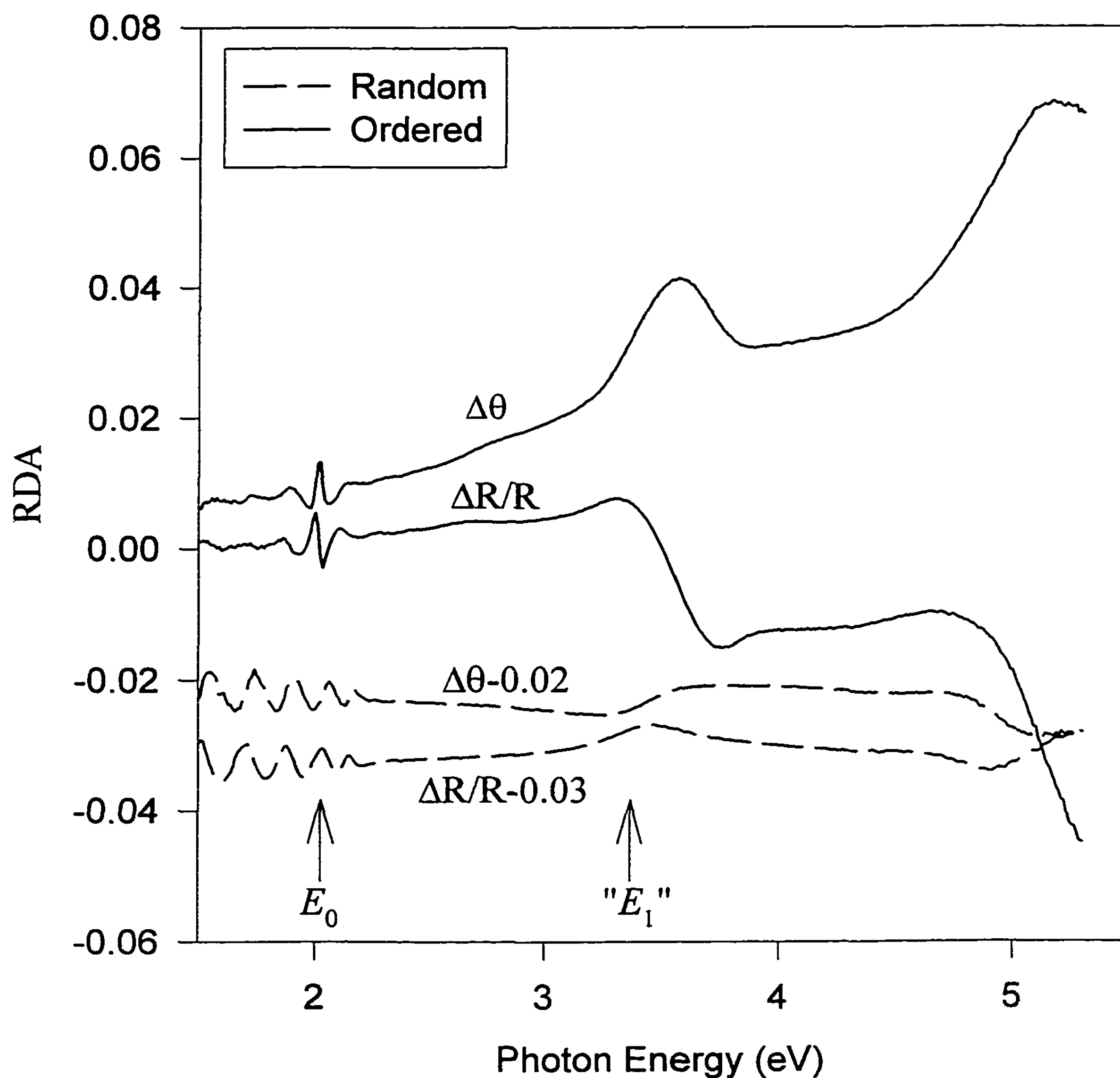

Figure 62. Real and imaginary parts of the RDA signal for ordered (solid lines) and random (dashed lines) $In_{0.48}(Ga_{1-x}Al_x)_{0.52}P/GaAs$. For clarity, the real and imaginary parts of the random sample have been displaced by –0.02 and –0.03, respectively. The positions of E_0 and E_1 are indicated by arrows.

Reproduced with permission of the copyright owner. Further reproduction prohibited without permission.

A typical RDA spectrum for ordered $Ga_{0.5}In_{0.5}P/GaAs$ is shown in Fig. 63. The first feature between 1.7 and 2.0 eV is due to the E_0 transition. This feature has basically the same shape as the corresponding E_0 feature in Fig. 62. The spin orbit splitting transition does not appear here because it is isotropic and independent of the light polarization.

The second feature around 2.2 eV corresponds to a peak which has been observed in the piezoreflectance spectrum.[147] Thus this may be a transition between the HH or LH valence band and a folded band in the conduction band. This folding is not due to strain because a (001) strain cannot create any polarization dependence effect along the (110) and (1-10) directions, which are equivalent. Thus it is due to ordering. Such a transition around 2.18 eV between the top of the valence band and a folded band has already been observed in electroreflectance spectra of GaInP[148].

Reproduced with permission of the copyright owner. Further reproduction prohibited without permission.

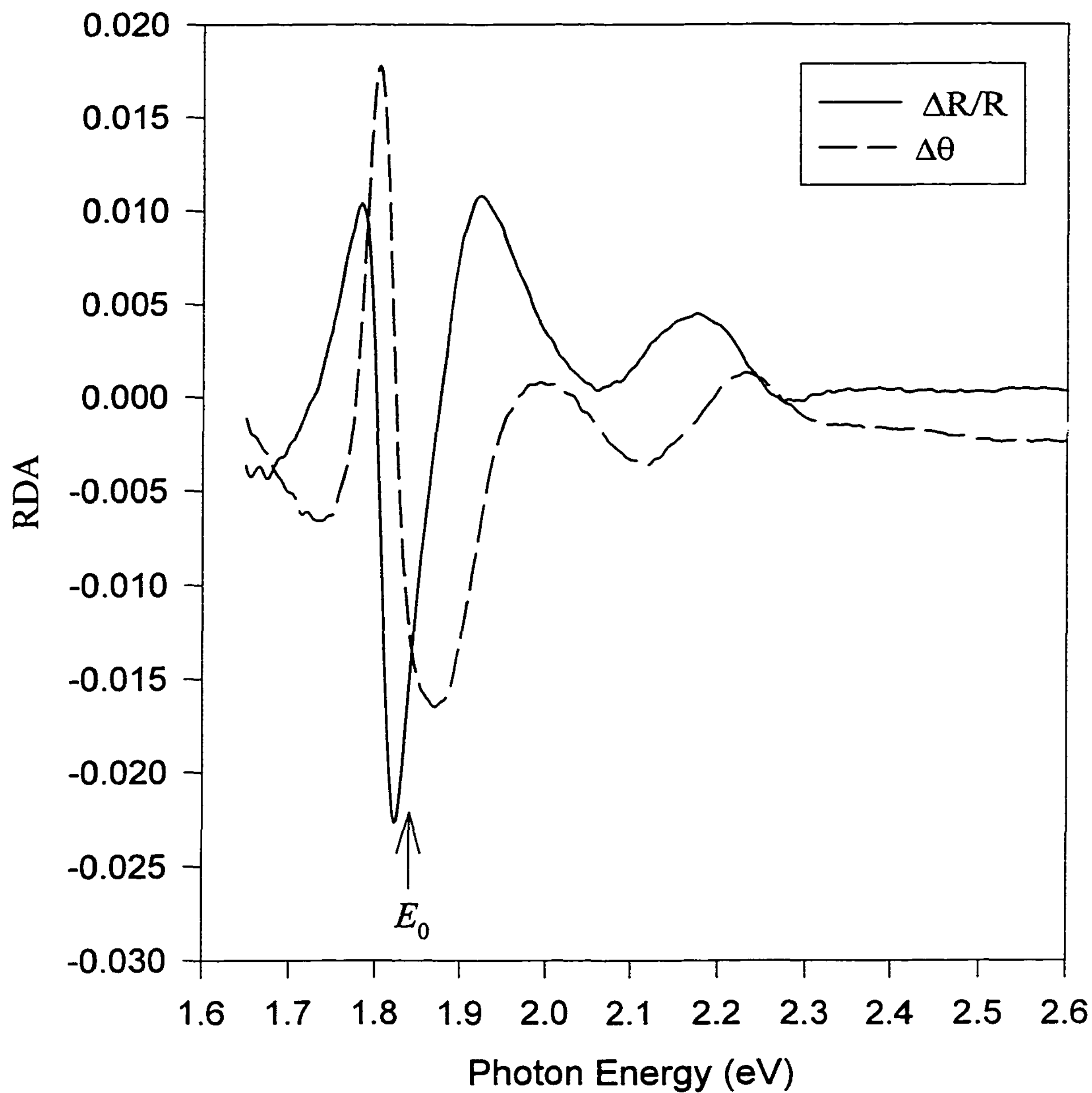

Figure 63. Real and imaginary parts of the RDA signal for ordered InGaP. The positions of E_0 is indicated by the arrow at the bottom of the figure.

Reproduced with permission of the copyright owner. Further reproduction prohibited without permission.

Chapter 3. Summary and Conclusions

In this thesis, we have investigated isotropic optical properties using SE and anisotropic optical properties using RDA.

To model the SE data, we have introduced a new model of the dielectric function for diamond and zincblende-type semiconductors. Our model is the first to include discrete as well as band-to-band Coulomb enhanced (BBCE) effects, i.e., continuum exciton at the several interband critical points (CPs), at the fundamental bandgap, the spin orbit split gap, and the higher lying E_1, $E_1+\Delta_1$ doublet, which are two dimensional (2D) in nature since the effective mass for these CP's in the <111>-type direction is much greater than that in the other two directions. Our analysis has yielded the only experimental evaluation of the exciton binding energies at the E_1, $E_1+\Delta_1$ CP's, R_1, except for one study based on low temperature (10 K) reflectivity which measured R_1 for CdTe and ZnTe.[2] Our analysis shows that the features in the vicinity of the E_1, $E_1+\Delta_1$ CP's are actually due to the bound exciton, which can be several hundred meV below the these CP's. The extracted R_1 values using our model are in good agreement with effective-mass **k•p** theory. Our results, particularly for exciton continuum effects at E_1, have considerable implications for recent first-principles band structure calculations which include exciton effects.

Reproduced with permission of the copyright owner. Further reproduction prohibited without permission.

We have measured the optical constants of $Zn_{0.53}Cd_{0.47}Se/InP$ in the range 0.8-5.5 eV. Our data exhibit four distinct CP structures which have been fit using a model dielectric function which includes excitonic and relevant BBCE profiles for not only E_0, $E_0+\Delta_0$ but also for E_1, $E_1+\Delta_1$. Because of the sharpness of our spectra, related to the high quality of our samples, we have been able to extract a number of imports materials parameters, including excitonic binding energies at both E_0, $E_0+\Delta_0$ and E_1, $E_1+\Delta_1$ as well as the influence of the $\Gamma_8^v - L_6^c$ indirect transition. The effects of the native oxide on the optical properties has been examined. We find the thickness of this oxide to be ≈ 20 Å.

Using spectral ellipsometry in the range 0.3-5.45 eV we have evaluated the dielectric function of a series of *n*- and *p*-doped relaxed $In_{0.66}Ga_{0.34}As$ samples of interest for TPV applications. The intrinsic band gap of 0.612 ± 0.01 eV corresponds to an In composition of 66 ± 1 %. The Burstein-Moss (BM) shift was taken into account using a Fermi level filling factor in addition to the excitonic and BBCE terms at the fundamental absorption edge. While for the *p*-type samples the BM shift exhibited no nonparabolic effects, the *n*-type samples had pronounced nonparabolicity at the highest doping level. These are in agreement with a recent banstructure calculation based on the Full Potential Linear Augmented Plane Wave Method.[95,149] We obtained the binding energy R_1 (~ 90 meV) of the 2D exciton associated with the E_1-R_1, $E_1+\Delta_1$-R_1 features. The shift of E_1-R_1, $E_1+\Delta_1$-R_1 with doping density also was evaluated, an effect which is related to surface electric fields.

Reproduced with permission of the copyright owner. Further reproduction prohibited without permission.

We used RDA spectroscopy at 300K to evaluate the sign and magnitude of the near surface electric field in NID, *n*-type and *p*-type LTG:GaAs (001). We also have performed a self-consistent Poisson's calculation to determine $\mathscr{E}(z)$. In contrast to a conventional SCR, in our material the field $\mathscr{E}(z)$ does not vary linearly with position. Even for the most heavily *p*-doped samples the band-bending is still *n*-type, although near flatband. Our experimentally determined "effective near surface electric fields" agree well with the calculation (midgap surface Fermi level pinning), yielding "effective depletion widths" ≤ 22Å except for the most heavily *p*-doped sample. For this sample, the experiment and simulation can be brought into accord by assuming $p=4\times10^{19}$ cm^{-3}, i.e., not all acceptors are electrically active.

We used RDA to study optical anisotropies induced by the difference of misfit (60°) dislocation density along the [110] direction compared to the $[1\bar{1}0]$ direction in InGaAs/AlGaAs/GaAs HEMT structures. This is the first use of RDA to study misfit dislocations caused by strain relaxation. The effectiveness of RDA for this problem is made possible by the lack of signal due to LEO and biaxial strain effects at E_0. Our RDA signal is correlated to the misfit dislocation densities.

We performed an RDA study of ordered $Ga_{0.5}In_{0.5}P$/GaAs and $In_{0.48}(Ga_{1-x}Al_x)_{0.52}P$/GaAs grown by MOCVD. For the $Ga_{0.5}In_{0.5}P$/GaAs, we observed a strong signal near the E_0 CP, which is due to the order induced valence band splitting. We also observed a transition near 2.2 eV in this material, which is possibly due to transitions from the split valence band to a zone folded L conduction band. For the $In_{0.48}(Ga_{1-x}Al_x)_{0.52}P$/GaAs

Reproduced with permission of the copyright owner. Further reproduction prohibited without permission.

samples, we observed strong signals near the E_0 and E_1 CPs for ordered samples but not for random samples. The signal near the E_0 CP had the same basic shape for both ordered materials.

Reproduced with permission of the copyright owner. Further reproduction prohibited without permission.

Appendix A. Extraction of Ellipsometric Parameters from Raw Data

The two most popular ways of determining the effect of optical components on light and thus the relationship between the ellipsometric parameters are the Mueller matrix formalism and the Jones matrix formalism. The advantage of matrix formalisms is that each component of the ellipsometer can be considered separately and the matrices multiplied to obtain the complete relationship between the incident light and the light at the detector for any sample and ellipsometer configuration. The Jones matrix formalism uses 2x2 complex matrices and is the simpler of the two. The Mueller matrix formalism uses 4x4 real matrices and is necessary to consider the case of partially polarized light. Further discussion of the Jones and Mueller matrix formalisms can be found in the works by Azzam and Bashara[42] and Röseler.[50]

A.1 A Brief Overview of Polarization States of Light

Completely polarized light can be represented as

$$\mathbf{E} = \mathrm{Re}[\mathscr{E}\hat{\mathbf{e}}e^{i\mathbf{k}^L \bullet \mathbf{r} - i\omega t}] \qquad \text{(A1a)}$$

Reproduced with permission of the copyright owner. Further reproduction prohibited without permission.

where $\mathscr{E}$ is the complex amplitude of the light (that is it contains phase information), ω is the angular frequency of the light, $\mathbf{k}^L$ is the wave vector of the light, t is time, and $\mathbf{r}$ is the position vector. This equation can be broken into components as

$$\mathbf{E} = \mathrm{Re}\left\{\begin{bmatrix} \mathscr{E}_p \\ \mathscr{E}_s \end{bmatrix} e^{i\mathbf{k}^L \bullet \mathbf{r} - i\omega t}\right\} = \mathrm{Re}\left\{\begin{bmatrix} |\mathscr{E}_p| e^{i\delta_p^L} \\ |\mathscr{E}_s| e^{i\delta_s^L} \end{bmatrix} e^{i\mathbf{k}^L \bullet \mathbf{r} - i\omega t}\right\} \tag{A1b}$$

where $\mathscr{E}_p$ and $\mathscr{E}_s$ are the electric field components parallel and perpendicular to the plane of incidence, respectively, while δ_p^L, and δ_s^L denote the corresponding phases for the components parallel and perpendicular to the plane of incidence, respectively. Thus the electric field as a function of time traces out an ellipse as shown in Fig. A-1. To make a connection to ellipsometry, we define the parameters, Ψ^L and Δ^L. Ψ^L is related to the tilt of the ellipse while Δ^L ($=\delta_p^L - \delta_s^L$) is related to the eccentricity of the ellipse, being 0° or 180° for linear polarization (flat ellipse) and 90° for the fattest ellipse (circular polarization if $\mathscr{E}_p = \mathscr{E}_s$). To summarize, in this notation,

$$\tan\Psi^L = \frac{|\mathscr{E}_p|}{|\mathscr{E}_s|} \qquad \Delta^L = \delta_p^L - \delta_s^L \tag{A2}$$

Reproduced with permission of the copyright owner. Further reproduction prohibited without permission.

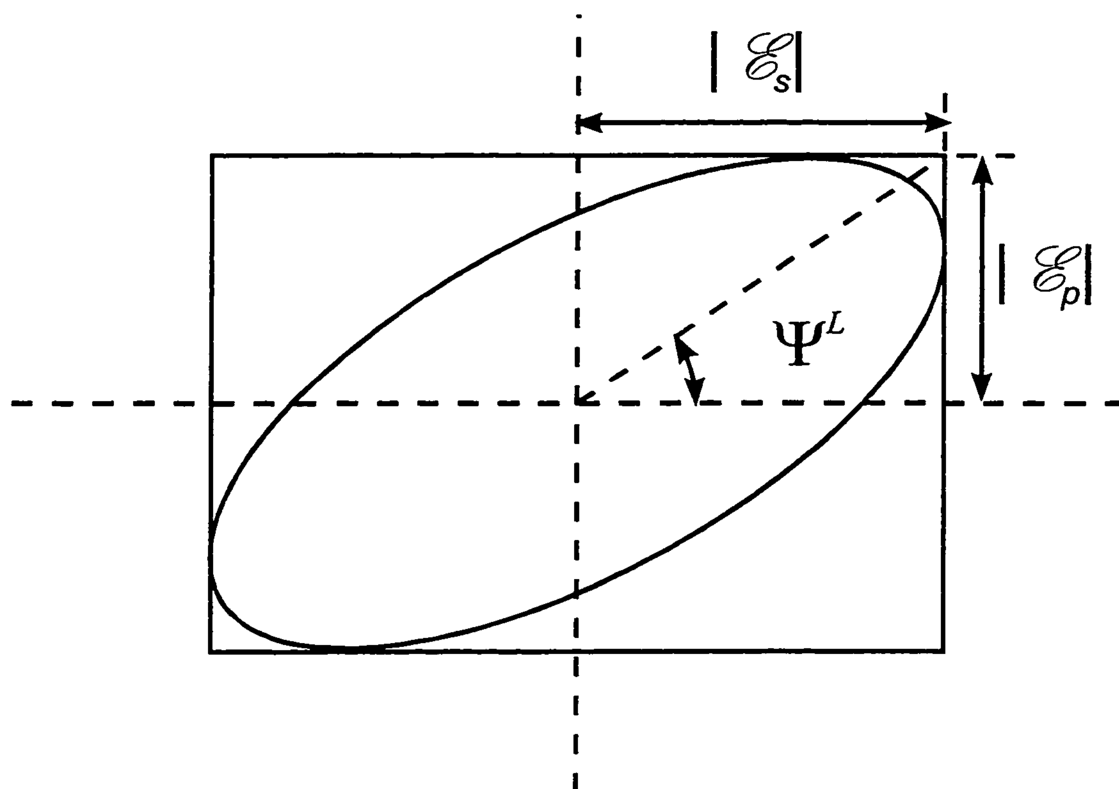

Figure A1. Path of electric field vector over time for elliptically polarized light. $\mathscr{E}_p$ and $\mathscr{E}_s$ are the electric field components parallel and perpendicular to the plane of incidence, respectively They are related to Ψ^L by $\tan\Psi^L = \frac{|\mathscr{E}_p|}{|\mathscr{E}_s|}$. The eccentricity of the ellipse is determined by the relative phase of the *s*- and *p*-polarized light, $\Delta^L = \delta_p^L - \delta_s^L$.

Reproduced with permission of the copyright owner. Further reproduction prohibited without permission.

If a sample characterized by Ψ and Δ [defined in Eq. (1)] is illuminated by incident light with equal in phase s- and p-components ($\Psi^L = 45°$ and $\Delta^L = 0°$), then the light reflected from the sample will have $\Psi^L = \Psi$ and $\Delta^L = \Delta$.

A.2 Mueller Matrix Formalism

The Mueller matrix formalism is defined in terms of the Stokes parameters of the light. For completely polarized light, these are defined as:

$$\begin{aligned} s_0 &= |\mathscr{E}_p|^2 + |\mathscr{E}_s|^2 \\ s_1 &= |\mathscr{E}_p|^2 - |\mathscr{E}_s|^2 \\ s_2 &= 2|\mathscr{E}_p||\mathscr{E}_s|\cos\Delta^L \\ s_3 &= 2|\mathscr{E}_p||\mathscr{E}_s|\sin\Delta^L \end{aligned} \quad \text{(A3)}$$

s_0 is proportional to the energy of the light wave, s_1 adds information about the tilt of the ellipse of polarization, while s_2 and s_3 add information about the eccentricity of the ellipse. From this we obtain the relations in terms of the ellipsometric angles as

$$\begin{aligned} s_1/s_0 &= -\cos 2\Psi^L \\ s_2/s_0 &= \sin 2\Psi^L \cos\Delta^L \\ s_3/s_0 &= \sin 2\Psi^L \sin\Delta^L \end{aligned} \quad \text{(A4)}$$

Reproduced with permission of the copyright owner. Further reproduction prohibited without permission.

We see that the four Stokes parameters are not independent for the case of completely polarized light since

$$s_0^2 = s_1^2 + s_2^2 + s_3^2 \tag{A5}$$

The above relations hold only for completely polarized light. For unpolarized light, $\mathscr{E}_p = \mathscr{E}_s$ and Δ^L is a rapidly varying random function ($\cos \Delta^L = \sin \Delta^L = 0$ on average), so $s_0 > 0$ and $s_1 = s_2 = s_3 = 0$ changing Eq. (A5) to

$$s_0 = s_{0u} + s_{0p} = s_{0u} + \sqrt{s_1^2 + s_2^2 + s_3^2} \tag{A6}$$

where s_{0u} is the intensity of the unpolarized portion of the light and s_{0p} is the intensity of the polarized portion of the light. Thus we can define a degree of polarization, *Pol*, as

$$Pol = \frac{s_{0p}}{s_0} = \frac{\sqrt{s_1^2 + s_2^2 + s_3^2}}{s_0} \le 1 \tag{A7}$$

The equality holding for the case of totally polarized light, where Eq. (A4) is valid.

Finally, the Mueller matrices are the matrices which transform the Stokes parameters of the light incident upon an optical element into those for light exiting the element. So, we have

Reproduced with permission of the copyright owner. Further reproduction prohibited without permission.

$$\mathbf{S_e} = \mathbf{M}\ \mathbf{S_i} \tag{A8}$$

where **M** is the Mueller matrix of the optical element. $\mathbf{S_e}$ and $\mathbf{S_i}$ are the are the Stokes vectors of the exiting and incident polarization state of the light respectively and of the form

$$\mathbf{S} = \begin{pmatrix} s_0 \\ s_1 \\ s_2 \\ s_3 \end{pmatrix} \tag{A9}$$

This allows one to calculate the intensity at the detector which is the s_0 component of the final product of the matrices of the optical elements of the instrument times the incident polarized light. The Matrices one needs are as follows:

Mueller matrix for a polarizer:

$$\mathbf{M_P} = \frac{1}{2}\begin{pmatrix} 1 & \cos 2P_\angle & \sin 2P_\angle & 0 \\ \cos 2P_\angle & \cos^2 2P_\angle & \sin 2P_\angle \cos 2P_\angle & 0 \\ \sin 2P_\angle & \sin 2P_\angle \cos 2P_\angle & \sin^2 2P_\angle & 0 \\ 0 & 0 & 0 & 0 \end{pmatrix} \tag{A10}$$

Reproduced with permission of the copyright owner. Further reproduction prohibited without permission.

where $P_\angle$ is the angle of the polarizer relative to the direction parallel to the plane of incidence. The Mueller matrix for the analyzer, $\mathbf{M_A}$, is the same except $P_\angle$ is replaced by $A_\angle$, the analyzer angle.

Mueller matrix for a phase retarder with retardation δ with fast and slow axes fixed at 45° and –45° with respect to the incident polarized light respectively:

$$\mathbf{M_R} = \begin{pmatrix} 1 & 0 & 0 & 0 \\ 0 & 1 & 0 & 0 \\ 0 & 0 & \cos\delta & \sin\delta \\ 0 & 0 & -\sin\delta & \cos\delta \end{pmatrix} \qquad \text{(A11)}$$

Mueller matrix of a reflecting surface (such as the sample):

$$\mathbf{M_S} = \frac{|\tilde{r}_p|^2 + |\tilde{r}_s|^2}{2} \begin{pmatrix} 1 & -\cos 2\Psi & 0 & 0 \\ -\cos 2\Psi & 1 & 0 & 0 \\ 0 & 0 & \sin 2\Psi \cos\Delta & \sin 2\Psi \sin\Delta \\ 0 & 0 & -\sin 2\Psi \sin\Delta & \sin 2\Psi \cos\Delta \end{pmatrix} \qquad \text{(A12)}$$

where $\tilde{r}_p$ and $\tilde{r}_s$ are the complex Fresnel reflection coefficients for light polarized parallel and perpendicular to the plane of incidence, respectively.

Reproduced with permission of the copyright owner. Further reproduction prohibited without permission.

Using these matrices, one obtains the Stokes vector for the light passing through a polarizer, then a retarder, bouncing off the sample, passing through an analyzer, and finally incident on the detector, $\mathbf{S_D}$ as

$$\mathbf{S_D} = \mathbf{M_A}\,\mathbf{M_S}\,\mathbf{M_R}\,\mathbf{M_P}\begin{pmatrix} I_0 \\ 0 \\ 0 \\ 0 \end{pmatrix} \qquad \text{(A13)}$$

where I_0 is the intensity of the beam on the polarizer.

The s_0 component of $\mathbf{S_D}$ gives the light intensity at the detector, I, which can be expressed as a function of the parameter varied during the measurement. If the incident light is partially polarized, the column vector on the right of the above expression should be modified, but this does not affect the determination of ellipsometric parameters assuming the polarizer is fixed and perfectly polarizing.

For a phase modulated ellipsometer, one expresses this in terms of the (time dependent) phase introduced at the modulator, $\delta(t)$. The expression below is for a polarizer angle, $P_\angle$, 45° greater than the modulator angle, $M_\angle$, which was the case with our instrument.

$$I = I_{DC} + I_S \sin\delta(t) + I_C \cos\delta(t) \qquad \text{(A14)}$$

where

Reproduced with permission of the copyright owner. Further reproduction prohibited without permission.

$$\begin{aligned}
I_{DC} &= I_0(1-\cos 2\Psi \cos 2A_{\angle}) \\
I_S &= I_0 \sin 2A_{\angle} \sin 2\Psi \sin\Delta \\
I_C &= I_0[\sin 2M_{\angle}(\cos 2\Psi - \cos 2A_{\angle}) + \sin 2A_{\angle} \cos 2M_{\angle} \sin 2\Psi \cos\Delta]
\end{aligned} \tag{A15}$$

For a rotating analyzer ellipsometer, one expresses I in terms of the analyzer angle, so

$$I = I_0 + I'_S \sin 2A_{\angle} + I'_C \cos 2A_{\angle} \tag{A16}$$

where

$$\begin{aligned}
I'_S &= I_0 \sin 2\Psi' \cos(\Delta + \delta) \\
I'_C &= -I_0 \cos 2\Psi' \\
\tan\Psi' &= \frac{\tan\Psi}{\tan P_{\angle}}
\end{aligned} \tag{A17}$$

In this case, δ is the phase retardation due to a retarder in the light path if one is present ($\delta = 0$ otherwise).

Reproduced with permission of the copyright owner. Further reproduction prohibited without permission.

A.3 Jones Matrix Formalism

Jones matrices transform two perpendicular components of polarized light in the form of Eq. (A1a) according to the optical element in question. A Jones matrix transforms the electric field vector incident on an optical element, $\mathbf{E} = \begin{bmatrix} \mathscr{E}_p \\ \mathscr{E}_s \end{bmatrix}$, into the electric field vector leaving the optical element, $\mathbf{E}' = \begin{bmatrix} \mathscr{E}'_p \\ \mathscr{E}'_s \end{bmatrix}$

$$\begin{aligned} \mathscr{E}'_p &= J_{pp}\mathscr{E}_p + J_{ps}\mathscr{E}_s \\ \mathscr{E}'_s &= J_{sp}\mathscr{E}_p + J_{ss}\mathscr{E}_s \\ &\text{or} \\ \mathbf{E}' &= \mathbf{JE} \end{aligned} \tag{A18}$$

Thus they are 2x2 complex matrices and only useful if the polarization state of the light is completely determined. Instead of calculating the light intensity at the detector directly as in the Mueller matrix formalism, in the Jones matrix formalism one calculates the electric field intensity parallel and perpendicular to the plane of incidence, and then the intensity based on these.

The matrices for the elements of an ellipsometer are as follows.

Jones matrix for a polarizer:

Reproduced with permission of the copyright owner. Further reproduction prohibited without permission.

$$\mathbf{J_P} = \begin{pmatrix} \cos^2 P_\angle & \sin P_\angle \cos P_\angle \\ \sin P_\angle \cos P_\angle & \sin^2 P_\angle \end{pmatrix} \tag{A19}$$

where $P_\angle$ is the angle of the polarizer relative to the direction parallel to the plane of incidence. The Jones matrix for the analyzer, $\mathbf{J_A}$, is the same except $P_\angle$ is replaced by $A_\angle$, the analyzer angle.

Jones matrix for a phase retarder with retardation δ with fast and slow axes fixed at 45° and –45° with respect to the incident polarized light respectively:

$$\mathbf{J_R} = \begin{pmatrix} \cos\frac{\delta}{2} + i\sin\frac{\delta}{2} & 0 \\ 0 & \cos\frac{\delta}{2} - i\sin\frac{\delta}{2} \end{pmatrix} \tag{A20}$$

where δ is the relative retardation between fast and slow axes.

Jones matrix of a reflecting surface (such as the sample):

$$\mathbf{J_S} = \begin{pmatrix} \tilde{r}_p & 0 \\ 0 & \tilde{r}_s \end{pmatrix} \tag{A21}$$

where $\tilde{r}_p$ and $\tilde{r}_s$ are the complex Fresnel reflection coefficients for light polarized parallel and perpendicular to the plane of incidence, respectively.

Reproduced with permission of the copyright owner. Further reproduction prohibited without permission.

Using these matrices, one obtains the electric field at the detector, $\mathbf{E_D}$, as

$$\mathbf{E_D} = \mathbf{J_A}\ \mathbf{J_S}\ \mathbf{J_R}\ \mathbf{J_P} \begin{pmatrix} \mathscr{E}_0 \\ \mathscr{E}_0 \end{pmatrix} \tag{A22}$$

where $\mathscr{E}_0$ is an electric field defined as $I_0 = 2\mathscr{E}_0^2$. Finally, taking the detected light intensity as $I = |\mathbf{E_D}|^2$, one arrives at Eqs. (A14) through (A17).

A.4 Higher Order Corrections For Rotating Analyzer Systems

The above analysis ignores several small but important corrections that must be made for accurate ellipsometry. First, polarizers are not ideal, particularly in the NIR in our case. In addition, all of the measurements were made both with and without a phase retarder in place. The combination and interpretation of these two sets of data can yield information about the sample and the quality of the measurement. Corrections for these effects as well as corrections for imperfect reflections at mirrors and the retarder were covered in section 1.4.3.

Reproduced with permission of the copyright owner. Further reproduction prohibited without permission.

A.5 Extraction of Ellipsometric Parameters for Imperfect Polarizers

This section follows the derivation given in Ref. 50. We will assume that the polarization characteristics of the polarizer and analyzer were identical. Then we considered that the polarizers are well characterized by their maximum and minimum transmission, τ_{max} and τ_{min} respectively. We further define the parameters

$$\cos\theta = \frac{\tau_{max} - \tau_{min}}{\tau_{max} + \tau_{min}}, \quad \text{and} \quad \sin\theta = \frac{2\sqrt{\tau_{max}\tau_{min}}}{\tau_{max} + \tau_{min}} \tag{A23}$$

Then the Mueller matrix for a partial polarizer is

$$\mathbf{M_P} = K\begin{pmatrix} 1 & \cos\theta\cos 2P_\angle & \cos\theta\sin 2P_\angle & 0 \\ \cos\theta\cos 2P_\angle & \cos^2 2P_\angle + \sin^2 2P_\angle \sin\theta & \sin 2P_\angle \cos 2P_\angle (1-\sin\theta) & 0 \\ \cos\theta\sin 2P_\angle & \sin 2P_\angle \cos 2P_\angle (1-\sin\theta) & \sin^2 2P_\angle + \cos^2 2P_\angle \sin\theta & 0 \\ 0 & 0 & 0 & \sin\theta \end{pmatrix} \tag{A24}$$

where $K=(\tau_{max} + \tau_{min})/2$ and $P_\angle$ is the polarizer angle. Of course for the analyzer matrix, $\mathbf{M_A}$, we use the same matrix only with the polarizer angle, $P_\angle$, replaced with the analyzer angle, $A_\angle$.

Reproduced with permission of the copyright owner. Further reproduction prohibited without permission.

For our case, the polarizer angle was fixed at 45°, so Eq. (A24) simplifies to

$$\mathbf{M}_{P=45^\circ} = K\begin{pmatrix} 1 & 0 & \cos\theta & 0 \\ 0 & \sin\theta & 0 & 0 \\ \cos\theta & 0 & 1 & 0 \\ 0 & 0 & 0 & \sin\theta \end{pmatrix} \tag{A25}$$

For the Sample reflection matrix, $\mathbf{M}_S$, we can still use Eq. (A12). One should remember that the values of Ψ and Δ appearing in Eq. (A12) should be interpreted as combined values including the effects of the eight mirrors in the system and possibly the retarder. Obtaining the values of Ψ and Δ for the sample based on these values is covered in section 1.4.3.4.

Another affect to be considered is that the incident beam could be partially polarized due to the presence of a polarizing beam splitter or the reflections off the several FTIR mirrors prior to arriving at the ellipsometer. In our case, this affect was completely negligible as we used the normal non-polarizing beam splitter configuration (each split undergoes on reflection at the beam splitter, one transmission through the beam splitter, and one normal incident mirror reflection as shown in figure 8). We include this affect in any case by assuming the incident light is partially polarized (but with no phase shift between the two eigenpolarization axes), that is

Reproduced with permission of the copyright owner. Further reproduction prohibited without permission.

$$\mathbf{S_I} = \begin{pmatrix} s_0 \\ s_1 \\ 0 \\ 0 \end{pmatrix} \tag{A26}$$

where $\mathbf{S_I}$ is the Stokes vector for the incident light and s_0 and s_1 are Stokes parameters for the (partially polarized) incident light as defined in Eqs. (A3)-(A9).

With these equations we can now get a corrected form for Eqs. (A13), (A16), and (A17).

$$\mathbf{S_D} = \mathbf{M_A}\ \mathbf{M_S}\ \mathbf{M_P} \begin{pmatrix} s_0 \\ s_1 \\ 0 \\ 0 \end{pmatrix} = \begin{pmatrix} s_0 K_{00} + s_1 K_{01} \\ s_0 K_{10} + s_1 K_{11} \\ s_0 K_{20} + s_1 K_{21} \\ s_0 K_{30} \end{pmatrix} \tag{A27}$$

where

$$\begin{aligned}
K_{00} &= 1 - \cos 2\Psi \cos\theta \cos 2A_\angle + \sin 2\Psi \cos\Delta \cos^2\theta \sin 2A_\angle \\
K_{01} &= \sin\theta(\cos\theta\cos 2A_\angle - \cos 2\Psi) \\
K_{10} &= [\cos\theta + \sin 2\Psi \cos\Delta(1-\sin\theta)\cos\theta \sin 2A_\angle]\cos 2A_\angle \\
&\qquad - \cos 2\Psi(\cos^2 2A_\angle + \sin^2 2A_\angle \sin\theta) \\
K_{11} &= \sin\theta(\cos^2 2A_\angle - c2\Psi\cos\theta\cos 2A_\angle + \sin\theta \sin^2 2A_\angle) \\
K_{20} &= [\cos\theta - \cos 2\Psi(1-\sin\theta)\cos 2A_\angle]\sin 2A_\angle \\
&\qquad + \sin 2\Psi \cos\Delta \cos\theta(\sin\theta\cos^2 2A_\angle + \sin^2 2A_\angle) \\
K_{21} &= \sin\theta[(1-\sin\theta)\cos 2A_\angle \sin 2A_\angle - \cos 2\Psi \cos\theta \sin 2A_\angle] \\
K_{30} &= -\sin 2\Psi \sin\Delta \sin\theta \cos\theta
\end{aligned}$$

Reproduced with permission of the copyright owner. Further reproduction prohibited without permission.

The intensity at the detector, $I = s_0^D$, is the top line of the last matrix in Eq. (A27) and can be rewritten as

$$I = I''_{DC} + I''_S \sin 2A_\angle + I''_C \cos 2A_\angle \tag{A28}$$

where

$$\begin{aligned} I''_{DC} &= s_0 - s_1 \cos 2\Psi \sin\theta \\ I''_S &= s_0 \sin 2\Psi \cos\Delta \cos^2\theta \\ I''_C &= -s_0 \cos 2\Psi \cos\theta + s_1 \sin\theta \cos\theta \end{aligned} \tag{A29}$$

As noted earlier, with our system, the incident light is very nearly unpolarized allowing us to approximate $s_1 \approx 0$. This approximation is particularly valid since s_1 only appears in Eq. (A29) in conjunction with sinθ (a small number for good polarizers). It is important to remember that for our system, the values of Ψ and Δ appearing in Eq. (A29) should be interpreted as combined values including the effects of the eight mirrors in the system and possibly the retarder. Obtaining the values of Ψ and Δ for the sample based on these values is covered in section 1.4.3.

Reproduced with permission of the copyright owner. Further reproduction prohibited without permission.

Appendix B. Effects of Light Focusing

As mentioned in section 1.4, the light beam in the FTIR ellipsometer is focused onto the sample with a half-angle of convergence of about 3°. This influences the measured ellipsometric parameters since there is no longer have a single well defined angle of incidence for the light, but rather a combination of light having several angles of incidence. The effects of focussing have been considered for PCSA null ellipsometers[150-152] and for RAE using the two-phase model.[153]

We consider the effects of focusing for a RAE on the measured ellipsometric parameters (Ψ and Δ) and the extracted dielectric function of an epilayer in a three-phase system. For clarity, we assume that the polarizer angle is 45°. Then Ψ and Δ for a single angle of incidence are equal to the Ψ^L and Δ^L of the light arriving at the analyzer. We also assume that the optical elements respond the same for focused and columnated light. Finally, we assume that the light is uniform and circular in cross section and that no part of the light beam is lost any optical element being smaller than the light beam. (These assumptions are not all met for our system, but the qualitative result of the calculation should not change. Notably, the light beam does fall off the detector as mentioned in section 1.4.2 and there is a dark spot in the center of the light beam due to the hole in the first focusing mirror for the laser beam needed for the FT.) With these assumptions, the effective measured value of the complex reflectance ratio, $\tilde{\rho}_{eff}$, takes the form of a average of $\tilde{\rho}$ over several angles of incidence weighted by intensity and geometry factors

Reproduced with permission of the copyright owner. Further reproduction prohibited without permission.

$$\tilde{\rho}_{eff} = \frac{\int_{\phi_{min}}^{\phi_{max}} \tilde{\rho}(\phi)\left[\left|\tilde{r}_p(\phi)\right|^2 + \left|\tilde{r}_s(\phi)\right|^2\right]\left[1 - \frac{\phi - \phi_0}{\phi_{max} - \phi_{min}}\right] d\phi}{\int_{\phi_{min}}^{\phi_{max}} \left[\left|\tilde{r}_p(\phi)\right|^2 + \left|\tilde{r}_s(\phi)\right|^2\right]\left[1 - \frac{\phi - \phi_0}{\phi_{max} - \phi_{min}}\right] d\phi} \tag{B1}$$

where ϕ_0, ϕ_{max}, and ϕ_{min} are the average, maximum, and minimum angles of incidence, respectively. Figure B1 shows the $\tilde{\rho}_{eff}(\phi_0 = 70°)$ (solid lines) compared to $\tilde{\rho}_{eff}(\phi_0 = 70°, \phi_{max} = 75°, \phi_{min} = 65°)$ (dashed lines) calculated for a three phase model consisting of a 1 μm 1.06×10^{19} *n*-doped $In_{0.66}Ga_{0.34}As$ (sample J in section 1.8.2) on an InP substrate. Focusing causes as about a 0.5° drop in Ψ, a 0.8° reduction in Δ, and a slight damping of the interference fringes in Δ below the bandgap of $In_{0.66}Ga_{0.34}As$. To see how these changes affect the inferred dielectric function, we have extracted a dielectric function for a three-phase model, a single angle of incidence, and our calculated $\tilde{\rho}_{eff}$ considering focusing effects, shown by the dashed lines in Fig. B2. The solid lines in Fig. B2 show the actual dielectric of $In_{0.66}Ga_{0.34}As$. The best data were obtained for an epilayer thickness of 1.015 μm (instead of 1 μm). For this best fit, there are deviations of up to 0.4 and large bumps below the bandgap in the dielectric function. The effects seen in Fig. B2 are probably larger than in our data since the actual focusing angle is probably less than that assumed for these calculations and interference effects were reduced for our samples since the interface between $In_{0.66}Ga_{0.34}As$ and InP was not abrupt, but instead was modeled to be about 100 Å. However, Fig. B2 shows how any inaccuracies in $\tilde{\rho}$ can be magnified in extracted dielectric functions.

Reproduced with permission of the copyright owner. Further reproduction prohibited without permission.

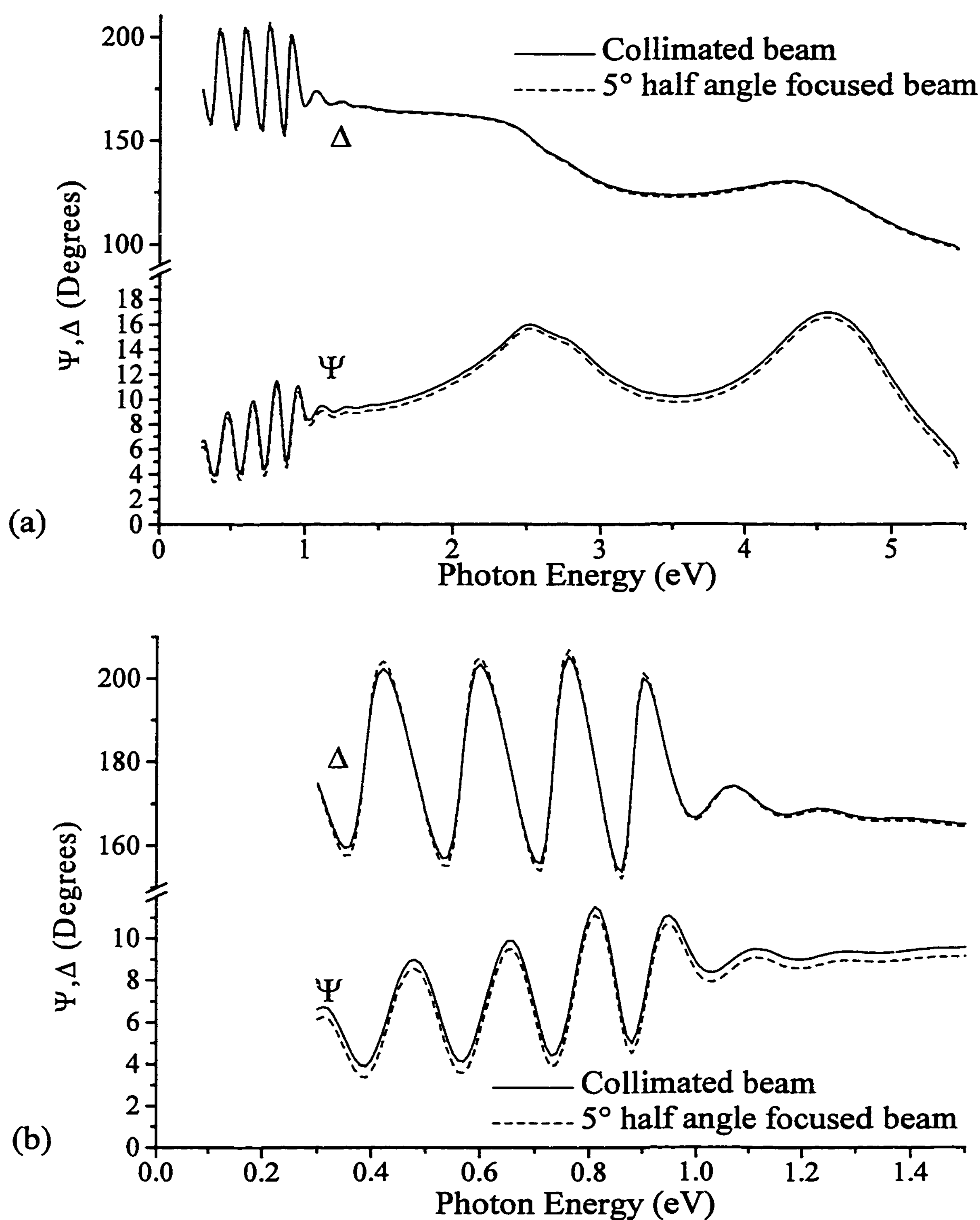

Figure B1. Simulation of ellipsometric parameters using a three phase model with and without focusing effects considered (solid and dashed lines, respectively). The structure consists of 1 μm 1.06×10^{19} *n*-doped $In_{0.66}Ga_{0.34}As$ (sample J in section 1.8.2) on an InP substrate. (a) Ψ and Δ for the range 0.3-5.5 eV. (b) Ψ and Δ near and below the bandgap of the $In_{0.66}Ga_{0.34}As$ layer - 0.3-1.5 eV.

Reproduced with permission of the copyright owner. Further reproduction prohibited without permission.

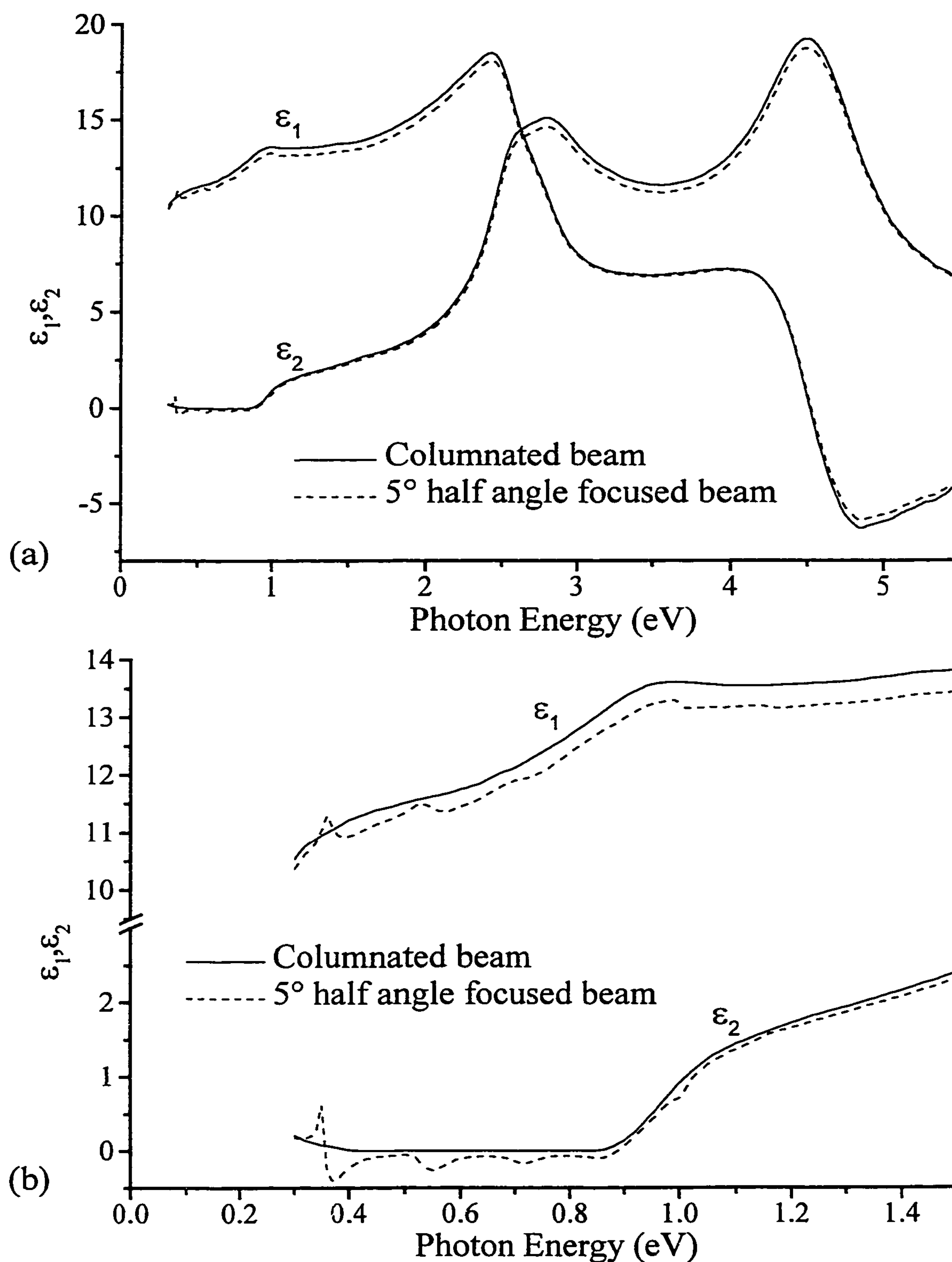

Figure B2. Dielectric function of the 1.06×10^{19} *n*-doped InGaAs layer as extracted using a three phase model with InP substrate for the ellipsometric parameters given in Fig. B1. (solid and dashed lines, respectively). The structure consists of 1 μm (sample J in section 1.8.2) on an InP substrate. (a) ε_1 and ε_2 for the range 0.3-5.5 eV. (b) Ψ and Δ near and below the bandgap of InGaAs: 0.3-1.5 eV.

Reproduced with permission of the copyright owner. Further reproduction prohibited without permission.

References

[1] T. Holden, P. Ram, F.H. Pollak, J.L. Freeouf, B.X. Yang, and M.C. Tamargo, Phys. Rev. B **56**, 4037 (1997).

[2] Y. Pétroff and M. Balkanski, Phys. Rev. B **3**, 3299 (1971).

[3] J.E. Rowe, F.H. Pollak, M. Cardona, Phys. Rev. Lett **22**, 933 (1969).

[4] M. Chandrapal and F.H. Pollak, Solid State Comm. **18**, 1263 (1976).

[5] C. Tanguy, Solid State Commun. **98**, 65 (1996).

[6] M. Chandrasekhar and F.H. Pollak, Phys. Rev. B **15**, 2127 (1977).

[7] P.Y. Yu and M. Cardona, *Fundamentals of Semiconductors: Physics and Materials Properties*, (Springer, Berlin, 1996).

[8] M. Muñoz, K. Wei, F.H. Pollak, J.L. Freeouf, and G.W. Charache, to be published Phys. Rev. B.

[9] M. Muñoz, K. Wei, F.H. Pollak, J.L. Freeouf, C.A. Wang, and G.W. Charache, submitted to J. Appl. Phys.

[10] K. Wei, F.H. Pollak, J.L. Freeouf, D. Shvydka, and A.D. Compaan, J. Appl. Phys. **85**, 7418 (1999).

[11] M. Rohlfing and S.G. Louie, Phys. Rev. Lett. **81**, 2312 (1998).

[12] S. Albrecht, L. Reining, R. Del Sole, and G. Onida, Phys. Rev. Lett. **80**, 4510 (1998).

[13] B. Drévillon and V. Yakovlev, in *Real Time Studies on the Growth and Structure of Thin Films*, ed. K. Vedam (Academic Press, New York, 1993).

Reproduced with permission of the copyright owner. Further reproduction prohibited without permission.

[14] I. Kamiya, D.E. Aspnes, L.T. Florez, and J.P. Harbison, Phys. Rev. B **24**, 15 894 (1992).

[15] D. E. Aspnes, J. P. Harbison, A. A. Studna, L. T. Florez, and M. K. Kelly, J. Vac. Sci. Technol. A **6**, 1127 (1988).

[16] O. Acher and B. Drévillon, Rev. Sci. Instrum. **63**, 5332 (1992).

[17] D.E. Aspnes and A.A. Studna, Phys. Rev. Lett. **54**, 1956 (1985).

[18] T. Holden, F.H. Pollak, J.L. Freeouf, D. McInturff, J.L. Gray, M. Lundstrom, and J.M. Woodall, Appl. Phys. Lett. **70**, 1107 (1997).

[19] T. Holden, W.D. Sun, F.H. Pollak, J.L. Freeouf, D. McInturff, and J.M. Woodall, Phys. Rev. B **58**, 7795 (1998).

[20] T. Holden, W.D. Sun, F.H. Pollak, J.L. Freeouf, D. McInturff, and J.M. Woodall, *Proceedings of the 24th International Conference on the Physics of Semiconductors*, Jerusalem, 1998, ed. D. Gershoni (World Scientific, Singapore)

[21] Y.H. Chen and Z. Yang, Appl. Phys. Lett. **73**, 1667 (1998).

[22] S.E. Acosta-Ortiz and A Lastras-Martínez, Phys. Rev. B **40**, 1426 (1989).

[23] H. Tanaka, E. Colas, I. Kamiya, D.E. Aspnes, and R. Bhat, Appl. Phys. Lett. **59**, 3443 (1991).

[24] Z. Yang, Y.H. Chen, and Y. Wong, Appl. Phys. Lett. **73**, 1520 (1998).

[25] Y.H. Chen, Z. Yang, R.G. Li, Y. Wong, and Z.G. Wang, Phys. Rev. B **55**, R7378 (1997).

[26] J. S. Luo, J. M. Olson, Sarah R. Kurtz, K. A. Bertness, M. E. Raikh, and E. V. Tsiper, Phys. Rev B **51**, 7603 (1994).

Reproduced with permission of the copyright owner. Further reproduction prohibited without permission.

[27] Z.C. Feng, E. Armour, I. Ferguson, R.A. Stall, T. Holden, L. Malikova, J.Z. Wan, F.H. Pollak, and M. Pavlosky, J. Appl. Phys. **85**, 3824 (1999).

[28] S.H. Wei and A. Zunger, Phys. Rev. B **51**, 14 110 (1995).

[29] J. S. Luo, J. M. Olson, and M.C. Wu, J. Vac. Sci. Technol. B **13**, 1755 (1995).

[30] L.F. Lastras-Martínez and A. Lastras-Martínez, Phys. Rev. B **54**, 10 726 (1996).

[31] K. Hingerl, T. Yasuda, T. Hanada, S. Miwa, K. Kimura, A. Ohtake, and T. Yao, J. Vac. Sci Technol B **16**, 2342 (1998).

[32] Z. Yang, G. K. Wong, I. K. Sou, and Y. H. Yeung, Appl. Phys. Lett. **66**, 2235 (1995).

[33] T. Yasuda, L. H. Kuo, K. Kimura, S. Miwa, C. G. Jin, K. Tanaka, and T. Yao, J. Vac. Sci. Technol. B **14**, 3052 (1996).

[34] B. Koopmans, B. Richards, P. Santos, K. Eberl, and M. Cardona, Appl. Phys. Lett. **69**, 782 (1996).

[35] P. Drude, Ann Phys. **32**, 584 (1887).

[36] P. Drude, Ann Phys. **34**, 489 (1888).

[37] P. Drude, Ann Phys. **39**, 481 (1890).

[38] E.D. Palik, *Handbook of Optical Constants* (Academic, Orlando, Fl 1985).

[39] E.D. Palik, *Handbook of Optical Constants II* (Academic, Orlando, Fl 1991).

[40] E.D. Palik, *Handbook of Optical Constants III* (Academic, Orlando, Fl 1997).

[41] D.E. Aspnes and A.A. Studna, Appl. Opt. **14**, 220 (1975).

[42] R.M.A. Azzam and N.M. Bashara, Ellipsometry and Polarized Light, (North Holland, Amsterdam, 1977).

Reproduced with permission of the copyright owner. Further reproduction prohibited without permission.

[43] D.E. Aspnes, J. Vac. Sci. Technol. **17** (1980) 1057.; Also see sec 1.5.2 for an explanation.

[44] K. Vedam, Thin Solid Films **313-314**, 1 (1998).

[45] B. Drévillon, J. Perrin, R. Marbot, A. Violet, and J.L. Dalby, Rev. Sci. Instrum. **53**, 969 (1982).

[46] B. Drévillon, Prog. in Cryst. Growth and Charact. **27**, 1-87 (1993).; O. Archer, E. Bigan, and B. Drévillon, Rev. Sci. Instrum. **60**, 65 (1989).

[47] D. E. Aspnes and A. A. Studna, Phys. Rev. B **27**, 985 (1983).

[48] D.E. Aspnes and J.B. Theeten, Phys. Rev. Lett. **43**, 1046 (1979).

[49] T. Yasuda and D. E. Aspnes, Applied Optics **33**, 7435 (1994).

[50] A. Röseler, *Infrared Spectroscopic Ellipsometry*, (Akademie-Verlag, Berlin, 1990).

[51] J.D. Jackson, *Classical Electrodynamics*, (John Wiley and Sons, New York, 1975), Ch. 7.

[52] D.E. Aspnes, in *Optical Properties of Solids: New Developments*, ed. B.O. Seraphin (North-Holland, Amsterdam, 1976), pp. 799-843.

[53] D. E. Aspnes, B. Schwartz, A. A. Studna, L. Derick, and L. A. Koszi, J. App. Phys **78**, 3510 (1977).

[54] D.E. Aspnes, Am. J. Phys. **50**, 704 (1982).

[55] J.D. Jackson, *Classical Electrodynamics*, (John Wiley and Sons, New York, 1975), Ch. 4.

[56] M.L. Cohen and J.R. Chelikowsky, *Electronic Structure and Optical Properties of Semiconductors*, (Springer-Verlag, New York, 1988).

Reproduced with permission of the copyright owner. Further reproduction prohibited without permission.

[57] N.W. Ashcroft and N.D. Mermin, *Solid State Physics*, (Saunders College Publishing, New York, 1976).

[58] M. Cardona, *Modulation Spectroscopy*, Solid State Physics, Suppl. 11 (Academic, New York 1967).

[59] S. M. Kelso, D. E. Aspnes, M. A. Pollack, and R. E. Nahory, Phys. Rev. B **26**, 6669 (1982).

[60] M. Erman, J.B. Theeten, P. Chambon, S.M. Kelso, and D.E. Aspnes, J. Appl. Phys. **56**, 2664 (1984).

[61] P. Lautenschlager, M. Garriga, S. Logothetidis, and M. Cardona, Phys. Rev. B **35** 9174 (1987).

[62] S. Adachi, Phys. Rev. B **41**, 1003 (1990); K. Sato and S. Adachi, J. Appl. Phys. **73**, 926 (1993); S. Adachi, T. Kimura, and N. Suzuki, J. Appl. Phys. **74**, 3435 (1993).

[63] R.J. Elliott, Phys. Rev. **108**, 1384 (1957).

[64] C.C. Kim and S. Sivanathan J. Appl Phys. **78**, 4003 (1995).

[65] D.D. Sell and P. Lawaetz, Phys. Rev. Lett. **26**, 311 (1971).

[66] A.R. Goñi, A. Cantarero, K. Syassen, and M. Cardona, Phys. Rev. B **41**, 10 111 (1990).

[67] M. Shinada and S. Sugano, J. Phys. Soc. Japan **21**, 1936 (1966).

[68] C. Tanguy, Phys. Rev. Lett. **75**, 4090 (1995).

[69] E.O. Kane, Phys. Rev. **180**, 852 (1969).

Reproduced with permission of the copyright owner. Further reproduction prohibited without permission.

---

[70] S. Adachi, *Physical Properties of III-V Semiconductor Compounds: InP, InAs, GaAs, GaP, InGaAs, and InGaAsP*, (John Wiley & Sons, New York, 1993), Chapter 8; S. Adachi, Phys. Rev. B **41**, 1003 (1990).

[71] M. A. Haase, J. Qiu, J.M. Depuydt, and H. Cheng, Appl. Phys. Lett. **59**, 1272 (1991); H. Jeon, J. Ding, W. Xie, M. Kobayashi, R.L. Gunshor, and A. V. Nurmikko, *ibid.* **59**, 3619 (1991); G.F. Nuemark, R.M. Park, and J.M. DePuydt, Phys. Today **47** (**6**), 26 (1994).

[72] S. Ivanov *et al*, Appl. Phys. Lett. **73**, 2104 (1998); S. Taniguchi *et al*, Electron. Lett. **32**, 552 (1996); A. Waag *et al*, J. Cryst. Growth **184/185**, 1 (1998)

[73] E. Kato, H. Noguchi, M. Nagai, H. Okuyama, S. Kijima, and A. Ishibashi, Electron.Lett.**34**, 282 (1998).

[74] G. Guha, J.M. DePuydt, J. Liu, G.E. Hofler, M.A. Haase, B.J. Wu, and H. Cheng, Appl. Phys. Lett. **63**, 3023 (1993).

[75] L.H. Kue, L. Salamanca-Riba, B.J. Wu, G. Hofer, J.M. Depuydt, and H. Cheng, Appl. Phys. Lett. **67**, 3298 (1995).

[76] S.Tomiya, H. Noguchi, Y. Sanaka, T. Hino, S. Taniguchi, and A. Ishibashi, Appl. Phys. Lett. **74**, 1824 (1999).

[77] L. Malikova, W. Krystek, F.H. Pollak, N. Dai, A. Cavus, and M.C. Tamargo, Phys. Rev. B **54**, 1819 (1996).

[78] F. Herman R.L. Kortum, C.D. Kuglin, and J.L. Shay, *Proceeding of the 1967 International Conference on II-VI Semiconducting Compounds*, edited by D.G. Thomas (Benjamin, New York, 1967), p. 503.

Reproduced with permission of the copyright owner. Further reproduction prohibited without permission.

[79] S. Adachi and T. Taguchi, Phys. Rev. B **43**, 9569 (1991).

[80] R. Dahmani, L. Salamanca-Riba, N.V. Nguyen, D. Chandler-Horowitz, and B.T. Jonker, J. Appl. Phys. **76**, 514 (1994).

[81] C.C. Kim, S. Sivananthan, Phys. Rev. B **53**, 1475 (1996).

[82] Y.D. Kim, S.L. Cooper, M.V. Klein, and B.T. Jonker, Appl. Phys. Lett. **62**, 2387 (1993).

[83] Y.D. Kim, M.V. Klein, S.F. Ren, Y.C. Chang, H. Luo, N. Samarth, and J.K. Furdyna, Phys. Rev. B **49**, 7262 (1994).

[84] J. Lee, B. Hong, J.S. Burnham, R.W. Collins, F. Flack, and N. Samarth, in *Diagnostic Techniques for Semiconductor Materials Processing II*, edited by S.W. Pang *et al.*, MRS Symposia Proceedings No. 406 (Materials Research Society, Pittsburgh, 1996), p. 377.

[85] J. Lee, B. Hong, R.W. Collins, A.R. Heyd, F. Flack, and N. Samarth, Appl. Phys. Lett. **69**, 2273 (1996).

[86] T. Holden, P. Ram, F.H. Pollak, J.L. Freeouf, B.X. Yang, and M.C. Tamargo, in *Proceedings of the 23rd International Conference on the Physics of Semiconductors, Berlin, 1996*, edited by M. Scheffler and R. Zimmermann (World Scientific, Singapore, 1996), p. 289.

[87] E. Snoeks, S. Herko, L. Zhao, B. Yang, A. Cavus, L. Zeng, and M.C. Tamargo, Appl. Phys. Lett. **70**, 2259 (1997).

[88] L.M. Liu *et al.*, J. Vac. Sci. Technol. B **13**, 2238 (1995).

Reproduced with permission of the copyright owner. Further reproduction prohibited without permission.

[89] F.A. Jenkins and H.E. White, *Fundamentals of Optics*, 3rd ed. (McGraw-Hill, New York, 1957), p. 472.

[90] J.R. Chelikowsky and M.L. Cohen, Phys. Rev. B **14**, 556 (1976).

[91] S. Ninomiya and S. Adachi, J. Appl. Phys. **78**, 4681 (1995).

[92] C.C. Kim, J.W. Garland, P.M. Raccah, Phys. Rev. B **45**, 11 749 (1992).

[93] C. Trallero-Giner, R. Zimmermann, M. Trinn, and R. Ulbrich, in *Proceedings of the 23rd International Conference on the Physics of Semiconductors, Berlin, 1996*, p. 345.

[94] J.E. Raynolds, C.R. Geller, G.W. Charache, T. Holden, and Fred H. Pollak, in *Proceedings of the 4th NREL Thermophotovoltaic Generation of Electricity Conference*, Denver, 1998, ed. T.J. Coutts, J.P. Breener, and C.S. Allman, AIP Conf. Proc. 460 (American Institute of Physics, Woodbury, 1999), p. 39.

[95] G.W. Charache, D.M. Depoy, J.E. Raynolds, P.F. Baldasara, K.E. Miyano, Todd Holden, Fred H. Pollak, P.R. Sharps, M.L. Timmons, C.B. Geller, W. Maanstadt, R. Asahi, and A.J. Freeman, J. Appl. Phys. **86**, 452 (1999).

[96] G.W. Charache *et al.*, J. Electron. Mat. **27**, 1038 (1998).

[97] C. Pickering, R. T. Carline, M. T. Emeny N. S. Garawal, and L. K. Howard, Appl. Phys. Lett. **60**, 2412 (1992).

[98] M. Kuball, M. K. Kelly, M. Cardona, K. Köhler, and J. Wagner, Phys. Rev. B **49**, 15 569 (1994).

[99] S.H. Pan, H. Shen, Z. Hang, F.H. Pollak, W. Zhuang, Q. Xu, A.P. oth, R. Masut, C. LeCelle, and D. Morris, Phys Rev B **38**, 3375 (1988).

Reproduced with permission of the copyright owner. Further reproduction prohibited without permission.

---

[100] J.E. Raynolds, C.B. Geller, G.W. Charache, T. Holden, and F.H. Pollak, in *Thermophotovoltaic Generation of Electricity: Fourth NREL Conerence*, edited by T.J. Coutts, J.P. Benner, and C.S. Allman, AIP Conf. Proc. **460**, 457 (1999).

[101] G.W. Charache, C.M. DePoy, J.L. Egley, R.J. Dziendziel, P.R. Sharps, M.L. Timmons, R. E. Fahey, K. Zhang, and J.M. Borrego, AIP Conf. Proc. **401**, 215 (1997).

[102] M. Cardona, F.H. Pollak, and K.L. Shaklee, J. Phys. Soc. Jpn., Suppl. **21**, 89 (1966).

[103] V.L. Berkovits, I.V. Makarenko, T.A. Minashvili, and V.I. Safarov, Fiz. Tekh. Poluprovodn. **20**, 1037 (1987) [Sov. Phys. Semicond. **20**, 654 (1986).

[104] D.E. Aspnes, E. Colas, A.A. Studna, R. Bhat, M.A. Koza, and V.G. Keramidas, Phys. Rev. Lett. **61**, 2782 (1988).

[105] See, for example, D.E. Aspnes, Mat. Res. Soc. Symp. Proc. **324**, 3 (1994); W. Richter, Phil. Trans. R. Soc. London **A344**, 453 (1993); O. Acher, S.M. Koch, F. Omnes, M. Defour, M. Razeghi, and B. Drévillon, J. Appl. Phys. **68**, 3564 (1990).

[106] *Proceedings of the Society of Photo-optic Instrumentation Engineers*, ed. F.H. Pollak, M. Cardona, and D.E. Aspnes (SPIE, Bellingham, 1990), Vol. **1286**, p. 31.

[107] C.C. Kim and S. Sivananthan, Mat. Res. Soc. Symp. Proc. **406**, 319 (1996).

[108] H.H. Farrell, M.C. Tamargo, T.J. Gmitter, A.L. Weaver, and D.E. Aspnes, J. Appl. Phys. **70**, 1033 (1991).

[109] M. Leibovitch, P. Ram, L. Malikova, F.H. Pollak, J.L. Freeouf, L. Kronik, B. Mishori, Y. Shapira, A.R. Clawson, and C.M. Hanson, J. Vac. Sci. Technol. B **14**, 3089 (1996).

Reproduced with permission of the copyright owner. Further reproduction prohibited without permission.

[110] K.C. Rose, S.J. Morris, D.I. Westwood, D.A. Woolf, R.H. Williams, and W. Richter, Appl. Phys. Lett. **66**, 1930 (1995).

[111] D. Paget, J.E. Bonner, V.L. Berkovits, P. Chiaradia, and J. Avila, Phys. Rev. B **53**, 4604 (1996).

[112] F.H. Pollak and M. Cardona, Phys Rev. **172**, 816 (1968).

[113] F.H. Pollak, in *Semiconductors and Semimetals*, vol. 55 (Paul, William, and Suski eds.), (Academic, Boston, 1998), p. 235.

[114] J.F. Nye, *Physical Properties of Crystals* (Oxford University Press, London, 1969), Ch. 7.

[115] M.S. Abrahams, J. Blanc, and C.J. Buiocchi, Appl. Phys. Lett. **21**, 185 (1972).

[116] J.P. Hirth and J. Lothe, *Theory of Dislocations* (Kreiger, Malabar, FL, 1992), p. 373.

[117] J.D. Eshelby, W.T. Read, and W. Shockley, Acta Metal. **1**, 251 (1953).

[118] K. Yamashita et al. - Phys. Rev. B, Vol. 53, No 23, p 15 713, 1996

[119] S.H. Wei and A. Zunger, Phys. Rev. B, **49**, 14 337 (1994).

[120] See, for example, M.R. Melloch, J.M. Woodall, E.S. Harmon, N. Otsuka, F.H. Pollak and D.D. Nolte, *Annual Review of Materials Science*, ed. B.W. Wessels, E.N. Kaufman, J.A. Giordmaine and J.B. Wachtman, Jr., Vol. **25**, p. 547 (1995) and references therein.

[121] R.M. Feenstra, J.M. Woodall, and G.D. Pettit, Phys. Rev. Lett. **71**, 1176 (1993).

[122] R.M. Feenstra, A. Vaterlaus, J.M. Woodall, and G.D. Pettit, Appl. Phys. Lett. **63**, 2528 (1993)].

Reproduced with permission of the copyright owner. Further reproduction prohibited without permission.

[123] S. Hong, R. Reifenberger, D.B. Janes, D. McInturff, and J.M. Woodall, Appl. Phys. Lett. **68**, 2258 (1996).

[124] S.M. Sze, in *Physics of Semiconductor Devices*, 2nd ed. (Wiley, New York, 1981).

[125] H. Shen, M. Dutta, L. Fotiadis, P.G. Newman, R.P. Moerkirk, W.H. Chang, and R.N. Sacks, Appl. Phys. Lett. **57**, 2118 (1990).

[126] Silvaco Data Systems, Santa Clara, CA 94054.

[127] H. Shen and M. Dutta, J. Appl. Phys. **78**, 2151 (1995).

[128] M. Meshkinpour, M.S. Goorsky, B. Jenichen, D.C. Streit, and T.R. Block, J. Appl. Phys. **81**, 3124 (1997).

[129] MRS Bull. **21**, 4 (1996), articles by A. Cullis, C. Roland, D.E. Jesson *et al.*, and F.K. LeGoues.

[130] Z.J. Radzimski, B.L. Jiang, G.A. Rozgonyi, T.P. Humpheys, N. Hamaguchi, and S.M. Bedair, J. Appl. Phys. **64**, 2328 (1988).

[131] D.H. Rich, T. George, W.T. Pike, J. Maserjian, F.J. Grunthaler, and A. Larsson, J. Appl. Phys. **72**, 5834 (1992).

[132] R. Köhler, Appl. Phys. A **58**, 149 (1994).

[133] P.F. Fewster, Semicond. Sci. Technol. **8**, 1915 (1993).

[134] V.M. Kaganer, R. Köhler, M. Schmidbauer, R. Opitz, and B. Jenichen, Phys. Rev. B **55**, 1793 (1997).

[135] G. Armelles, J. Meléndez, and P. Castrillo, Phys. Rev. B **49**, 17 444 (1994).

Reproduced with permission of the copyright owner. Further reproduction prohibited without permission.

[136] D.C. Streit, K.L. Tan, R.M. Dia, J.K. Liu, A.C. Han, J.R. Velebir, S.K. Wang, T.Q. Trinh, P.D. Chow, P.H. Liu, and H.C. Yen, IEEE Electron Device Lett. **12**, 149 (1991).

[137] M. Meshkinpour, M.S. Goorsky, G. Chu, D.C. Streit, T. Block, and M. Wojtowicz, Appl. Phys. Lett. **66**, 748 (1995).

[138] A. Gomyo, T. Suzuki, K. Kobayashi, S. Kawata, I. Hino, and T. Yuasa, Appl. Phys. Lett. **50**, 673 (1987).

[139] M. Kondow, H. Kakibayashi, and S. Minagawa, J. Cryst. Growth **99**, 291 (1988).

[140] D.J. Friedman, J.G. Zhu, A.E. Kibbler, J.M. Olson, and J. Moreland, Appl. Phys. Lett. **63**, 1774 (1993).

[141] A. Zunger and S. Mahajan, in *Handbook on Semiconductors*, edited by T.S. Moss and S. Mahajan (Elsevier Science B.V., 1994), Vol. 3, p. 1399.

[142] See, for example, W. Liu, E. Beam III, T. Kim, and A. Khatibzadeh, Int. J. High Speed Electron. Syst. **5**, 411 (1994) and refemeces therein.

[143] H. Sugawara, K. Itaya, H. Nozaki, and G. Hatakoshi, Appl. Phys. Lett. **61**, 1775 (1992).

[144] S.-H. Wei, B.B. Laks, and A. Zunger, Appl. Phys. Lett. **62**, 1937 (1993); S.-H. Wei and A. Zunger, Appl. Phys. Letts. **64**, 1676 (1994).

[145] S. Froyen, A. Zunger, and A. Mascarenhas, Appl. Phys. Lett. **68**, 2852 (1996).

[146] A.G. Thompson, R.A. Stall, P. Zawadzki, and G.H. Evans, J. Electron. Mater. **25**, 1494 (1995).

Reproduced with permission of the copyright owner. Further reproduction prohibited without permission.

[147] R.G. Alonso, A. Mascarenhas, G.S. Horner, K.A. Bertness, S.R. Kurtz, and J.M. Olson, Phys. Rev. B **48**, 11 833 (1993).

[148] S.R. Kurtz - J. Appl. Phys., Vol. 74, No 6, p 4 130, 1993

[149] J.E. Raynolds, C.R. Geller, G.W. Charache, T. Holden, and F.H. Pollak, in *Proceedings of the 4th NREL Thermophotovoltaic Generation of Electricity Conference*, Denver, 1998 ed. T.J. Coutts, J.P. Breener, and C.S. Allman, AIP Conf. Proc. **460** (American Institute of Physics, Woodbury, 1999), p. 39.

[150] K.K. Svitashev, A.I. Semenko, L.V. Semenenko, and V.K. Sokolov, Opt. Spectrosc. (USSR) **30**, 288 (1971).

[151] K.K. Svitashev, A.I. Semenko, L.V. Semenenko, and V.K. Sokolov, Opt. Spectrosc. (USSR) **34**, 542 (1973).

[152] D.O. Barsukov, G.M. Gusakov, and A.A. Komarnitskii, Opt. Spectrosc. (USSR) **64**, 782 (1988).

[153] J. Kircher, R. Henn, M. Cardona, P.L. Richards, and G.P. Williams, J Opt Soc Am B **14**, 705 (1997).

Reproduced with permission of the copyright owner. Further reproduction prohibited without permission.